

# DISSERTATION

SUBMITTED TO THE  
COMBINED FACULTIES FOR THE NATURAL SCIENCES AND FOR MATHEMATICS  
OF THE RUPERTO-CAROLA UNIVERSITY OF HEIDELBERG, GERMANY  
FOR THE DEGREE OF  
DOCTOR OF NATURAL SCIENCES

presented by:

**Florian Salopiata, M.Sc. Chemistry**

born in Freudenstadt, Germany

Oral examination: 19.12.2017



INVESTIGATION OF MOLECULAR MECHANISMS OF  
THERAPY RESISTANCE IN LUNG CANCER  
BY MATHEMATICAL MODELING

**Referees:** Prof. Dr. U. Klingmüller  
Prof. Dr. D.-P. Herten



*Whoever dedicates his life to searching out particular connections of nature will spontaneously be confronted with the question how they harmoniously fit into the whole.*

Werner Heisenberg



## Publications

Doleschel, D., Rix, A., Arns, S., Palmowski, K., Gremse, F., Merkle, R., **Salopiata, F.**, Klingmüller, U., Jarsch, M., Kiessling, F., Lederle, W. Erythropoietin improves the accumulation and therapeutic effects of carboplatin by enhancing tumor vascularization and perfusion. *Theranostics* **5**, 905–918 (2015). [PubMed:26000061].

Merkle, R., Steiert, B., **Salopiata, F.**, Depner, S., Raue, A., Iwamoto, N., Schelker, M., Hass, H., Wäsch, M., Böhm, M.E., Mücke, O., Lipka, D.B., Plass, C., Lehmann, W.D., Kreutz, C., Timmer, J., Schilling, M., Klingmüller, U. Identification of Cell Type-Specific Differences in Erythropoietin Receptor Signaling in Primary Erythroid and Lung Cancer Cells. *PLoS Comput. Biol.* **12**, e1005049 (2016). [PubMed:27494133].

Kuchenov, D., Laketa, V., Stein, F., **Salopiata, F.**, Klingmüller, U., Schultz, C. High-Content Imaging Platform for Profiling Intracellular Signaling Network Activity in Living Cells. *Cell Chem Biol* **23**, 1550–1559 (2016). [PubMed:27939899].

Robichon, K., Maiwald, T., Schilling, M., Schneider, A., Willemsen, J., Kreutz, C., Ehlting, C., Huang, J., Chakraborty, S., Huang, X., Böhm, **Salopiata, F.**, M.E., Damm, G., Seehofer, D., Lang, P.A., Bode, J.G., Binder, M., Bartenschlager, R., Timmer, J., Klingmüller, U. Interferon-induced antiviral response is enhanced by an Interleukin1 $\beta$ -mediated transient autocrine feedback, *submitted*.

Rodriguez-Gonzalez, A., Schelker, M., Raue, A., Steiert, B., **Salopiata, F.**, Adlung, L., Böhm, M.E., Stepath, M., Depner, S., Wagner, M.C., Merkle, R., Kramer, B.A., Lattermann, S., Wäsch, M., Franke, A., Klipp, E., Wuchter, P., Ho, A.D., Lehmann, W.D., Jarsch, M., Schilling, M., Timmer, J., Klingmüller, U. Model-optimized anaemia treatment in Non-Small-Cell Lung Carcinoma patients, *submitted*.

**Salopiata, F.**, Hass, H., Hänselmann, S., Qiang, Y., Steiert, B., Kreutz, C., Schneider, Braun, F., Dvornikov, D., M., Meister, M., Warth, A., Muley, T., Thomas, M., Raue, A., Rohr, K., Herten, D.-P., Schilling, M., Timmer, J., Klingmüller, U. Receptor Expression Ratio of EGFR and MET Determines Resistance to EGFR Inhibition in Lung Cancer, *submitted*.

Haenselmann S., Yserentant K., Braun F., Chmielewicz W., **Salopiata, F.**, Klingmüller U., Herten, D.P., The Degree of Labeling of SNAPf-tag and HaloTag for different single-molecule labeling conditions, *in preparation*.



## Abstract

Lung cancer is the leading cause of cancer-related deaths world-wide. Due to late diagnosis and early metastatic spread most patients cannot undergo surgery and systemic therapies have to be applied. Most of those patients receive chemotherapy and patients with activating mutation in the epidermal growth factor receptor (EGFR) can receive targeted therapies with tyrosine kinase inhibitors (TKIs) against EGFR. In case of chemotherapy, many patients suffer from anemia and have to be treated e.g. with erythropoiesis stimulating agents (ESAs). Yet, treatment with ESAs is suspected to induce resistance against the chemotherapeutic drug. Many lung cancer patients treated with EGFR-TKIs also rapidly develop therapy resistance against the treatment. This resistance can be mediated by upregulation of a related receptor tyrosine kinase, the hepatocyte growth factor (HGF) receptor MET. To understand the complex mechanisms leading to therapy resistance, a systems biology approach was applied in this work.

To investigate the differential responses of ESAs on healthy or tumor cells, a mathematical model was developed that identifies cell type-specific differences and that predicts possible targets for combinational therapies to inhibit survival signaling in tumor cells, but not in healthy erythroid progenitors. Evidence was obtained that the erythropoietin receptor of endothelial cells is phosphorylated upon ESAs stimulation leading to increased vascularization and accessibility of chemotherapeutics in xenograft mouse models. To determine an optimal ESA dose for each anemic cancer patient, a mathematical model of ESAs depletion and induced signal transducer and activator of transcription (STAT)5 signal activation was developed. It was shown on the phosphorylation level of STAT5 that ESAs with a low binding affinity such as the pegylated CERA induce tumor cells less than healthy erythroid progenitors compared to ESAs with a high binding affinity such as Epo $\beta$ . Therefore, ESAs with low binding affinity were proposed as safer option to treat chemotherapy-related anemia.

To identify the mechanism causing MET-mediated resistance against EGFR-TKIs, time- and dose-resolved activation of signal transduction components in two non-small-cell lung cancer cell lines was measured upon stimulation with EGF, HGF or co-stimulation. A cell type-specific enhanced activation of MET upon co-stimulation was observed. Using a mathematical model to describe the cell-specific dynamics and using single-molecule live-cell microscopy, it could be identified that formation of EGFR:MET heterodimers with a reduced internalization rate is the mechanism leading to enhanced activation of MET upon co-stimulation. Further, it was shown that the EGFR to MET protein expression ratio determines the strength of the enhancement explaining the observed cell type specificity. This effect was found to influence efficacy of EGFR-TKIs by the formation of TKI-inhibited heterodimers. It was shown that by decreasing the expression of MET by the pharmacologic antibody MM-131, the efficacy of EGFR-TKIs is increased suggesting an EGFR/MET expression ratio-based patient stratification and novel combinatorial treatments to reduce therapy resistance. In sum, this work provides several new insights into mechanisms of signal transduction of cancer cells affecting EGFR-TKI efficacy and ESA safety and suggests mechanism-based treatment strategies to increase the therapy response.



## Zusammenfassung

Lungenkrebs verursacht weltweit die meisten krebsbedingten Todesfälle. Aufgrund der späten Diagnose und frühen Metastasenbildung sind die meisten Patienten inoperabel und systemische Therapien wie Chemotherapie müssen angewendet werden. Patienten mit aktivierender Mutation in dem epidermalen Wachstumsfaktor-Rezeptor (EGFR) können zielgerichtete Therapien mit Tyrosinkinaseinhibitoren (TKIs) gegen EGFR erhalten. Viele Chemotherapie-Patienten leiden an Anämie und müssen z.B. mit Erythropoese-stimulierenden Substanzen (ESAs) behandelt werden, die möglicherweise jedoch Resistenz gegen die Chemotherapie induzieren. Auch viele Lungenkrebs-Patienten, die mit EGFR-TKIs behandelt werden, entwickeln schnell Therapieresistenz, die durch verstärkte Expression einer verwandten Rezeptor-Tyrosinkinase, des Hepatozytenwachstumsfaktor (HGF)-Rezeptors MET, vermittelt werden kann. Um die komplexen Mechanismen der Therapieresistenz zu verstehen, wurde in dieser Arbeit ein systembiologischer Ansatz angewendet.

Um die unterschiedlichen Antworten von ESAs auf gesunde oder Tumor-Zellen zu untersuchen, wurde ein mathematisches Modell entwickelt, das Zelltyp-spezifische Unterschiede identifizieren und mögliche Zielstrukturen vorhersagen kann, die Tumorzellen, aber nicht gesunde erythroide Vorläuferzellen inhibieren. Es wurde nachgewiesen, dass der Erythropoietin-Rezeptor von Endothelzellen bei ESA-Stimulation phosphoryliert wird, was zu einer erhöhten Vaskularisierung und Zugänglichkeit von Chemotherapeutika in Xenograft-Mausmodellen führt. Um eine optimierte ESA-Dosis für unter Anämie leidende Krebspatienten zu bestimmen, wurde ein mathematisches Modell des ESA-Abbaus und der induzierten Signalaktivierung von STAT5 entwickelt. Es wurde gezeigt, dass ESAs mit einer niedrigen Bindungsaffinität Tumorzellen weniger induzieren als gesunde erythroide Vorläuferzellen. Sie wurden daher als sicherere Behandlungsoption von Chemotherapie-bedingter Anämie vorgeschlagen.

Um den Mechanismus der MET-vermittelten Resistenz gegen EGFR-TKIs zu identifizieren, wurde die Aktivierung von Signaltransduktionskomponenten in zwei Lungenkrebszelllinien nach Stimulation mit EGF, HGF oder Co-Stimulation zeit- und dosis aufgelöst gemessen. Eine Zelltyp-spezifische verstärkte Aktivierung von MET unter Co-Stimulation wurde beobachtet. Unter Verwendung eines mathematischen Modells zur Beschreibung der zellspezifischen Dynamik und unter Verwendung von Einzelmolekül-Mikroskopie konnte die Bildung von EGFR:MET-Heterodimeren mit einer reduzierten Internalisierungsrate als zugrunde liegender Mechanismus identifiziert werden. Weiterhin wurde gezeigt, dass das EGFR zu MET Expressionsverhältnis den Umfang der Verstärkung bestimmt und dass dieser Effekt die Wirksamkeit von EGFR-TKIs durch Inhibierung der Heterodimere beeinflusst. Es wurde gezeigt, dass die Wirksamkeit von EGFR-TKIs durch eine Verringerung der Expression von MET durch den pharmakologischen Antikörper MM-131 erhöht wird. Dieser Mechanismus legt eine Verwendung des EGFR/MET-Expressionsverhältnisses zur Patientenstratifizierung nahe und sagt neuartige Kombinations-Behandlungen zur Reduzierung von Therapieresistenz vorher. Zusammengefasst liefert diese Arbeit verschiedene neue Einblicke in Mechanismen der Signaltransduktion, welche die Wirksamkeit von EGFR-TKIs und ESAs beeinflussen, und schlägt Strategien vor um das Ansprechen auf die Therapien zu erhöhen.



# Contents

<b>Abstract</b>	<b>III</b>
<b>Zusammenfassung</b>	<b>V</b>
<b>Acronyms</b>	<b>XI</b>
<b>1 Introduction</b>	<b>1</b>
1.1 Lung cancer therapy . . . . .	1
1.1.1 Therapeutic EGFR inhibitors . . . . .	2
1.1.2 Chemotherapy in lung cancer . . . . .	4
1.1.3 Anemia in lung cancer . . . . .	6
1.2 Erythropoietin receptor signal transduction . . . . .	7
1.3 Epidermal growth factor receptor signal transduction . . . . .	8
1.4 MET receptor signal transduction . . . . .	13
1.5 EGFR/MET crosstalk . . . . .	15
1.6 Systems biology . . . . .	16
1.6.1 Mathematical models of the EpoR-pathway . . . . .	20
1.6.2 Mathematical models of the EGFR and MET pathways . . . . .	21
1.7 Therapy resistance . . . . .	22
1.7.1 EGFR-TKI resistance . . . . .	22
1.7.2 Chemotherapy resistance . . . . .	27
1.8 Objectives . . . . .	30
<b>2 Results</b>	<b>31</b>
2.1 Impact of Epo on erythroid progenitor and lung cancer cells during chemotherapy . . . . .	31
2.2 Erythropoietin alters vascularization and drug supply in mouse xenografts . . . . .	38
2.3 Binding kinetics of erythropoiesis stimulating agents changes cellular responses . . . . .	40
2.4 EGFR and MET receptor abundance influence EGFR-TKI efficacy . . . . .	46
2.4.1 Quantitative measurements of protein abundance of signaling components . . . . .	46

2.4.2	Quantitative analysis of EGF/HGF-induced signal transduction responses . .	50
2.4.3	Development of a mathematical model of EGFR and MET signal transduction	53
2.4.4	Validation of EGFR:MET heterodimerization by live-cell imaging . . . . .	57
2.4.5	Reduction of the mathematical model of EGFR:MET heterodimerization . .	64
2.4.6	EGFR to MET expression ratio determines enhanced MET phosphorylation .	65
2.4.7	Reduced EGFR:MET heterodimer internalization causes enhanced MET phos- phorylation . . . . .	68
2.4.8	HGF rescues cells from EGFR-TKI-induced inhibition . . . . .	71
2.4.9	Influence of EGFR-TKI treatment on MET phosphorylation . . . . .	72
2.4.10	Influence of TKI treatment and EGF/HGF co-stimulation on cell viability . .	73
2.4.11	Influence of EGFR/MET ratio on EGFR-TKI-induced cell death . . . . .	74
2.4.12	Clinical significance of EGFR-TKI treatment . . . . .	76
<b>3</b>	<b>Discussion</b>	<b>81</b>
3.1	Impact of Epo on erythroid progenitor and lung cancer cells during chemotherapy .	81
3.2	Erythropoietin alters vascularization and drug supply in mouse xenografts . . . . .	84
3.3	Binding kinetics of erythropoiesis stimulating agents changes cellular responses . . .	85
3.4	EGFR and MET receptor abundance influence EGFR-TKI efficacy . . . . .	88
3.5	Proposed further investigations . . . . .	100
<b>4</b>	<b>Material and methods</b>	<b>101</b>
4.1	Molecular biology techniques . . . . .	101
4.1.1	Polymerase chain reaction . . . . .	101
4.1.2	Molecular cloning of DNA fragments . . . . .	101
4.1.3	Transformation of E. coli cells . . . . .	102
4.1.4	Purification of plasmid DNA . . . . .	102
4.1.5	Construction of plasmids . . . . .	102
4.1.6	Methylation analysis . . . . .	105
4.2	Cell Culture Techniques . . . . .	106
4.2.1	Culture of human lung cancer cell lines . . . . .	106
4.2.2	Culture of Phoenix amphi/eco cells . . . . .	106
4.2.3	Culture of human umbilical vein endothelial cells . . . . .	107
4.2.4	Culture of patient-derived tumor cell lines . . . . .	107
4.2.5	Transfection of Phoenix amphi cells . . . . .	107
4.2.6	Retroviral spin transduction . . . . .	108

4.2.7	Flow cytometry . . . . .	108
4.3	Protein biochemistry . . . . .	109
4.3.1	Cell stimulation and lysis . . . . .	109
4.3.2	Immunoprecipitation . . . . .	109
4.3.3	SDS-PAGE . . . . .	110
4.3.4	Coomassie gels . . . . .	111
4.3.5	Immunoblot analysis . . . . .	111
4.3.6	Mass spectrometry . . . . .	111
4.3.7	Purification of recombinant proteins . . . . .	114
4.3.8	Determination of molecules per cell . . . . .	114
4.3.9	Proliferation analysis . . . . .	115
4.3.10	Microscopy . . . . .	116
4.3.11	Image analysis . . . . .	117
4.4	Mathematical modeling . . . . .	117
4.5	Patient data analysis . . . . .	118
<b>5</b>	<b>Bibliography</b>	<b>119</b>
<b>6</b>	<b>Appendix</b>	<b>141</b>
	<b>Acknowledgements</b>	<b>161</b>



## Acronyms

ABC	ATP-binding cassette
ADAM	a disintegrin and metalloproteinase
ALK	anaplastic lymphoma kinase
ATP	adenosine triphosphate
AUC	area under the curve
BCL	B-cell lymphoma
BFU-E	burst forming unit - erythroid
BSA	bovine serum albumin
CBL	Casitas B-lineage Lymphoma
CFU-E	colony forming unit - erythroid
CISH	cytokine-inducible SH2-domain containing protein
DEP	density-enhanced phosphatase
EGF	epidermal growth factor
EGFR	epidermal growth factor receptor
EML	echinoderm microtubule-associated protein-like
Epo	erythropoietin
EpoR	erythropoietin receptor
ERK	extracellular signal-regulated kinase
ESA	erythropoiesis stimulating agent
FCS	fetal calf serum
GAB	GRB2-associated binder
GRB	growth factor receptor-bound protein
GSH	glutathione
GST	glutathione S-transferase
Hb	hemoglobin
HB-EGF	heparin-binding EGF-like growth factor
HER	human epidermal growth factor receptor

HGF	hepatocyte growth factor
HGFL	HGF-like protein
HIF1 $\alpha$	hypoxia-inducible factor 1 $\alpha$
HSP	heat shock protein
HUVEC	human umbilical vein endothelial cells
IP	immunoprecipitation
IP <sub>3</sub>	inositol 1,4,5-trisphosphate
JAK	Janus kinase
JNK	c-Jun N-terminal kinase
MAPK	mitogen activated protein kinase
MEK	MAPK/ERK kinase
MMR	mismatch repair
mTORC	mammalian target of rapamycin complex
NER	nucleotide excision repair
NSCLC	non-small-cell lung cancer
ODE	ordinary differential equation
PD	programmed cell death protein
PDK	3-phosphoinositide-dependent kinase
PFS	progression-free survival
PI3K	phosphatidylinositol-4,5-bisphosphate 3-kinase
PIP <sub>2</sub>	phosphatidylinositol 4,5-bisphosphate
PIP <sub>3</sub>	phosphatidylinositol 3,4,5-trisphosphate
PLC $\gamma$	phospholipase C $\gamma$
PTB	phosphotyrosine-binding
PTEN	phosphatase and tensin homolog
PTP	protein tyrosine phosphatase
ROS	reactive oxygen species
RSK	p90 ribosomal S6 kinase

RTK	receptor tyrosine kinase
S6K	p70 ribosomal S6 kinase
SH	SRC homology
SHC	SH2 domain protein C
SHP	SRC homology region 2 domain-containing phosphatase
SOCS	suppressor of cytokine signaling
STAT	signal transducer and activator of transcription
TGF $\alpha$	transforming growth factor $\alpha$
TIRF	total internal reflection fluorescence
TKI	tyrosine kinase inhibitor
VEGF	vascular endothelial growth factor
wt	wild type



# 1 Introduction

## 1.1 Lung cancer therapy

Lung cancer is the leading cause of cancer-related deaths due to high incidence and high mortality.<sup>[1,2]</sup> This is caused by the high intrinsic mutation rate of lung tissue leading to aggressive tumors with early metastasis and a relatively late diagnosis at advanced stages. Therefore, about 70 % of the patients is inoperable and can only be treated with radiation and/or systemic therapies.<sup>[3]</sup> Unfortunately, the relapse rates of these systemic treatments are extremely high.

Lung cancer is classified in small-cell lung carcinoma (SCLC) with a prevalence of 15 % and non-small-cell lung cancer (NSCLC) with a prevalence of 85 %. NSCLC can be subdivided in large cell carcinoma (15 %), squamous carcinoma (30 %) and the most prevalent form adenocarcinoma (40 %).<sup>[4]</sup> Until 2004, there was no discrimination between the single histological subgroups regarding the suggested therapy of the patient.<sup>[5]</sup> The mutation in the epidermal growth factor receptor (EGFR) was later identified to determine the therapy response to targeted inhibition of EGFR in patients leading to a stepwise personalization of lung cancer therapy. By today, subdividing patients according to their driver oncogenes becomes more and more practical in therapy of lung cancer patients, e.g. >15 % of NSCLC patients harbor a mutation in RAS and 5 - 20 % harbor a mutation in EGFR (Figure 1.1A).<sup>[6]</sup> While patients with early disease stages (I-II) can undergo surgery and radiotherapy, the fraction of early stage diagnosed patients is only about 25 %, while roughly 70 % of the patients have advanced stage disease (III-IV) at the time of diagnosis.<sup>[7]</sup>

Patients with advanced stage NSCLC are inoperable and the currently applied systemic standard therapies are depicted in Figure 1.1B. Besides chemotherapy, there are drugs against the EGFR approved by the FDA for patients with a mutation in the EGFR such as the EGFR-tyrosine kinase inhibitors (TKIs) erlotinib, gefitinib and afatinib.<sup>[5]</sup> They show a pronounced prolongation of the progression-free survival (PFS), e.g. for erlotinib from 5-7 months PFS for standard chemotherapy to 10-13 months PFS in first-line setting. For patients with a translocation in anaplastic lymphoma kinase (ALK) leading to an echinoderm microtubule-associated protein-like (EML)4-ALK fusion protein, the ALK inhibitors crizotinib and ceritinib are applied. For this subset of patients, treat-

ment with ALK inhibitors leads to a PFS of 9-14 months compared to 5-7 months, but unfortunately there is no improvement of overall survival.<sup>[5]</sup>

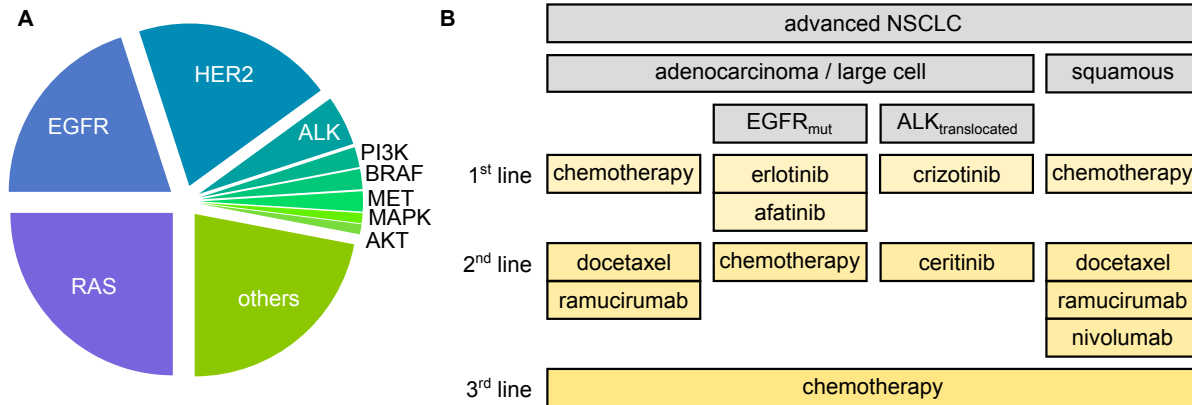


**Figure 1.1: Overview of the currently applied therapy of advanced stage NSCLC patients.**  
**A:** Schematic frequencies of driver mutations in NSCLC.<sup>[6,8]</sup> **B:** Treatment according to mutation status for the individual steps of recurrence, adapted from Thomas *et al.*<sup>[5]</sup>

Besides the currently approved therapeutic options, there are several further drugs under investigation, including the inhibition of immune escape by programmed cell death protein (PD)-1 and PD-ligand (PD-L)1 inhibition. While immunotherapy is the first therapy substantially increasing the long term survival of cancer patients, response rates are with about 20 % still very low.<sup>[5]</sup> Beside this, recent studies showed that activated EGFR causes high expression of PD-L1 leading to immune escape of EGFR mutated tumors.<sup>[9]</sup> Further, combinational therapies of chemotherapy with heat shock protein (HSP)90, Janus kinase (JAK), BRAF, vascular endothelial growth factor (VEGF) or MAPK/ERK kinase (MEK) inhibitors are investigated.<sup>[5]</sup> Interestingly, it was shown that a mutation in the EGFR excludes mutations in KRAS, NRAS and MEK, while BRAF mutations can occur.<sup>[10]</sup> These observations are not yet used for therapeutic approaches. Also epigenetic drugs are investigated, such as histone deacetylase and DNA methyltransferase1 inhibitors, that showed promising results to pretreat tumors prior to chemotherapy, while their mechanism of action is controversially discussed.<sup>[11]</sup>

### 1.1.1 Therapeutic EGFR inhibitors

In 90 % of the patients with EGFR driver mutation, patients harbor a primary mutation in the EGFR that is either a L858R point mutation or  $\Delta E746-A750$  deletion leading to increased kinase activity.<sup>[12]</sup> For the L858R mutation this is accompanied by a reduced affinity for adenosine triphosphate (ATP) (Table 1.1).<sup>[13]</sup> Both mutations are suggested to cause constitutive activation by destabilization of the autoinhibited state of the receptor in which the receptor is present without

**Table 1.1: Binding affinities of different EGFR mutants for ATP and gefitinib.** Michaelis-Menten constant  $K_m$  for ATP and the dissociation constant  $K_D$  of gefitinib is depicted for different EGFR mutations. The ratio of  $K_D/K_m$  is a measure for the inhibitory potential of gefitinib.<sup>[13]</sup>

EGFR mutation	$K_m(ATP)$	$K_D(gefitinib)$	$K_D/K_m, \cdot 10^{-3}$
wild type (wt)	5.2 $\mu$ M	35 nM	6.8
T790M	5.9 $\mu$ M	4.6 nM	0.78
L858R	148 $\mu$ M	2.4 nM	0.016
L858R/T790M	8.4 $\mu$ M	10.9 nM	1.3

bound ligand.<sup>[13]</sup> Erlotinib and gefitinib are first generation EGFR inhibitors binding competitively in the ATP binding pocket of the EGFR kinase domain. Gefitinib has an even higher affinity for L858R mutated EGFR compared to wild type (wt) potentially leading to reduced side effects of the drug. The EGFR-TKI erlotinib (tarceva) was first approved by the FDA in 2004 for second line and in 2013 also for first line treatment for all NSCLC patients independent from mutation status. This approval was amended in 2016 and since then erlotinib is indicated only for L858R mutation in the EGFR and exon 19 or 21 deletions in EGFR. There are two other approved EGFR-TKIs routinely applied in the clinics, gefitinib (iressa) and afatinib (gilotrif). They are also approved by the FDA for patients with a mutation in the EGFR. Unfortunately, in almost all cases the patients develop resistance against these EGFR-TKIs. In about 50% of the cases, this is caused by a secondary T790M mutation in the EGFR, often referred to as resistance mutation.<sup>[14]</sup> Yet, the T790M mutation mainly affects the binding of ATP to the active site of the EGFR kinase. Because the initial L858R mutation reduces the affinity of EGFR to ATP, shown by the Michaelis-Menten constant  $K_m$  of the EGFR variants for ATP in Table 1.1, gefitinib is highly active in cells with this mutation, but not in cells harboring EGFR wild type. Upon acquisition of the secondary T790M mutation, the ATP binding affinity is recovered to normal levels. The dissociation constant  $K_D$  of gefitinib binding to the EGFR shows the reduced affinity for wt EGFR. The ratio of  $K_D/K_m$  is a measure for the inhibitory potential that decreases by two orders of magnitude after secondary T790M mutation mainly due to recovery of the ATP binding affinity.<sup>[13]</sup> This leads to reduced EGFR inhibition by the competitive EGFR-TKIs.

Afatinib is a second generation inhibitor harboring a Michael acceptor group leading to a covalent binding to Cys<sup>797</sup> of EGFR to circumvent this problem. Unfortunately, the efficiency of this drug for T790M mutated EGFR was lower than expected. Therefore, a new set of inhibitors was designed to directly target the T790M mutation and to circumvent the sterical repulsion of Met<sup>790</sup> reaching higher binding affinities. Members of the third generation, for example WZ4002, AZD9291 or CO-1686, are currently under investigation.<sup>[15]</sup> AZD9291 (tagrisso/osimertinib) has been approved

by the FDA in 2015 for patients with metastatic NSCLC with T790M mutation after EGFR-TKI treatment. There are currently more EGFR-TKIs under investigation, such as the first generation EGFR-TKI icotinib that was reported to be superior to gefitinib in a phase III trial regarding PFS and adverse effects.<sup>[16]</sup>

Yet, upon application of third generation inhibitors, a tertiary C797S mutation in EGFR was reported that removes Cys<sup>797</sup> that forms the covalent bond with the inhibitor leading to an escape of therapy.<sup>[17]</sup> Therefore, the development of a fourth generation of inhibitors is ongoing that allosterically inhibits EGFR.<sup>[17]</sup>

Apart from inhibitors targeting the tyrosine kinase, there are also monoclonal antibodies binding to the extracellular domain of the EGFR in its inactive state preventing ligand binding and receptor activation and leading to receptor degradation.<sup>[18]</sup> An in lung cancer approved therapeutic antibody is cetuximab (erbitux). Cetuximab is applied in patients with advanced stage lung cancer and histological expression of the EGFR in combination with chemotherapy, because studies showed an increase in survival from 10.1 to 11.3 months in first line setup.<sup>[19,20]</sup> Necitumumab (portrazza) is a further monoclonal antibody targeting EGFR that is approved by the FDA only for squamous lung cell carcinoma in combination with chemotherapy. Also the combination of EGFR-TKIs with monoclonal EGFR antibodies, for example afatinib with cetuximab, showed promising results, maybe due to parallel targeting of total and phosphorylated EGFR.<sup>[21]</sup>

### 1.1.2 Chemotherapy in lung cancer

Chemotherapy was the first available systemic cancer therapy and is still together with irradiation and resection the most commonly applied cancer treatment. The term was coined in the early 1900s by Paul Ehrlich and implies the use of small molecules or chemicals for disease therapy, while nowadays anti-neoplastic drugs are usually called chemotherapeutics. The first chemotherapeutic drug for cancer therapy, an analogue of mustard gas, was discovered by chance during World War I to have an anti-proliferative effect on the fast growing blood cells.<sup>[22]</sup> Cisplatin or cis-diamminedichloroplatinum(II+) was described in 1973 as cancer therapeutic (Figure 1.2).<sup>[23]</sup> Since then, a large set of chemotherapeutics has been developed. While all chemotherapeutics in the modern sense are cytotoxic agents and block cell proliferation in, the mechanisms of action are different or not completely understood. There are several classes of chemotherapeutics. Most common are still platinum-based compounds such as cisplatin, carboplatin or oxaliplatin (Figure 1.2), but also nucleobase or nucleotide analogues such as fluoruracil or gemcitabine are standardly applied. Apart from them, there are also taxanes such as paclitaxel and docetaxel that disrupt disassembly of microtubules, vinca alkaloids such as vinorelbine that prevent the assembly of microtubules

or anthracycline antibiotics such as doxorubicin that prevent replication by intercalating in the DNA/RNA.

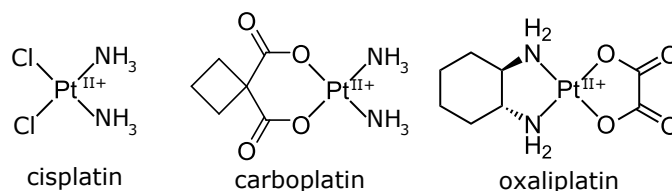


**Figure 1.2: Structure of common Pt-based chemotherapeutics.** The platin(II+)-complexes of cisplatin, carboplatin and oxaliplatin are depicted.

The common underlying principle is that fast proliferating cells such as cancer cells are affected stronger than slowly proliferating healthy cells. Therefore, common adverse effects are based on inhibition of healthy fast dividing cells. For example, this involves the loss of hair, nausea and gastrointestinal distress. Especially the blood cells belong to the fast dividing cells in the body and therefore chemotherapy causes the loss of red blood cells leading to anemia and fatigue. This is the reason, why chemotherapy-treated patients very often receive additional treatment with erythropoiesis stimulating agents (ESAs) or blood transfusions to counteract the anemia.

Cisplatin is one of the most commonly used chemotherapeutics in lung cancer and is therefore used as exemplary chemotherapeutics in this work. Cisplatin is chemically inert in a solution containing 100 mM chloride ions such as blood plasma or cell culture medium. Inside the cell, the chloride levels are much lower at 5 mM and therefore the chloride ions dissociates from the Pt(II+)-complex leading to an aquatic Pt(II+)-complex that is a strong electrophile. This reactive species bind to a variety of nucleophiles, including nucleic acids and sulfur containing proteins.<sup>[24]</sup> It is suspected that Pt(II+) forms a reservoir with thioethers, for example in metallothioneins, which are then slowly released to the DNA-complex,<sup>[25]</sup> while binding to sulfhydryl residues such as in glutathione (GSH) generate a more inert complex.<sup>[26]</sup> The main target of cisplatin is the DNA, where it forms covalent 1,2- or 1,3-intrastrand crosslinks with the  $N^7$  of purine bases that were suspected to cause DNA unwinding leading to recognition of DNA damage.<sup>[27]</sup> Interstrand crosslinks occur at lower frequency of 1-2%, but induce double strand breaks during replication which are suspected as critical lesions in cell cycle arrest.<sup>[28]</sup>

These DNA lesions lead to mutations and genomic instability, but also to activation of cell cycle checkpoints to delay cell cycle progression. This provides time for the cell to repair the DNA or to undergo apoptosis, if the lesions are too severe.<sup>[24]</sup> There are several DNA repair mechanisms such as the nucleotide excision repair (NER) system and the mismatch repair (MMR) system which regulate the cell cycle checkpoints and activate different pro- or anti-apoptotic signals involved in cisplatin-

induced cytotoxicity. Further, the tumor suppressor p53 plays an important role in cisplatin-induced apoptosis which is a complex process and involves pro- as well as anti-apoptotic signals.<sup>[24]</sup> This includes activation of the PI3K/AKT- and MAPK-pathways. p53 is a short-lived protein that is regulated by the E3 ubiquitin ligase MDM2 and regulates the expression of several B-cell lymphoma (BCL)2-family members, such as BCL-xL, BAD, BAX or BIM leading to cytochrome c release from the mitochondria and formation of the apoptosome.<sup>[29]</sup> This causes cleavage of the initiator caspase-9 and subsequent cleavage of the executor caspase-3 leading to degradation of multiple cellular components and apoptosis.<sup>[24]</sup> Apart from that, there is also evidence that crosslinking of mitochondrial DNA might cause cisplatin-induced apoptosis.<sup>[30]</sup>

### 1.1.3 Anemia in lung cancer

Anemia is characterized by the reduced capacity of the blood to transport oxygen. This is caused by reduced levels of hemoglobin (Hb) that is mostly correlated with low levels of erythrocytes or with the lack of iron that is required as cofactor of the hemoglobin protein for oxygen transport. Anemia is frequently observed in lung cancer patients, reaching up to 90% at the advanced stages of the disease.<sup>[31]</sup> As erythrocytes exhibit a short half-life of three to four months, they are constantly regenerated in healthy humans. Therefore, the cytotoxic effect of chemotherapeutics on the fast proliferating erythroid progenitors has a strong impact on the number of mature erythrocytes.<sup>[32,33]</sup> Apart from that, tumor-associated inflammation decreases half-life of erythrocytes and platinum-based chemotherapy is nephrotoxic affecting erythropoietin (Epo)-producing cells in the renal cortex.<sup>[32,34]</sup> To treat cancer patients suffering from anemia, either blood transfusions or erythropoiesis stimulating agents (ESAs) are applied. ESAs are mostly analogs of the endogenous cytokine Epo that is mainly produced in the kidney upon reduced oxygen partial pressure in the blood. It induces proliferation and differentiation on the burst forming unit - erythroid (BFU-E) and colony forming unit - erythroid (CFU-E) stage of erythropoiesis in the bone marrow (Figure 1.3).<sup>[35]</sup>

Therapeutically available ESAs comprise Epo $\alpha$ , Epo $\beta$ , CERA and NESP. Yet, treatment with ESAs is controversially discussed and clinical trials applying ESAs were terminated due to adverse effects.<sup>[36,37]</sup> Moreover, the EpoR was reported to be present on tumor cells implying the risk to induce proliferation or anti-apoptotic signaling in cancer cells.<sup>[37,38]</sup> However, concerns regarding the specificity of the antibody-based analyses have been raised,<sup>[39]</sup> and the expression of EpoR on tumor cells is controversially discussed.<sup>[40]</sup> Nevertheless, it was reported that EpoR levels on lung cancer cells are much lower compared to the expression on hCFU-E,<sup>[41,42]</sup> but their accurate detection remains challenging what may lead to the contradictory results in the literature. On the

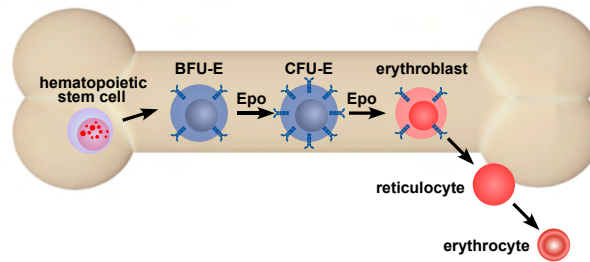


**Figure 1.3: Influence of Epo on erythropoiesis.** Schematic representation of the process of erythropoiesis. Hematopoietic stem cells in the bone marrow differentiate step-wise to erythrocytes by the erythropoietin (Epo)-dependent burst forming unit - erythroid (BFU-E) and colony forming unit - erythroid (CFU-E) stages. The stages that are influenced by Epo are indicated, as well as EpoR expression. Reticulocytes eject their nucleus and leave the bone marrow and subsequently mature to erythrocytes.

other hand, the availability of blood for transfusions is limited and the transfusions could cause several adverse effects such as iron overload, thromboembolic events or increased risk of infection. As both therapeutic approaches have their drawbacks, the underlying mechanisms need to be understood to improve the timing and dosing of anemia treatment in cancer. The optimization of the response and safety of ESA treatment in cancer is an important task regarding therapy of lung cancer patients.

## 1.2 Erythropoietin receptor signal transduction

Cytokines play diverse roles in the human body in an autocrine, paracrine or endocrine manner. They can be subdivided, depending on their function, in interferons, interleukins, tumor necrosis factors, colony-forming factors and chemokines. This work focuses on Epo which belongs to the colony-forming factors. It is a glycosylated protein of 166 amino acids that binds to its cognate receptor EpoR, a type I cytokine receptor. As cytokine receptors lack an intrinsic kinase domain they are dependent on the recruitment of kinases such as JAKs. There are four members of the JAK family, JAK1, JAK2, JAK3 and TYK2. JAK2 is the main kinase involved in EpoR signal transduction. Upon ligand binding, the receptor undergoes conformational changes leading to the activation of JAK2. Subsequently, JAK2 phosphorylates itself and the EpoR at multiple tyrosine residues. The eight phosphorylated tyrosine residues of the EpoR serve as docking sites for multiple signaling proteins leading to the activation of the signal transducer and activator of transcription (STAT)5, the mitogen activated protein kinase (MAPK) and the phosphatidylinositol-4,5-bisphosphate 3-kinase (PI3K)/AKT signaling pathways. The phosphorylations at Tyr<sup>343</sup> or Tyr<sup>401</sup> of the receptor lead to recruitment of STAT5 via its SRC homology (SH)2 domain. There

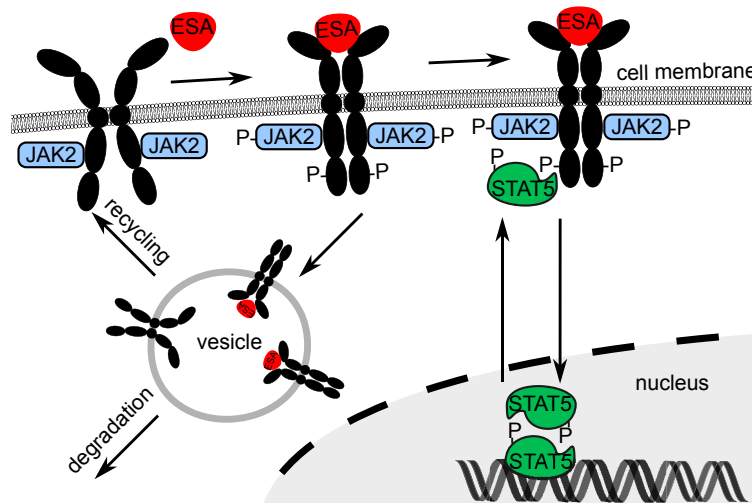


**Figure 1.4: Scheme of Epo signaling and induced JAK2-STAT5 signaling.** ESAs such as Epo bind to the receptor dimer and thereby activates JAK2 leading to phosphorylation of itself and the receptor. Subsequently, STAT5 is recruited, phosphorylated and shuttled to the nucleus. Phosphorylation is indicated by (P).

are two isoforms of STAT5, STAT5A and STAT5B that have a sequence identity of 93% and were reported to show no preference for dimerization.<sup>[43]</sup> Subsequently, STAT5 is phosphorylated at Tyr<sup>694</sup> for STAT5A and at Tyr<sup>699</sup> for STAT5B, dissociates and dimerizes via its SH2 domain. The STAT5 dimer translocates to the nucleus and induces target gene transcription. The induced genes include the negative regulators *cytokine-inducible SH2-domain containing protein (CISH)* and *suppressor of cytokine signaling (SOCS)3*. A schematic overview of EpoR signaling is shown in Figure 1.4. Interestingly, it was found that Epo can convey information on a broad range of ligand concentration that is necessary for the body to respond to acute hypoxia.<sup>[44]</sup> It was shown that the broad range of response to the ligand is mediated by a fast receptor turnover even in the absence of the ligand and a large intracellular pool of receptors.<sup>[44]</sup> It was found that only 1 – 5% of receptors are located on the cell surface in hematopoietic cells.<sup>[45,46]</sup>

### 1.3 Epidermal growth factor receptor signal transduction

As already described, receptor tyrosine kinases (RTKs) play a major role in tumor development and progression by the induction of proliferative, anti-apoptotic and migratory signals in the cancer cells and their inhibition is a promising approach in several tumor types. In lung cancer, two commonly deregulated RTKs are the epidermal growth factor (EGF) and MET receptor.<sup>[47]</sup> Their properties and functions will be described in the following sections.

EGFR is a member of the human epidermal growth factor receptor (HER) family, consisting of EGFR (HER1, ErbB1), HER2 (ErbB2, NEU), HER3 (ErbB3) and HER4 (ErbB4). Their structure is depicted in Figure 1.5.<sup>[48,49]</sup> Without ligand, the receptors are in a closed form, where domain II and IV are bound to each other. For HER2, there is no known ligand and HER2 always exists in the open conformation enabling permanent dimerization with other activated HER members.<sup>[48]</sup> Upon ligand binding to domain I and III of the other HER members, domain II and IV dissociate and the conformation of the receptor opens for dimerization. After ligand-mediated dimerization, the kinase domains of both monomers form an asymmetric dimer in which one kinase allosterically activates the other (Figure 1.5).<sup>[50]</sup> The kinase domains consist of an ATP binding pocket, an activation loop and a catalytic loop. The kinase of HER3 has been reported to be inactive based on measurements of the isolated kinase domain in solution.<sup>[48]</sup> On the contrary, Shi *et al.* reported that the HER3 kinase is active, if it is recruited to a lipid bilayer and that two HER3 receptors in a homodimer are able to successfully transphosphorylate each other.<sup>[51]</sup> Although the activity is about 1 000-fold reduced compared to the EGFR kinase, they suggest that it might be enough to induce the activating phosphorylation of the kinase of its binding partner. These activating phosphorylations usually increase the RTKs activity by 150- to 1 000-fold.<sup>[51]</sup>

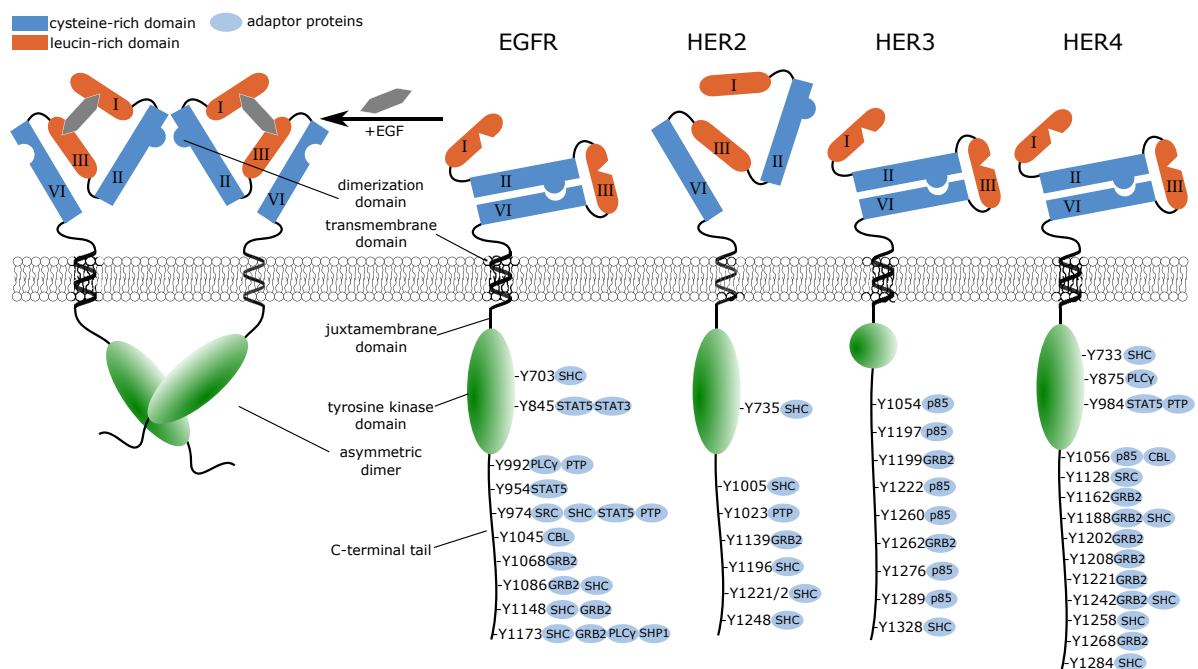


**Figure 1.5: Overview of the HER receptor family.** The domains of the four HER receptors are indicated as well as important tyrosine (Y) phosphorylation sites and the recruited adaptors. Upon ligand binding to domain I and III, domain II and IV dissociate and domain II induces dimer formation with an other HER member indicated schematically on the left side. Structurally, the HER members are similar, but HER2 has no known ligand and HER3 has impaired kinase function. The tyrosine residues phosphorylated upon EGF-binding are indicated with their adaptor proteins.<sup>[48,49,52,53]</sup>

It was reported that the HER members exist as monomers without ligand,<sup>[48]</sup> but there is also evidence for preformed inactive dimers that are activated upon ligand binding.<sup>[54,55]</sup> In that study, Tao *et al.* used a bimolecular fluorescence complementation assay to show that all HER members have preformed, inactive homo- and heterodimers, except of HER3 homodimers and heterodimers with cleavable HER4. Ligand binding and receptor phosphorylation then leads to the activation of signaling cascades, gene transcription and cellular responses. In normal cells 40 000 - 100 000 EGFR molecules per cell are expressed. In most solid tumors EGFR is commonly overexpressed reaching up to  $2 \cdot 10^6$  molecules per cell.<sup>[56]</sup>

**EGFR Ligands** There are many ligands known for the HER family. EGFR is known to bind EGF, transforming growth factor  $\alpha$  (TGF $\alpha$ ), betacellulin, amphiregulin, epiregulin, epigen and heparin-binding EGF-like growth factor (HB-EGF), while HER3 is bound by neuregulin 1-2 and HER4 by neuregulin 1-4, HB-EGF, epiregulin and betacellulin.<sup>[57]</sup> They all share the EGF motif which is 35-40 amino acids long, but EGF is one of the ligands inducing strongest EGFR homo- and heterodimerization<sup>[58]</sup> and was therefore used for the analysis in this work. EGF is a 53 amino acid long polypeptide derived from a large precursor and is in humans predominately produced in the kidney, while in mice the submaxillary gland is the major source of EGF. While EGF plays an important role in embryonic development, tissue regeneration and ion transport, there is no obvious phenotype of knock-out mice.<sup>[59]</sup>

**Activation of signaling cascades** As depicted in Figure 1.5, several adaptor proteins are recruited to the phosphorylated tyrosin residues of the receptors upon activation. The phosphorylated residues are bound by SH2 domains and phosphotyrosine-binding (PTB) domains and the adaptors subsequently mediate the activation of signaling cascades. The adaptor protein SRC also phosphorylates the EGFR at Tyr<sup>845</sup> in the activation loop of the kinase domain that leads to increased kinase activity.<sup>[60]</sup> The main induced signaling pathways of EGFR are the MAPK-pathway and the PI3K/AKT-pathway.

For the MAPK-pathway (Figure 1.6), growth factor receptor-bound protein (GRB)2 binds the receptor at the phosphorylated sites indicated in Figure 1.5 via its SH2 domain.<sup>[48,49]</sup> GRB2 harbors besides the SH2 domain an SH3 domain that recruits the guanine nucleotide exchange factor SOS to the receptor.<sup>[61]</sup> SOS also binds directly to the receptor or to SH2 domain protein C (SHC) that is bound to the receptor by its PTB domain. Once SOS is recruited to the membrane, it exchanges the GDP of the RAS-GDP complex by GTP and thereby activates RAS.<sup>[62]</sup> The RAS-GTP complex activates the serine/threonine kinases RAF (MAP3K) that induces phosphorylation

of the dual-specificity tyrosine/threonine kinase MEK (MAP2K).<sup>[63]</sup> This kinase phosphorylates the MAP kinase extracellular signal-regulated kinase (ERK) on two residues. ERK subsequently shuttles to the nucleus and induces target gene transcription. Nuclear phosphorylated ERK activates multiple MAP kinase-activated protein kinases by phosphorylation such as RSK, MNK or MSK. ERK has more than 180 targets thereby promoting to diverse cellular responses such as proliferation, cell growth, migration, metabolism, differentiation or survival. ERK also activates the p90 ribosomal S6 kinase (RSK) leading to phosphorylation of the ribosomal protein S6 and subsequently to upregulation of translation and cell growth.<sup>[64,65,66]</sup>

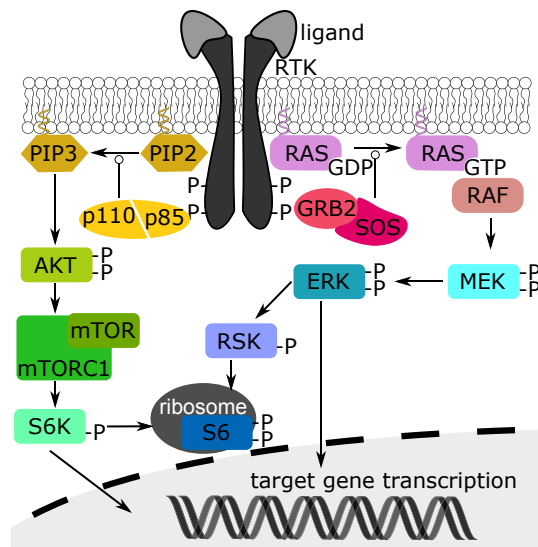


**Figure 1.6: Schematic representation of the MAPK- and PI3K/AKT-pathway.** A schematic RTK with bound ligand with the two signaling cascades is shown. Phosphorylation is indicated by (P).

The PI3K/AKT-pathway (Figure 1.6) is initiated by recruitment of the p85 regulatory subunit of the heterodimeric class I PI3K to the phosphorylated receptor directly by its SH2 domains or by the adaptor protein GRB2-associated binder (GAB)1. Thereby, the p110 catalytic subunit is recruited to the cell membrane and induces catalysis of the formation of phosphatidylinositol 3,4,5-trisphosphate (PIP<sub>3</sub>) from phosphatidylinositol 4,5-bisphosphate (PIP<sub>2</sub>). This reaction can be reversed by the phosphatase and tensin homolog (PTEN). PIP<sub>3</sub> subsequently recruits protein kinase B (PKB, or AKT) via the plextrin homology (PH) domain to the membrane where it is phosphorylated at Thr<sup>308</sup> and Ser<sup>473</sup> by the 3-phosphoinositide-dependent kinase (PDK)1 and the mammalian target of rapamycin complex (mTORC)2. Phosphorylated AKT induces inhibitory phosphorylations of TSC1/2 that leads to the activation of mTORC1 and subsequent phosphorylation of the p70 ribosomal S6 kinase (S6K). S6K then phosphorylates the ribosomal protein S6.<sup>[67,68]</sup> Interestingly, the EGFR has no direct binding sites for p85 and depends on adaptor proteins to

activate the PI3K/AKT-pathway such as GAB1 or the activation of PI3K/AKT-pathway mediated by RAS-GTP. On the other hand, HER3 has 6 SH2 binding sites for p85 (Figure 1.5) leading to very strong activation of PI3K signaling.<sup>[48,66,69]</sup>

Next to the PI3K and MAPK-pathway, EGFR also activates  $\text{Ca}^{2+}$ -signaling. It is induced by the recruitment of phospholipase C  $\gamma$  (PLC $\gamma$ ) that hydrolyzes  $\text{PIP}_2$  and release inositol 1,4,5-trisphosphate ( $\text{IP}_3$ ) and diacyl glycerol.  $\text{IP}_3$  is released to the cytoplasm and leads to an opening of  $\text{Ca}^{2+}$ -channels.<sup>[61]</sup> EGFR also activates the JAK1-3/STAT3/5-pathway.<sup>[70]</sup>

The EGFR signaling network comprises several negative feedbacks to reduce signaling on the receptor level. For example protein kinase C can be recruited to the receptor and phosphorylate Thr<sup>654</sup> of the EGFR and thereby negatively regulate receptor activity. Further, there are several phosphatases know to interact with the EGFR, such as SRC homology region 2 domain-containing phosphatase (SHP)1/2, protein tyrosine phosphatase (PTP)1 and density-enhanced phosphatase (DEP)1. It is also known that pERK introduces an inactivating phosphorylation in SOS<sup>[61]</sup> and activated ERK was described to negatively regulate EGFR.<sup>[71]</sup> Since the MAPK- and PI3K/AKT-pathways are the canonical signal transduction pathways of EGFR as well as MET, these pathways were investigated within this work.

**EGFR internalization and degradation** Receptor internalization and degradation is a common mechanism of RTKs to attenuate signals. In the context of cancer it is also of interest, since EGFR is overexpressed in many tumor types and cancer-associated mutations in EGFR were described to lead to reduced degradation.<sup>[72]</sup> Further, it is well established that EGFR induces signaling from the early endosome leading to downstream activation.<sup>[73,74]</sup> Apart from that, EGFR is also described to shuttle to the nucleus acting as transcriptional regulator<sup>[65,75]</sup> and to the mitochondria, where it phosphorylates cytochrome c oxidase (COX)2 and thereby regulates apoptosis.<sup>[76]</sup> The mechanism of EGFR internalization can either be clathrin-independent or clathrin-dependent. For the clathrin-dependent path, the E3 ubiquitin-protein ligase Casitas B-lineage Lymphoma (CBL) is recruited to the SH3 domain of GRB2 or to Tyr<sup>1045</sup> of EGFR (Figure 1.5). CBL then induces EGFR ubiquitination leading to recruitment of clathrin and subsequent endocytosis of the clathrin-coated pits.<sup>[61]</sup> It is assumed that for high EGF concentrations the clathrin-independent mechanism predominates, as the clathrin-dependent path is saturated.<sup>[77]</sup> If EGFR is dephosphorylated and deubiquitinated, EGFR can be fast recycled to the cell surface from the early endosome or otherwise enters the late endosome. There it is recognized by the endosomal sorting complexes required for transport and either fused with the lysosome and degraded or fused with the perinuclear endocytic recycling compartments leading to slow receptor recycling.<sup>[73]</sup> The clathrin-dependent path has a

preference for recycling leading to a prolonged signal for low doses of EGF. It has been shown that also the ligand influences clathrin dependency as well as the degradation pathway. TGF $\alpha$  for example is less pH stable in the endosome leading to decreased receptor activation and ubiquitination inducing increased receptor recycling, while EGF is more pH stable leading to increased degradation. The basal receptor turnover of EGFR without ligand is dependent on the mutation status and listed in Table 1.2.<sup>[78]</sup> Interestingly, it was shown that heterodimers of EGFR with other HER members fail to recruit CBL<sup>[79]</sup> leading to an increased stability of the HER heterodimers compared to the homodimers.<sup>[58,80]</sup> As described in subsection 1.1.1, the endocytosis can also be mediated by EGFR inhibitors. While antibodies such as cetuximab induce receptor degradation without leading to autophosphorylation, small molecule inhibitors such as gefitinib affect EGFR degradation only in some cell lines.<sup>[77]</sup>

**Table 1.2: Receptor half-life of EGFR.** Basal receptor half-life of different EGFR mutants based on Greig *et al.*<sup>[78]</sup>

EGFR mutation	wild type	L858R	L858R+T790M	$\Delta$ E746-A750
half-life	28 h	10 h	9.2 h	7.5 h

## 1.4 MET receptor signal transduction

MET receptor is expressed in epithelial cells of many organs and plays an important role in embryogenesis, wound healing and cell motility.<sup>[81]</sup> MET receptor is synthesized as precursor and is cleaved during shuttling to the cell membrane by FURIN in a  $\alpha$ - and  $\beta$ -chain and is linked again by disulfide bonds. The structure of MET is shown in Figure 1.7, the extracellular part consists of an N-terminal SEMA domain building a seven-bladed propeller structure, a cysteine rich region and a stalk-like structure consisting of four immunoglobulin-like domains. The intracellular MET consists of a juxtamembrane region, the tyrosine kinase and a C-terminal tail.<sup>[82]</sup> Upon ligand binding to the MET receptor, it dimerizes and the intrinsic kinase is activated by conformational changes in the transmembrane region. Subsequently, Tyr<sup>1230</sup>, Tyr<sup>1234</sup> and Tyr<sup>1235</sup> in the kinase domain get phosphorylated leading to an increased kinase activity. Autophosphorylation at Tyr<sup>1349</sup> and Tyr<sup>1356</sup> at the C-terminal tail is required for recruitment of adaptor proteins such as GRB2, SHC, PLC $\gamma$ , p85 and SRC. Unique to MET is the ability to directly recruit GAB1 without requirement of other adaptors (Figure 1.7).<sup>[81]</sup> These adaptors activate the PI3K and MAPK signaling cascade as described for EGFR in section 1.3. Further, SRC that is recruited to MET activates the focal adhesion kinase inducing cell migration via integrins and cadherins.<sup>[82]</sup> Downregulation of phosphorylated MET occurs by PTPs such as DEP1, LAR or PTP1B.<sup>[81]</sup> MET receptor exhibits

moderate expression levels in normal lung tissue, while its mRNA/protein is overexpressed in 1/3 of the adenocarcinomas. Interestingly, in squamous carcinoma the MET levels only rarely exceed levels of normal lung tissue.<sup>[83]</sup>

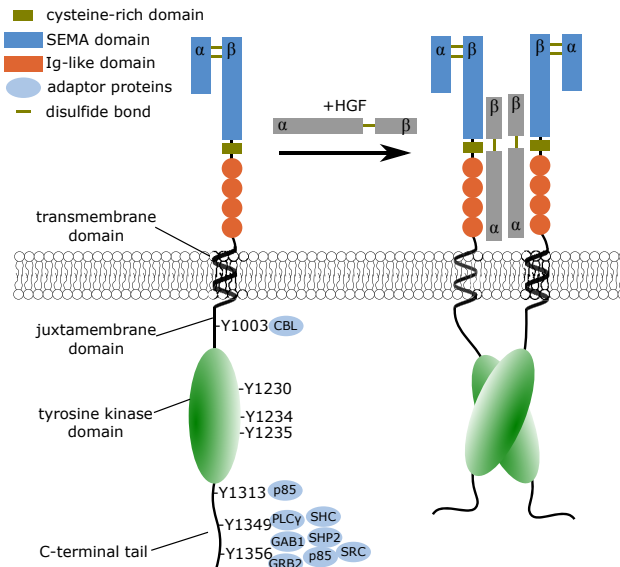


**Figure 1.7: Schematic representation of the structure and dimerization of MET receptor with bound HGF.** Upon binding of HGF, MET receptor dimerizes and forms a homodimer indicated on the right side of the figure.<sup>[82,84]</sup> The tyrosine (Y) residues phosphorylated upon HGF-binding are indicated with their adaptor proteins.

**MET Ligand** In contrast to the EGFR, there is only one ligand known for the MET receptor and that is HGF which is also known as scatter factor due to its strong induction of cell migration. It is processed from a pro-form leading to two subunits, the 69 kDa  $\alpha$ -chain and the 34 kDa  $\beta$ -chain (Figure 1.7). While the  $\alpha$ -chain has high affinity for MET, the receptor is only activated by binding of the  $\beta$ -chain. The main source of HGF are stromal cells affecting multiple cell types throughout the body. HGF has mainly mitogenic, motogenic, 3D-morphogenic and anti-apoptotic effects and plays an important role during embryonic liver development and liver regeneration.<sup>[85]</sup>

**MET Degradation** MET receptor is also endocytosed and either degraded or recycled dependent on ligand-induced phosphorylation like the EGFR. Endocytosis of MET is mainly clathrin-mediated, while MET stays signaling competent in the early endosome.<sup>[82]</sup> Phosphorylation at tyrosine 1003 in the juxtamembrane region leads to the recruitment of CBL and receptor ubiquitination. Dependent on this, the internalized MET receptor is then sorted either for recycling or degradation.<sup>[82]</sup> Apart from this, MET is also degraded via shedding by metalloproteases such as

ADAM (a disintegrin and metalloproteinase) on the plasma membrane.<sup>[86]</sup> The half-life of MET receptor on the surface without ligand was determined to be in the range of 5.6 h in breast cancer cell lines.<sup>[87]</sup>

## 1.5 EGFR/MET crosstalk

The EGFR and MET signal transduction pathways are closely interlinked, since both receptors were identified by cluster analysis of their signaling networks to belong to the same class of RTKs and share downstream targets.<sup>[88]</sup> Several studies showed that dual inhibition of EGFR and MET effectively inhibits tumor growth.<sup>[89,90,91]</sup> There are several studies available showing a synergistic behavior of EGF and HGF e.g. on invasiveness in mammary cell lines<sup>[92]</sup> or on proliferation and AKT and MET phosphorylation.<sup>[91]</sup> This was assumed to be mediated by EGFR:MET heterodimerization that is found in some studies using co-immunoprecipitation.<sup>[93]</sup> Yet, EGFR:MET heterodimers were detectable only in some cell lines, e.g. it was reported that EGFR:MET heterodimers form in tumor cells, but not in hepatocytes.<sup>[94]</sup>

Apart from that, also directed interactions either from EGF to MET or from HGF to EGFR have been described. Yet, the described interactions are either highly context-specific or multi-factorial regulating phosphorylated and total levels on time-frames between minutes and days.

Regarding the activation from **HGF to EGFR**, it was found that cells secrete HB-EGF 6 to 24 hours post HGF stimulation.<sup>[47]</sup> It was also reported that MET-mediated resistance to EGFR-TKIs is conferred by transactivation from MET to HER3 signaling,<sup>[95]</sup> while in breast cancer, it was shown that EGFR phosphorylation at Tyr<sup>845</sup>, Tyr<sup>992</sup> and Tyr<sup>1068</sup> is maintained by MET activation via SRC even in the presence of EGFR-TKIs 30 min post inhibition.<sup>[96]</sup>

Regarding the activation from **EGF to MET**, it has been described that EGF leads to upregulation of MET via sprouty2<sup>[97]</sup> or via hypoxia-inducible factor 1 $\alpha$  (HIF1 $\alpha$ ) independent of hypoxia.<sup>[98]</sup> It was also described that EGF activates MET after 1 to 2 days via SRC-induced increased MET protein abundance.<sup>[99]</sup> In colon cancer cells, transactivation from EGFR to MET within 5 min has been reported to be mediated by prostaglandin E<sub>2</sub> in a EGFR kinase-dependent manner.<sup>[100]</sup> On the other hand, in pancreatic cancer cells it was shown that the EGF-induced transactivation of EGFR to MET after 3 min is mediated by reactive oxygen species (ROS) and the transactivation required NADPH oxidase activity.<sup>[101]</sup> Breindel *et al.*<sup>[102]</sup> showed in a 32D cell model system that EGFR activation is sufficient to induce MET phosphorylation that could occur directly, through EGF-induced activation of MET autophosphorylation or other associated kinases. The crosstalk was suspected to occur by the regulation of protein expression levels and MAPK-mediated activa-

tion of MET. Apart from this, the authors found that expression of the EGFR leads to increased MET stability increasing the basal half-life without stimulus from 3.5 h to 5.5 h.<sup>[102]</sup> In transformed epithelial cells that secrete TGF $\alpha$ , MET was found to be constitutively phosphorylated by autocrine activation of the EGFR.<sup>[94]</sup> Apart from these directed activating interactions there are also negative feedbacks described, such as the secretion of metalloproteases upon EGF stimulation leading to MET depletion.<sup>[47]</sup>

Further, other interaction partners have been suspected to mediate EGFR/MET crosstalk, such as HER2/3 or RON that transactivates MET in the absence of HGF<sup>[81]</sup> or the adaptor protein GAB1. It was found by Stommel *et al.*<sup>[90]</sup> that activated MET and EGFR compete for the binding to GAB1. They showed that overexpression of constitutively active EGFR leads to increased recruitment of GAB1 to the EGFR and a reduction of GAB1:MET complexes, while activation of downstream targets is unaffected. They found that dual inhibition of MET and EGFR is required to block downstream signaling in glioblastoma. Finally, a study by Tanizaki *et al.* suggested a direct crosstalk by the formation of EGFR:MET heterodimers leading to transactivation of the other receptor.<sup>[93]</sup>

## 1.6 Systems biology

Cellular processes are in general highly complex and entangled, thus focusing research on one molecule might not be sufficient to mechanistically understand cellular interactions. Therefore, systems biology combines molecular biological assays with mathematical analyses to understand the cell on its network-level. This understanding of the underlying properties and functionalities that are emerging from the interplay of multiple components is crucial, since the whole is greater than the sum of its parts. The analysis of these complex and nonlinear systems is achieved by the development of mathematical models. Models are abstract representations of a system that explain certain features and allow to predict the behavior of a system.<sup>[103]</sup> Although all models are simplifications of the reality, they can be useful to address specific questions and correct within their domain of definition. Models can help to clarify concepts, postulate and test hypotheses by a precise mathematical definition. Further, they can help to visualize certain aspects and to perform experiments *in silico* that may be time-consuming or not feasible.

There are two strategies for model development, one can either start from prior knowledge of molecular interactions of a subsystem in a bottom-up approach or start with a holistic description of the system in a top-down approach. The top-down approach is usually applied for high-throughput

data to identify interactions of a network and is a data-driven approach that requires little prior knowledge. The bottom-up approach focuses on detailed mechanisms and allows for quantitative predictions within a defined system.

Apart from this classification, there are multiple types of mathematical models used in systems biology. Which model is suited best, depends on the addressed question and the intended computational effort. Models comprise different quantities classified as constants, variables and parameters. While constants are fixed values such as the Avogadro's number  $N_A$ , parameters are determined experimentally or theoretically such as a reaction rate constant  $k$  and therefore change considering new experiments or model structures. Variables have free values such as the concentration of a reactant and have a time-dependent behavior  $c(t)$ .<sup>[103]</sup>

**Statistical models** Statistical models are utilized to identify relations between measured data and help to extract underlying structures of the biological system.<sup>[103]</sup> Statistical models comprise regression analyses e.g. for identification of a linear relationship, data mining analyses such as cluster analysis to identify groups of data sharing a similar behavior and multivariate analysis such as principle component analysis to separate objects into classes with maximal distance.

**Agent-based models** In agent-based models each component has a defined location and state. For each component specific rules are set which allow to change the state of the component according to their surrounding components. This approach can be computationally less demanding compared to other modeling approaches. By defining only the rules for single agents there still may be emerging properties on the systems level that were not defined *ab initio*.<sup>[103]</sup>

**Network models** Network models consist of nodes and edges, which in the context of systems biology usually describe proteins or genes as nodes and their interactions as edges. The size of these networks can range from small subnetworks to a holistic description of the cell using omics-data. Depending on the underlying biological question there are several types of network models utilized.<sup>[104]</sup>

*Boolean models* are typically large networks with binary interactions to identify the connectivity of components such as gene regulatory networks. Nodes represent genes or proteins and edges their possible interaction which are either on or off.<sup>[105]</sup>

*Bayesian models* are usually a special type of probabilistic graphs that describe the nodes as continuous or discrete random variables and the edges as their conditional dependencies. Each node has a probability function depending on the parental nodes and thereby cyclic structures

are not possible. They can provide the probability of a certain output that was not measured experimentally as well as the probability for a specific interaction. [106,107]

*Stoichiometric models* are often used for metabolic networks and are based only on the information of stoichiometry and reversibility of cellular reactions. Stoichiometric networks can be described by an  $n \times m$  matrix, in which  $n$  denotes the number of species and  $m$  the number of reactions. This analysis is particular suited for metabolic networks, since therein the flux from input to output needs to obey the conservation of mass and stoichiometries are usually well known. Therein, one is interested in comparing the fluxes through the network in steady-state which can be identified utilizing flux balance analysis. [108]

*Stochastic models* are typically applied, if particle numbers are small and non-deterministic effects can not be neglected. While according to the law of large numbers probabilities of single states cancel out, they may not be neglected in all cases especially for cases with low copy numbers. [109]

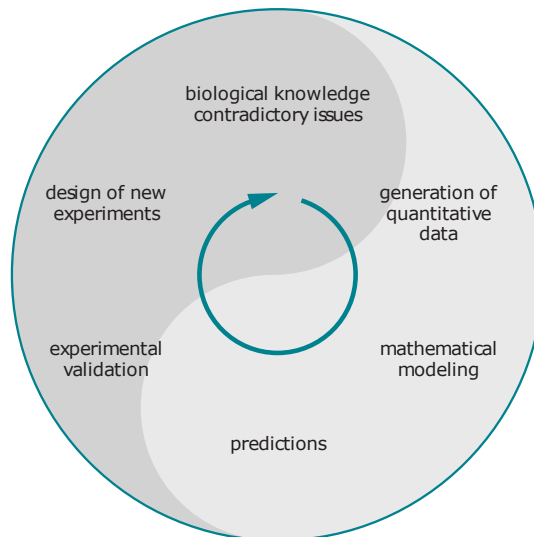


**Figure 1.8: Scheme of the iterative cycle of model development using a systems biology approach.** Adapted from Kitano *et al.* [110]

*Mechanistic models* are usually smaller networks focusing on the biochemical interactions and mechanisms and are typically based on differential equations, as these resemble biochemical reaction kinetics. Assuming the cell as a well-stirred reactor, ordinary differential equations (ODEs) are applied, while for investigations of spatial dynamics partial differential equations are used. [108]

*Pharmacokinetic* and *pharmacodynamic models* are especially important for clinical questions. While pharmacodynamics describes the effect of a drug on the body, pharmacokinetics describes how the body affects the drug e.g. by metabolization or excretion. [111]

Especially for the development of mechanistic model, the availability of quantitative and reproducible data in a time- and dose-resolved manner is essential. This data can be used in an iterative

cycle of model refinement (Figure 1.8).<sup>[104]</sup> To develop a hypothesis of a mechanistic model, prior biochemical knowledge is combined with quantitative data. This hypothesis is then translated in a mathematical frame of coupled ODEs with a given set of parameters  $\theta$  and the model is calibrated using the quantitative time- and dose-resolved data. In this process the ODE system is solved analytically or numerically for a set of initial start-parameters  $\theta_0$  to obtain the corresponding model trajectory  $g(x(t_i), \theta_0)$ . The trajectory is defined by the parameters  $\theta$  and the model components  $x(t_i)$  at a given time  $t_i$ . The distance between the data  $y(t_i)$  and the model trajectory  $g(x(t_i), \theta)$  is a measure for the goodness of the parameter estimation and is determined by an objective function, e.g. the  $\chi^2$ -function resulting from a log-transformation of the maximum likelihood  $L$  estimate assuming Gaussian distributed measurement noise (Equation 1.1). Therein,  $\sigma$  is the standard deviation and  $i$  is the summation index over all data points.

$$-2 \log(L) = \chi^2(\theta) = \sum_i \left( \frac{y(t_i) - g(x(t_i), \theta)}{\sigma_i} \right)^2 + const. \quad (1.1)$$

In an iterative process, the objective function is minimized by changing the model parameters  $\theta$  comprising rate constants, initial concentrations and offset parameters. All  $n$  parameters span an  $n$ -dimensional hypersurface and different algorithms are available to determine minima of this surface. It was shown that especially gradient-based optimization algorithms are superior in determining the minima of the objective function in mechanistic models.<sup>[112]</sup> Yet, to be sure that the minimum is the global and not a local minimum, usually a multi-start approach for  $\theta_0$  is used, using e.g. Monte-Carlo methods or Latin hypercube sampling, as a screening of the complete parameter space is computationally demanding even for a small  $n$ .<sup>[112]</sup> If the same minimum is found for multiple distinct initial parameters, the probability is high that this is the global minimum. This is particularly important, as different minima might have a completely different biological meaning and mechanisms of action.

After determination of the global minimum, the accuracy of a resulting parameter can be calculated by varying this parameter while reoptimizing all other parameters. This approach is called profile likelihood estimation and is able to reliably calculate the confidence intervals of an estimated parameter within the typically non-linear setting of biological models. If the parameter has no boundaries of 95 % confidence, it is called non-identifiable. There are practical and structural non-identifiabilities.<sup>[113]</sup> While structural non-identifiability is mainly caused by the model structure, practical non-identifiability is caused by the quality and amount of data. The use of identifiable parameters for predictions is required to obtain conclusive results. Further, an adequate number of free model parameters  $\theta$  should be used compared to the number of data points to avoid overfitting.

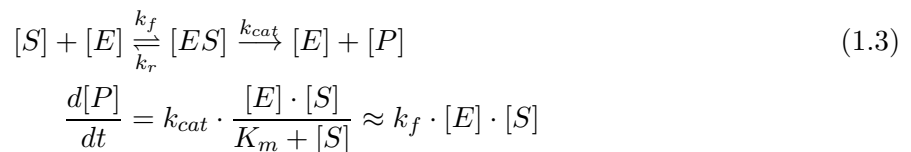
A further important aspect is the steady-state of the model. Thereby, it is assumed that the model is at  $t = 0$  in a dynamic equilibrium before a perturbation occurs.<sup>[114]</sup> This constraint helps to reduce the amount of free model parameters  $\theta$  and thereby improves the performance of the parameter optimization process which is especially important in large biological systems. Within this work, an algorithm developed by Rosenblatt *et al.*<sup>[114]</sup> was applied that analytically solves the steady-state constraint leading to non-negative and simple expressions for the steady-state equations.

To determine the effect of a specific parameter  $p_i$  on the model output  $K$ , a sensitivity analysis can be performed according to Equation 1.2, wherein  $S_{p_i}^K$  is the sensitivity of the parameter  $p_i$  on the model readout  $K$ .

$$S_{p_i}^K = \frac{p_i}{K} \cdot \frac{\partial K}{\partial p_i} \quad (1.2)$$

If the model can capture the dynamic behavior of the data, it can be used to design and predict new experiments. By iterative steps of validation or refining of the model it converges to a meaningful tool to gain insights into biological processes and to analyze the properties on the systems-level.

Within this work, ODE-based mathematical modelling was utilized to describe signal transduction in lung cancer, as this approach is suitable to mechanistically describe biochemical reactions. Thereby, some assumptions were made to reduce computational effort such as neglecting the spatial distribution of the cellular components and assuming the cell as a well-stirred reactor with a large number of molecules per species. Enzymatic reactions were approximated by mass action kinetics that can be derived from the Michaelis-Menten enzyme kinetics (Equation 1.3), if the reaction of the enzyme/substrate complex  $[ES]$  to the product is fast compared to formation of  $[ES]$  or likewise if the substrate concentration  $[S]$  is much smaller than the Michaelis-Menten constant  $K_m = \frac{k_r + k_{cat}}{k_f}$  or if  $[ES]$  is small. For signal transduction networks these are usually reasonable assumptions.



### 1.6.1 Mathematical models of the EpoR-pathway

Several mathematical pathway models of EpoR signal transduction have been described mainly focusing on the JAK2/STAT5 cascade. For example the nuclear shuttling of STAT5 has been identified by Swameye *et al.*<sup>[115]</sup> as a crucial mechanism regulating cellular response to Epo. It was shown by an ODE-based dynamic pathway model by Bachmann *et al.* (Figure 1.9A) that the integral of phosphorylated STAT5 in the nucleus over time can be directly linked to cell survival.<sup>[116]</sup>

This model comprises Epo-induced activation of JAK2 and EpoR as well as STAT5 shuttling, the induced negative regulators CIS and SOCS3 and the phosphatase SHP1. A mathematical model of receptor trafficking by Becker *et al.* (Figure 1.9B) revealed that fast receptor turnover is a key feature of Epo signal transduction granting a linear response over a broad dynamic range of Epo stimulation. The model focused on the receptor-ligand interaction and receptor trafficking testing several mechanisms of information processing. Both models depicted in Figure 1.9 were used as starting point for the investigations within this work.

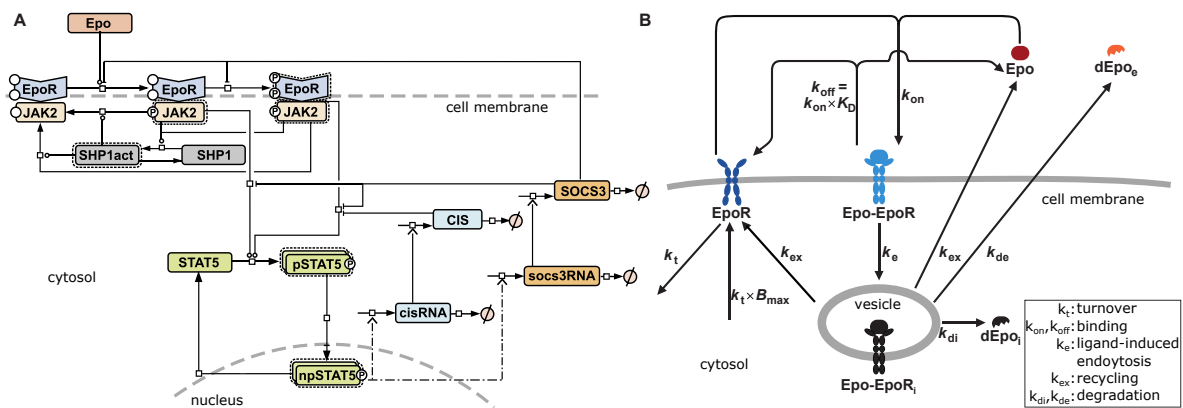


**Figure 1.9: Schemes of previously established mathematical models of EpoR signal transduction.** **A:** Pathway model of Epo-induced JAK/STAT signal transduction by Bachmann *et al.* focusing on activation of STAT5 and survival readout.<sup>[116]</sup> **B:** Receptor model for EpoR trafficking by Becker *et al.* describing receptor-ligand interactions, receptor degradation, turnover and recycling.<sup>[44]</sup>

### 1.6.2 Mathematical models of the EGFR and MET pathways

Due to its role in growth, survival, proliferation and differentiation, the EGFR signaling cascade is one of the best-studied signaling pathways.<sup>[117,118]</sup> The previously established models have been integrated by Oda *et al.* leading to a complete model of HER family signal transduction with more than 300 species and 200 reactions.<sup>[118]</sup> Species of this mathematical model include 10 ligands, 10 receptors, 61 enzymes, 10 transcription factors and 22 adaptor proteins. This complete model showed a bow-tie structure of the EGFR signaling pathway, in which a large variety of ligand:receptor complexes converges to a conserved core of only few signal transducers such as GTPases and PIPs that activate a large number of signaling cascades including transcriptional regulators. As this model is too complex to investigate a specific question, a reduced model structure was applied in this work. Also the interaction of EGFR with their inhibitors has been addressed by mathematical modeling. Kleinman *et al.*<sup>[119]</sup> found that a fast turnover of receptor phosphorylation has implications on the mechanism of action of EGFR-TKIs.

While EGFR signal transduction has been the aim of intensive research including mathematical modeling, MET signaling has been less studied. Yet, a study of D'Alessandro *et al.* identified the network structure and feedback regulation of MET receptor signaling in primary mouse hepatocytes.<sup>[120]</sup> They found several negative feedbacks within the MET signaling cascade including for example a feedback from AKT to RAF and from RSK to SOS. They also found positive feedbacks such as a feedback from ERK to PI3K and RAF and from RAS to PI3K. Some of these identified feedbacks will be used for this work. So far, there are no dynamic pathway models of the EGFR and MET crosstalk described. While there has been a Boolean model of EGFR and MET signal transduction reported by Singh *et al.*,<sup>[121]</sup> this model was developed mainly to investigate the influence on cell migration and proliferation in keratinocytes. To gain detailed knowledge on the EGFR/MET crosstalk, not only the connectivity of the signaling cascade, but also information on the kinetic rates is important.

### 1.7 Therapy resistance

The term therapy resistance is used for two types of resistance.<sup>[122]</sup> Primary or intrinsic resistance usually means that the patient does not show a response within the first 2-4 months of treatment. This can be caused e.g. by somatic alterations reducing drug efficiency. On the other hand, in case of secondary or acquired resistance patients show a response or stable disease for at least 6-8 months of treatment and subsequently develop disease progression still on the drug. While this work focuses mainly on acquired resistance, insights in this area might also be applied to primary resistance to improve response rates by pre-therapy stratification of the patients.

#### 1.7.1 EGFR-TKI resistance

Development of resistance against EGFR inhibitors is a major obstacle in lung cancer therapy as almost all patients develop resistance against EGFR-TKI treatment.<sup>[5]</sup> Although this is an intensively investigated field with numerous described mediators of resistance, a complete understanding of the cellular processes causing resistance is yet missing. A schematic overview of identified mediators of resistance is shown in Figure 1.10. Most common is the development of the resistance mutation T790M in 55% of the cases. *HER2* and *MET* amplification are also likely mediators of therapy resistance.

First, it is of interest whether the formation of resistance is an evolutionary process of clonal selection or whether alterations occur *de novo*. This question was recently addressed by high-complexity barcoding.<sup>[123]</sup> The authors of this study found that therapy mostly selects pre-existing subclones.

This is in line with results suggesting that  $2/3$  of the mutations differ within one microdissected tumor.<sup>[124]</sup> Hata *et al.* found on the other hand, that there is an early and late occurrence of acquired resistance that is caused by clonal selection and by *de novo* mutation of EGFR, respectively, suggesting that both possibilities occur during disease progression.<sup>[125]</sup>

The second question is, at which step resistance occurs. This could be pre-target, on-target or post-target. There is not much evidence for pre-target resistance that e.g. would prevent EGFR-TKIs from entering the cell. On the contrary, it is described that erlotinib can reverse ATP-binding cassette (ABC)B1-mediated multidrug resistance.<sup>[126]</sup> On-target resistance that alters binding of the drug to the receptor by secondary mutations in EGFR constitutes a major fraction and was discussed in subsection 1.1.1. As described above, this is maybe the best understood and addressable mediator of resistance, as there are already four generations of EGFR-TKIs. Post-target resistance on the other hand, is more diverse and less understood. While there are many reports, discussing causes of alterations in the efficacy of the inhibitor, there is not much known about their interplay. For example, the transformation of NSCLC to small-cell lung carcinoma (SCLC) or epithelial–mesenchymal transition are described processes leading to EGFR-TKI resistance.<sup>[5]</sup> The next paragraphs will give a short overview about the described mediators of post-target resistance.

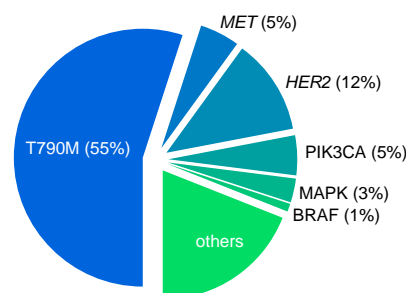


**Figure 1.10: Schematic overview of mediators of EGFR-TKI resistance.** Most common mediators of therapy resistance are the T790M mutation in EGFR and amplification of *HER2* and *MET*.<sup>[127]</sup>

**Mutations** Development of secondary mutations decreasing efficacy of EGFR-TKIs are very common especially in lung cancer, as it is besides melanoma the cancer with the highest mutation rate.<sup>[128]</sup> This might be even enhanced by some tumors by genomic instability caused by global hypomethylation that increases adaptability of the tumor to various therapies.<sup>[124]</sup>

Frequently, mutations occur in PI3K (5%) and BRAF (1-2%) leading to resistance,<sup>[127]</sup> while mutations in KRAS, NRAS and MEK seem to occur exclusively with EGFR activating mutations.<sup>[5,10]</sup> This effect seems to be lung-specific and is not found for example in colon cancer.<sup>[129]</sup> Further, there are several rare primary mutations in the EGFR, mainly exon 20 insertions, (5%) that initiate tumor growth, but are not susceptible to EGFR-TKI treatment.<sup>[127]</sup>

**Apoptosis** Apoptotic signaling of many cancer cells is deregulated to escape therapy-induced cell death. In lung cancer this can be realized through inhibition of pro-apoptotic activators via BH3, through loss of the BCL2 effectors BAX and BAK or through the increase of the anti-apoptotic protein BCL2.<sup>[130]</sup> p53 signaling plays a major role in regulation of apoptosis and was described above in subsection 1.1.2. Beside this, there is an increasing focus on the controversial role of autophagy in therapy resistance. While autophagy has a cell protective function and autophagy inhibitors are reported to act synergistic with EGFR-TKI treatment, autophagy is also the first step to apoptosis and initiators of autophagy are reported to restore EGFR-TKI sensitivity.<sup>[131]</sup>

**Alterations in protein abundance** Many studies have been performed analyzing changes in protein or mRNA abundance in resistant tumor cells. Yet, the underlying mechanism of these regulations remains often unclear. One already mentioned alteration is the amplification of the *MET* receptor. The frequency of *MET* amplification in NSCLC causing therapy resistance ranges from 5% to 20%.<sup>[124]</sup> There are studies showing that this amplification might already preexist in the treatment-naive tumor. Schildhaus *et al.* found high levels of *MET* amplification in 3% of the cases and intermediate amplification in 6% of drug-naive patients independent from histological subgroup and EGFR/RAS mutation status.<sup>[132]</sup> Turke *et al.* also found preexisting *MET* amplification in rare tumor cells in 5 out of 27 patients. After EGFR-TKI treatment, 4 of those patients developed therapy resistance mediated by *MET* amplification.<sup>[133]</sup> These results suggest that a screening for rare *MET* amplification before EGFR-TKI treatment might be beneficial to stratify patients that are likely to develop therapy resistance. In line with this, MET and pMET are reported to be downregulated upon EGFR-TKI treatment in EGFR-TKI sensitive cells.<sup>[134]</sup> This important role of MET might be caused by the fact that both EGFR and MET belong to the same class of RTKs<sup>[88]</sup> and, as both genes are located on chromosome 7, that polysomy of chromosome 7 is common in lung cancer. Interestingly, immunohistochemic staining showed that MET levels are higher at the tumor edge stressing the role of MET in metastasis.<sup>[83]</sup> Therefore, therapeutic MET inhibitors have been investigated in lung cancer either alone or in combination with EGFR-TKIs. While a phase II trial showed promising results,<sup>[135]</sup> the phase III trial of ARQ197, a MET kinase inhibitor, was discontinued because of futility (NCT01244191). A phase III trial (METLung) of efficacy of onartuzumab (MetMab), an inhibitory MET antibody, in combination with erlotinib versus erlotinib alone showed no benefit of the combinatorial treatment in *MET*-amplified patients in the second or third line of treatment.<sup>[136]</sup> A better stratification might be required to target MET effectively in a specific subset of patients.

The upregulation of other HER members has also been reported. While HER3 seems to be reduced upon EGFR-TKI treatment in resistant cells,<sup>[137]</sup> it is controversial whether EGFR, HER2 and HER3 are upregulated in resistant cells or only show increased phosphorylation.<sup>[138,139]</sup> Yalowitz *et al.* reported an upregulation of phosphorylated and total EGFR and HER2 caused by p53 mutations.<sup>[140]</sup> Further, it was shown that dual inhibition of EGFR and HER3 is effective in resistant cell lines, but not the inhibition of HER3 alone<sup>[138]</sup> and that the loss of HER3 leads to reduced growth of EGFR mutated lung tumors in a mouse model system.<sup>[141]</sup> A recent study of Pupo *et al.* showed for a MET-TKI that the drug also inhibited MET endocytosis, leading to increased number of MET molecules per cell and an overshoot of MET phosphorylation after withdrawal of the drug.<sup>[142]</sup> This might be caused by density-induced phosphorylation of MET that was previously described by Wickramasinghe *et al.*<sup>[143]</sup> and might be an explanation for the controversial results and stress the importance of dynamic measurements. Insulin-like growth factor 1 receptor expression levels and activation was also described to induce EGFR-TKI resistance.<sup>[144]</sup> Apart from MET, HGF is reported to lead to gefitinib resistance in lung adenocarcinoma.<sup>[145]</sup>

Apart from the receptors, pretreatment levels of BIM (BCL2L1) seem to be predictive for EGFR-TKI response.<sup>[146]</sup> A frequently occurring polymorphism in the BIM gene leads to altered splicing of BIM and therefore to an increased BIM expression. The RTK AXL is also reported to be activated by upregulation in 20 % of EGFR-TKI resistant tumors.<sup>[127]</sup> Apart from that, there are several more proteins that seem to play a role in therapy resistance and are reported to be upregulated in resistant tumor cells, e.g. MAPK,<sup>[127]</sup> ROR1,<sup>[147]</sup> EBP1,<sup>[148]</sup> ABCC2,<sup>[127]</sup> MUC4<sup>[149]</sup> or CRIPTO1.<sup>[5]</sup> Other proteins are described to be downregulated such as PTEN or NF1.<sup>[127]</sup>

**Heterodimerization of receptors** As most of the current therapies target the receptors, the receptor interactions highly influence therapeutic outcome. Therefore, it is not surprising that heterodimerization events have been reported to influence EGFR-TKI sensitivity. Regarding heterodimers of the HER family members, it was reported that HER2 is the preferred binding partner of all HER family members<sup>[69]</sup> as it is always able to dimerize with its missing ligand binding function. There are reports that HER3 is only tumorigenic in combination with HER2.<sup>[150]</sup> While it is reported that HER heterodimers fail to recruit CBL leading to reduced EGFR degradation and increased receptor abundance,<sup>[77]</sup> it is also reported that in EGFR-TKI resistant cells upregulation of EGFR leads to increased heterodimerization with HER2 and HER3 and to their transactivation.<sup>[139]</sup> According to this study patients would benefit from EGFR and HER2/3 dual inhibition. A study of Kiuchi *et al.* reported that EGFR:HER3 heterodimers are increased after EGFR-TKI therapy.<sup>[151]</sup> The authors also showed that the HER4 CYT2 splice variant forms heterodimers with

EGFR that compete for CBL and thereby protect EGFR from EGF induced degradation. This leads to enhanced migration by EGFR:HER4 heterodimerization and to prolonged signal activation. Thereby, EGFR:HER4 heterodimerization might play a role in therapy resistance in breast cancer.<sup>[151]</sup> An other study showed that currently used drugs such as erlotinib, gefitinib or lapatinib reduce EGFR homodimers, but not heterodimers with other HER members.<sup>[152]</sup>

Beside this, the heterodimerization of HER family members with MET is of interest. It was shown that *MET*-amplified lung cancer signals through HER3 mediating resistance to EGFR-TKIs<sup>[95]</sup> and that downregulation of HER3 is required for EGFR-TKI sensitivity.<sup>[153]</sup> In contrast, HER3 was also reported to be reduced upon EGFR-TKI treatment in resistant cells.<sup>[137]</sup> Apart from this, it has been described that EGFR:MET heterodimers are formed and that *MET* amplification leads to HER1-3 phosphorylation that is not inhibited by gefitinib.<sup>[93]</sup> Further, there are promising results of a bispecific EGFR/MET antibody which is effective against resistant cells with low toxicity that showed anti-tumor activity in xenografts in combination with a third generation EGFR-TKI.<sup>[154]</sup> Novel four-in-one antibodies against EGFR, HER2/3 and VEGF are more effective in resistant cells as they are suspected to disrupt HER/MET crosstalk.<sup>[155]</sup>

RON with its ligand HGF-like protein (HGFL) or MSP is a RTK functionally and structurally related to the MET receptor that is co-expressed with MET in many cancers and forms heterodimers with MET.<sup>[156]</sup> Investigations showed that RON expression is required for oncologic addiction to MET. There is also evidence for transphosphorylation of RON after EGF stimulation and a RON-dependent MET and EGFR phosphorylation after HGFL stimulation.<sup>[156]</sup> As knockout of RON lead to activation of MET signaling, it might be necessary to co-target MET and RON in patients.

**Tumor environment** The tumor microenvironment comprises immune cells, fibroblasts and endothelial cells, but also the extracellular matrix. The tumor environment is getting more and more in focus of investigations, as the tumor cells closely interact with surrounding non-tumor cells and they also modulate each other.<sup>[157]</sup> For example, it was shown that cancer-associated fibroblasts secrete HGF that induces proliferation and migration in the tumor cells.<sup>[158]</sup> Further, it was shown that local differences in drug concentration within the tumor bulk can facilitate formation of resistance.<sup>[159]</sup>

**Chemotherapy-induced EGFR-TKI resistance** Whether chemotherapeutic drugs reduce the efficacy of EGFR-TKIs or not, is controversially discussed. It has been reported that tumors are less sensitive to EGFR-TKIs after chemotherapy compared to first-line EGFR-TKI treatment.<sup>[124,160]</sup> This is speculated to be caused by the loss of PTEN during chemotherapy and subsequent activa-

tion of AKT. Therefore, erlotinib is now also approved for first-line treatment. Yet, a combined treatment of erlotinib with chemotherapy compared to chemotherapy alone did not improve therapy outcome in two clinical trials (TRIBUTE, TALENT).<sup>[161]</sup> Gefitinib showed the same result in the INTACT 1 and 2 trials.<sup>[162]</sup> Contrarily, van Schaeybroeck *et al.* reported a synergistic effect of EGFR-TKI and cisplatin in a subset of cell lines that show increased EGFR phosphorylation after stimulation with cisplatin and suggested that a better stratification might be needed to identify patients that benefit from combined first-line treatment.<sup>[163]</sup> Apart from that, it has also been reported that chemo- and radiotherapy-induced ROS lead to EGFR phosphorylation by inactivation of redox-sensitive, cysteine-based PTPs indicating that patients might benefit from subsequent EGFR-TKI treatment.<sup>[77]</sup> It was also reported that stress such as UV irradiation or chemotherapeutic agents induce EGFR degradation in a p38-dependent manner. Inhibition of this degradation path led to a reduced efficacy of chemotherapeutic drugs, while inhibition of EGFR by gefitinib could restore cytotoxicity. These results are in favor of a combinatorial treatment.<sup>[164]</sup>

### 1.7.2 Chemotherapy resistance

There are several suggested mechanisms of cisplatin resistance. As for resistance against EGFR-TKI treatment, they can as well be subdivided in pre-, on- and post-target resistance.<sup>[30]</sup>

**Pre-target resistance** Pre-target resistance occurs before cisplatin can bind to the DNA. Although cisplatin was initially thought to enter the cell by passive diffusion due to its linear and non-saturable uptake, it has been later reported that the efficiency of cisplatin can be actively impaired by reducing the cisplatin uptake in the cytosol mediated by copper transporter 1 or increasing the cisplatin export via ATP7B.<sup>[24]</sup> There are also other transmembrane proteins involved in this process such as cystic fibrosis transmembrane conductance regulator and ABCC2. Apart from this, cisplatin can also be absorbed inside the cell through increased levels of scavengers such as GSH or glutathione S-transferase (GST).<sup>[26,165]</sup> The GSH-Pt(II+) complex can then be actively transported out of the cell by glutathione transporters.<sup>[24]</sup>

**On-target resistance** Resistance can also be mediated by affecting the DNA repair mechanism leading to the apoptotic DNA damage response. Especially the NER and the MMR system can remove the cisplatin induced DNA damage. Apart from that, the increasing functionality of the homologous recombination system by compensatory mutations in breast cancer type 1/2 susceptibility protein has been shown to favor cisplatin resistance.<sup>[166]</sup> It was also shown in lung cancer that resistant cells harbor mutations in the mitochondrial DNA affecting the respiratory chain.<sup>[30]</sup> Be-

side this, compromising the apoptotic machinery can lead to cisplatin resistance (subsection 1.1.2). Apart from the loss of p53 activity, there are other apoptotic proteins involved including p38<sup>MAPK</sup>, c-Jun N-terminal kinase (JNK)1 and BCL2 family members.

**Off-target resistance** Besides this, resistance can occur at the signaling level activating alternative anti-apoptotic pathways such as HER2 leading to AKT activation. Moreover, proteins of the autophagy system and HSPs were reported to mediate resistance.<sup>[30]</sup> The role of EGFR in chemoresistance is discussed controversially, since there is the possibility to treat patients with chemotherapy and EGFR-TKIs in combination or sequentially. While trials showed that combinatorial treatment of EGFR-TKI with chemotherapy is not better than chemotherapy alone,<sup>[161,162]</sup> there are studies available that chemotherapy is less effective after first-line EGFR-TKI treatment.<sup>[167]</sup> Yet, there is evidence for both sequential approaches.

On one hand it was reported that chemoresistant cells have a two- to three-fold higher sensitivity to gefitinib caused by the upregulation of HER2/3, but not EGFR, and by the upregulation of EGFR ligands leading to enhanced EGFR-pathway activation.<sup>[168]</sup> Li *et al.* showed that EGFR inhibition increases cisplatin sensitivity.<sup>[169]</sup> And it was also shown that EGF has a protective function against cisplatin damage mediated by interleukin-1 $\beta$  secretion.<sup>[170]</sup>

These results would be in favor of a combined treatment, but on the other hand Yamaguchi *et al.* showed that gefitinib inhibits caspase-independent cell death via activation of FOXO3a and via reduced amounts of ROS.<sup>[171]</sup> In breast cancer cells, it was shown that heregulin induces p21<sup>WAF1/CIP1</sup> expression being protective against cisplatin-induced genotoxic damage.<sup>[172]</sup> Mandic *et al.* demonstrated that EGFR stimulation leads to increased cisplatin sensitivity due to higher proliferation.<sup>[173]</sup> These findings rather speak against combinational treatment of chemotherapy and EGFR-TKIs.

**Drug-induced resistance** As already described, ESAs are commonly applied drugs in cancer-associated anemia. Yet, their role in cisplatin resistance is controversially discussed.<sup>[46]</sup> Some studies investigating the role of ESAs compared to placebo in chemotherapy-receiving patients found a significant decreased survival in ESA-treated patients,<sup>[174,175]</sup> while others reported the safety of ESA treatment.<sup>[176,177]</sup> The adverse effect of ESAs in decreasing cisplatin efficiency was suggested to be caused by expression of EpoR and Epo in tumor cells.<sup>[38,178]</sup> Dagnon *et al.* found expression of EpoR on protein and mRNA level in NSCLC tumors in 96 % of the samples.<sup>[178]</sup> As they found also HIF1 $\alpha$  co-expression, they suggested a hypoxia-mediated expression of EpoR and Epo in tumor tissue. These findings led to concerns of treating anemic patients with recombinant ESAs.

The concerns were supported by the results that Epo induces STAT5, AKT and ERK signaling in NSCLC. While Epo was reported to not induce proliferation in tumor cells, there are investigations in chemotherapy-treated cells showing increased survival upon Epo co-treatment.<sup>[179,180]</sup> Interestingly, a study in patients not treated with recombinant ESAs showed also a reduced 5-year survival for tumors expressing high levels of EpoR.<sup>[181]</sup> Yet, concerns have been raised regarding the specificity of EpoR antibodies<sup>[39]</sup> and since many of the studies rely on antibody-based analyses, the role of ESAs in chemotherapy is controversially discussed.<sup>[46]</sup> A study performed by Sinclair *et al.* showed that there are no elevated levels of EpoR mRNA in tumor versus normal tissue.<sup>[182]</sup> In summary, although the findings are contradictory, this might highlight a context-specific or diverse role of ESAs in cancer therapy.

**Environment** The tumor microenvironment emerged as a highly important factor in cancer development and therapy, as tumor cells can reprogram surrounding cells to promote tumor growth and metastasis.<sup>[157]</sup> As most tumors arise from epithelial tissue, their size is limited to a diameter of 2 mm due to lacking vascularization.<sup>[183]</sup> Therefore, tumor-associated endothelial cells need to form new vessels for tumor propagation and anti-angiogenic drugs such as regorafenib targeting VEGF receptor are approved for cancer therapy. It was found that endothelial cells also express EpoR and that Epo treatment leads to proliferation, migration and release of VEGF in endothelial cells.<sup>[46]</sup> It is believed that hypoxic tumor tissue is more chemoresistant mediated by HIF1 $\alpha$ , as patients with low oxygen pressure in the tumor show worse survival.<sup>[184]</sup> This is suspected to be caused by increased genetic instability, downregulation of DNA repair and upregulation of HIF1 $\alpha$  leading to VEGF and Epo secretion.<sup>[185,186]</sup> Although recombinant ESAs improve tumor oxygenation only in some studies, anemia is suspected to increase hypoxic conditions and therefore risk.<sup>[46,187]</sup>

## 1.8 Objectives

One of the major problems in therapy of lung cancer patients is development of therapy resistance. Although most patients show a good response after first line of therapy, most of them will relapse. This holds true for chemotherapy as well as targeted therapy, which are in most cases the only option for patients with a late stage metastatic disease.

Therefore, the aim of this work was to understand the mechanisms leading to therapy resistance. Specifically, the role of Epo in chemotherapy will be investigated regarding induction of chemoresistance. Further, the interplay of EGF and MET receptor in NSCLC will be investigated regarding resistance to EGFR-TKIs. Specifically, the following questions will be addressed:

- What are the differences of Epo-induced signal transduction in CFU-E and NSCLC cells?  
(section 2.1)
- What is the impact of Epo treatment in combination with chemotherapy *in vivo*?  
(section 2.2)
- How does the binding kinetics of erythropoiesis stimulating agents influence the cellular response?  
(section 2.3)
- What is the mechanism of MET expression in therapy resistance against EGFR-TKIs?  
(section 2.4)

To address these questions, a systems biology approach will be utilized. Quantitative data of signal transduction pathways will be generated and utilized to calibrate mathematical models. By model predictions and validations the underlying mechanism of therapy resistance will be investigated to predict optimized therapeutic options to improve the therapy response.

## 2 Results

### 2.1 Impact of Epo on erythroid progenitor and lung cancer cells during chemotherapy

The role of erythropoietin (Epo) in treating chemotherapy-related anemia is controversially discussed, because it is suspected that Epo can also induce tumor cell survival (subsection 1.1.3). Epo-induced cell survival has previously been linked to the activation of the Janus kinase (JAK)2/signal transducer and activator of transcription (STAT)5 signal transduction.<sup>[116]</sup> To investigate the impact of Epo on tumor growth, the Epo-induced JAK2/STAT5 signal transduction was compared between erythroid progenitor cells and a non-small-cell lung cancer (NSCLC) cell line. The work shown in this section was performed in collaboration with R. Merkle (DKFZ Heidelberg) and B. Steiert (University of Freiburg) and was published in Merkle *et al.*<sup>[188]</sup>

As a model system for healthy cells depending on Epo-induced signal transduction, murine primary erythroid progenitor cells were isolated at the colony forming unit - erythroid (mCFU-E) stage by R. Merkle. The human NSCLC cell line H838 was chosen to represent the tumor. To test whether the cells express a functional erythropoietin receptor (EpoR), an immunoblot analysis was performed as part of this work. It was shown that mCFU-E cells as well as H838 cells express the EpoR and respond to Epo treatment (Figure 2.1A). A band corresponding to the phosphorylated EpoR was detected after stimulation of the cells with either 5 U/mL Epo $\alpha$  for 10 min in mCFU-E cells or 10 U/mL Epo $\beta$  for 10 min in NSCLC cells. As the levels of the EpoR are rather low in H838 cells, the HA-tagged human EpoR<sup>[44]</sup> was stably overexpressed in these cells by retroviral transduction (H838-HA-hEpoR cells). A characterization of H838-HA-hEpoR cells is shown in the right panel of Figure 2.1A, depicting that the total levels of EpoR are increased. A slight shift to higher molecular weight is most likely caused by the HA-tag fused to EpoR in these cells. The phosphorylation of EpoR could also be detected in H838-HA-hEpoR cells.

To test the comparability of the 5 U/mL Epo $\alpha$  and 10 U/mL Epo $\beta$  stimulus, an immunoblot analysis was performed in H838 cells that were stimulated with either 5 U/mL Epo $\alpha$  or 10 U/mL Epo $\beta$  for up to 240 min (Figure 2.1B). The phosphorylation of the EpoR was monitored over time indicating

that the response in signal transduction to Epo $\alpha$  or to Epo $\beta$  was comparable. The phosphorylation of STAT5 was measured after 10 min showing also no change in response to both Epo derivatives. The results indicate that the respective doses of ligand induce in H838 cells the same phosphorylation response level of EpoR and STAT5.

To determine the amount of EpoR overexpression in H838-HA-hEpoR cells, the band corresponding to the EpoR was quantified by immunoblotting in wild type H838 cells and H838-HA-hEpoR cells as part of this work. As shown in Figure 2.1C, the transduced H838-HA-hEpoR cells showed a 172-fold increase in total EpoR expression. Interestingly, by comparing the relative amount of phosphorylated EpoR in H838-HA-hEpoR cells with wild type H838 cells, the EpoR phosphorylation was found to be increased only by a factor of approximately 12-fold. This could be caused by either a reduced transport of the overexpressed receptor to the plasma membrane or a limitation in JAK2 abundance in H838-HA-hEpoR cells that was reported to act as chaperone and thereby increases surface expression of EpoR.<sup>[189]</sup>

Further, to determine the absolute number of Epo receptors per cell, recombinant protein standards of the glutathione S-transferase (GST)-tagged cytoplasmic domain of the human and murine EpoR were applied.<sup>[190]</sup> The recombinant standards were used to generate a calibration curve shown exemplary for H838-HA-hEpoR cells in Figure 2.1D. The experimental error was determined using error propagation accounting for the error of the linear regression of the calibration curve, for the number of counted cells and for the standard deviation of the endogenous receptor signal. Thereby, it was found that H838 cells harbor  $3\,600 \pm 1\,200$  and H838-HA-hEpoR cells harbor  $620\,000 \pm 200\,000$  hEpoR molecules per cell, while mCFU-E cells express  $4\,300 \pm 2\,200$  mEpoR molecules per cell. Because the average cellular volume of mCFU-E cells of  $700\,\mu\text{m}^3$  is much smaller than the volume of H838 cells with  $14\,000\,\mu\text{m}^3$ ,<sup>[188]</sup> the number of Epo receptors per cell surface is even lower in wild type H838 cells.

To test to which extent the JAK2/STAT5 signaling cascade is activated upon Epo stimulation in NSCLC cells, quantitative immunoblotting and mass spectrometric analyses of JAK2 and STAT5 were performed. Figure 2.1E shows the degree of phosphorylation of STAT5 in H838 and H838-HA-hEpoR upon stimulation with different doses of Epo $\beta$  for 20 min determined by mass spectrometry. The degree of STAT5 phosphorylated was determined as the fraction of phosphorylated STAT5A per total STAT5A. Applying a saturating Epo dose in H838 cells only a small fraction of STAT5 of less than 3% was phosphorylated, while up to 60% of STAT5 was phosphorylated in H838-HA-hEpoR cells. These results showed that the NSCLC cell line H838 expresses a functional EpoR and that these cells respond to Epo treatment.

## 2.1 Impact of Epo on erythroid progenitor and lung cancer cells during chemotherapy

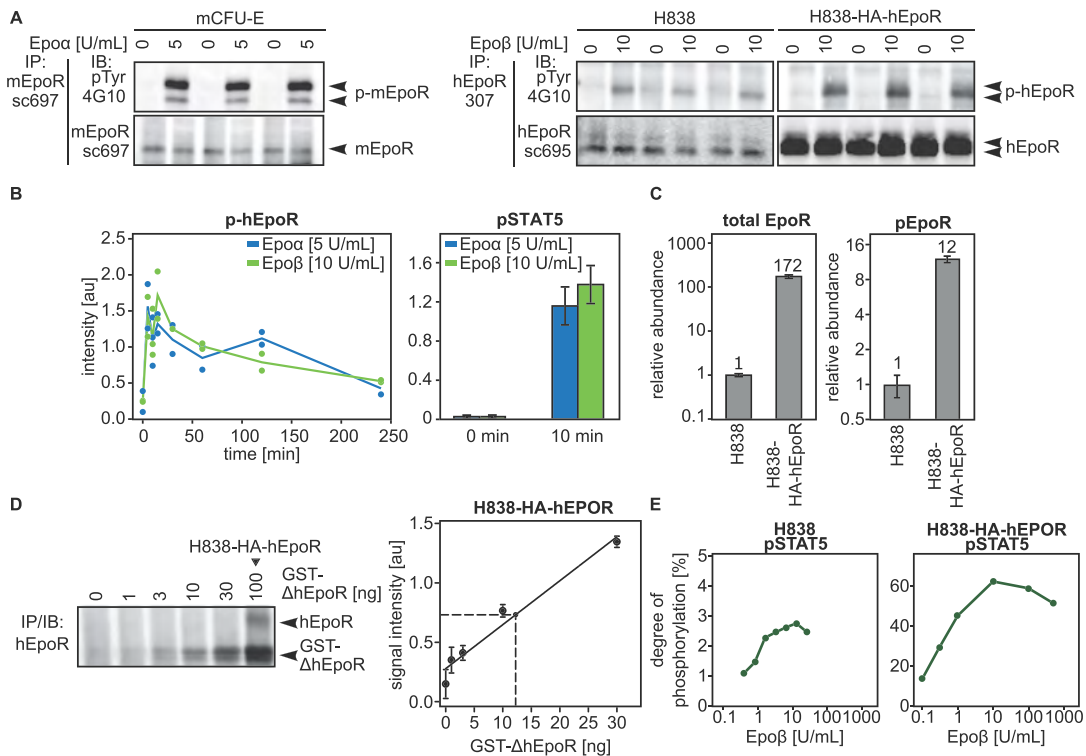


**Figure 2.1: Expression and functionality of EpoR.** **A:** Immunoblot (IB) analysis of phosphorylated and total EpoR in mCFU-E, H838 and H838 cells stably transduced with HA-tagged human EpoR (H838-HA-hEpoR) after subjection to immunoprecipitation (IP) against EpoR. Cells were induced by 5 U/mL Epo $\alpha$  for CFU-E cells and 10 U/mL Epo $\beta$  for H838 cells for 10 min. **B:** H838 cells were stimulated with 5 U/mL Epo $\alpha$  or 10 U/mL Epo $\beta$  for the indicated time points and phosphorylated EpoR and STAT5 was measured by immunoblotting. Error bars represent SD of biological replicates ( $n = 3$ ). **C:** Quantification of the total and phosphorylated amount of EpoR in H838-HA-hEpoR cells compared to wild type H838 cells by immunoblotting. The error bar represents standard deviation of three biological replicates. **D:** Determination of EpoR molecules per cell in H838-HA-hEpoR by immunoblotting with a recombinant standard (GST- $\Delta$ hEpoR). The right panel shows the quantification of three biological replicates. The intensity of the cellular EpoR and the corresponding amount of calibrator is indicated by a dashed line. Error bars represent standard deviation. **E:** Mass spectrometric analysis of the degree of STAT5 phosphorylation in H838 and H838-HA-hEpoR cells treated with the indicated doses of Epo $\beta$  for 20 min. The average degree of STAT5 phosphorylation of two biological replicates is shown.

After demonstrating that the EpoR is activated and signal transduction of the human NSCLC cell line H838 is induced by stimulation with Epo, the question was addressed to which extent Epo influences cell viability upon cisplatin treatment of H838 cells. A cell viability assay was performed by R. Merkle in H838 cells treated with or without Epo in combination with cisplatin and demonstrated that while Epo alone had no effect on proliferation in these cells, the cells can be rescued from cisplatin-induced cell death by co-treatment with Epo.<sup>[188]</sup> This suggested that in the

presence of Epo H838 and H838-HA-hEpoR cells are less affected by cisplatin treatment indicating that Epo contributes to resistance against chemotherapeutic agents.

To investigate the response of lung cancer as well as of healthy cells to cisplatin and Epo and to identify cell type-specific responses of Epo in the healthy and the tumor context, a method to identify cell type-specific differences in the parameters of ordinary differential equation (ODE)-based signal transduction models was developed by B. Steiert. Thereby, all parameters were initially assumed to be cell type-independent. Then, a penalization term was introduced for each parameter that restricts the parameters with linearly increasing strength to be equal for all cell types ( $L_1$  prior method). Subsequently, the data for the different cell lines was used simultaneously for parameter estimation of one combined mathematical model and the  $L_1$  regularization term was stepwise increased. The likelihood ratio was then used to determine the parsimonious model with only significant cell type-specific parameters. This  $L_1$  regularization method was applied to a previously developed mathematical model of Epo-induced signal transduction of the JAK2/STAT5 pathway in mCFU-E cells (Figure 1.9)<sup>[116]</sup> to describe the difference in signal transduction in H838, H838-HA-hEpoR and mCFU-E cells (Figure 2.2) applying the D2D framework.<sup>[191]</sup>

The mathematical model was calibrated with time- and dose resolved quantitative immunoblot and mass spectrometric data as well as absolute numbers of molecules per cell of H838, H838-HA-hEpoR and mCFU-E cells. Representative time-resolved signal transduction data is depicted in Figure 2.2. The signal transduction data for mCFU-E cells was obtained from Bachmann *et al.*,<sup>[116]</sup> mRNA expressions of *CISH* and *SOCS3* were measured by R. Merkle and immunoblot data of phosphorylated EpoR, phosphorylated STAT5 and total STAT5 was measured as part of this work. The initial concentration of EpoR were determined as part of this work and initial concentrations of JAK2 and STAT5 were described previously.<sup>[116]</sup> The measured initial concentrations were fixed in the model. While the dynamics of EpoR phosphorylation is comparable in mCFU-E cells, wild type H838 cells and H838-HA-hEpoR cells, the STAT5 phosphorylation of wild type H838 cells is more transient compared the H838-HA-hEpoR cells. Figure 2.2 depicts the mathematical model trajectories for the model with only cell type-specific parameters, for the model with no cell type-specific parameters and the parsimonious model that was identified by the  $L_1$  regularization method. The trajectories showed that the model with no cell type-specific parameters cannot capture the dynamics of H838 and CFU-E cells at the same time, especially regarding the kinetic of total STAT5 and *suppressor of cytokine signaling (SOCS)3* mRNA, while the mathematical model with only cell type-specific parameters can describe the data. Yet, the later model has a high degree of freedom due to a large amount of free parameters. Many of these parameters have different values in the individual cell lines without biological background due to small fluctuations in the data. The

parsimonious model contains only 7 out of 26 cell type-specific parameters and still captured the dynamics of the experimental data. The 26 tested parameters contained the 25 kinetic rates and the initial concentration of the protein tyrosine phosphatase (PTP).

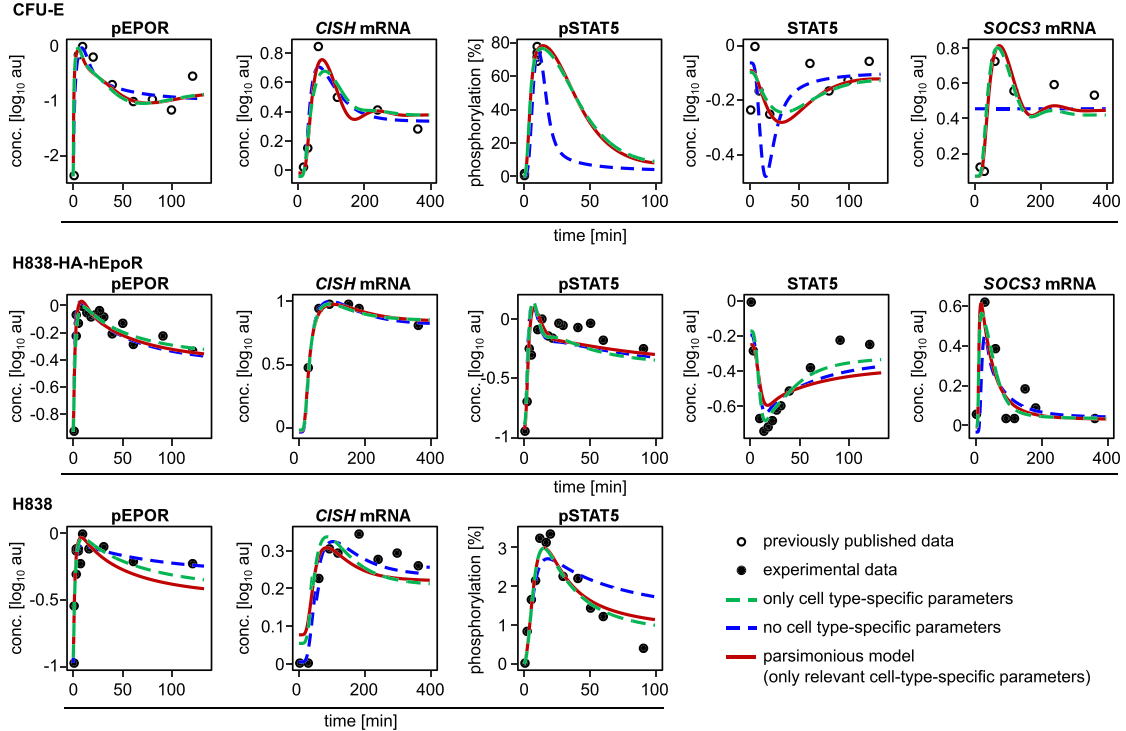


**Figure 2.2: Calibration of the mathematical model.** Selection of the quantitative signal transduction data for CFU-E, H838 and H838-HA-hEpoR cells measured by quantitative immunoblot, qRT-PCR and mass spectrometry. This includes mRNA expression of the EpoR targets *CISH* and *SOCS3* measured by R. Merkle as well as phosphorylated EpoR and JAK2, cytoplasmic STAT5 and the degree of STAT5 phosphorylation measured as part of this work. The circles represent previously published CFU-E data.<sup>[116]</sup> The complete data set used for model calibration is available in Merkle *et al.*<sup>[188]</sup>

The 7 parameters identified as cell type-specific were, the *CISH* mRNA turnover rate, the activation rate of EpoR by JAK2 and the activation rate of JAK2 by Epo with higher values in mCFU-E cells and the delay in *SOCS3* mRNA production, the *SOCS3* promoter activity, the import rate of pSTAT5 into the nucleus and the nuclear deactivation rate of STAT5 with lower values in mCFU-E cells. The cell type-specific parameters are indicated in the model scheme in Figure 2.3.

To identify possible therapeutic targets, a sensitivity analysis was performed for H838 and mCFU-E cells by B. Steiert. As readout, the integral amount of nuclear phosphorylated STAT5 was calculated at 60 min post stimulation ( $K$ ), which was previously correlated in mCFU-E cells with cell survival.<sup>[116]</sup> The control coefficient  $S_{p_i}^K = \frac{p_i}{K} \cdot \frac{\partial K}{\partial p_i}$  was calculated for all model parameters  $p_i$ . Interestingly, the sensitive parameters did not entirely overlap with the cell type-specific parameters and the control coefficients differed between H838 and mCFU-E cells. As depicted in Figure 2.3

in light blue, six parameters showed a larger coefficient in H838 than in mCFU-E cells. The larger the control coefficient  $S_{p_i}^K$ , the stronger is the impact of the parameter  $p_i$  on the biological readout, in this case the integral amount of nuclear phosphorylated STAT5 that was shown to correspond to cell survival.<sup>[116]</sup> Because the six parameters with larger  $S_{p_i}^K$  values in H838 might affect tumor cells stronger than healthy cells, they could be considered as therapeutic targets.

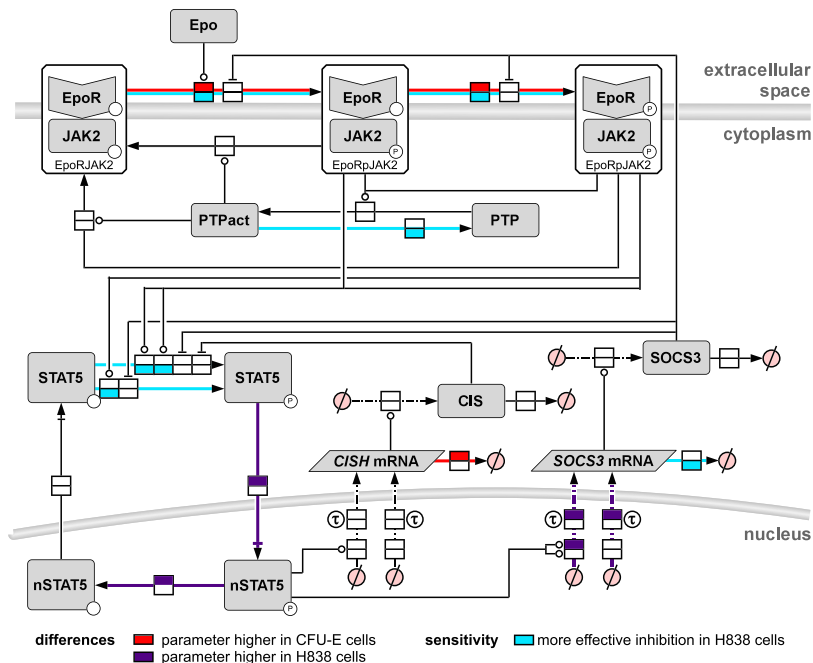


**Figure 2.3: Model structure with cell type-specific and sensitive parameters.** Schematic representation of the ODE-based mathematical model of Epo signal transduction according to the Systems Biology Graphical Notation.<sup>[192]</sup> The mathematical model was developed by B. Steiert. The EpoR-JAK2 complex is sequentially phosphorylated upon Epo binding and induces phosphorylation and translocation to the nucleus of STAT5. Nuclear (n) STAT5 induces transcription of *CISH* and *SOCS3* mRNA with a delay  $\tau$ . The cell type-specific parameters are indicated in red (higher in mCFU-E) or purple (higher in H838). Parameters identified by the sensitivity analysis as possible therapeutic targets are indicated in light blue.

Most of the identified sensitive parameters were related to the Epo receptor complex and activation of STAT5. The differences in the ratio of cytoplasmic and nuclear volume in H838 and mCFU-E cells may explain the cell type-specificity of STAT5 import to the nucleus. Further, STAT5 has two additional binding sites in the murine *SOCS3* promoter providing an explanation for the altered activation rates. Interestingly, the activation rate of JAK2 by Epo and the activation rate of the EpoR by JAK2 were identified as cell type-specific. Since the sensitivity analysis predicted that these reactions are more sensitive to inhibition in H838 cells compared to mCFU-E cells, they represent potential drug targets. One reason for this might be the different binding affinities of the applied human recombinant Epo on the murine EpoR. Moreover, JAK2 is highly expressed

in mCFU-E cells, while JAK2 concentrations might be limiting in H838 cells. Although further species-related alterations can not be excluded by this analysis, the inhibition of JAK2 in the context of Epo-treated anemia during chemotherapy might be promising according to the obtained results. As there are JAK2 inhibitors approved for clinical application, this could be a potential aim of a study to extend the label of existing drugs for new indications to improve response in chemotherapy-treated lung cancer patients by decreasing the anti-apoptotic effect of Epo-treatment in the tumor cells only.

In sum, the expression of EpoR in the tumor cell line H838 and in mCFU-E cells was quantified and the dynamics of the signal transduction of the Epo-induced JAK2/STAT5 pathway was determined. Using the quantitative data, a mathematical model was calibrated to describe H838, H838-HA-hEpoR and mCFU-E cells simultaneously and JAK2 was identified as potential drug target to inhibit Epo-induced signal transduction in tumor cells, but not in healthy erythroid progenitor cells.

## 2.2 Erythropoietin alters vascularization and drug supply in mouse xenografts

In the previous section, it has been shown that Epo increases survival of cisplatin-treated cells.<sup>[188]</sup> However, Epo might also affect the tumor environment, especially vascularization, and thereby alter response to chemotherapeutic agents. To investigate *in vivo* the impact of Epo on tumor growth upon carboplatin treatment, experiments in mice were performed in collaboration with D. Doleschel (University of Aachen).<sup>[193]</sup> Two NSCLC cell lines were applied for generation of a xenograft mouse model harboring the EpoR performed by D. Doleschel *et al.*, H838 cells that were shown in section 2.1 to express the EpoR and A549 cells that were previously reported to express EpoR, but eight times less than H838 cells.<sup>[194]</sup> The mice were treated with 60 mg/kg carboplatin either alone or in combination with 5 and 20  $\mu\text{g}/\text{kg}$  Epo $\beta$ . The tumor size was monitored for up to 3 weeks (Figure 2.4A). For H838 cells as well as A549 cells the tumor growth in combination with Epo was reduced. The co-treatment with 5  $\mu\text{g}/\text{kg}$  Epo $\beta$  was sufficient to decrease the tumor size and the co-treatment with 20  $\mu\text{g}/\text{kg}$  Epo $\beta$  did not further decrease the tumor size. While the mice treated with carboplatin suffered from chemotherapy-induced anemia and decreased hemoglobin (Hb)-levels, the Hb-levels were normalized in the Epo-treated group.

Using a near infrared labeled EpoR-probe it was previously observed that Epo is adsorbed in the tumor and the tumor endothelium.<sup>[194]</sup> However, the expression of functional EpoR on HUVECs has been controversially discussed.<sup>[46]</sup> As part of this work it was investigated, if Epo induces signal transduction and proliferation of endothelial cells. For this purpose the human umbilical vein endothelial cells (HUVEC) cell line was tested for EpoR expression and activation by quantitative immunoblotting. Parental BaF3 cells that express no detectable levels of the EpoR were used as negative control. As positive control BaF3 cells were stably transduced with HA-tagged human EpoR (BaF3-HA-hEpoR) as described in Becker *et al.*<sup>[44]</sup> Figure 2.4B shows the response in EpoR phosphorylation of HUVEC, parental BaF3 and BaF3-HA-hEpoR cells that were stimulated with 15 U/mL Epo $\beta$  for 10 min or left untreated. A band corresponding to the phosphorylated and total EpoR was detected in HUVEC cells showing a 2.8-fold increased amount of phosphorylated EpoR after stimulation as quantified in biological triplicates. A slight shift of the EpoR band to higher molecular weight could be detected in BaF3-HA-hEpoR compared to HUVEC cells most likely due to the increased mass of the EpoR fused to the HA-tag.

To investigate the impact of Epo on vessel density and tumor hypoxia, immunofluorescent stainings of tumor sections were performed by D. Doleschel with antibodies against CD31<sup>+</sup> and HIF1 $\alpha$ , respectively. Immunofluorescent stainings of tumor sections at day 21 revealed an increase in vessel

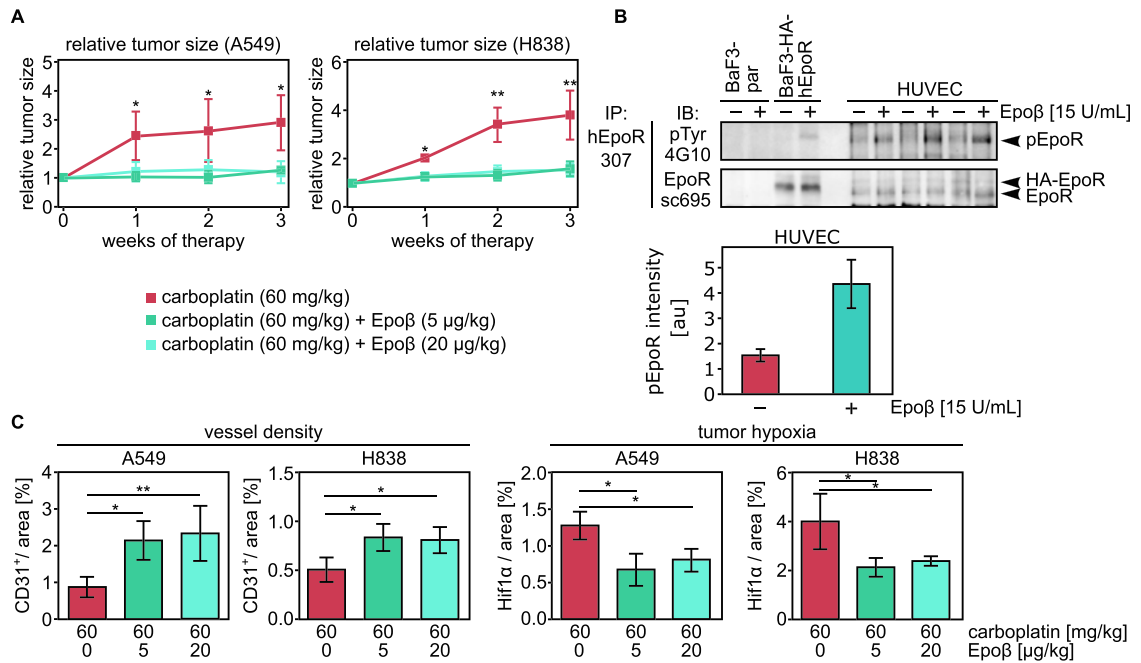


**Figure 2.4: Impact of Epo on carboplatin response.** **A:** Relative tumor size of a xenograft system applying H838 and A549 cells. The tumor size was quantified by 3D ultrasound by D. Doleschel, and the average of  $n = 5$  mice is shown,  $* = p < 0.05$   $** = p < 0.01$ . **B:** Analysis of EpoR in HUVECs by quantitative immunoblotting. The cells were stimulated for 10 min with 15 U/mL Epoβ (+) or left untreated (-). As positive and negative control,  $1 \cdot 10^6$  BaF3 cells were used either transduced with HA-hEpoR or left parental. Cytoplasmic cell lysates were subjected to immunoprecipitation (IP) applying 150 μg protein for BaF3 cells and 1500 μg protein for HUVECs cells. Quantification of the signal intensity of phosphorylated EpoR in HUVEC cells is shown below. Error bars represent standard deviation of three biological replicates. **C:** Immunofluorescent staining of tumor sections with anti-CD31<sup>+</sup> or HIF1α in mice treated with 60 mg/kg carboplatin alone or co-treated with 5 and 20 μg/kg Epoβ performed by D. Doleschel. Tumor sections were taken at day 21. Shown is the average of 5 mice,  $* = p < 0.05$ ,  $** = p < 0.01$ .

density (Figure 2.4C, left panel) in tumors co-treated with Epo and a reduced tumor hypoxia (Figure 2.4C, right panel) in xenografts based on H838 as well as A549 cells.

This led to the conclusion that co-treatment with Epo leads to increased tumor vascularization and perfusion causing increased accessibility of the chemotherapeutic drug and thereby reduced tumor growth in carboplatin treated mice. These results suggest that co-administration of Epo in chemotherapy might improve therapeutic outcome. Yet, further investigations are needed to translate these findings to the human context, since vascularization might be different in a xenograft model compared to the human system.

## 2.3 Binding kinetics of erythropoiesis stimulating agents changes cellular responses

Erythropoiesis stimulating agents (ESAs) are widely used to treat chemotherapy-related anemia in cancer.<sup>[195]</sup> Yet, as described above, ESAs have a diverse role in cancer therapy such as induction of survival signaling of tumor cells as well as a potential increase of drug accessibility by vascularization. Depending on the context, one aspect might be dominating and thereby explain the controversial results in literature regarding benefit or risk of ESA treatment.<sup>[46]</sup> The concerns raised regarding the specificity of EpoR antibodies further complicate the experimental findings. To improve the quantification of the EpoR and determine receptor expression-dependent responses to ESAs, an assay was developed by A. Rodriguez (DKFZ Heidelberg) based on ligand depletion and a previously published mathematical model of Epo signal transduction in murine CFU-E cells.<sup>[44]</sup> The authors of that study showed that a large intracellular pool of EpoR combined with a fast turnover leading to fast ligand depletion is a main feature of this signaling pathway. Starting from this basis, an integrative mathematical model of the human context was developed taking the absolute number of Epo binding sites in healthy and in tumor cells into account.

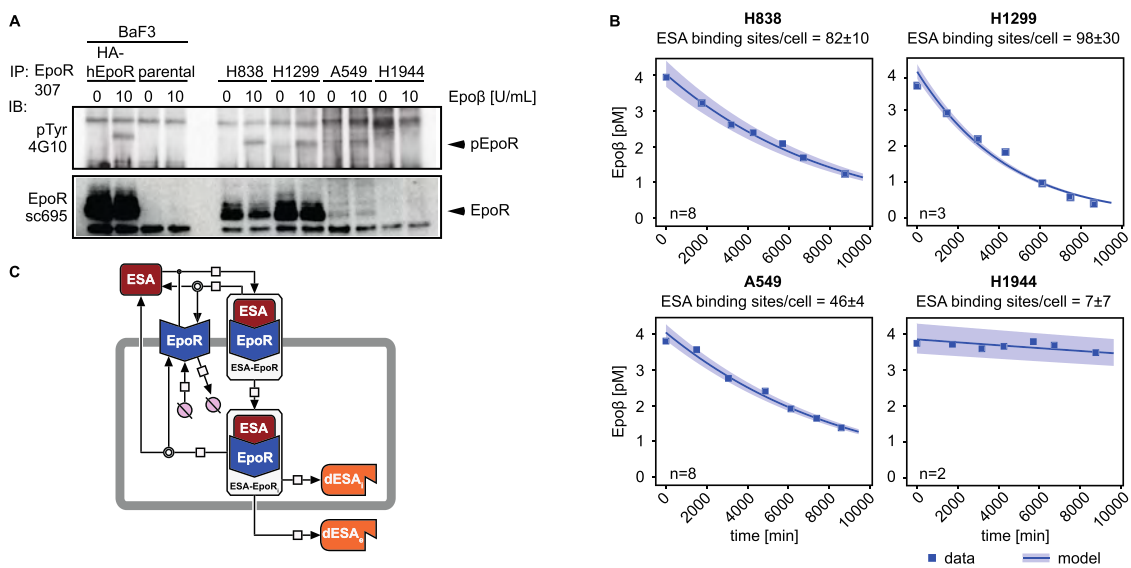


**Figure 2.5: Development of a mathematical ESA model of the human context.** **A:** Parental BaF3 cells, BaF3 cells overexpressing EpoR and four NSCLC cell lines were stimulated with 10 U/mL Epoβ for 10 min. A quantitative immunoblot (IB) analysis was performed after immunoprecipitation (IP) against EpoR. **B:** Measurement of the Epoβ concentration in the cellular supernatant over time in four NSCLC cell lines (H838, H1299, A549 and H1944) measured by A. Rodriguez. Data of a representative experiment is shown as dots, the splines represent the trajectories estimated by the mathematical model. The number of biological replicates and the determined number of ESA binding sites is indicated in the figure. The shading represents the model-estimated error of the data. **C:** Structure of the mathematical Epo model described in Becker *et al.*<sup>[44]</sup>

First, to identify a set of NSCLC cell lines with distinct expression of EpoR, an immunoblot analysis of EpoR was performed in H838, H1299, A549 and H1299 cells (Figure 2.5A). To verify that the EpoR in the selected cell lines is functional and phosphorylated, their response to Epo $\beta$  was analyzed by quantitative immunoblotting. Parental BaF3 cells that express no detectable levels of EpoR were used as negative control. As positive control, BaF3 cells were stably transduced with HA-tagged human EpoR (BaF3-HA-hEpoR) described in Becker *et al.*<sup>[44]</sup> Phosphorylated and total EpoR could be detected from cytoplasmic lysates after IP against EpoR. Phosphorylation of EpoR is induced upon stimulation with Epo $\beta$  after 10 min in BaF3-HA-hEpoR cells and in H838, H1299 and A549 cells. While H1299 and H838 cells showed strong EpoR expression, A549 cells express less and H1944 showed no detectable amounts of EpoR.

To accurately determine the number of Epo binding sites per cell surface as well as the binding constants of different ESAs to the human EpoR, ELISA measurements of ESAs in the cellular supernatant (Figure 2.5B) were performed by A. Rodriguez. The depletion kinetics of the respective ESA and the number of cells per volume was used as input for a previously published mathematical model of EpoR trafficking<sup>[44]</sup> (Figure 2.5C) to determine the ESA binding sites per cell, the association rate constant  $k_{\text{on}}$ , the dissociation rate constant  $k_{\text{off}}$  and the dissociation constant  $K_{\text{D}} = \frac{k_{\text{off}}}{k_{\text{on}}}$  of ligand binding to the receptor. Apart from Epo $\beta$ , also Epo $\alpha$ , CERA and NESP were investigated. These compounds differ mainly by their glycosylation pattern. While Epo $\beta$  and Epo $\alpha$  are similar to the endogenous Epo and exhibit high receptor affinity (low  $K_{\text{D}}$ ), CERA and NESP show low receptor affinity (high  $K_{\text{D}}$ ) and are covered with polyethylene glycol or hyper-glycosylated, respectively. Epo $\beta$  and CERA were further investigated as two distinct ESAs.

The relative abundance of total EpoR determined by immunoblotting is in line with the numbers of ESA binding sites obtained by the model using the ESA depletion kinetics. While the number of ESA binding sites determines rather the surface expression of EpoR, the EpoR band corresponds to the number of cytoplasmic EpoR molecules. Yet, the phosphorylation of EpoR is a good approximation of surface expression. The measurements support the developed method to calculate the number of ESA binding sites, since the immunoblot analysis showed the same trend as the values calculated by the model.

To investigate the ESA-induced activation of human erythroid progenitors, CD34<sup>+</sup> cells were isolated from cord blood and differentiated into hCFU-E cells by M. Wagner (DKFZ Heidelberg). The schedule applied for generation of hCFU-E cells is depicted in Figure 2.6A. The time after differentiation was optimized to yield the maximal amount of hCFU-E by M. Wagner by a time-dependent colony-forming assay (Figure 2.6B) indicating that after four days of differentiation the cells are mostly at the hCFU-E stage. For further experiments this timepoint was utilized. The

ESA depletion of hCFU-E and  $CD34^+$  cells as negative control was measured by A. Rodriguez (Figure 2.6C). As expected, hCFU-E cells showed depletion of  $Epo\beta$  in the cellular supernatant, while no significant number of ESA binding sites was determined by the model in  $CD34^+$  cells. The obtained number of ESA binding sites per hCFU-E cell of  $433 \pm 44$  is much higher compared to the NSCLC cell lines that harbor less than 100 ESA binding sites per cell. As described in section 2.1, CFU-E cells are much smaller compared to the NSCLC cell lines indicating a very sparse surface expression of  $EpoR$  on NSCLC cell lines.

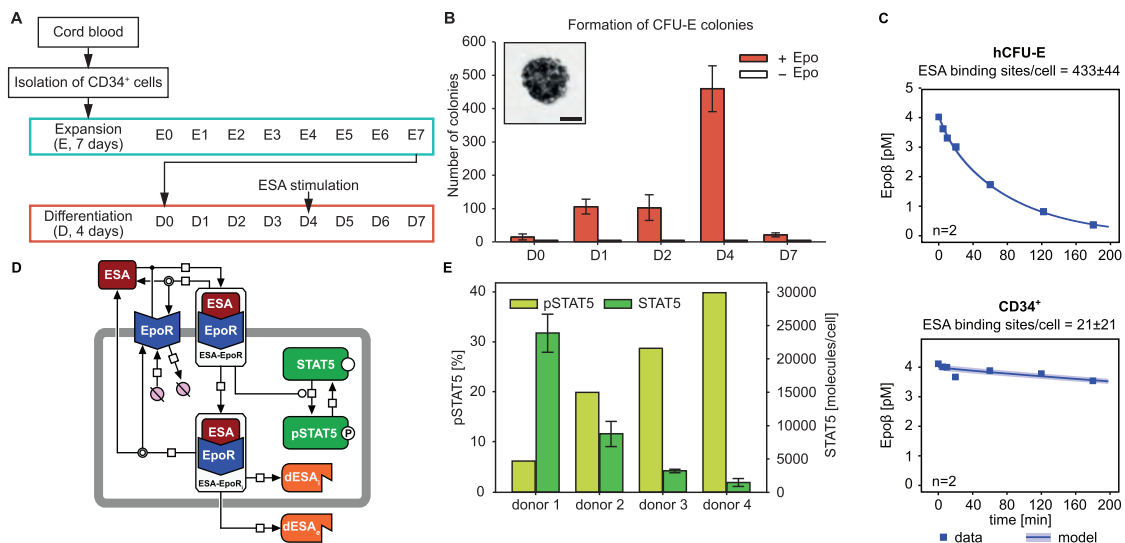


**Figure 2.6: Total amount of phosphorylated STAT5 is constant in different hCFU-E donors.**

**A:** Schedule of isolation of human  $CD34^+$  cells and differentiation into hCFU-E cells. The cells were isolated by Auto-MACS from cord blood of healthy donors. For differentiation, the cells were seeded in media containing  $mIL-3$  (10 ng/mL),  $mSCF$  (50 ng/mL) and  $Epo\alpha$  (6 U/mL).<sup>[196]</sup> **B:** Colony formation of 7500 differentiated cells after seven days of cultivation in medium containing MethoCult with and without 6 U/mL  $Epo$  performed by M. Wagner. Error bars represent SD of three biological replicates. A representative picture of a colony after staining with benzidine is depicted (scale bar 0.1 mm). **C:** Measurement of the  $Epo\beta$  concentration in the cellular supernatant over time in hCFU-E and  $CD34^+$  cells measured by A. Rodriguez. Data of a representary experiment is shown as dots, the splines represent the trajectories estimated by the mathematical model. The shading represents the model-estimated error of the data. **D:** Structure of the extended  $Epo$  model including  $STAT5$  activation based on Becker *et al.*<sup>[44]</sup> **E:** hCFU-E cells were stimulated with different doses  $Epo\beta$  and CERA, lysed and subjected to immunoprecipitation against  $STAT5A/B$ . Total and phosphorylated  $STAT5$  was measured by mass spectrometry using an one-source peptide standard. Depicted is the quantified degree of  $STAT5$  phosphorylation upon stimulation with a saturating CERA concentration (30 000 pM) as well as the number of  $STAT5$  molecules per cell calculated according to Equation 2.1. Error bars depict standard deviations based on five replicate measurements from the same donor.

To investigate ESA-induced activation of NSCLC and hCFU-E cells, mass spectrometric measurements of STAT5 phosphorylation were performed as part of this work, since the activation of STAT5 is correlated with ESA-induced cell survival and the accurate detection of EpoR phosphorylation by mass spectrometry or immunoblotting in hCFU-E cells remains challenging. For this purpose, the Epo $\beta$ -induced dynamics of STAT5 phosphorylation was measured by mass spectrometry in H838 and H838-HA-hEpoR cells. The data was used to calibrate an extended model of EpoR signaling developed by B. Steiert (University of Freiburg). The previously described mathematical model of receptor trafficking was extended to incorporate also STAT5 activation (Figure 2.6D).

The mathematical model suggested that the response of any cell type might be altered depending on the number of Epo receptors on the cell surface as well as on the binding affinities of the respective ESA. To validate this, an ESA dose inducing the same response in hCFU-E cells expressing high levels of EpoR was determined by mass spectrometric dose-response experiments. For the experiment, cord blood was obtained from four different donors and the isolated CD34<sup>+</sup> erythroid progenitors were differentiated into hCFU-E by M. Wagner. Subsequently, the degree of STAT5 phosphorylation was measured by mass spectrometry using a heavy isotope labeled one-source peptide/phosphopeptide standard of STAT5A upon stimulation with different doses of Epo $\beta$  and CERA. Interestingly, the maximal degree of STAT5 phosphorylation was found to be highly donor specific (Figure 2.6E). Yet, it was found that the total amount of STAT5 was inversely correlated with the degree of phosphorylation leading to a conserved total amount of phosphorylated STAT5 between the different hCFU-E donors.

To determine the total amount of phosphorylated STAT5A per hCFU-E cell ( $\frac{pSTAT5A}{cell_{CFU}}$ ), the mass spectrometric measurements of H838 cells were used as calibration, since the number of STAT5 molecules per cell in these cells was previously published ( $90\,000 \frac{STAT5}{cell_{838}}$ ).<sup>[188]</sup> Since the intensities of mass spectrometric measurements vary between the single measurements, the intensity per input  $\frac{Int}{n}$  also varies from experiment to experiment. Yet, within one experiment the intensity per input is the same for endogenous *STAT5A* and heavy labeled *STAT5A\** of the one-source standard that was spiked into every sample. By this, the signals obtained in hCFU-E cells were calibrated with signals from H838 cells according to Equation 2.1. The input of the endogenous STAT5A in H838 was calculated according to Equation 2.2. The input of the heavy *STAT5A\** was approximated by the volume of the added one-source standard for H838 and hCFU-E cells (Equation 2.3). Therein, the number of cells used for the experiment  $CELLS_{838}$  and the fraction of STAT5A per total STAT5 were used. The amount of input STAT5A ( $n(STAT5A)_{CFU}$ ) was calculated as average of all measured data points. The total amount of phosphorylated STAT5A per hCFU-E cell was then calculated by Equation 2.4 using the obtained  $n(STAT5A)_{CFU}$ , the number of cells employed

for the experiment  $CELLS_{CFU}$  as well as the phosphorylation degree of each data point. Since Figure 2.6E indicates that the total amount of  $pSTAT5A$  per cell is conserved for different donors, this measure was used for further analysis and to scale the  $pSTAT5$  measurements of the four donors.

$$\frac{n(STAT5A)_{838}}{Int(STAT5A)_{838}} : \frac{n(STAT5A^*)_{838}}{Int(STAT5A^*)_{838}} = \frac{n(STAT5A)_{CFU}}{Int(STAT5A)_{CFU}} : \frac{n(STAT5A^*)_{CFU}}{Int(STAT5A^*)_{CFU}} \quad (2.1)$$

$$n(STAT5A)_{838} = 90\,000 \frac{STAT5}{cell_{838}} \cdot CELLS_{838} \cdot \left( \frac{STAT5A^*}{STAT5} \right)_{838} \quad (2.2)$$

$$n(STAT5A^*) \propto Volume_{one-source\ standard} \quad (2.3)$$

$$\frac{pSTAT5A}{cell_{CFU}} = \frac{n(STAT5A)_{CFU}}{CELLS_{CFU}} \cdot \left( \frac{pSTAT5A}{STAT5A} \right)_{CFU} \quad (2.4)$$

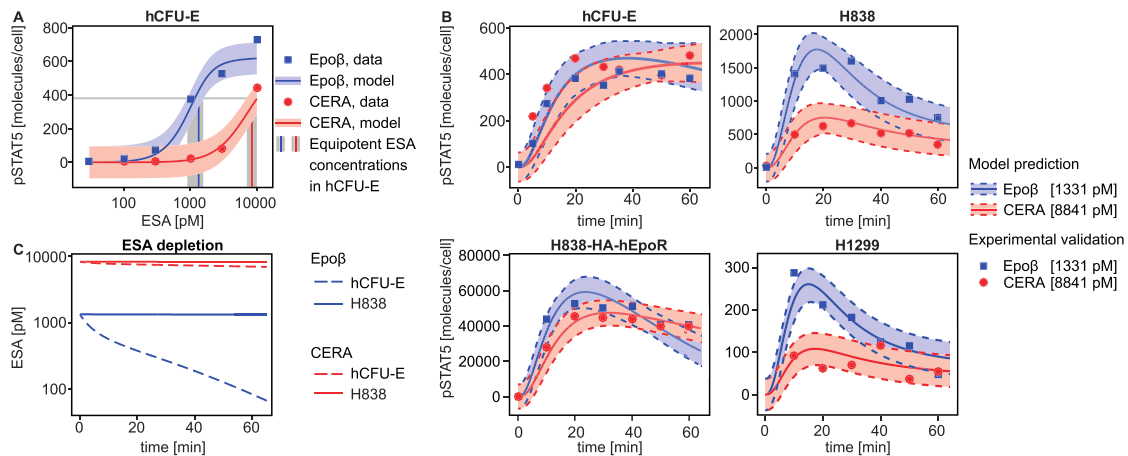


**Figure 2.7: Tumor cells show stronger activation with Epo compared to CERA applying the equipotent doses defined in CFU-E cells.** **A:** Determination of the equipotent dose of Epo $\beta$  and CERA in hCFU-E cells by mass spectrometric measurement of STAT5 phosphorylation after 30 min. The equipotent doses are indicated with a vertical line. **B:** Dynamics of STAT5 activation in cells with high expression of EpoR (hCFU-E and H838-HA-hEpoR) and in cells with low abundance of EpoR (H838 and H1299) upon stimulation with the equipotent ESA dose. Data points represent an exemplary experiment ( $n = 2$ ) and the delimited shading represents the model prediction. **C:** Model prediction of the ESA concentration in the supernatant over time starting from the equipotent ESA dose by B. Steiert.

Using this calibration, the doses leading to the same total amount of phosphorylated STAT5 after 30 min were determined as 1 331 pM Epo $\beta$  and 8 841 pM CERA and are indicated by vertical lines in Figure 2.7A. The doses were set to match roughly the half-maximal activation ( $EC_{50}$ ) on one hand to obtain a strong signal with good signal to noise ratio and on the other hand to avoid

saturation effects. These doses were applied to two tumor cell lines expressing low levels of EpoR as well as hCFU-E cells and H838-HA-hEpoR with high abundance of the EpoR. Figure 2.7B shows the time-dependent response of STAT5 phosphorylation to the identified equipotent doses of Epo $\beta$  and CERA for up to 60 min. While hCFU-E and H838-HA-hEpoR cells show comparable response to both treatments, Epo $\beta$  activates H838 and H1299 cells stronger compared to CERA. This is caused by the depletion of the respective ligands (Figure 2.7C). Since Epo $\beta$  has a high affinity for the receptor, the required molar concentration is low and it is quickly consumed by hCFU-E cells due to receptor internalization and lysosomal degradation. CERA on the other hand has low affinity for the receptor, the required molar concentration is high and CERA is degraded to a much smaller fraction. Therefore, more Epo is needed for equipotent activation of hCFU-Es. As there is no depletion in H838 and H1299 cells due to low number of Epo binding sites, treatment with the equipotent dose of Epo $\beta$  leads to over-activation of STAT5 signaling. This result suggests that CERA might be the safer option to treat patients and avoid strong activation of survival signaling in tumor cells by high local concentrations.

The established mathematical model was utilized to investigate the impact of different ESAs in a clinical context. For this purpose, the mathematical model was extended by B. Steiert and A. Rodriguez by pharmacokinetics and pharmacodynamics to describe the actual ESA dose *in vivo*. This model was calibrated using the measured Hb-levels and the ESA concentrations in patients co-treated with or without chemotherapy over time provided by Roche Diagnostics. Thereby, it was possible to determine the essential patient-specific parameters and the response to the ESA treatment. The identified parameters were the number of Epo binding sites per patient and the Hb-degradation rate. Using these parameters it was possible to calculate the optimal individual ESA dose at each point in time. The model suggested that according to the current guidelines for ESA dosing most patients receive either too high or too low doses. It was shown that knowledge of the Hb degradation rate using only the dynamics of Hb-levels after start of chemotherapy is sufficient to predict the required first ESA dose. Moreover, it was shown retrospectively in an independent cohort by A. Rodriguez that a fraction of patients treated according to the current guidelines has an increased risk of decease. The mathematical model could help to improve therapy outcome, decrease risk of overdosing the patient with ESAs and increase patient well-being due to normalized Hb-levels.

## 2.4 EGFR and MET receptor abundance influence EGFR-TKI efficacy

Mutations in growth factor receptors such as the epidermal growth factor receptor (EGFR) are implicated in the development of cancer and therefore tyrosine kinase inhibitors (TKIs) against EGFR are applied in cancer therapy. Resistance against this targeted therapy is frequently emerging by amplification of the hepatocyte growth factor (HGF) receptor MET. Yet, the mechanism of MET-mediated EGFR-TKI resistance remained unknown.

In this work the impact of MET receptor expression on the efficacy of TKIs against the EGFR was addressed by investigation of the interaction on the signal transduction level of both receptors. Reduced EGFR-TKI efficacy correlates with therapy resistance. Three NSCLC cell lines were selected as a model system to represent a distinct subset of lung tumor cells. The cell lines were selected according to their EGFR mutation status and MET expression levels. While the H838 cell line is EGFR and MET wild type, H1650 cells have a  $\Delta$ E746-A750 deletion in the EGFR and a *MET* gene amplification, whereas H1975 cells harbor a L858R activating mutation and a T790M resistance mutation in the EGFR and overexpress MET. To investigate the impact of altered protein abundance on signal transduction three additional NSCLC cell lines, H23, H1703 and H1299 cells, were selected harboring the wild type EGFR.<sup>[197,198]</sup>

### 2.4.1 Quantitative measurements of protein abundance of signaling components

Because the fluxes of a specific reaction depend not only on the rate constants, but also on the concentration of the reactants, an accurate knowledge of the numbers of molecules per cell is essential to investigate signal transduction induced by EGF and HGF in different cellular systems. For this purpose, the total numbers of EGFR and MET protein were measured by quantitative immunoblotting. Recombinant protein standards were synthesized in *E. coli* cells for EGFR and MET receptor. The recombinant standards comprise a SBP or GST-tag that is utilized for purification of the protein. The tags were fused to the cytoplasmic domain of the receptors that contain the epitope recognized by the antibodies applied for detection of the endogenous receptor. The generated vectors for the SBP-tagged fusion proteins are shown in the appendix (V01,V02). After purification, the concentration of the protein was determined by calibration to a BSA standard curve as shown exemplarily for the MET calibrator in Figure 2.8A. The obtained concentration of the recombinant standards was utilized to generate a calibration curve to correlate signal intensity of the endogenous receptor with the number of applied epitopes of the recombinant standard by linear regression (Figure 2.8B). Based on this calibration curve and the number of cells loaded to the gel, the number of molecules per cell was calculated. The obtained values of the number of

receptors per cell is depicted in Table 2.1. The error was determined by error propagation using the error of the cell counting, the error of the linear regression and the error of the biological replicates of the endogenous signal ( $n = 3$ ). The obtained error for the immunoblot analysis is relatively large reaching up to 50 %.

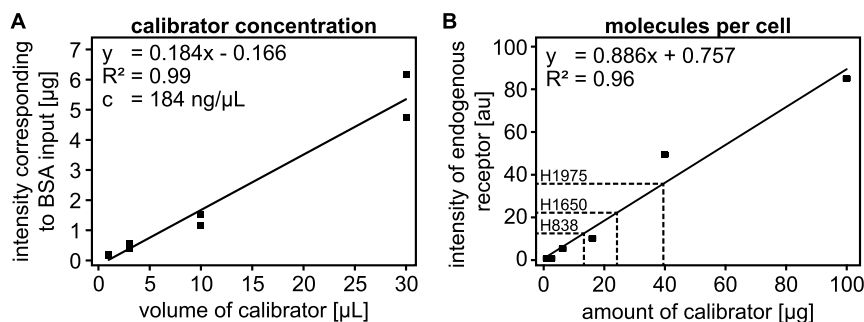


**Figure 2.8: Determination of the number of MET molecules per cell by a recombinant protein standard.** **A:** Different amounts of the recombinant MET calibrator were loaded on a SDS-PAGE together with a BSA calibration curve and the protein amount was measured by Coomassie staining. The signal intensity corresponding to the BSA input in  $\mu\text{g}$  was calculated by the intensity of the known amount of applied BSA. The slope of the shown graph represents the concentration of the calibrator ( $n = 2$ ). **B:** Different amounts of the recombinant protein were loaded on a SDS-PAGE together with lysates of H838, H1650 and H1975 cells. The recombinant standard was utilized to generate a calibration curve. The signal intensities of the endogenous MET receptor and the corresponding amount of calibrator is indicated by a dashed line. Error bars represent SD ( $n = 3$ ). The obtained numbers of receptors per cell are displayed in Table 2.1.

**Table 2.1: Number of receptor molecules per cell determined by quantitative immunoblotting.** Errors represent SD.

	H838	H1650	H1975
<b>MET</b>	108 000 $\pm$ 40 000	168 000 $\pm$ 43 000	566 000 $\pm$ 290 000
<b>EGFR</b>	586 000 $\pm$ 190 000	5 120 000 $\pm$ 1 800 000	4 100 000 $\pm$ 1 500 000

For a more accurate determination and to obtain the number of molecules per cell on a global proteome level, a mass spectrometric analysis was performed applying the proteome ruler method.<sup>[199]</sup> By this approach, the signal intensities of histone peptides are used to determine the number of proteins per cell. As cancer cells exhibit a highly abnormal karyotype, the ploidy of the cell lines had to be determined. To obtain absolute numbers of the ploidy, three lung cancer cell lines with a known most frequent number of chromosomes per cell, also termed as modal chromosome number, (H292: 47, H441: 52, H661: 142, obtained from ATCC)<sup>[200]</sup> were included for calibration in the measurements. These cells and the six examined lung cancer cell lines (H838, H1650, H1975, H23, H1703 and H1299) were stained with propidium iodide (PI) and the fluorescence intensity was measured by flow cytometry. The measured particles were gated to obtain single cells as exemplary

shown in Figure 2.9A for H1299 cells. As control for the PI staining, unstained cells were measured (right panel of Figure 2.9A), but showed no significant PI signal intensity.

The PI signal of the cell lines with known modal chromosome number is shown in Figure 2.9B. These cell lines were used for a linear regression using the mode of the PI-channel to calculate the ploidy of the remaining cell lines. The ploidy was approximated by the modal chromosome number divided by 23. The PI signal of two out of the six investigated cell lines is exemplary shown in Figure 2.9C. As one would expect from cancer cells, the cells show a substantial fraction of cells in S and G<sub>2</sub>/M-phase although the cells were growth factor depleted prior to experiment. Yet, the cells were growth factor depleted to obtain the ploidy in the same cellular state utilized also for mass spectrometric measurements. As expected, the PI-signal of the cells showed additional peaks indicating a highly abnormal karyotype of those cancer cells e.g. for H1975 cells (Figure 2.9C). Because of this aneuploidy, the mean DNA content was calculated using the average of the PI-signal, as the DNA content is supposed to correlate with the amount of histones. The obtained values for the ploidy of the investigated cell lines are shown in Figure 2.9D and were applied as input for the proteome ruler calibration.

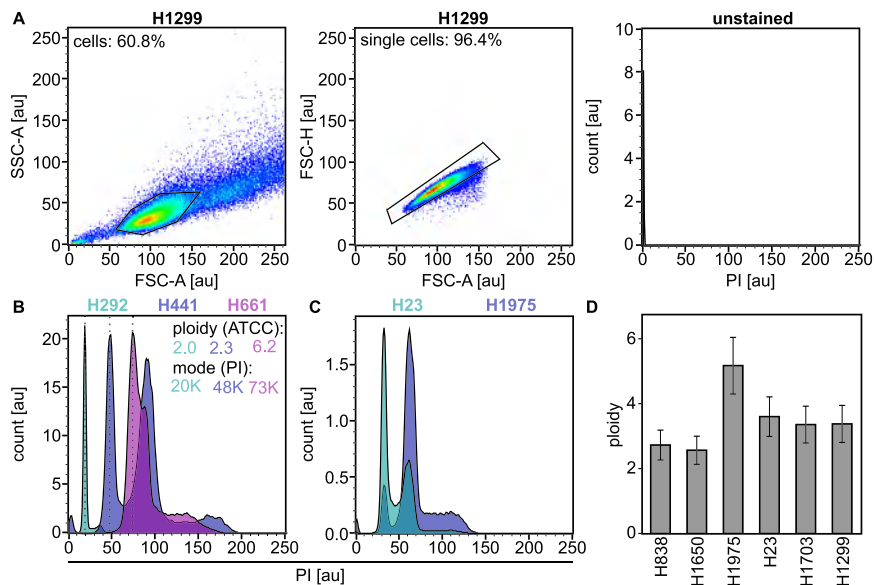


**Figure 2.9: Determination of the ploidy of a set of nine lung cancer cell lines.** **A:** Gating strategy to remove cell aggregates from the analysis representatively shown for H1299 cells. The right panel shows the PI-signal of an unstained control. FSC: forward scatter, SSC: side scatter, A: area, H: height. **B:** PI-signal distribution for H292, H441 and H661 cells that have a documented modal chromosome number.<sup>[200]</sup> The measured mode of the PI-signal is indicated in the figure by a dotted line and was used for calibration of the signal intensities. **C:** PI-signal distribution of H23 and H1975 cells. **D:** Determined ploidy levels of the six investigated NSCLC cell lines. Error bars represent the uncertainty of the linear regression.

The proteome of the six NSCLC cell lines was measured by an in-gel digestion procedure of four fractions per cell line using the total cell lysate. The lysates were digested with trypsin and the peptides were measured by an LC-MS orbitrap device. The normalization to the histone signals was performed in cooperation with M. Stepath (DKFZ Heidelberg) and A. Gorol (DKFZ Heidelberg) using the Perseus software. The obtained numbers of molecules per cell are depicted in Table 2.2.

**Table 2.2: Number of molecules per cell determined by mass spectrometry.** Selection of important signaling components. The number of molecules per cell was determined using the proteome ruler method ( $n = 1$ ).<sup>[199]</sup> n.d. = not detectable.

Cell line (ploidy)	H838 (2.72±0.46)	H1650 (2.57±0.43)	H1975 (5.17±0.87)	H661 (6.71±1.13)	H1703 (3.36±0.57)	H1299 (3.38±0.57)
<b>MET</b>	1 700	4 600	30 000	n.d.	600	2 000
<b>EGFR</b>	110 000	280 000	290 000	120 000	230 000	200 000
<b>AKT1</b>	13 000	14 000	37 000	47 000	13 000	48 000
<b>ERK1</b>	130 000	260 000	230 000	350 000	79 000	140 000
<b>ERK2</b>	660 000	680 000	1 600 000	2 000 000	460 000	1 300 000
<b>KRAS</b>	6 000 000	990 000	1 800 000	2 800 000	950 000	1 900 000
<b>TP53</b>	n.d.	n.d.	160 000	50 000	n.d.	n.d.

The numbers of molecules per cell show rather small fold change of up to three-fold of the cytoplasmic signaling components such as AKT1, while the receptors show a strong variation ranging from 1 700 MET molecules per cell for H838 to 30 000 for H1975 cells which is a more than 17-fold increase. Although the absolute values deviate strongly from the determination of the number of molecules per cell by immunoblotting, the relative expression values of the receptors are comparable between the two techniques e.g. the increased MET expression in H1650 compared to H838 cells is 1.6 determined by immunoblot analysis and 2.7 determined by mass spectrometry. This might be caused by the low peptide coverage, the fraction of detected peptides per protein, of the receptors by mass spectrometric measurement after the tryptic digestion. While the cytoplasmic proteins AKT1 and ERK1 had a high coverage from 50 % to 75 %, the MET receptor coverage was only 15 %. Interestingly, the EGFR coverage was reasonable good with 50 %.

Since the interactions with extracellular stimuli leading to cellular responses take place at the cell membrane, the protein expression was determined directly on the cell surface by a technique based on quantitative flow cytometry (qFACS) measurements. To obtain the number of molecules per cell surface a previously described algorithm was applied that correlates surface expression measured by quantitative flow cytometry with RNA expression levels.<sup>[201]</sup> The cell surface expression levels of MET and the human epidermal growth factor receptor (HER) family members were cal-

culated from receptor gene expression data, which were measured by RNAseq obtained from the Cancer Cell Line Encyclopedia (CCLE),<sup>[202]</sup> by H. Hass (University of Freiburg). To calculate the number of receptor molecules per surface area (Figure 2.10), the surface of the examined cells was determined by confocal microscopy by D. Dvornikov (DKFZ Heidelberg) in cells stably expressing GFP.<sup>[203]</sup> The obtained size of the cell surface of H838 and H1650 cells is depicted in Table 2.3. While the calculated levels of MET, HER2 and HER3 were comparable in both cell lines, H1650 cells harbored  $179 \pm 54$  EGFR/ $\mu\text{m}^2$ , whereas only  $39 \pm 16$  EGFR/ $\mu\text{m}^2$  were present on the cell surface of H838 cells. HER4 was not detectable in both cell lines.

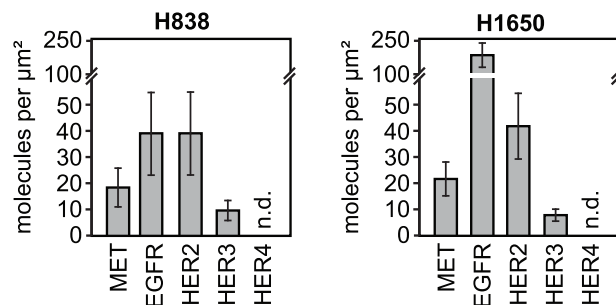


**Figure 2.10: Number of molecules per cell surface.** The numbers of EGF and MET receptors per  $\mu\text{m}^2$  is depicted for H838 and H1650 cells determined by RNAseq measurements obtained from the CCLE database<sup>[202]</sup> calculated by H. Hass.<sup>[201]</sup> n.d. = not detectable.

To compare the three techniques the number of molecules per cell surface was calculated for all measurements using the quantified cell surface area and assuming that all receptors are present on the cell surface. The obtained values are depicted in Table 2.3. The error of the immunoblot analysis is relatively large. The measurements obtained by mass spectrometry for EGFR are in a similar range compared to the qFACS-based algorithm, while MET values are one order of magnitude lower. This could be explained by the low peptide coverage of MET compared to EGFR and therefore an underestimation of the expression values. The interaction of the receptors at the cell surface was investigated within this work. Therefore, the measurements obtained by the qFACS-based algorithm were utilized for further investigation, because the analysis by mass spectrometry and immunoblotting is based on the total cytoplasmic fraction of the cell and because it is a very rough estimation that all receptors are located on the cell membrane.

#### 2.4.2 Quantitative analysis of EGF/HGF-induced signal transduction responses

To investigate whether stimulation with epidermal growth factor (EGF) has an impact on HGF signaling or vice versa, the dynamics of signal transduction after stimulation with 40 ng/mL EGF, with 40 ng/mL HGF or upon co-stimulation of both ligands was measured by quantitative im-

munoblotting in three NSCLC cell lines. In the left panel of Figure 2.11, an exemplary immunoblot of the two most distinctively responding cell lines H838 and H1650 is shown. As expected, the cells showed an induction of EGFR phosphorylation after addition of its ligand EGF, while addition of HGF had no impact on EGFR phosphorylation. Similarly, MET phosphorylation was induced by HGF, but not by EGF.

The quantification of  $n \geq 3$  independent replicates is shown in the right panel of Figure 2.11. As one would expect, since EGFR and MET are two distinct receptor tyrosine kinases (RTKs), co-stimulation of the cells with EGF and HGF had no impact on the phosphorylation strength and dynamics of the EGFR in both cell lines. While co-stimulation had also no effect on MET phosphorylation in H838 cells, H1650 cells showed an enhanced phosphorylation of MET receptor upon co-stimulation. For better visibility, the area under the curve (AUC) from 0 to 100 min was calculated and was plotted for each stimulus besides the time-course data. A t-test of the respective AUC of single- versus co-stimulation using Bonferroni correction showed a significant increase of MET phosphorylation in H1650 cells. Because H838 and H1650 cells showed the most distinct behavior compared to H1975 cells, the analysis was focused on them. In sum, two effects could be observed in the NSCLC cells: an enhanced MET phosphorylation upon co-stimulation and the cell line specificity of this effect.

To investigate whether the enhanced activation of MET upon EGF and HGF co-stimulation is also visible on the intracellular signaling components, the activation of the two main signaling cascades of both receptors, the mitogen activated protein kinase (MAPK) and phosphatidylinositol-4,5-bisphosphate 3-kinase (PI3K)/AKT pathway, were investigated by quantitative immunoblotting (Figure 2.12). To avoid systematic errors, the sample loading was randomized.<sup>[204]</sup>

The dynamics of AKT, MAPK/ERK kinase (MEK) and extracellular signal-regulated kinase (ERK) phosphorylation was measured after stimulation with 40 ng/mL EGF, 40 ng/mL HGF or co-stimulation for up to 100 min. Figure 2.13 shows the quantification of  $n \geq 3$  biological replicates. The phosphorylation of the downstream targets increased with a peak time of about 10 min and

**Table 2.3: Number of receptor molecules per cell surface.** EGFR and MET surface expression was calculated based on quantitative immunoblotting and mass spectrometry or determined by a qFACS-based algorithm. Errors represent SD.

[molecules/ $\mu\text{m}^2$ ]	<b>H838</b> ( $1300 \pm 500 \mu\text{m}^2$ )		<b>H1650</b> ( $2200 \pm 590 \mu\text{m}^2$ )	
	<b>MET</b>	<b>EGFR</b>	<b>MET</b>	<b>EGFR</b>
<b>Immunoblot</b>	$83.0 \pm 31$	$451 \pm 150$	$76.3 \pm 33$	$2330 \pm 1400$
<b>Mass spectrometry</b>	1.31	84.6	2.09	127
<b>qFACS</b>	$18.2 \pm 7.4$	$38.8 \pm 16$	$21.5 \pm 6.5$	$179 \pm 54$

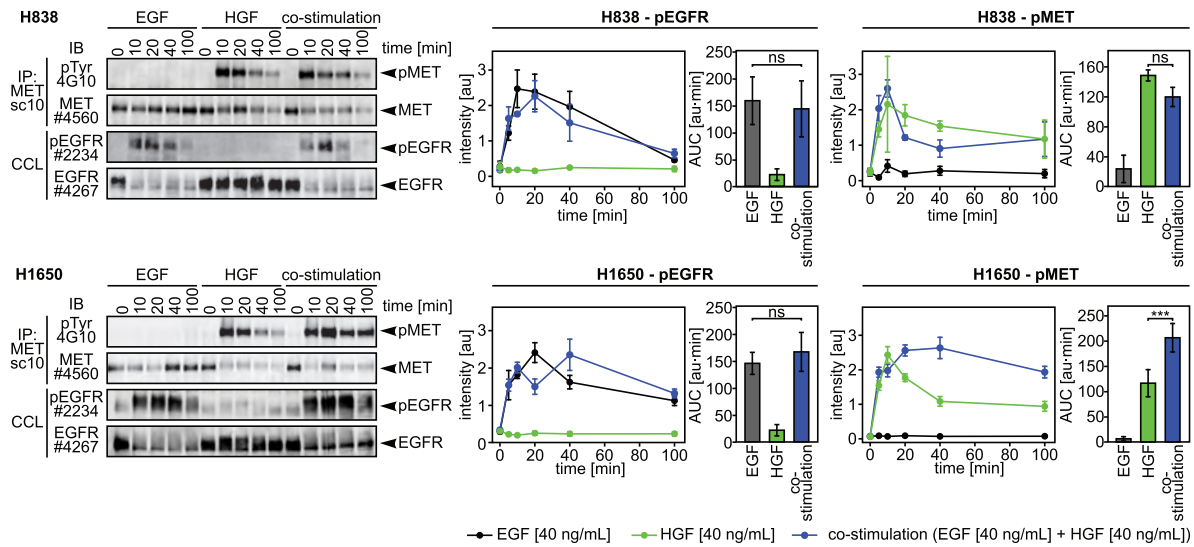


**Figure 2.11: Dynamics of EGFR and MET phosphorylation after ligand stimulation.** Exemplary immunoblots (IB) used for quantification of the signaling dynamics of H838 and H1650 cells after stimulation with EGF, HGF or co-stimulation. Cytoplasmic cell lysates (CCL) were used for detection of EGFR and MET was detected after immunoprecipitation (IP). The right panel shows time-resolved signal transduction data of phosphorylated EGFR and MET. Measured data with standard deviation from all replicates ( $n \geq 3$ ) using sample randomization is shown as dots with error bars. Quantification of the AUC for each stimulus corresponding to the data. Significance was tested using two-grouped t-test corrected for multiple testing (Bonferroni), ns = not significant, \*\*\* =  $p < 0.00025$ .

then slowly decreased over time. While the dynamics of MEK and ERK is similar in both cell lines, the phosphorylation of AKT is transient in H838 cells and more sustained in H1650 cells. This could be caused by a mutation in the phosphatase and tensin homolog (PTEN), a negative regulator of AKT signaling, in H1650 cells. It can further be observed that the enhanced phosphorylation upon co-stimulation shown in Figure 2.11 is not visible for the downstream targets in H1650 cells. This might be caused by an early saturation of the downstream components compared to the receptor level. H838 cells on the other hand showed an increased phosphorylation upon co-stimulation. Yet, using saturating concentrations of 40 ng/mL ligand it is difficult to state, whether the phosphorylation is additive or more than additive.

To investigate the enhanced activation of the signaling cascades upon co-stimulation with non-saturating concentrations, the response of H838 and H1650 cells to different doses of EGF, HGF or co-stimulation was tested 10 min after stimulation (subsection 2.4.5, Figure 2.21). Exemplary immunoblots are depicted in Figure 6.5 and Figure 6.6 in the appendix. This information was used to determine the  $EC_{50}$  concentrations of the ligands in both cell lines. In H838 cells 1 ng/mL EGF and 1.6 ng/mL HGF were found for the  $EC_{50}$  of MEK phosphorylation, while H1650 cells exhibited  $EC_{50}$  values of 2.8 ng/mL EGF and 7.5 ng/mL HGF. While a time-course analysis applying these

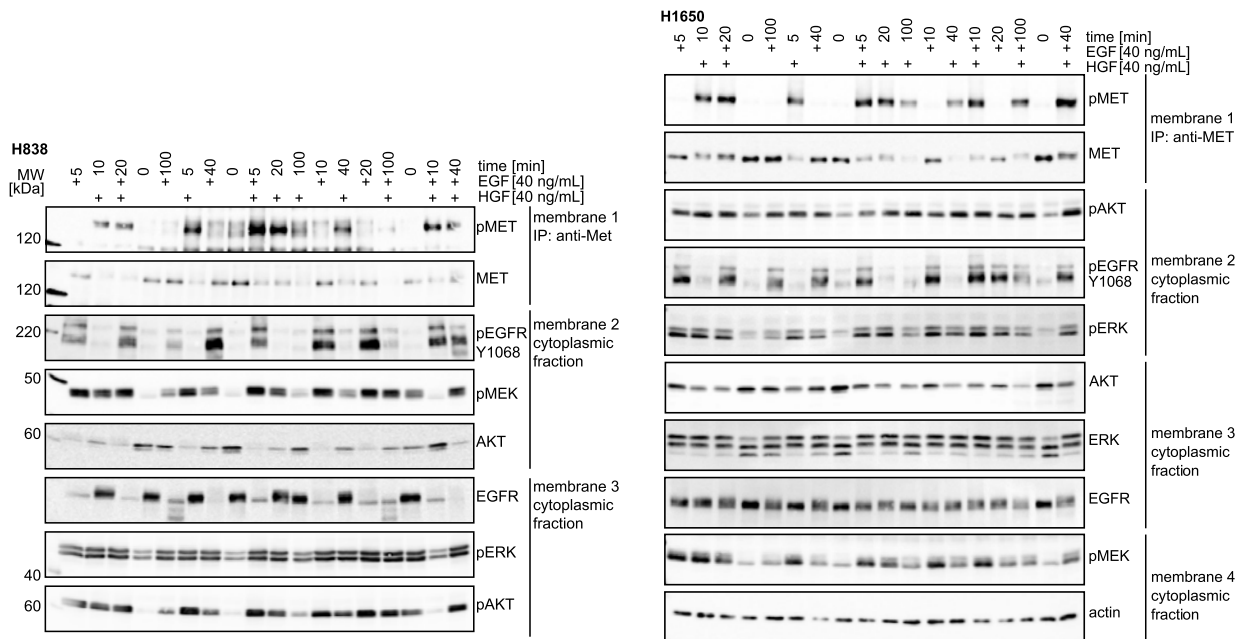


**Figure 2.12: Exemplary immunoblot of H838 and H1650 cells.** H838 and H1650 cells were stimulated with 40 ng/mL EGF or 40 ng/mL HGF or co-stimulated with both ligand for the indicated time points. Phosphorylated and total proteins were quantified by immunoblotting. Sample loading was randomized to avoid systematic blotting errors.<sup>[204]</sup> MET phosphorylation levels were detected after immunoprecipitation (IP). The remaining proteins were detected from cytoplasmic cell lysate. All utilized antibodies are listed in Table 4.4.

concentrations showed no significant enhanced activation upon EGF and HGF co-treatment, the obtained data was utilized to calibrate the mathematical model. Apart from that, also measurements at a shorter and longer time-scale were performed indicating that receptors were phosphorylated within 20 s after ligand addition, while downstream targets such as ERK or AKT were phosphorylated 40 s after EGF stimulation and 120 s after HGF stimulation. This data was required to determine the upper and lower boundaries of the kinetic parameters for ligand activation. The complete data set was utilized for calibration of the mathematical model described in subsection 2.4.3 and is depicted in the appendix in Figure 6.3 and Figure 6.4.

### 2.4.3 Development of a mathematical model of EGFR and MET signal transduction

To identify the mechanism leading to the enhanced MET phosphorylation upon co-stimulation as well as the cell line-specificity of this effect, a mathematical model was developed. A mechanistic ODE-based pathway model was constructed in collaboration with H. Hass (University of Freiburg). The data described in subsection 2.4.2 was utilized as input to calibrate the model.

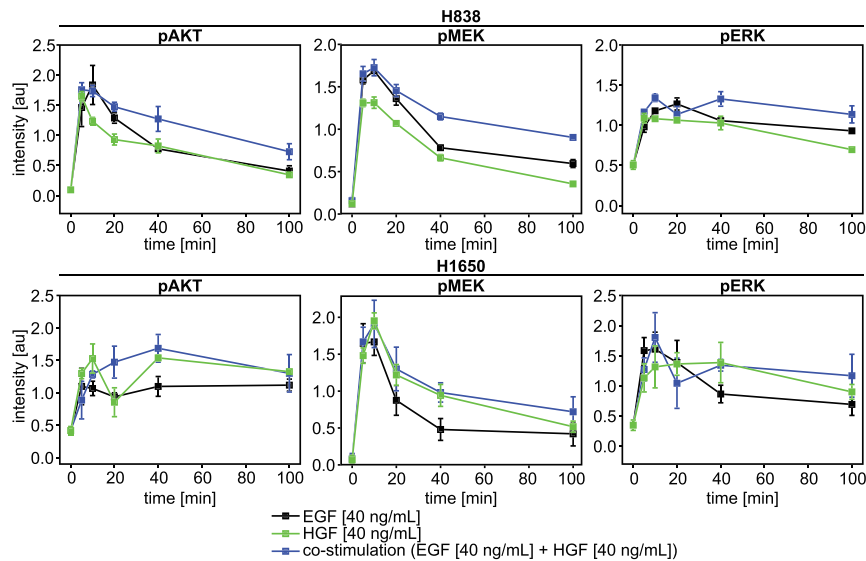


**Figure 2.13: Time-resolved signal transduction data of downstream components for H838 and H1650 cells.** Both cell lines were stimulated with 40 ng/mL EGF, HGF or co-stimulation. The dynamic phosphorylation of AKT, MEK and ERK was monitored by quantitative immunoblotting. Displayed is the average  $\pm$  standard deviation ( $n \geq 3$ ).

A core model was developed comprising EGFR and MET ligand binding, dimerization, internalization with subsequent degradation or recycling as well as downstream activation of the PI3K/AKT- and the MAPK-pathway.<sup>[58,66,205]</sup> Figure 2.14A depicts the model structure according to the Systems Biology Graphical Notation.<sup>[192]</sup> Both cell lines were described simultaneously utilizing the experimentally measured receptor surface levels (Figure 2.10) as constraints for the initial values. All remaining parameters were assumed to be cell type-independent, apart from a single rate constant of AKT deactivation that was assumed to be cell type-specific due to an activating point mutation in PTEN in H1650 cells. The resulting model trajectories after parameter estimation are depicted in Figure 2.14B as lines. However, the core model itself was not able to capture the enhanced MET phosphorylation in H1650 cells indicating a missing interaction.

Different hypotheses were included into the core model that have the potential to explain the observed cell type-specific enhanced MET phosphorylation. First, a negative feedback from downstream constituents such as phosphorylated ERK as suggested for EGFR by Klinger *et al.*<sup>[71]</sup> was tested. However, this hypothesis was not able to describe the enhanced MET phosphorylation in H1650 cells (Figure 2.14C). To further validate this model-based result, the enhanced MET phosphorylation upon co-stimulation in H1650 cells was measured in combination with inhibitors against downstream components as well as an inhibitor of transcription. Pretreatment of H1650 cells for 30 min with 1  $\mu$ M of the AKT inhibitor AKT VIII and 1  $\mu$ M of the MEK inhibitor U0126 to block all downstream activation (Figure 2.15A) resulted in decreased levels of MET phosphorylation.

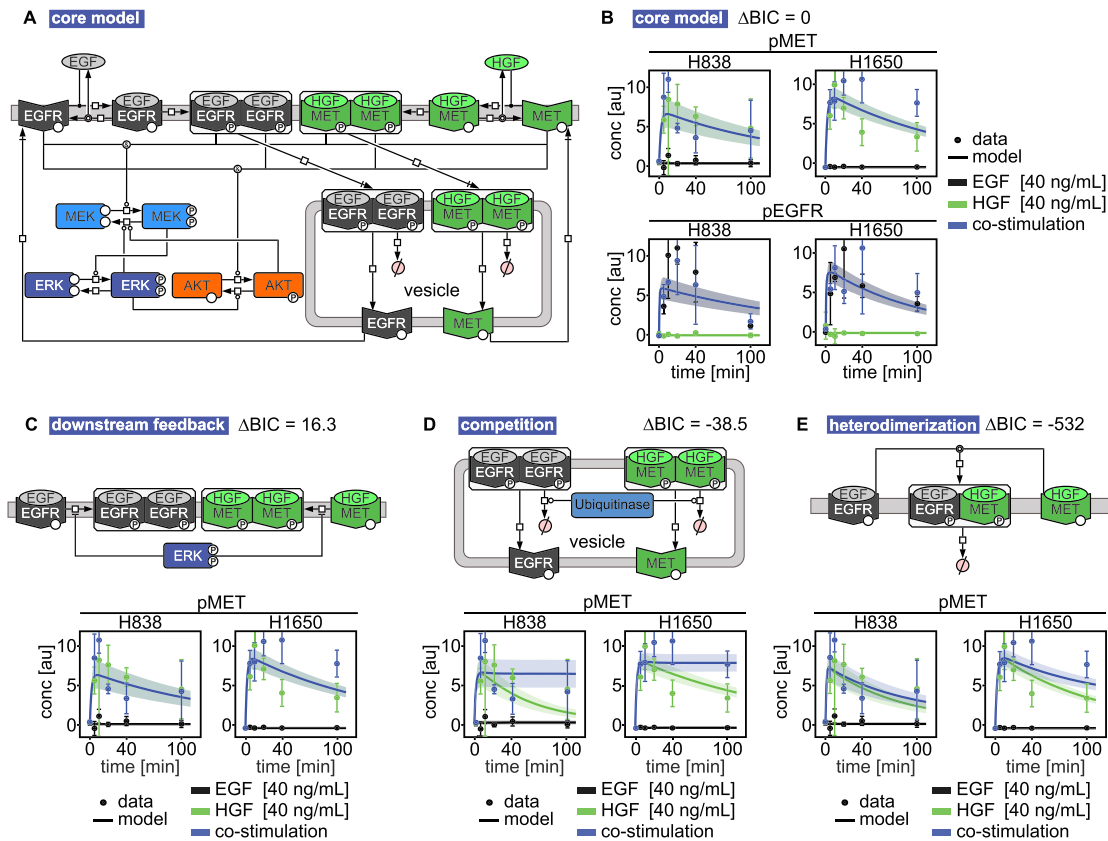


**Figure 2.14: Hypothesis testing based on receptor response in H838 and H1650 cell lines.** **A:** Structure of the ODE-based core model according to the Systems Biology Graphical Notation,<sup>[192]</sup> including EGFR and MET receptors with the PI3K/AKT- and MAPK-pathway. The model was developed by H. Hass. **B:** Dynamics of the receptor phosphorylation for H838 and H1650 cells. Experimental data is shown as dots, the trajectories of the core model corresponding to the best parameter estimation are depicted as lines. The shading corresponds to the estimated error of the model. The error bars on the data represent the model-scaled measurement uncertainty of the biological replicates. **C-E:** Different hypotheses to describe the enhanced MET phosphorylation upon co-stimulation. Experimental data of MET phosphorylation is shown as dots, trajectories of the respective model extension are shown as lines. The shading corresponds to the estimated error of the model. The error bars on the data represent the model-scaled measurement uncertainty of the biological replicates. For all model hypotheses, differences in Bayesian information criterion ( $\Delta\text{BIC}$ ) with respect to model (E) are shown. **C:** Extension of the core model by a negative feedback loop from phosphorylated ERK to both receptors. **D:** Addition of a negative regulator, in this case a limited ubiquitinase that restricts receptor degradation for EGFR and MET at the same time. **E:** Expansion of the core model by a direct EGFR:MET heterodimerization led to a good description of the enhanced MET phosphorylation upon co-stimulation and the lowest  $\Delta\text{BIC}$  value of all tested hypothesis.

However, the strength of enhancement determined as fold increase of the AUC upon co-stimulation compared to HGF treatment alone showed no change after inhibitor treatment (Figure 2.15C). The inhibition of transcription by 20  $\mu\text{g}/\text{mL}$  cycloheximide 30 min prior to stimulation showed increased levels of MET phosphorylation compared to DMSO control (Figure 2.15B). Yet, the strength of

enhanced MET phosphorylation was still comparable to control cells (Figure 2.15C). This led to the conclusion that enhanced activation of MET phosphorylation is not caused by feedbacks.

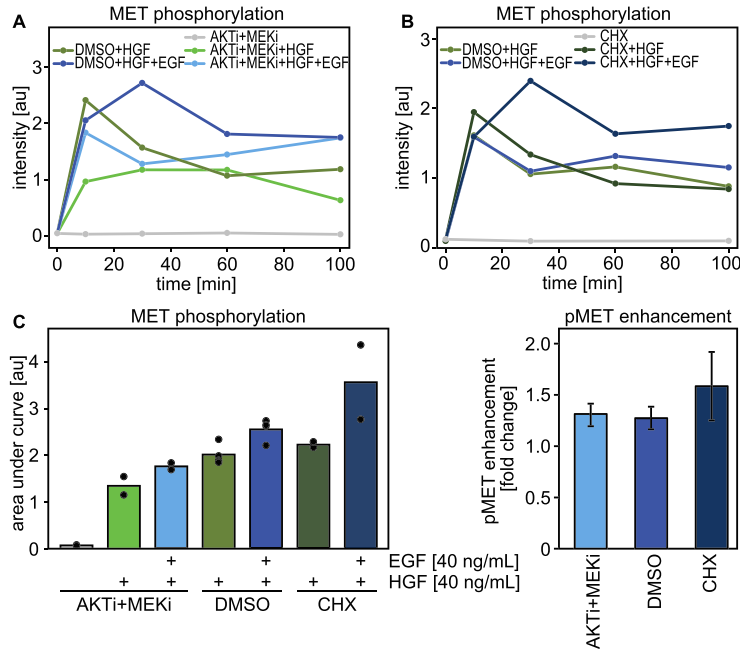


**Figure 2.15: Verification of the independence of the enhanced MET phosphorylation upon co-stimulation on downstream activation.** **A:** MET phosphorylation dynamics after 30 min pretreatment with 1  $\mu$ M AKT inhibitor (AKTi) and 1  $\mu$ M MEK inhibitor (MEKi) or with DMSO control measured by immunoblotting after stimulation with 40 ng/mL HGF or co-stimulation with 40 ng/mL HGF and 40 ng/mL EGF. **B:** MET phosphorylation dynamics after 30 min pretreatment with 20  $\mu$ g/mL cycloheximide (CHX) or DMSO control measured by immunoblotting after stimulation with 40 ng/mL HGF or co-stimulation with 40 ng/mL HGF and 40 ng/mL EGF. **C:** The left panel shows the area under the curve (AUC) of two independent replicates of the data shown in (A) and (B). The right panel indicates the strength of the enhanced MET phosphorylation calculated as  $\frac{AUC_{EGF+HGF}}{AUC_{HGF}}$  that is neither inhibited by inhibition of downstream signaling nor by inhibition of transcription.

As a second hypothesis, the effect of a common degradation mechanism that could be rate limiting leading to reduced MET receptor degradation was analyzed (Figure 2.14D). This could be mediated by a common ubiquitinase for EGFR and MET such as CBL that is reported to target both receptors and that is suspected to be already limiting for high doses of EGF leading to a clathrin-independent degradation for high ligand concentrations.<sup>[77,82]</sup> Yet, this hypothesis failed to explain the cell type-specificity.

Finally, a direct interaction of EGFR and MET through heterodimerization was assumed, which was previously suggested for some cell types by *in vitro* co-IP experiments.<sup>[93,94,155]</sup> This model extension led to a good description of the cell type-specific enhanced MET phosphorylation (Figure 2.14E). The model suggested that the enhanced phosphorylation of MET receptor is caused by a reduced internalization rate of the EGFR:MET heterodimers.

Additional model hypotheses were tested such as the incorporation of a common phosphatase or the incorporation of a further HER family member into the receptor dimerization and trafficking (Figure 6.1, appendix). The model extension by a phosphatase could not explain enhancement of MET phosphorylation. The incorporation of an additional HER family member could capture the dynamics of receptor phosphorylation, but resulted in a large model structure with a high degree of freedom. A comparison by the Bayesian information criterion<sup>[206]</sup> for all models strictly favored the model containing only EGFR and MET heterodimerization.

In sum, a mathematical pathway model was developed and used to identify EGFR and MET heterodimer formation as mechanism describing the cell line-specificity of the enhanced MET phosphorylation.

#### 2.4.4 Validation of EGFR:MET heterodimerization by live-cell imaging

To validate the selected model hypothesis of EGFR and MET heterodimerization and to directly observe the MET:EGFR heterodimers *in vivo*, a live-cell imaging analysis of single receptor molecules was performed. For the live-cell imaging, cells were labeled by fluorescent tagging of the receptors and retroviral expression of these fusion proteins. As a good time-resolution and laser intensity is needed to perform single-molecule tracking, fluorescent organic dyes were used rather than less photostable fluorescent proteins or relatively large nanoparticles. Therefore, the commercially available SNAPf-tag and the HALO-tag were fused to the C-terminus of MET and EGFR cDNA respectively and co-transduced in H838 cells. A schematic representation of the resulting reporter cell line is shown in Figure 2.16A.

##### Establishment of fluorescent reporter cell lines for live-cell imaging

For the generation of the MET-HALO fusion protein, the human MET cDNA was cloned into the retroviral pMOWS-puro vector backbone. The cDNA of the HALO-tag was introduced into the plasmid to yield the pMOWS-MET-HALO (V09, appendix) construct. The H838 cell line stably expressing this plasmid showed  $10.4 \pm 3.1$ -fold overexpression of the MET receptor compared to wild type H838 cells as determined by quantitative immunoblotting. However, as detected by immunoblot analysis this cell line showed constitutive phosphorylation of the endogenous as well as the overexpressed MET receptor in absence of HGF.

Because it has been described in the literature that high expression of the MET receptor can lead to its ligand-independent activation,<sup>[143]</sup> the vector backbone was changed to the retroviral pBABE vector that yields lower expression levels but a similar transduction efficiency.<sup>[203]</sup> This was also

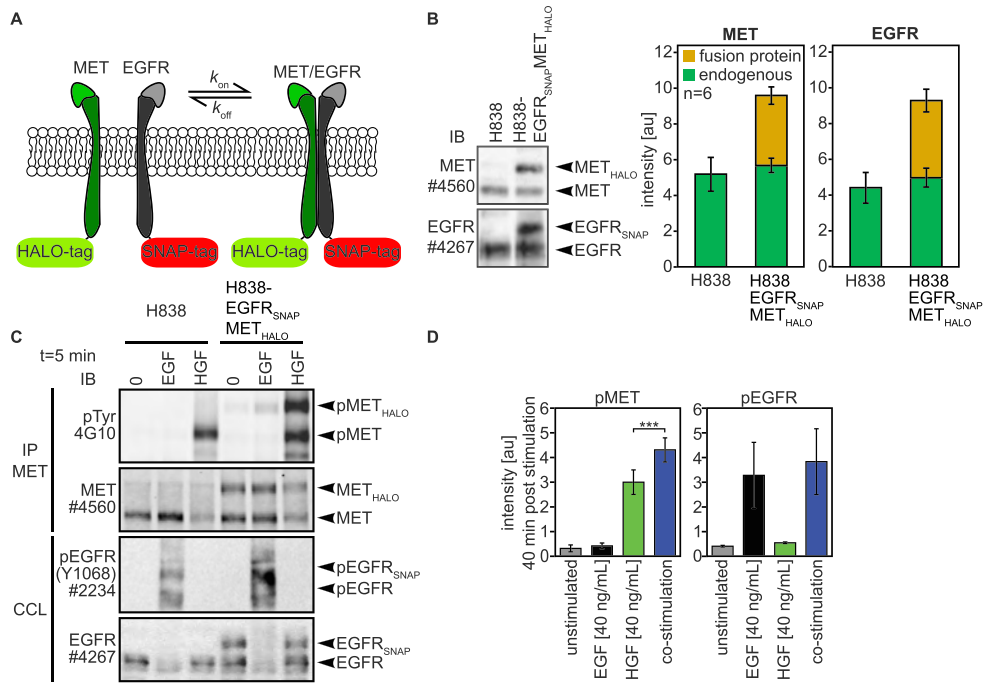


**Figure 2.16: Establishment of a fluorescent reporter cell line.** **A:** Schematic structure of the tagged receptors for quantification of EGFR:MET heterodimerization. The association ( $k_{on}$ ) and dissociation ( $k_{off}$ ) rate constants are indicated. **B:** Left panel: Analysis of the retrovirally transduced pBABE-EGFR-SNAP (EGFR<sub>SNAP</sub>) and pBABE-MET-HALO (MET<sub>HALO</sub>) construct in H838 cells. The proteins were detected by immunoblotting of cytoplasmic cell lysates (CCL) using anti-MET and anti-EGFR antibodies. Right panel: Quantification of the amount of overexpression of EGFR<sub>SNAP</sub> and MET<sub>HALO</sub> compared to endogenous receptor and wild type cells ( $n = 6$ ), error bars represent the standard deviation (SD). **C:** Immunoblot analysis of the functionality of the EGFR<sub>SNAP</sub> and MET<sub>HALO</sub> fusion proteins. H838 and H838-EGFR<sub>SNAP</sub>MET<sub>HALO</sub> cells were stimulated with 40 ng/mL EGF or HGF for 5 min or left untreated. **D:** Quantification of phosphorylated MET and EGFR in H838-EGFR<sub>SNAP</sub>MET<sub>HALO</sub> cells after stimulation with 40 ng/mL EGF-, HGF- or co-stimulation for 40 min. Significantly enhanced MET phosphorylation is visible in H838-EGFR<sub>SNAP</sub>MET<sub>HALO</sub> cells, while EGFR shows no co-stimulation effect. Error bars represent three biological replicates and significance was tested by t-test, \*\*\* =  $p < 0.001$ .

preferable for single-molecule analysis, as first test experiments had shown that the expression of the pMOVS vector is too high to track single molecules. Therefore, the engineered MET-HALO fusion protein was subcloned into the pBABE vector backbone resulting in the pBABE-MET-HALO construct (V13, appendix). Cells expressing this plasmid showed a low degree of MET overexpression (Figure 2.16B) and no substantial basal activation of the MET receptor, while the induction of phosphorylation by HGF as well as the degradation of the receptor after stimulation remained functional (Figure 2.16C). Thus, this construct provided a good system to study MET receptor dynamics *in vivo*.

For generation of the EGFR-SNAP fusion protein, the EGFR cDNA was extracted from H1975 cells using reverse transcription and PCR amplification. This approach resulted in cDNA encoding for the wild type (wt) receptor as well as the mutant EGFR containing T790M and L858R mutation. Both cDNAs were subcloned in the retroviral pMOWS vector backbone leading to pMOWS-EGFR(wt)-neo (V04, appendix) and pMOWS-EGFR(act)-puro (V05, appendix). Subsequently, the EGFR(wt) cDNA was fused C-terminally to the SNAPf-tag and subcloned in the retroviral pBABE vector backbone resulting in the pBABE-EGFR-SNAPf-neo vector (V14, appendix). H838 cells stably expressing this construct showed a low degree of EGFR overexpression as determined by immunoblot analysis (Figure 2.16B). The cells exhibited also no basal activation without ligand, induction of phosphorylation by EGF and degradation of the protein after stimulation (Figure 2.16C).

Stable co-expression of both described fusion proteins in H838 cells resulted in the H838-EGFR<sub>SNAP</sub>-MET<sub>HALO</sub> cell line. To test, whether these cells show enhanced MET phosphorylation upon co-stimulation, they were stimulated with 40 ng/mL EGF, HGF or co-stimulation for 40 min. The analysis of phosphorylated MET and EGFR by immunoblotting showed a significantly enhanced MET phosphorylation upon co-stimulation and no co-stimulation effect on the EGFR phosphorylation (Figure 2.16D). Although H838 did not exhibit enhanced MET activation upon co-stimulation before, the H838-EGFR<sub>SNAP</sub>MET<sub>HALO</sub> cell line showed enhanced MET phosphorylation on the population level. Because on purpose no single cell clones were picked, the expression of the tagged EGFR and MET varies between single cells giving rise to cells with distinct expression of EGFR and MET on the single cell level that was also observable by life-cell imaging. Therefore, the engineered cell line is a useful model cell line to investigate the EGFR:MET heterodimer-mediated enhanced MET activation.

To generate a positive and negative control for fluorescent labeling and the tracking algorithm, a reporter was designed in collaboration with S. Hänselmann (University of Heidelberg) combining a membrane anchor, GFP, the HALO-tag and, separated by a helical linker, the SNAPf-tag and a HIS-tag. The membrane anchor contains the N-terminus of the Lyn kinase that harbors the signal for myristoylation and palmitoylation<sup>[207]</sup> granting membrane localization of the fluorescent reporter. The helical linker consisted of 25 repeating amino acids forming a stiff  $\alpha$ -helical structure of 3.6 nm length that was designed according to Arai *et al.*<sup>[208]</sup> A schematic representation of the reporter is depicted in Figure 2.17A indicating the application as positive and negative control for dimer formation. Two-color labeling of the SNAPf-tag and the HALO-tag resulted in a permanently co-localized state that was applied as positive control for dimer formation. Simultaneous labeling of the HALO-tag with two distinct dyes results in not co-localized particles that were ap-

plied as negative, non-dimer control. The Lyn-GFP-HALO-SNAP (GHS) reporter was retrovirally transduced in H838 cells resulting in H838-GHS cells. The expression of the reporter was verified by immunoblotting using an anti-GFP antibody (Figure 2.17B). H838 cells transduced with GFP were utilized as control for the staining. Because a band corresponding to the GHS construct could be detected at 80 kDa, the complete reporter is present within the cell and is not cleaved.

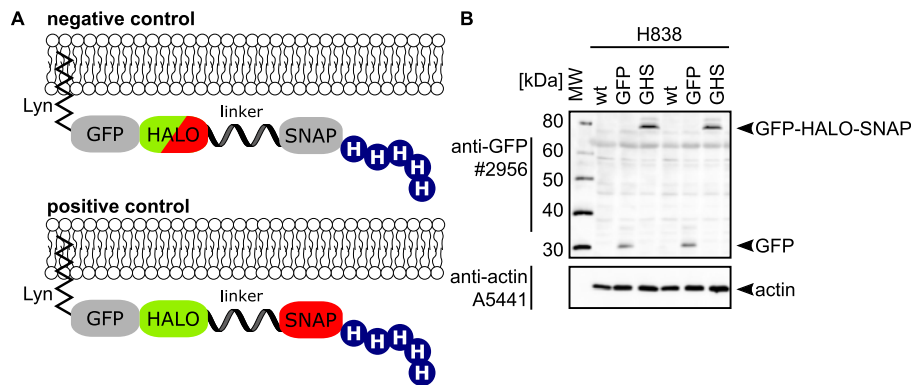


**Figure 2.17: Establishment of a negative and positive control cell line.** **A:** Scheme of the fluorescent reporter protein Lyn-GFP-HALO-SNAP (GHS) used for negative and positive controls consisting of LynMyrPalm membrane anchor<sup>[209]</sup>, EGFP, the HALO-tag, a helical linker<sup>[208]</sup>, the SNAP-tag and a HIS-tag. For negative control the HALO-tag was simultaneously labeled with 10 nM HALO-TMR ligand and 10 nM SiR-HALO-tag ligand (a gift from K. Johnson). **B:** Analysis of the retrovirally transduced GHS construct in H838 cells resulting in H838-GHS cells. H838 cells expressing GFP were utilized as control. The proteins were detected by immunoblotting of cytoplasmic cell lysate (CCL) using an anti-GFP antibody.

### Live-cell imaging reveals heterodimer formation of EGFR and MET

To observe the receptor dynamics *in vivo*, the H838-GHS and H838-EGFR<sub>SNAP</sub>MET<sub>HALO</sub> cells were examined by total internal reflection fluorescence (TIRF) microscopy. The signals of the single receptors were tracked and used for a hidden Markov model to determine dimerization events. All microscopic measurements were performed by S. Hänselmann (University of Heidelberg). The registration, particle tracking and classification was performed by Y. Qiang (University of Heidelberg). To directly test EGFR:MET heterodimerization, living H838-EGFR<sub>SNAP</sub>MET<sub>HALO</sub> cells were specifically labeled with 10 nM HALO-tag ligand fused to the tetramethylrhodamine dye (HALO-TMR) and 10 nM of the SNAP-tag ligand benzyl guanine fused to the silicon rhodamine dye (SiR-BG) overnight. Subsequently, the dyes were washed away and the cells were growth factor depleted for at least 1 h. The cells were either stimulated with 40 ng/mL EGF, HGF or co-stimulation or left untreated. The fluorescence on the basal plasma membrane was measured by two-color TIRF microscopy at 50 frames/sec for at least 500 frames. An exemplary picture

of the transmitted light, the SiR-BG and the HALO-TMR channel is depicted in Figure 2.18A. Emission light from TMR and SiR was spectrally separated and each channel was projected to half of the camera chip, resulting in 104 nm pixel size. The obtained movies were utilized for image analysis. The images of the two channels needed to be registered by acquisition of images of fluorescent beads before each measurement day and by calculation of a non-rigid registration matrix. Image registration and probabilistic particle tracking<sup>[210]</sup> was performed by Y. Qiang as well as the assignment of dimerization events by a two-state hidden Markov model using the Euclidean distance between the receptors.<sup>[211]</sup> An exemplary trajectory of an EGFR<sub>SNAP</sub> and a MET<sub>HALO</sub> receptor. The dimer state identified by the hidden Markov model is indicated in blue. An exemplary particle distance and the corresponding classification is depicted in Figure 2.18C indicating heterodimer formation and dissociation and thereby proving the presence of EGFR:MET heterodimers *in vivo*. The dimer duration  $\tau$ , the time a dimer pair stays together, is indicated in the figure.

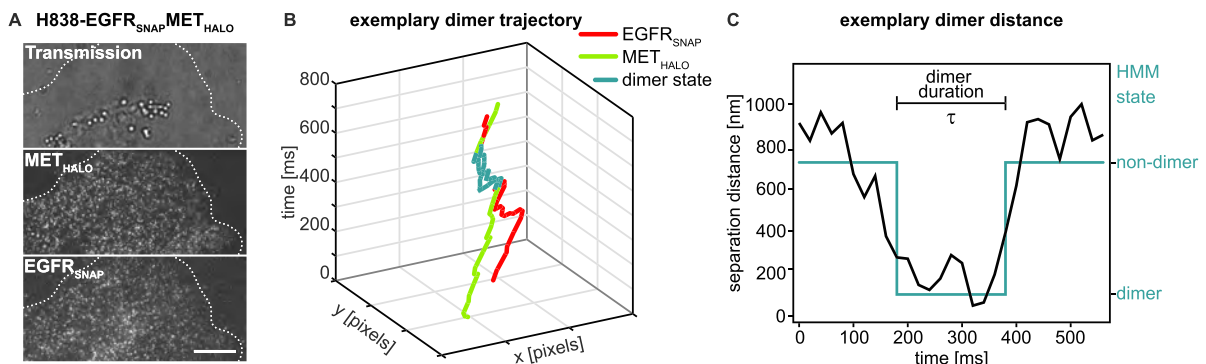


**Figure 2.18: Live-cell imaging and tracking analysis reveals EGFR:MET heterodimerization.** **A:** Exemplary TIRF image of H838-EGFR<sub>SNAP</sub>MET<sub>HALO</sub> cells labeled with 10 nM HALO-TMR and 10 nM SiR-BG overnight. Shown is the transmission image, the EGFR<sub>SNAP</sub> and the MET<sub>HALO</sub> channel measured after laser excitation with 561 nm and 640 nm, respectively. The cell outline is indicated by a dotted line and the scale bar corresponds to 10  $\mu$ m. The images were taken by S. Hänselmann. **B:** Exemplary trajectory of an EGFR<sub>SNAP</sub> and a MET<sub>HALO</sub> particle after image registration and particle tracking performed by Y. Qiang measured with 50 frames/sec by S. Hänselmann. The x- and y-axes represent the spatial localization and the z-axis the particle movement in time. The dimer state is indicated in blue. **C:** Euclidean distance between two monomers over time and determination of dimer and non-dimer state using a hidden Markov model analyzed by Y. Qiang.

**Determination of the dissociation rate constant of EGFR:MET heterodimers by image analysis**

To quantify the ligand dependency of EGFR:MET heterodimerization, the stability of EGFR:MET heterodimers  $\tau$  upon stimulation with EGF, HGF or co-stimulation or in an unstimulated setting was determined as part of this work. A measure for stability is the dissociation rate constant  $k_{\text{off}}$  of the heterodimers which can be calculated according to Equation 2.5 or hence Equation 2.6.<sup>[212]</sup>

$$p(\tau) = A \cdot e^{-k_{\text{off}} \cdot \tau} \quad (2.5)$$

$$\langle \tau \rangle = \int \tau \cdot p(\tau) d\tau = \frac{1}{k_{\text{off}}} \quad (2.6)$$

The probability distribution of  $\tau$  was determined by a normalized histogram of all measured heterodimer durations using a binning of three frames (Figure 2.19A). The distribution was used for two-parameter exponential regression to obtain the apparent dissociation rate constant  $k_{\text{off}}$  for all conditions. The obtained values are depicted in (Figure 2.19B) indicating also the dynamic range of the analysis by the positive and negative controls. Strikingly, the apparent  $k_{\text{off}}$  is decreased upon co-stimulation with EGF and HGF compared to unstimulated from  $17.4 \pm 0.1 \text{ s}^{-1}$  to  $14.1 \pm 0.1 \text{ s}^{-1}$  indicating that heterodimers are formed upon co-stimulation. Because the  $k_{\text{off}}$  is already decreased for EGF stimulated cells, the results indicate that the presence of EGF is sufficient to promote heterodimerization. This effect might be caused by the structure of the two receptors described in section 1.3 and section 1.4. While EGFR exhibits a closed conformation in the absence of ligand preventing dimerization, MET has no such limitation. It is important to mention that homodimer formation cannot be resolved with this approach. In addition, bleaching of the dyes, loss of particle tracks due to a high particle density may affect the quantitative result, therefore the results may be considered as a qualitative increase in heterodimer stability upon EGF stimulation.

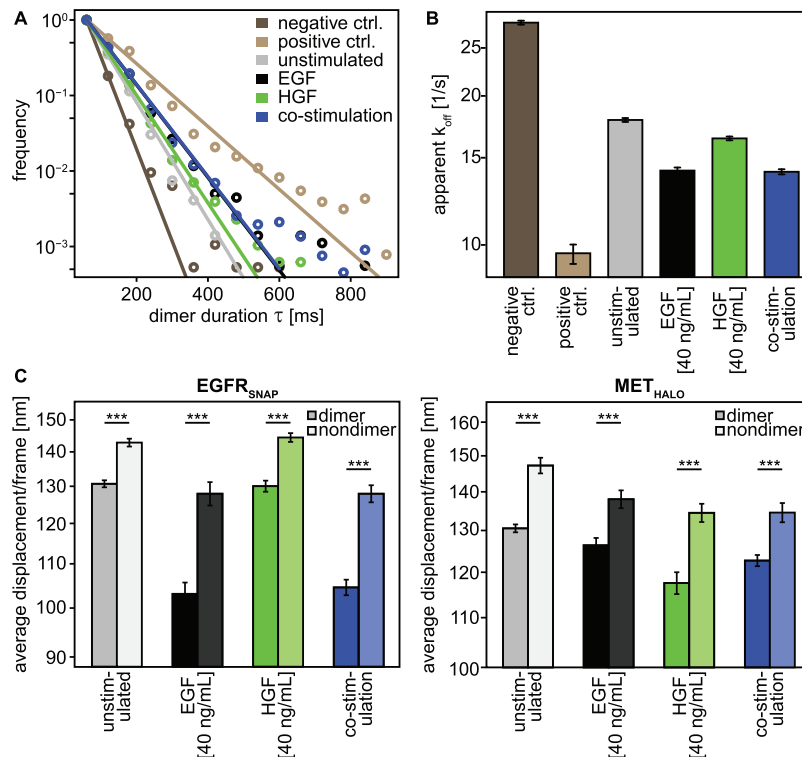


**Figure 2.19: Analysis of the live-cell imaging reveals EGF-dependent EGFR:MET heterodimerization.** **A:** Tracking analysis of H838-EGFR<sub>SNAPE</sub>MET<sub>HALO</sub> cells stimulated with 40 ng/mL EGF, HGF, co-stimulation or left unstimulated and of H838-GHS cells as positive and negative control. The duration of the detected dimerization events  $\tau$  is plotted against their frequency with dots. The data was used for two-parameter exponential regression, indicated by lines. Per condition  $n \geq 7000$  dimer trajectories were recorded. **B:** The resulting values of the apparent  $k_{off}$  obtained from the exponential regression in (A) for all conditions. The error bars depict the error of the regression, performed with R (package: nls, Version 3.3.2). **C:** Average displacement per frame of the detected EGFR<sub>SNAPE</sub> and MET<sub>HALO</sub> particles classified as dimer or non-dimer for all conditions. Error bars represent the SEM of individual cells ( $n \geq 19$ ). Significance was tested using t-test, \*\*\* =  $p < 0.001$ .

Further, the average displacement per frame was analyzed for both receptors as a measure for receptor mobility on the cell surface which is expected to be reduced for receptor dimers due to increased molecular weight. As indicated in Figure 2.19C, the average displacement per frame of EGFR and MET depending on the stimulus and the classification in dimer or non-dimer states by the hidden Markov model. As expected, the receptors classified as dimer exhibit a decreased mobility compared to non-dimer particles. Since this effect is already visible in the unstimulated case, this may indicate that a small fraction of dimers is already formed in the absence of ligand. Further, it is evident that the mobility of EGFR is reduced upon stimulation with EGF or co-stimulation for the dimer as well as the non-dimer state. This is most likely caused by formation of EGFR homo- and heterodimers and the recruitment of adaptor proteins to the active receptor complex. Yet, the effect on the dimer class is stronger indicating a formation of EGF-dependent

EGFR:MET heterodimers. Interestingly, the average displacement per frame of MET is already decreased for stimulation with EGF indicating that EGFR:MET heterodimers are formed. This effect is stronger for the non-dimer case, but this might be caused by the large fraction of unlabeled EGF receptors. Since stimulation with EGF alone decreased displacement of MET and stimulation with HGF alone did not decrease displacement of EGFR, this result is in line with the observed EGF-dependency of the heterodimer formation.

To summarize, a single-molecule microscopy assay with fluorescently labelled receptors was established in living cells that provides evidence for the presence of EGFR:MET heterodimers in H838 cells. Further, the heterodimer formation was found to be dependent only on EGF, which is in line with the mechanistic model.

#### 2.4.5 Reduction of the mathematical model of EGFR:MET heterodimerization

For a rational dissection of the underlying mechanisms leading to enhanced MET phosphorylation upon co-stimulation with EGF and HGF, the model size was reduced to tailor the complexity to the information content of the data. The modeling was performed by H. Hass (University of Freiburg). For model reduction, reaction rates without statistically significant impact on the agreement between model and data, e.g. being arbitrary fast or zero, identified by the parameter profile likelihood approach were removed from the model according to Maiwald *et al.*<sup>[213]</sup>

First, the internalized dephosphorylated receptor states could be omitted. Hence, internalized receptors can be either directly degraded or recycled to the cell surface. As second reduction, the negative feedbacks between MAPK and PI3K could be neglected, since receptor trafficking is sufficient to capture the dynamics of the downstream components. Third, the degradation of internalized EGFR:MET heterodimers could be omitted, as the model suggested this reaction to be arbitrary slow within the experimental time-frame of up to 100 min. The resulting reduced mathematical model is shown in Figure 2.20 according to the Systems Biology Graphical Notation.<sup>[192]</sup>

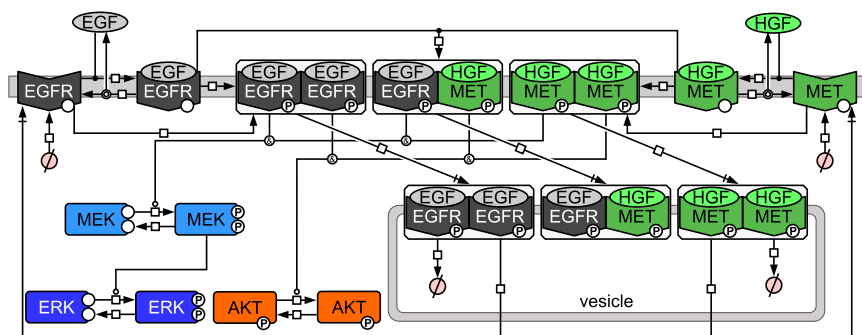


**Figure 2.20: Structure of the final model.** Schematic representation of the ODE-based mathematical model according to the Systems Biology Graphical Notation.<sup>[192]</sup>

This model was capable to capture the dynamic signal transduction data for both cell lines simultaneously (Figure 2.21) including the cell type-specific enhanced MET phosphorylation as well as time- and dose-dependent measurements of the receptors, AKT, MEK and ERK. While H838 cells showed a transient activation of AKT, the AKT phosphorylation of H1650 cells was sustained. This was taken into account by a cell type-specific AKT deactivation rate which could be caused by a mutation in PTEN in H1650 cells. Interestingly, for the downstream components  $EC_{50}$  values around 1 ng/mL and for the receptors around 10 ng/mL ligand were obtained independent of the cell line. All data used for model calibration is depicted in Figure 6.3 and Figure 6.4 in the appendix. Parameter estimation resulted in a completely identifiable model with all profile likelihood estimations of all dynamic parameters shown in Figure 6.2 in the appendix.

The calibrated model was utilized to identify the mechanism leading to enhanced MET phosphorylation upon co-stimulation and the cell line-specificity of this effect. According to the model, the internalization/degradation rate of EGFR:MET heterodimers is reduced compared to MET:MET homodimers causing sustained MET phosphorylation and increased heterodimer formation upon co-stimulation. Further, the model predicted the EGFR to MET expression ratio to determine the amount of heterodimer formation and hence the strength of enhanced MET phosphorylation explaining the cell line-specificity of the effect.

Overall, the final model was capable to describe time- and dose-dependent receptor and downstream response in two NSCLC cell lines assuming, apart from a single rate constant affected by a point mutation, only differences in initial receptor expression.

#### 2.4.6 EGFR to MET expression ratio determines enhanced MET phosphorylation

To validate the predicted impact of the EGFR to MET expression ratio, wild type EGFR was retrovirally overexpressed in H838 cells that did not exhibit enhanced MET phosphorylation upon co-stimulation beforehand leading to the stable H838-EGFR(wt) cell line. Because the mutation status of the EGFR is suspected to influence receptor trafficking,<sup>[72,73]</sup> also EGFR harboring L858R and T790M activating mutation was overexpressed in H838 cells resulting in the H838-EGFR(act) cell line. To determine the EGFR to MET expression ratio in the transduced cells, the fold overexpression of the EGFR was determined in these cell lines by immunoblotting compared to H838 cells (Figure 2.22A). H838-EGFR(wt) cells overexpressed EGFR  $3.1 \pm 0.4$  -fold and H838-EGFR(act) cells  $3.3 \pm 0.5$  -fold ( $n \geq 6$ ). The dynamics of receptor phosphorylation was monitored by quantitative immunoblotting in both cell lines after stimulation with 40 ng/mL EGF, HGF or co-stimulation (Figure 2.22B) in two independent replicates, respectively. As expected, H838-EGFR(act) cells showed no significant induction of EGFR phosphorylation due to their activating

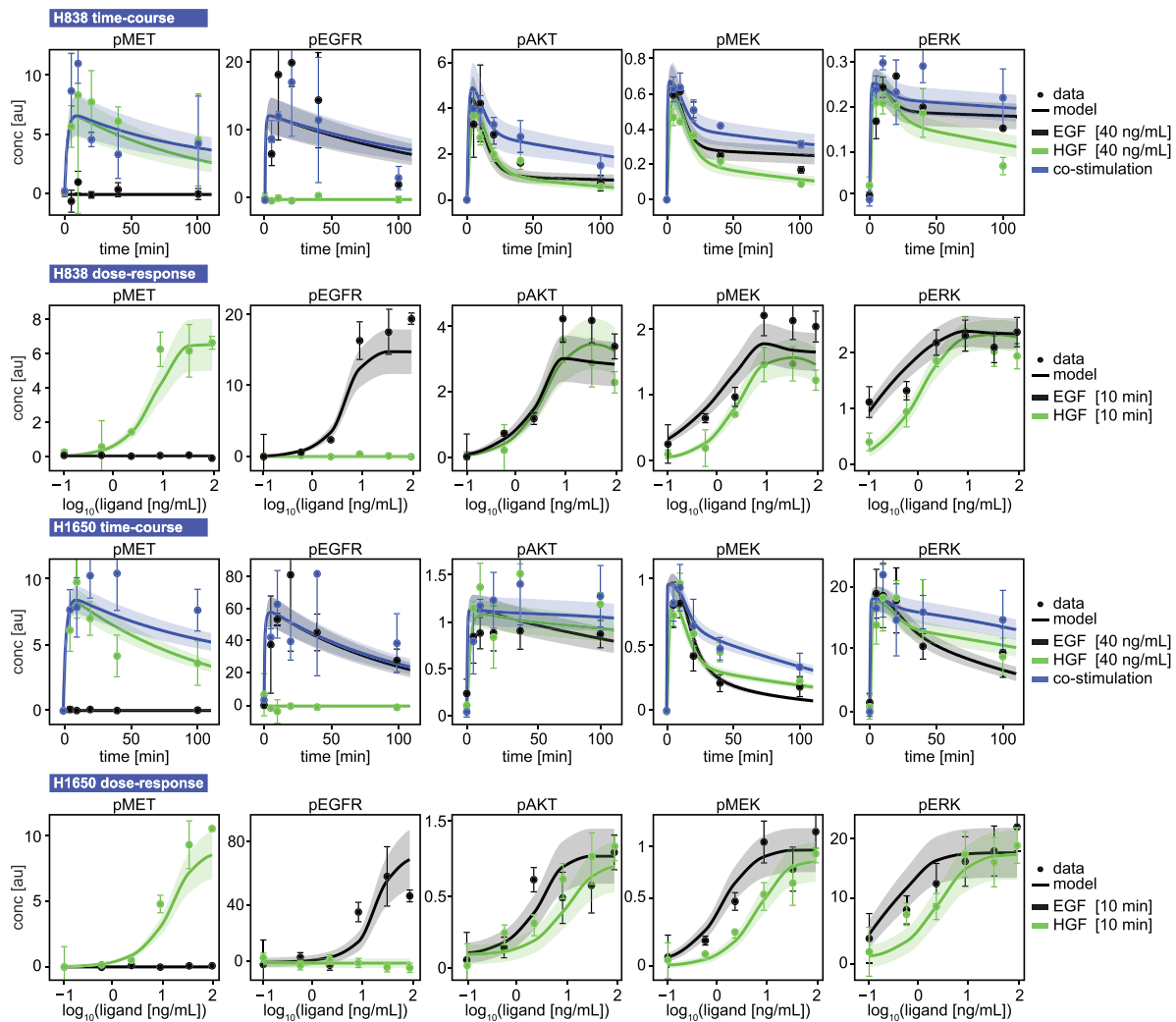


**Figure 2.21: Data utilized for model calibration.** Exemplary time- and dose-resolved signal transduction data of H838 and H1650 cells used for model calibration is shown as dots. The cells were either stimulated with 40 ng/mL EGF, 40 ng/mL EGF, or co-stimulation for the indicated timepoints or stimulated with different doses of EGF and HGF for 10 min. The dynamics of protein phosphorylation was measured by quantitative immunoblotting ( $n \geq 3$ ). Model trajectories after parameter estimation shown as lines, the shading represents the estimated error of the model. The error bars on the data represent the model-scaled measurement uncertainty of the biological replicates.

mutation, while H838-EGFR(wt) cells showed an induction of EGFR phosphorylation upon EGF stimulation. Strikingly, H838 cells overexpressing the EGFR showed an enhanced MET phosphorylation upon co-stimulation and a dynamic behavior comparable to H1650 cells independent of their mutation status. This is also evident from the quantification of the AUC of MET phosphorylation from 0 to 100 min of the overexpressing cell lines compared to the wild type cell lines described in subsection 2.4.2 (Figure 2.22C). The EGFR/MET ratio of H838-EGFR(wt) (E/M ratio = 6.8) and H838-EGFR(act) (E/M ratio = 6.9) cells is comparable to the EGFR/MET ratio of H1650

(E/M ratio = 8.4). In line with the model predictions, both cell lines showed enhanced MET phosphorylation dependent on the EGFR/MET ratio regardless of their mutation status.

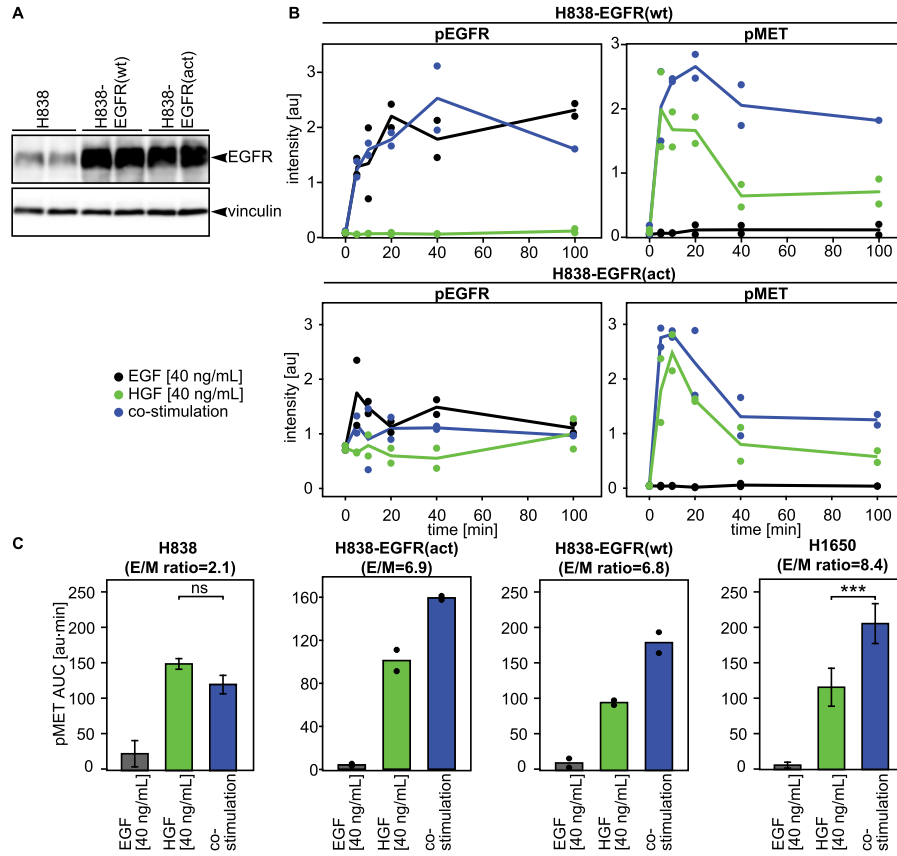


**Figure 2.22: Impact of EGFR overexpression on enhanced MET phosphorylation.** **A:** Determination of fold overexpression in H838-EGFR(wt) and H838-EGFR(act) cells compared to wild type H838 cells. The fold overexpression was determined after adjusting protein concentration of the lysates (average  $\pm$  SD,  $n \geq 6$ ). **B:** Dynamic data of EGFR and MET phosphorylation of two independent replicates measured by immunoblotting. Data is shown as dots and lines represent the average of both replicates. **C:** Area under the curve (AUC) of the dynamics of MET phosphorylation shown in (B) showing enhanced MET phosphorylation after co-stimulation in H838 cells overexpressing EGFR. Significance was tested using two-grouped t-test corrected for multiple testing (Bonferroni), ns = not significant, \*\*\* =  $p < 0.00025$ .

To support these findings, the EGFR and MET cell surface expression was determined by H. Hass for a larger panel of 24 cancer cell lines according to Hass *et al.*<sup>[201]</sup> and as described in subsection 2.4.1. The median EGFR/MET ratio of this panel of cell lines was applied as threshold to separate the examined cell lines in two groups showing a high EGFR/MET expression ratio ( $> 4$ ) or a low EGFR/MET expression ratio ( $< 4$ )(Figure 2.23A). Eight cell lines with a distinctive ratio were selected for further analysis, marked in red for low EGFR/MET and in blue for high EGFR/MET ratio. These cell lines were tested for enhanced MET phosphorylation either by the AUC of MET phosphorylation from 0 to 100 min or by measurements 40 min post stimulation (Fig-

ure 2.23B). Cell lines with a high EGFR/MET ratio (upper panel) exhibited an enhanced MET phosphorylation, while cell lines with a low EGFR/MET ratio (lower panel) showed no increased effect after co-stimulation. Exemplary immunoblots of H23 and H1703 cells are depicted in Figure 6.7 and Figure 6.8 in the appendix. Furthermore, the mathematical model was applied to predict the strength of enhanced MET phosphorylation using the integral fold change between co- and HGF-stimulation. The model was able to predict the strength of the ratio-dependent enhanced MET phosphorylation that was in line with the experimental results (Figure 2.23C).

To summarize, the enhanced MET phosphorylation upon co-stimulation is dependent on the EGFR to MET expression ratio and independent from the mutation status. The mathematical model was able to correctly predict the strength of the enhancement.

#### **2.4.7 Reduced EGFR:MET heterodimer internalization causes enhanced MET phosphorylation**

As described in subsection 2.4.5, the model predicted the reduced EGFR:MET heterodimer internalization rate to cause the cell context-specific enhanced MET phosphorylation upon co-stimulation. To validate this model hypothesis, the total MET expression was detected by immunoblot analysis 40 min post stimulation with EGF, HGF or co-stimulation (Figure 2.24A). As expected, H838, H1650 and H838-EGFR(wt) cells showed a decrease in MET levels of about 40 % upon HGF stimulation compared to unstimulated cells and no effect upon EGF stimulation. Strikingly, total MET levels were unaffected by co-stimulation with EGF and HGF in H838 cells that showed no enhancement. In H1650 and H838-EGFR(wt) cells that exhibit enhanced MET phosphorylation, total MET degradation was reduced upon co-stimulation to only 20 % indicating reduced degradation of EGFR:MET heterodimers. This finding is in line with the mathematical model prediction and further strengthens the heterodimer hypothesis.

To validate this reduced internalization also *in vivo*, labeled H838-EGFR<sub>SNAP</sub>MET<sub>HALO</sub> cells were stimulated with 40 ng/mL EGF, HGF or co-stimulation or left untreated and the fluorescence intensity on the basal cell membrane was measured with 1 frame/min for up to 30 min by S. Hänselmann (University of Heidelberg) using TIRF microscopy. The cells were manually outlined using ImageJ and the cellular fluorescence intensity without background subtraction was determined as part of this work. Figure 2.24B shows the fluorescence dynamics of a representative cell per condition for the MET<sub>HALO</sub> construct. While the fluorescence intensity is constant for unstimulated and EGF-stimulated cells, HGF-stimulated cells show a strong and co-stimulated cells show a weak decay of the fluorescence intensity.

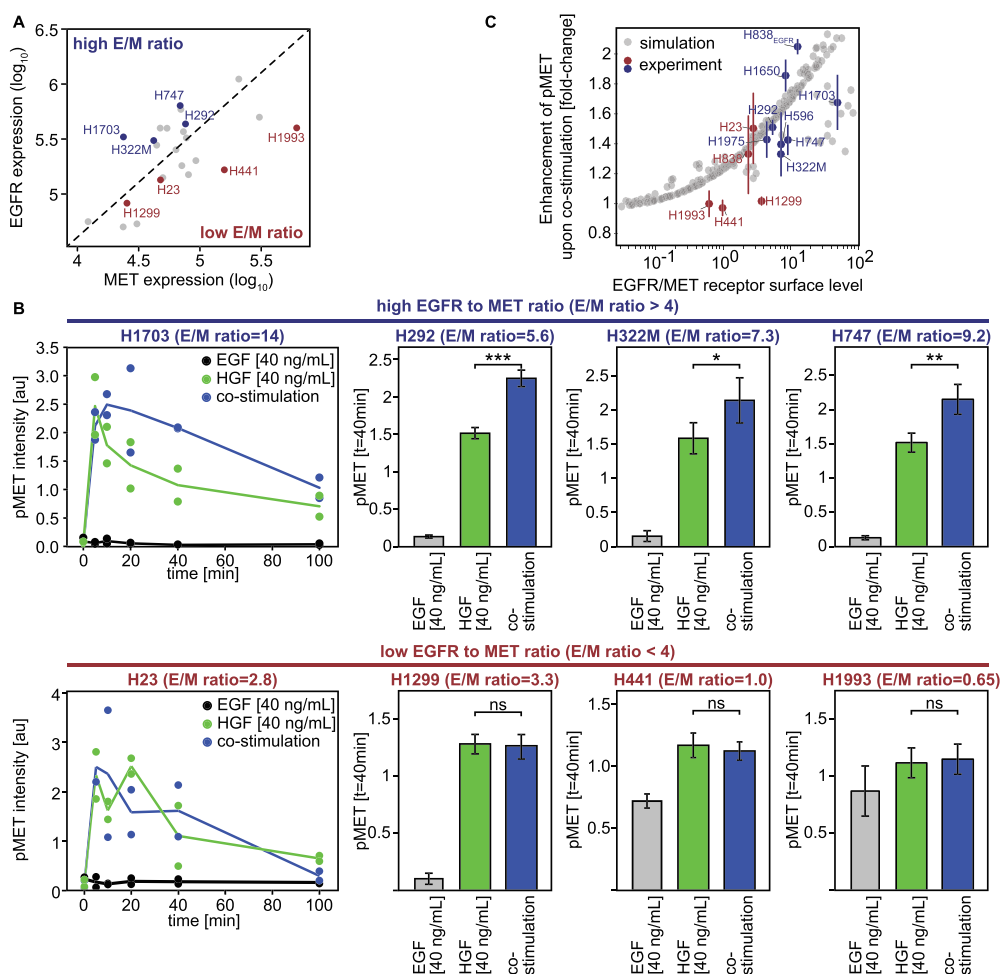


**Figure 2.23: Validation of the ratio dependency by a larger set of NSCLC cell lines.** **A:** Stratification of a set of cancer cell lines according to their EGFR and MET expression levels. The cells were separated in high and low EGFR/MET (E/M) ratio and a subset of cells marked in red and blue was further analyzed. **B:** Time-resolved immunoblot data of MET phosphorylation or measurements after 40 min for cell lines harboring different EGFR/MET ratios. The upper panel shows cell lines with a high EGFR/MET ratio, whereas the lower panel depicts cell lines with a low EGFR/MET ratio. Error bars represent SD ( $n \geq 4$ ). Significance was tested by t-test, ns = not significant, \* =  $p < 0.05$ , \*\* =  $p < 0.01$ , \*\*\* =  $p < 0.001$ . **C:** Model prediction of enhanced MET activation. Shown is a model prediction for 500 random EGFR and MET initial concentrations. As measure for enhancement, the integral fold change between co- and HGF-stimulation was calculated and compared with the fold change of co-stimulated cells compared to HGF alone shown in (B) by H. Hass.

The loss of intensity over time is a combined effect caused by receptor internalization and photo bleaching and was used for two-parameter exponential regression for 9 – 20 cells per condition to determine the receptor removal rate (Figure 2.24C). The HALO-TMR dye used for MET labeling shows negligible photo bleaching, as the receptor removal rate of unstimulated cells is comparable to zero. On the other hand, SiR-BG used for labeling EGFR showed a bleaching or basal turnover of  $10 \text{ min}^{-1}$ . As expected, stimulation with HGF increases MET internalization and stimulation

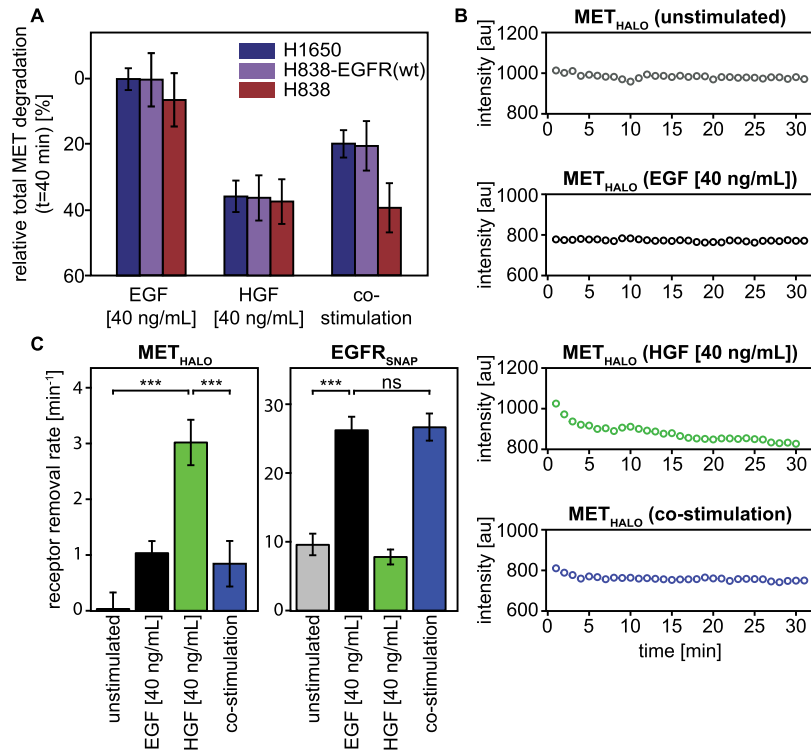


**Figure 2.24: Reduced MET internalization upon co-stimulation.** **A:** For H1650, H838 and H838-EGFR(wt), the total MET depletion was measured 40 min post EGF-, HGF- or co-stimulation,  $\pm$  SEM ( $n \geq 3$ ). H1650 and H838-EGFR(wt) cells show a significant increase of MET stability after co-stimulation compared to HGF alone ( $p = 0.017$ , t-test), while H838 show no significant change. **B:** Exemplary decay of the fluorescent signal on the basal membrane of MET<sub>HALO</sub> in H838-EGFR<sub>SNAP</sub>-MET<sub>HALO</sub> cells labeled with 10 nM HALO-TMR overnight measured by TIRF microscopy. Microscopic measurements were performed by S. Hänselmann. **C:** Receptor removal rate obtained by exponential regression of (B). Plotted is the average of  $n = 9 - 20$  cells  $\pm$  SEM. Significance was tested by t-test, ns = not significant, \*\*\* =  $p < 0.001$ .

with EGF increases EGFR internalization. Strikingly, co-stimulation had no effect on EGFR internalization, while MET internalization was strongly reduced supporting the results obtained by immunoblotting and the model hypothesis. Interestingly, HGF had no effect on EGFR removal rate, while EGF increased MET removal rate compared to the untreated control. This might be caused by the EGF-induced heterodimer formation and subsequent slow internalization. In sum, the model prediction of a reduced heterodimer internalization rate could be validated by immunoblot analysis and live-cell imaging.

### 2.4.8 HGF rescues cells from EGFR-TKI-induced inhibition

To investigate the impact of the EGFR-TKI erlotinib on signal transduction and cell survival, an appropriate dose of erlotinib was determined for the use in cell culture experiments. For this purpose, phosphorylation of EGFR, MEK, ERK and AKT was measured 5 min after stimulation of H1650 cells with 40 ng/mL EGF either with or without 30 min pretreatment with different doses of erlotinib (Figure 2.25A). As expected, EGFR-TKI treatment inhibits EGF-induced phosphorylation of EGFR and the downstream components in a dose-dependent manner. The control treatment with DMSO had no impact on the phosphorylation levels. For further experiments, a dose of 1.5  $\mu$ M erlotinib was applied that showed for all investigated proteins almost complete inhibition of phosphorylation.

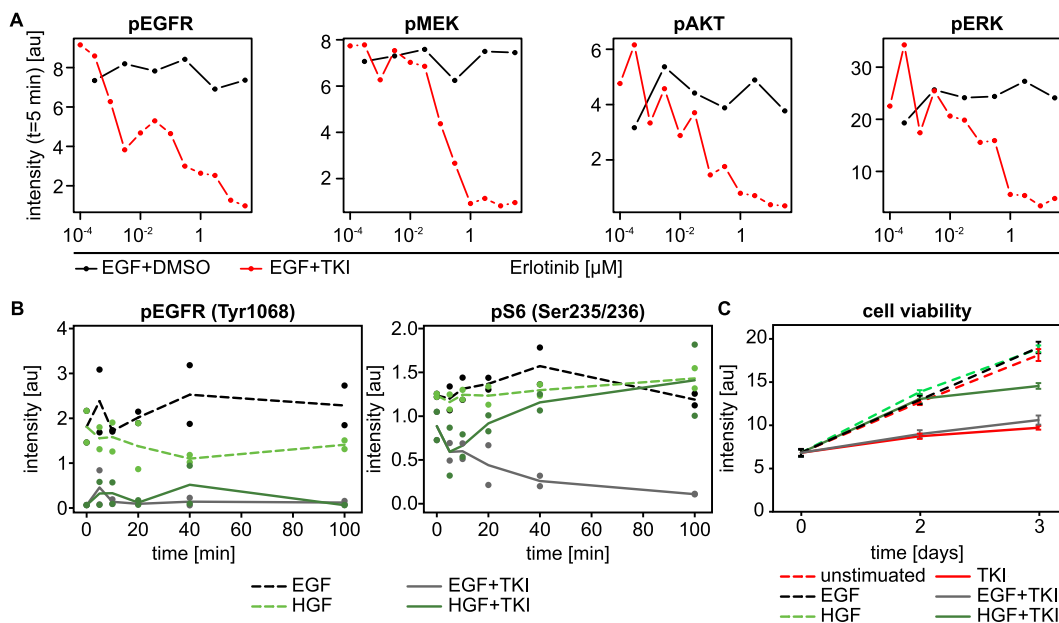


**Figure 2.25: HGF can rescue cells from inhibition with EGFR-TKIs.** **A:** H1650 cells were treated with different doses of the EGFR-TKI erlotinib or DMSO 30 min before stimulating the cells with 40 ng/mL EGF for 5 min. The phosphorylation of EGFR and downstream targets was measured by immunoblotting to determine an applicable concentration of erlotinib for further experiments ( $n = 1$ ). **B:** H1975 cells were treated with 1  $\mu$ g/mL of the EGFR-TKI afatinib or DMSO 30 min prior to stimulation of the cells with 40 ng/mL EGF or 40 ng/mL HGF for the indicated time points. The dynamics of phosphorylated EGFR and S6 was measured by immunoblotting from cytoplasmic cell lysates ( $n = 2$ ). Dots represent the data of single replicates, the average is shown as lines. **C:** H1975 cells seeded in medium containing 10% FCS were treated with 1  $\mu$ g/mL of the EGFR-TKI WZ4002 30 min prior to stimulation of the cells with 50 ng/mL EGF or 50 ng/mL HGF for the indicated time points. The cell viability was measured using a resazurin-based assay ( $n = 6$ ). Error bars represent standard deviation.

To analyze the impact of EGFR-TKIs on signal transduction and proliferation of cancer cells stimulated with EGF or HGF, the NSCLC cell line H1975 that harbors T790M and L858R mutation in EGFR and that exhibits strong basal activation of EGFR was treated with the mutant selective EGFR-TKI afatinib. The dynamics of receptor and downstream phosphorylation was measured by immunoblotting upon stimulation with 40 ng/mL EGF or 40 ng/mL HGF with or without co-treatment with 1 µg/mL afatinib (Figure 2.25B). As expected, the phosphorylation of EGFR exhibited a high basal level independent of EGF stimulation due to the activating mutation that could be decreased with the EGFR-TKI afatinib. Interestingly, the basal level of S6 phosphorylation was also decreased by afatinib treatment, but could be restored upon stimulation with HGF. Since phosphorylation of S6 is correlated with cell proliferation, this indicates that HGF can rescue H1975 cells from EGFR-TKI-induced inhibition of proliferation. The cell viability of H1975 cells was measured for up to three days either unstimulated or upon stimulation with 50 ng/mL EGF or 50 ng/mL HGF with or without co-treatment with the mutant selective EGFR-TKI WZ4002 (Figure 2.25C). As expected, the cancer cells proliferate in the unstimulated control and this proliferation is reduced upon EGFR-TKI treatment. In line with the results of the immunoblot analysis, the proliferation can be restored upon stimulation with HGF, while stimulation with EGF had no effect of the inhibited cell proliferation. In sum, the results indicated that stimulation with HGF rescues cells from TKI-induced inhibition.

### 2.4.9 Influence of EGFR-TKI treatment on MET phosphorylation

To investigate the impact of EGFR-TKI treatment on enhanced MET phosphorylation upon co-stimulation, the enhancement was measured 40 min post stimulation after 30 min pretreatment either with 1.5 µM erlotinib or with 0.4 mM DMSO in cells harboring either a high (H1650) or low (H838) EGFR to MET expression ratio. A schematic representation of the impact of EGFR-TKI treatment on MET phosphorylation is shown in Figure 2.26A indicating the indirect inhibition of MET phosphorylation by EGFR:MET heterodimer formation.

MET phosphorylation was measured by immunoblotting in H838 and H1650 cells (left panel of Figure 2.26B) and the signal intensities of four biological replicates were quantified (right panel of Figure 2.26B). As expected, MET shows enhanced phosphorylation upon co-stimulation without EGFR-TKI pretreatment in H1650 cells, but not in H838 cells. Interestingly, in H1650 cells pretreatment with erlotinib significantly reduced the MET phosphorylation level even below the levels of HGF stimulation alone. At the same time, the EGFR-TKI shows no impact on MET phosphorylation in H838 cells indicating that there is no off-target inhibition of MET. This is in line with the hypothesis of EGFR:MET heterodimer formation, as the transphosphorylation in EGFR:MET

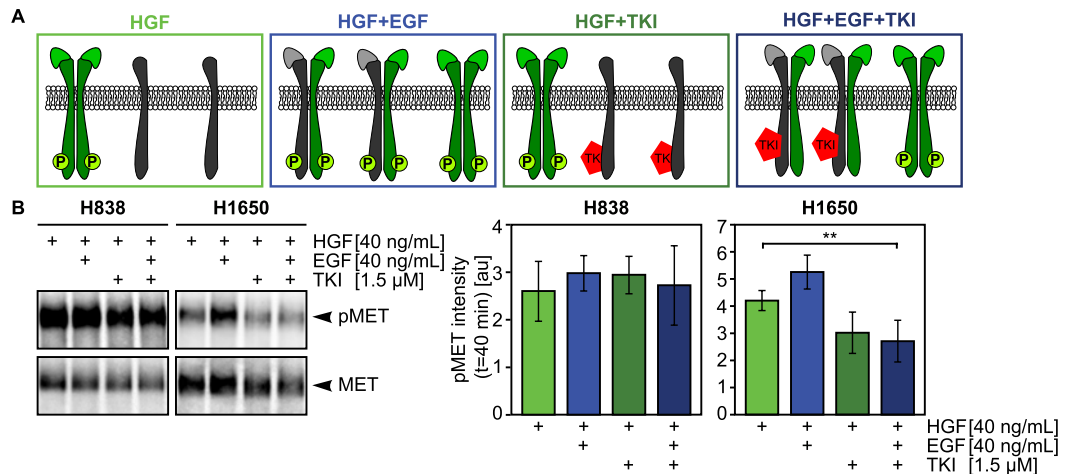


**Figure 2.26: Erlotinib has an impact on MET phosphorylation through heterodimer formation.** **A:** Scheme of the influence of EGFR-TKI treatment on MET signaling in presence or absence of EGFR-TKI. EGFR is depicted in grey and MET in green. **B:** Immunoblot analysis of H838 and H1650 cells with or without pretreatment with 1.5 μM of erlotinib for 30 min and subsequent stimulation with HGF or co-stimulation with EGF and HGF for 40 min. The right panel shows the average of four biological replicates ± SD. Significance was tested by t-test, \*\* =  $p < 0.01$ .

heterodimers is inhibited by the EGFR-TKI reducing MET phosphorylation levels. Interestingly, the MET phosphorylation level is already slightly reduced in the presence of HGF and erlotinib. This might be caused by the basal formation of heterodimers that was also observed by live-cell imaging (subsection 2.4.4).

#### 2.4.10 Influence of TKI treatment and EGF/HGF co-stimulation on cell viability

To investigate the impact of TKI treatment on cellular proliferation and survival, the cell viability upon stimulation with EGF, HGF and the EGFR-TKI erlotinib was measured in a set of lung cancer cell lines using the resazurin-based CellTiter-Blue assay (Figure 2.27). Interestingly, the proliferative responsiveness to EGF and HGF highly differed between the individual cell lines. While some cell lines did not respond at all to both stimuli such as H441 and H552 cells, H838 and H1650 cells showed a strong increase in cell viability upon stimulation with EGF as well as HGF. Therefore, H838 and H1650 cell lines were used for further analysis of the cell viability.

An increase in  $\log_{10}$ -transformed relative cell viability could be observed upon co-stimulation with EGF and HGF visible, e.g. in H838-EGFR(wt) cells from  $0.33 \pm 0.01$  (EGF) and  $0.14 \pm 0.02$  (HGF) to  $0.48 \pm 0.02$  (EGF+HGF). Yet, the effect was not more than additive. Interestingly, in H292 cells a strong reduction of cell viability upon stimulation with EGF was observed that was consistent in several independent experiments. Because a time-resolved measurement of cell proliferation showed an increase in cell viability over time, a density-mediated cell death could be excluded.

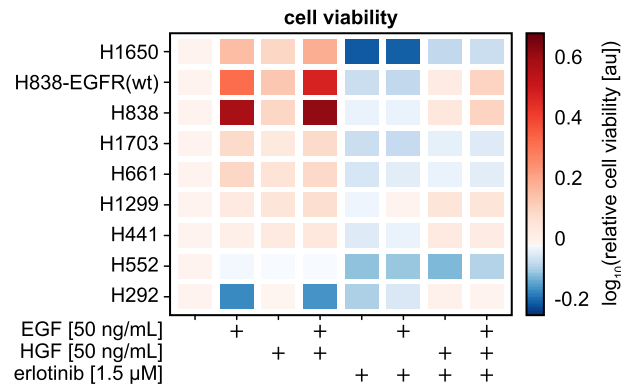


**Figure 2.27: Cell viability in different lung cancer cell lines.** Cell viability was measured by the CellTiter-Blue assay in a panel of NSCLC cell lines stimulated with EGF, HGF and co-treated with the EGFR-TKI erlotinib 3 – 6 days after stimulation. Shown is the average log-transformed cell viability of  $n = 6$  biological replicates of a representy experiment scaled to the unstimulated control.

The EGFR-TKI erlotinib reduced cell viability in all cell lines independent of EGF stimulation. The addition of HGF counteracted this inhibition and rescued cells from TKI-induced cell death. The effect of co-stimulation on TKI-treated cells described in subsection 2.4.9 was also visible on cell viability level. Yet, this effect is not significant due to the large variation, e.g. for H1703 cells the cell viability is decreased upon HGF and erlotinib treatment by  $-0.028 \pm 0.020$  and it is further decreased upon treatment with EGF, HGF and erlotinib by  $-0.035 \pm 0.028$ .

#### 2.4.11 Influence of EGFR/MET ratio on EGFR-TKI-induced cell death

To investigate whether the EGFR to MET expression ratio has an impact on EGFR-TKI treatment, the mathematical model was utilized to predict the strength of enhancement in dependency of the EGFR/MET ratio by H. Hass. According to the model, the amount of EGFR-TKI inhibited EGFR:MET heterodimers per total MET increases with increasing EGFR/MET ratio leading to a higher efficacy of the EGFR-TKI (Figure 2.28A). The previously defined threshold of the EGFR to MET ratio of four is indicated in the figure. Interestingly, the threshold separates the cells roughly at 50% of MET that is inhibited by the TKI. Because changes in the dynamics affecting less than 50% of MET could lead to weak effects, the threshold defined in subsection 2.4.6 is reasonable and supported by the model.

This effect is caused by the increased amount of heterodimers per MET receptor in cells with a high EGFR/MET ratio and consequently reduced transphosphorylation of EGFR-TKI-bound heterodimers. A schematic representation is depicted in Figure 2.28B for the high and low EGFR/MET ratio case indicating that EGFR-TKI treatment has increased efficacy in cells with a high EGFR to MET ratio, as it can also target MET signaling indirectly through EGFR:MET heterodimers.

In a *MET* amplified case with low EGFR/*MET* ratio the EGFR-TKI efficacy would be reduced accordingly. This reduced efficacy is also evident by the absence of *MET* inhibition by EGFR-TKI in H838 cells compared to H1650 cells depicted in Figure 2.26B.

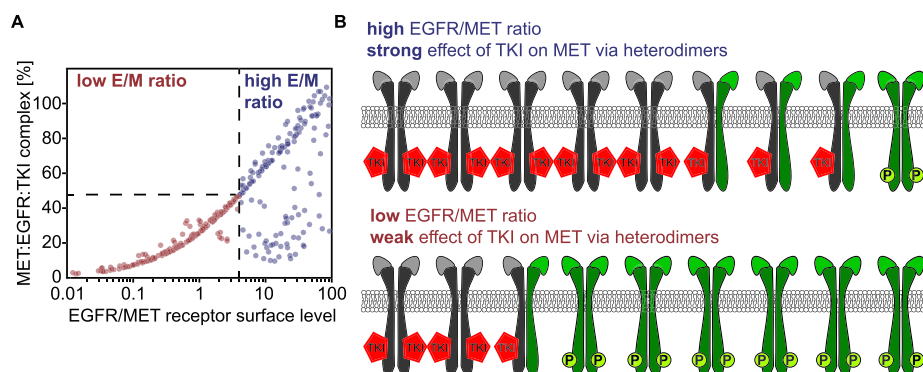


**Figure 2.28: Predicted impact of EGFR/*MET* expression ratio on EGFR-TKI treatment efficacy.** **A:** Model prediction of the fraction of *MET* receptors bound to a EGFR-TKI-inhibited EGFR dependent on the EGFR/*MET* (E/M) ratio providing an estimate of EGFR-TKI efficacy on *MET* signaling. Model prediction was performed by H. Hass. **B:** Scheme of the influence of EGFR-TKI treatment on *MET* signaling for cells with high and low EGFR (grey) to *MET* (green) ratio.

To verify the effect of EGFR:*MET* heterodimerization on EGFR-TKI treatment, the EGFR/*MET* ratio was altered in H838 cells by retroviral overexpression or siRNA knock-down of EGFR or *MET* respectively (Figure 2.29A). For overexpression the pMOWS-EGFR(wt) (V04, appendix) and the pMOWS-*MET*-HALO (V09, appendix) construct were applied representing the *EGFR* or *MET* amplified scenario. The siRNA knock-down efficiency and overexpression of EGFR and *MET* was validated by immunoblotting compared to non-targeting siRNA or wild type H838 cells. The workflow of the proliferation experiments is depicted in Figure 2.29B. In those cells the cell viability was measured upon treatment with different doses of erlotinib and subsequent stimulation with 50 ng/mL EGF and HGF after 3 days. Figure 2.29C shows that increasing the EGFR/*MET* ratio either by overexpression of EGFR or knock-down of *MET* increased EGFR-TKI efficacy, while decreasing the EGFR/*MET* ratio by *MET* overexpression or EGFR knock-down had the opposite effect. Two additional cell lines (H1650 and H23) showed comparable behavior using siRNA knock-down (Figure 2.29D). This observation is in line with the hypothesis that a low EGFR/*MET* ratio reduces EGFR-TKI efficacy and vice versa. This indicates that EGFR/*MET* expression ratio influences cellular survival and proliferation upon EGFR-TKI treatment.

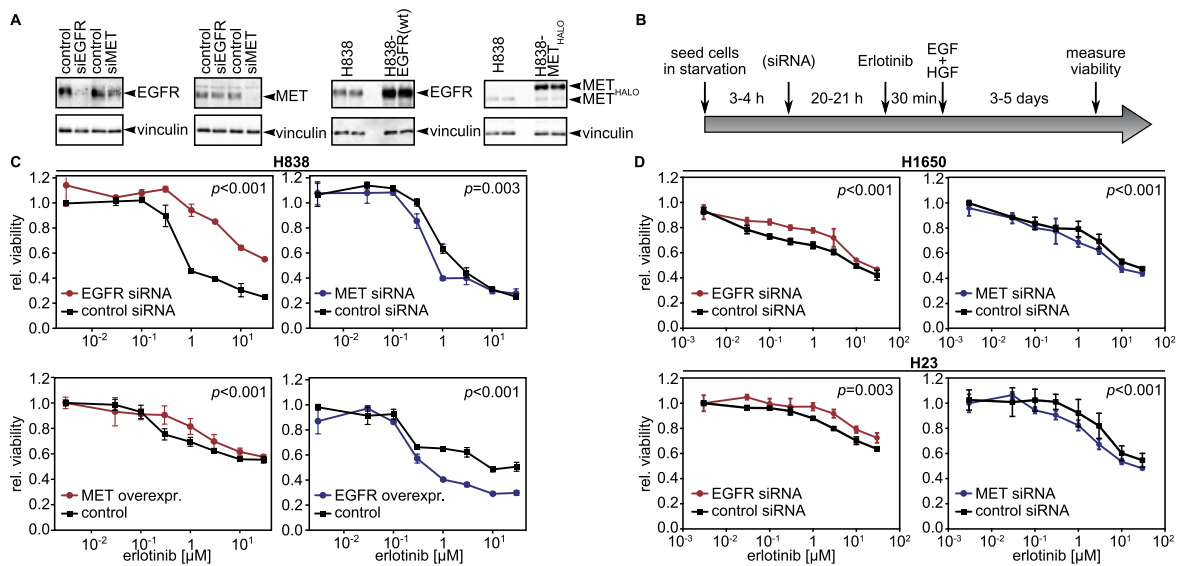


**Figure 2.29: EGFR/MET expression ratio influences EGFR-TKI treatment efficacy.** **A:** H838 cells were treated with siRNA against EGFR, MET or non-targeting siRNA for 24 h and knock-down efficiency was tested from cytoplasmic cell lysates by immunoblotting. H838 cells were retrovirally transduced with wild type (wt) EGFR or MET<sub>HALO</sub> and the receptor overexpression compared to H838 cells was determined from cytoplasmic cell lysates by immunoblotting. Utilized antibodies are listed in Table 4.4. **B:** Schematic overview of the schedule of proliferation experiments. **C-D:** Cells were seeded without growth factors and were treated after 3 h with siRNA against EGFR, MET or non-targeting siRNA for knock-down. After 24 h cells were treated with different doses of erlotinib and subsequently treated with 50 ng/mL EGF and HGF. Cell viability was measured after 3 days and is normalized to untreated cells. Error bars represent SD ( $n = 3$ ), the significance was tested using two-way ANOVA. **C:** Cell viability of H838 cells with the amount of EGFR and MET either increased by stable retroviral transduction or decreased by siRNA treatment. **D:** In H1650 and H23 cells MET and EGFR levels were decreased by siRNA treatment.

#### 2.4.12 Clinical significance of EGFR-TKI treatment

To validate the developed hypothesis in a more patient-related setting, primary tumor cells were isolated by M. Meister (Thoraxklinik Heidelberg) and M. Schneider (Thoraxklinik Heidelberg) from tumor tissue of a 60 year old female (stage IV, papillary adenocarcinoma, 20 pack years) and a 71 year old female (stage IIIB, solid adenocarcinoma, 30 pack years) who underwent resection. They utilized the tissue to generate the patient-derived tumor cell lines 4950T and 170162T, respectively. The patient-derived tumor cell lines were used for cell viability assays in the presence of siRNA to alter the EGFR/MET expression ratio as part of this work. The knock-down was verified by immunoblot analysis after 24 h (Figure 2.30A). The results show that siRNA against EGFR and MET effectively downregulates receptor expression leading to increased or decreased EGFR to MET expression ratio. Because the cell viability was measured as combined effect over three days, an exact expression ratio cannot be determined. The patient-derived tumor cell lines were

exposed to different doses of erlotinib and 50 ng/mL EGF and HGF after 3 days (Figure 2.30B). As expected, both patient-derived tumor cell lines showed a significant decrease in erlotinib efficacy upon siRNA against EGFR and an increase after knock-down of MET. Moreover, the expression of EGFR and MET was analyzed in tumor versus normal tissue obtained from the MERAV<sup>[214]</sup> database indicating that not only MET amplification but also EGFR downregulation could be a mediator of resistance in EGFR-TKI-treated patients (Figure 2.30C).

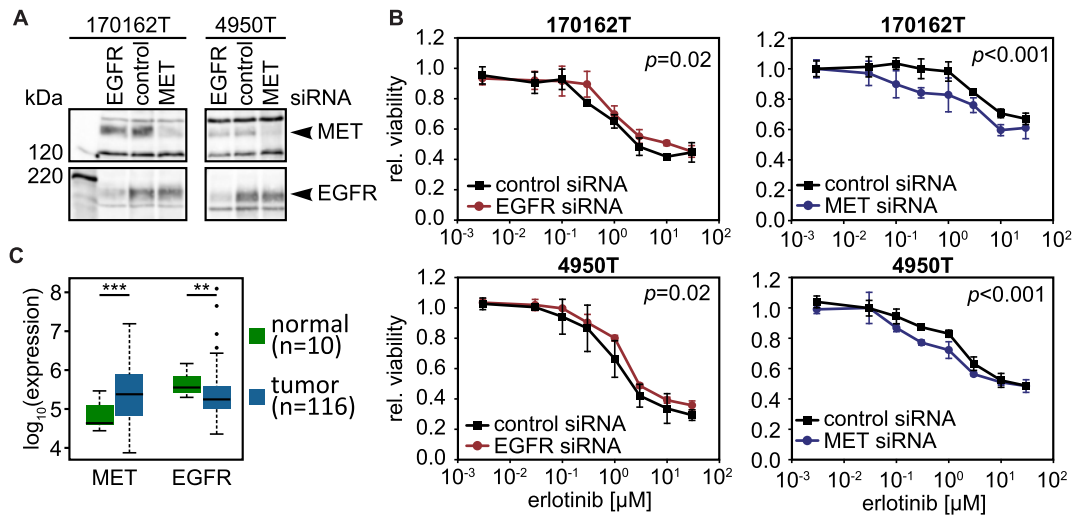


**Figure 2.30: Influence of EGFR to MET ratio on EGFR-TKI treatment in patient-derived tumor cell lines.** **A:** Patient-derived tumor cell lines were treated with siRNA against EGFR, MET or non-targeting siRNA for 24 h and MET and EGFR expression was measured by immunoblotting. **B:** Patient-derived tumor cell lines 4950T and 170162T were preincubated with siRNA against EGFR or MET for 24 h and subsequently stimulated with different doses erlotinib and 50 ng/mL EGF and HGF. Cell viability was measured three days after stimulation and was normalized to untreated cells. Error bars represent SD ( $n = 3$ ) and the significance was tested using a two-way ANOVA. **C:** EGFR and MET expression levels in normal versus tumor lung tissue were obtained from the MERAV database.<sup>[214]</sup> Significance was tested by t-test, \*\*\* =  $p < 0.001$ , \*\* =  $p < 0.01$ .

These results highlight that the receptor ratio influences therapy efficacy. In cooperation with M. Meister and M. Schneider it was shown that overall patient survival is related to the EGFR to MET ratio (Figure 2.31A, left panel) in a cohort of 362 lung cancer patients who underwent resection. The patients with an EGFR/MET ratio  $> 1$  have a better outcome compared to patients with a low EGFR/MET ratio. Yet, the dataset contains patients receiving different treatments and no patients with first line EGFR-TKI treatment, as these patients do not undergo surgery and there is no tissue material available for investigation. If one assumes that a high EGFR/MET ratio and a prolonged activation of MET signaling causes increased proliferation, these results are in line with the developed hypothesis, since chemotherapy affects fast proliferating cells stronger. The separation of the survival curves in Figure 2.31A is also stronger, if one selects only chemotherapy

treated patients (right panel). Yet, due to the large fraction of censored patients through recent recruitment of the patients only four events are left in the high EGFR/MET arm leading to a non-significant effect ( $p = 0.116$ ).

Nevertheless, a recent study by Park *et al.* showed by testing survival data of EGFR-TKI-receiving patients for different stratification parameters that patients with a high EGFR/MET ratio have a better prognosis.<sup>[215]</sup> These results can be mechanistically explained by the findings of this work.

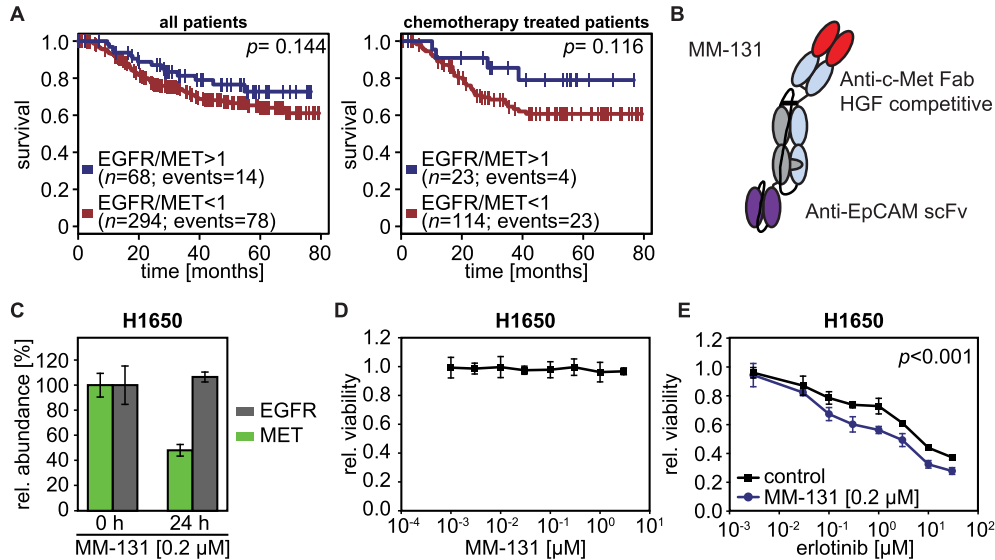


**Figure 2.31: Influence of EGFR/MET ratio on EGFR-TKI treatment.** **A:** Patient survival stratified according to their EGFR/MET expression levels based on RNA samples. mRNA expression was measured by M. Meister and M. Schneider. Significance was tested with log-rank test. **B:** Structure of the MM-131 antibody provided by Merrimack Pharmaceuticals. **C:** H1650 cells were treated with 0.2  $\mu$ M MM-131 for 24h and the total EGFR and MET receptor levels were measured by immunoblotting. Shown is the average  $\pm$  SEM ( $n = 7$ ). **D:** H1650 cells were pretreated with increasing concentrations of MM-131 for 24h and subsequently stimulated with 50 ng/mL EGF and HGF. Cell viability was measured three days after stimulation and error bars represent SD ( $n = 6$ ). **E:** H1650 cells were pretreated with 0.2  $\mu$ M MM-131 for 24h and subsequently treated with different doses erlotinib and 50 ng/mL EGF and HGF. Cell viability is normalized to untreated cells and error bars represent SD ( $n = 3$ ). The significance was tested using a two-way ANOVA.

To test whether the increase of EGFR-TKI efficacy is also achievable by pharmacological downregulation of the MET receptor, the potency of the therapeutic bi-specific, bi-valent antibody MM-131 to decrease MET expression was examined. The antibody was developed and kindly provided by Merrimack Pharmaceuticals. It binds to MET and EpCam, a receptor frequently upregulated in various cancer types (Figure 2.31B). Interestingly, MM-131 was found to downregulate MET expression within 24 hours after treatment in H1650 cells, while EGFR levels remained constant (Figure 2.31C). Measurements of the cell viability upon pretreatment of H1650 cells with different doses of MM-131 for 24h and subsequent co-stimulation with 50 ng/mL EGF and HGF revealed

that MM-131 treatment cannot significantly down-regulate cell viability (Figure 2.31D). Strikingly, application of erlotinib succeeding MM-131 pretreatment significantly increased the efficacy of the EGFR-TKI (Figure 2.31E). Thus, the MET antibody was able to restore sensitivity of cells possessing a low EGFR/MET ratio with respect to EGFR-TKI treatment.

The results obtained in this work suggest that patients need to be stratified according to their EGFR to MET expression ratio. Patients with high EGFR/MET ratio can be treated with EGFR-TKIs, while patients with low EGFR/MET ratio would benefit from a combined treatment with EGFR-TKIs and a MET antibody that is able to downregulate MET expression, such as MM-131. Since it is reported that MET is amplified in about 1% of the treatment-naive tumor cells,<sup>[133]</sup> it might be that all EGFR-TKI-treated patients would benefit from a co-treatment with antibodies that downregulate total MET expression.



## 3 Discussion

By combining quantitative time- and dose-resolved protein data with mathematical modeling, the presented work suggests strategies to prevent and overcome therapy resistance in the treatment of lung cancer patients. The investigated treatments include the two main systemic therapeutic approaches currently applied in non-small-cell lung cancer (NSCLC), chemotherapy and targeted therapy using epidermal growth factor receptor (EGFR)-tyrosine kinase inhibitors (TKIs). An ordinary differential equation (ODE)-based mathematical modeling approach identified Janus kinase (JAK)2 as potential target for a combinatorial treatment to overcome erythropoiesis stimulating agent (ESA)-induced resistance against chemotherapy in anemic lung cancer patients, while not affecting healthy erythroid progenitors. Moreover, ESAs with weak binding affinity showed increased induction of signal transduction in healthy cells compared to tumor cells. Regarding resistance against EGFR-TKIs, the expression ratio of the EGF and MET receptors affected the formation of EGFR:MET heterodimers and prolonged MET signal transduction. This effect resulted in a decreased efficacy of EGFR-TKIs in cells with a high EGFR to MET expression ratio compared to cells with a low EGFR to MET expression ratio. Treatment with the therapeutic antibody MM-131 decreased the EGFR/MET ratio and thereby synergized with EGFR-TKIs in the inhibition of cell proliferation. Therefore, drugs downregulating abundance of MET are promising candidates for a combined treatment to improve therapeutic outcome.

### 3.1 Impact of Epo on erythroid progenitor and lung cancer cells during chemotherapy

The role of erythropoietin (Epo) in treating chemotherapy-related anemia is controversially discussed, since it is suspected that Epo can also induce tumor cell survival. Clinical trials investigating the role of ESAs compared to placebo in chemotherapy-receiving patients found a significantly decreased survival in patients treated with ESAs,<sup>[174,175]</sup> while other trials reported the safety of ESA treatment.<sup>[176,177]</sup>

Within this work, a comparison of signal transduction induced by Epo treatment between murine colony forming unit - erythroid (mCFU-E) cells and a NSCLC cell line that was performed in cooperation with R. Merkle (DKFZ Heidelberg) and B. Steiert (University of Freiburg) identified JAK2 as potential target to inhibit Epo signal transduction in NSCLC cells without affecting healthy erythroid progenitor cells.<sup>[188]</sup>

The expression of the erythropoietin receptor (EpoR) in lung cancer cells is of concern<sup>[40]</sup> as EpoR expression poses a risk to induce proliferation or anti-apoptotic signaling in cancer cells.<sup>[37,38]</sup> The presence of the EpoR in tumor cells was previously detected by immunoblot analysis in five breast cancer cell lines.<sup>[38]</sup> A study by Dagnon *et al.* showed by immunohistochemical staining of NSCLC sections the presence of EpoR in 96 % of the patients as well as presence of EpoR mRNA in tumor cells.<sup>[178]</sup> They suggested expression of the EpoR and Epo in tumor tissue mediated by hypoxia as they detect also co-expression of hypoxia-inducible factor 1 $\alpha$  (HIF1 $\alpha$ ) in the tumor tissue. While in some reports Epo was reported to not induce proliferation in NSCLC cells<sup>[216]</sup> and breast cancer cells<sup>[217]</sup>, others observed the induction of proliferation upon Epo stimulation in renal carcinoma cells<sup>[218]</sup> or breast cancer cells.<sup>[38]</sup> While the question whether Epo induces proliferation in tumor cells is controversially discussed, even in studies with the same cell line,<sup>[40]</sup> evidence that Epo treatment rescues cells from chemotherapy-induced apoptosis is accumulating.<sup>[179,180]</sup> Besides these controversial results, concerns about the specificity of the utilized EpoR antibodies have been raised, especially in immunohistochemical assays.<sup>[39]</sup> Several antibodies against the EpoR were shown to detect the highly abundant protein HSP70. A study of Sinclair *et al.* reported that EpoR transcript levels in tumor cells were lower compared to healthy tissue and that despite mRNA expression no EpoR surface expression was observed by <sup>125</sup>I-Epo binding assays.<sup>[46]</sup>

In this work, expression of the EpoR was confirmed by quantitative immunoblotting in the NSCLC cell line H838. Cells without and with exogenous expression of the EpoR were utilized as negative and positive control to specifically quantify the bands corresponding to total and phosphorylated EpoR in a tumor cell lines by immunoblot analysis. The detection of Epo-induced phosphorylated STAT5 by mass spectrometry provides further evidence for EpoR expression in H838 cells.

Cell type-specific differences of the JAK2/signal transducer and activator of transcription (STAT)5 signal transduction in tumor and healthy cells were identified by a combined model of H838 cells, H838 cells overexpressing HA-tagged hEpoR (H838-HA-hEpoR) and mCFU-E cells based on an L<sub>1</sub> regularization and on model calibration with time- and dose-resolved signaling data. Previously, cell type-specific differences were determined based on differential gene expression or genomic mutations,<sup>[219]</sup> while the presented approach can also resolve dynamic and mechanistic differences and estimate parameter differences in analogy to classical backward elimination.<sup>[220]</sup> With this approach,

seven cell type-specific parameters were predicted. First, the turnover rate of *cytokine-inducible SH2-domain containing protein (CISH)* mRNA and second the delay in *SOCS3* mRNA production were found to be cell type-specific. The cell line specificity of mRNA delay is in line with previous results by global run-on sequencing that transcription rates can vary for the same gene in different cell types.<sup>[221]</sup> Third, the JAK2-induced activation rate of the EpoR and fourth the Epo-induced activation rate of JAK2 were determined to be cell type-specific. While differences in the activation rate of the EpoR and JAK2 might be caused by different affinities of human Epo to the murine EpoR on mCFU-E cells, the concentration of JAK2 might also be limiting in H838 cells. It was previously proposed that JAK2 functions as chaperone for the EpoR and thereby enhances its cell surface expression.<sup>[189]</sup> Fifth, the *suppressor of cytokine signaling (SOCS)3* promoter activity and sixth the nuclear import rate of phosphorylated STAT5 were found to be cell type-specific. The alteration of the import rate of phosphorylated STAT5 into the nucleus might be affected by the smaller nuclear to cytoplasmic volume ratio of H838 cells compared to mCFU-E cells, since it was previously reported that smaller nuclei have a higher import rate.<sup>[222]</sup> Seventh, the deactivation rate of nuclear phosphorylated STAT5 was determined to be cell type-specific. A potential enzyme catalyzing this reaction is the dual-specificity phosphatase DUSP3 that was previously reported to dephosphorylate pSTAT5 in the nucleus of IFN $\beta$ -induced cells.<sup>[223]</sup>

A sensitivity analysis predicted that treatments with targeted inhibitors reduce Epo-induced survival signaling in lung cancer cells, while only marginally affecting survival of healthy erythroid progenitor cells. The import rate of STAT5 was found to be highly sensitive in mCFU-E cells. This is in line with previous reports that identified the parameters of nuclear shuttling of JAK2/STAT5 signal transduction as the most sensitive to perturbations.<sup>[115]</sup> The Epo-induced activation rate of JAK2 and the activation rate of the EpoR by phosphorylated JAK2 showed high sensitivities in H838 cells. Accordingly, inhibition of JAK2 in Epo-treated patients might affect lung cancer cells to a higher extent than healthy cells. There are several JAK2 inhibitors approved by the FDA such as ruxolitinib in treatment of myelofibrosis.<sup>[224]</sup> While a phase II study combining ruxolitinib with chemotherapy in lung cancer patients was terminated due to a lack of sufficient efficacy (NCT02119650), the status of anemia and ESA treatment in those patients was not assessed. Further studies are required to investigate the impact of JAK2 inhibition on Epo-treated patients.

In sum, basic as well as clinical research will benefit from the developed tool that facilitates the identification of potential drug targets to affect cancer cells without impairing healthy cells.

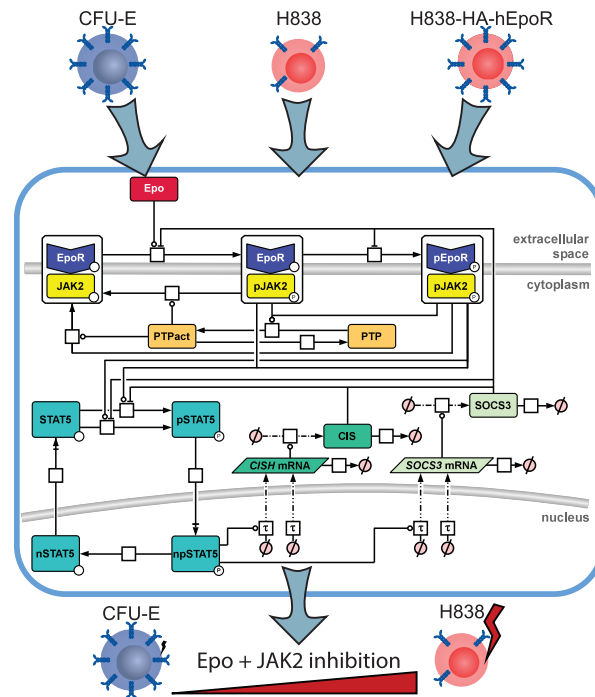


**Figure 3.1: Prediction of drug targets for treatment of chemotherapy-related anemia.** Quantitative data of erythroid progenitor cells (mCFU-E), a NSCLC cell line (H838) and H838 cells overexpressing HA-tagged EpoR (H838-HA-hEpoR) was combined in a mathematical model of JAK2/STAT5 signaling. The model identified inhibition of JAK2 as potential combinational treatment in Epo-treated anemic lung cancer patients to inhibit signaling in tumor cells, but not in healthy erythroid progenitor cells.

### 3.2 Erythropoietin alters vascularization and drug supply in mouse xenografts

The examination of the impact of co-treatment with Epo on tumor growth in chemotherapy-receiving mice in a xenograft model in collaboration with D. Doleschel (University of Aachen)<sup>[193]</sup> showed by quantitative immunoblotting that human umbilical vein endothelial cells (HUVEC) express the EpoR and that the EpoR is phosphorylated upon Epo treatment. This result is in line with a previous study that showed by *in vitro* assays an increased proliferation of HUVEC cells upon Epo stimulation.<sup>[225]</sup> Likewise, a study by Warren *et al.* showed upon Epo stimulation in HUVEC cells a reduction of apoptosis induced by lipopolysaccharide treatment.<sup>[226]</sup> Phosphorylation of the EpoR in HUVEC cells has been suggested previously by immunoblotting detecting tyrosine phosphorylation from cytoplasmic cell lysates.<sup>[225]</sup> In the presented work, immunoprecipitation against EpoR was performed with subsequent detection of Epo-induced phosphorylation of the EpoR. A cell line without EpoR expression and with retroviral overexpression of EpoR was utilized as positive control confirming the specificity.

Within this work, the carboplatin-treated xenograft mice showed a decreased tumor growth upon Epo-stimulation.<sup>[193]</sup> Other pre-clinical studies applying only Epo and no combinatorial treatment with a chemotherapeutic drug showed enhanced tumor growth upon stimulation with Epo in mouse models.<sup>[227,228]</sup> The reduced tumor growth observed upon Epo treatment in the presented work can be explained by the increased tumor perfusion as well as increased drug accessibility upon Epo stimulation. The reduction in tumor growth is also in line with previous investigations indicating a reduced tumor growth due to increased drug accumulation in murine xenograft models treated with 5-fluoruracil in combination with Epo.<sup>[229]</sup> Yet, it is not clear to which extent the vascularization is changed in a xenograft model compared to authentic solid tumors.

While anti-angiogenic drugs such as the therapeutic VEGF antibody bevacizumab are approved in combination with chemotherapy to reduce the supply of tumors with oxygen and nutrients,<sup>[230]</sup> recent studies showed that this inhibitor can also increase metastasis through an increased leakiness of the vessels.<sup>[231]</sup> Therefore, it is suggested that normalization of vascularization that was observed upon Epo stimulation might be more effective than inhibition of vascularization by bevacizumab to increase drug supply and immune response and to reduce tumor cell escape through leaky tumor vessels.<sup>[232]</sup> Concluding, increased tumor vascularization and perfusion might be an explanation for the observed improved therapeutic response upon treatment of carboplatin-treated xenograft mice with Epo.

### **3.3 Binding kinetics of erythropoiesis stimulating agents changes cellular responses**

Within this work, ESAs with different binding affinities were shown by a mathematical model of ESA-induced signal transduction in collaboration with A. Rodriguez (DKFZ Heidelberg) to distinctively affect healthy human and tumor cells. The model was based on ESA depletion data from cellular supernatants and the dynamics of STAT5 phosphorylation upon ESA stimulation.

The number of Epo receptors per surface in four NSCLC cell lines was accurately determined to levels below 100 ESA binding sites per cell by the developed mathematical model. Whereas the specificity of the EpoR detection by immunoblotting was critically discussed in literature (section 3.1), the developed assay has the advantage that it does not depend on antibodies against EpoR. The kinetic rate constants obtained by the model and used to determine the number of ESA binding sites are in line with the kinetic rates of a previous published model of EpoR trafficking using iodinated Epo binding assays.<sup>[44]</sup>

The phosphorylation of EpoR upon stimulation with Epo was validated in the investigated NSCLC cell lines by immunoblot analysis and the dynamics of the phosphorylation of Epo-induced STAT5 was quantitatively assessed by mass spectrometry. The observed induction of phosphorylation of the EpoR is in line with the previously reported detection of phosphorylated STAT5 upon Epo stimulation in H838 cells by immunoblot analysis.<sup>[216]</sup> Because the activation of STAT5 was previously correlated with survival in CFU-E cells,<sup>[116]</sup> the results suggest that tumor cells expressing a functional EpoR could exhibit increased survival upon stimulation with ESAs. Adverse effects of ESA-treated patients have previously been reported. Acs *et al.* showed that Epo reduces cisplatin-induced apoptosis in cervical carcinoma cells.<sup>[179]</sup> Todaro *et al.* reported an increased proliferation and reduced inhibition by chemotherapy of breast cancer stem-like cells upon stimulation with Epo.<sup>[180]</sup> Some clinical trials investigating the role of ESAs compared to placebo in chemotherapy-receiving patients found a significant decreased survival in ESA-treated patients,<sup>[174,175]</sup> while other trials reported the safety of ESA treatment.<sup>[176,177]</sup> These observations indicate that ESAs have a diverse role in chemotherapy and, depending on the context, co-treatment with ESAs might be beneficial or disadvantageous. While for example the induction of JAK2/STAT5 signaling in tumor cells by ESAs was shown within this work that was correlated with cell survival,<sup>[116]</sup> in section 3.2 it was described that ESA co-treatment reduces tumor growth by increasing drug accessibility. Interestingly, a study in patients not treated with recombinant ESAs showed also a reduced 5-year survival for patients with tumors expressing high levels of the EpoR as detected by immunohistochemical staining from 158 resected stage I NSCLC patients.<sup>[181]</sup> This result indicates that also endogenous Epo might affect therapy response and therefore a better understanding of the mechanisms of response to ESAs is required also in cases without co-treatment of anemic lung cancer patients with ESAs.

Within this work, a mechanistic mathematical model was established that describes the signal transduction induced by different ESAs in healthy and tumor cells. This model suggested that the JAK2/STAT5 signal transduction of cells with low expression of EpoR such as cancer cells is induced less by ESAs with a low binding affinity. Utilizing the mathematical model, Epo $\beta$  was found to be an ESA with high affinity and CERA an ESA with low binding affinity. Applying the equipotent dose of Epo $\beta$  and CERA in healthy human erythroid progenitors led to the same dynamics of STAT5 in hCFU-E cells and H838-HA-hEpoR cells, while H838 and H1299 cells with low amount of EpoR showed stronger activation of STAT5 signaling upon Epo $\beta$  stimulation compared to stimulation with CERA. These results indicate that treatment of anemic cancer patients with low affinity ESAs such as CERA or NESP might be safer, since STAT5 signal transduction in erythroid progenitor cells

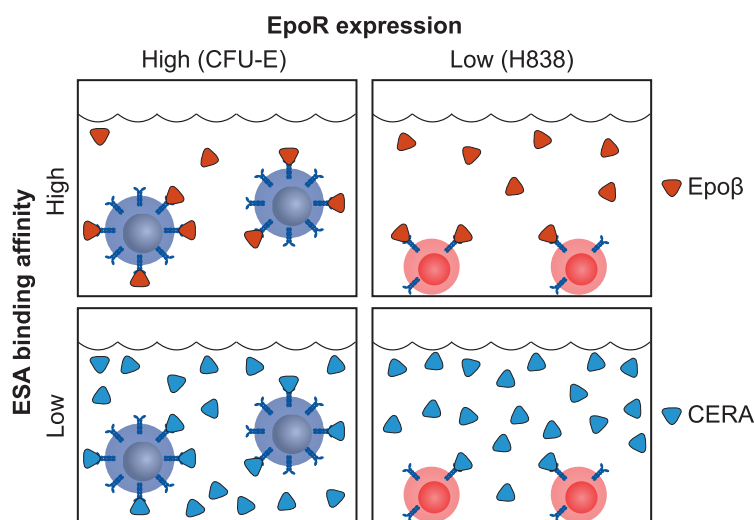


**Figure 3.2: Characterization of different ESAs in stimulation of healthy and tumor cells.** For equipotent activation of healthy CFU-E cells, low molar concentrations of Epo $\beta$  and high concentrations of CERA are required. In CFU-E cells the Epo $\beta$  is rapidly depleted by the high surface expression of EpoR, while H838 cells degrade less EpoR leading to stronger activation of signal transduction compared to the equipotent CERA dose.

is equally induced, but stimulation of tumor cells is reduced. The impact of different ESAs on vascularization still needs to be clarified.

While it is well known that a single receptor can have distinct responses for different ligands, demonstrated e.g. for G-protein coupled receptors by Malnic *et al.*,<sup>[233]</sup> and that alterations in receptor expression can modulate the cellular response, shown e.g. for interferon receptor in cardiac myocytes and fibroblasts by Zurney *et al.*,<sup>[234]</sup> this work now demonstrates the impact of receptor abundance on response to ligands with altered binding affinities. This effect might be specific for the EpoR, because EpoR pathway was reported to have a high basal turnover and rapid ligand depletion as key feature.<sup>[44]</sup> Yet, the effect of ligand binding and receptor occupancy is getting more and more in focus of clinical research as pharmacodynamic studies correlate the effect of fractional receptor occupancy with the effect of the ligand.<sup>[235]</sup>

The model developed as part of this work was utilized as basis for extending the model by a pharmacokinetic/pharmacodynamic model of ESA treatment. The extended model was able to describe the response to ESAs in healthy and anemic patients in two retrospective clinical trials (NCT00072059 and NCT00327535) and predict the minimal efficacious ESA dose for every patient. This extended model has the potential to solve the controversy regarding ESA treatment of anemic lung cancer patients<sup>[46]</sup> by personalizing therapy of lung cancer patients.

### 3.4 EGFR and MET receptor abundance influence EGFR-TKI efficacy

For more than a decade, EGFR-TKIs have been applied in NSCLC patients harboring activating mutations in the EGFR leading to almost doubled progression-free survival time compared to standard chemotherapy.<sup>[127]</sup> However, amplification of the MET receptor was correlated with therapy resistance in a substantial proportion of patients.<sup>[8]</sup> Yet, the underlying mechanism of action remained unknown.

Within this work, a mathematical pathway model was established to describe the impact of MET in EGFR-TKI resistance. Extensive time- and dose-resolved immunoblot data of two NSCLC cell lines revealed a cell line-specific enhancement of MET phosphorylation upon epidermal growth factor (EGF) and hepatocyte growth factor (HGF) co-stimulation. The data was utilized to calibrate the model and to test different mechanisms of action. Through model predictions and experimental validation, it was established that cells harboring a high EGFR to MET expression ratio have increased number of MET receptors bound in EGFR:MET heterodimers upon co-stimulation and that these EGFR:MET heterodimers exhibit a slower internalization than MET:MET homodimers leading to enhanced MET phosphorylation and increased efficacy of EGFR-TKIs.

#### Enhancement of MET phosphorylation upon co-stimulation with EGF and HGF

By time-resolved measurements of the phosphorylation dynamics in NSCLC cell lines, it was shown that EGF stimulation alone had no effect on MET phosphorylation and HGF stimulation had no effect on EGFR phosphorylation. While co-stimulation with EGF and HGF had no effect in H838 cells, H1650 cells showed an enhanced activation of MET phosphorylation leading to a prolonged phosphorylation signal.

The involvement of different factors was suggested in literature to mediate EGFR and MET crosstalk indicate the controversy of the field. The results obtained within this work are in line with reports by Puri *et al.* about synergism of EGF and HGF co-stimulation on cell proliferation in three NSCLC cell lines compared to single treatments.<sup>[91]</sup> The authors of this study also report a synergistic effect of EGF and HGF on AKT and MET phosphorylation in H1838 and A549 cells. However, how long the cells were stimulated with the ligands was not reported and the authors detected MET phosphorylation at tyrosine Tyr<sup>1003</sup> that induces MET degradation. Further, they observed a shift in molecular weight of the phosphorylated MET band upon stimulation with EGF that remained unexplained. A recent study by Werbin *et al.* showed enhanced phosphorylation of MET receptor upon EGF and HGF co-stimulation in breast cancer cells.<sup>[236]</sup> However, they observed increased MET phosphorylation 5 min post stimulation with EGF and HGF, while the re-

sults of the presented work indicate a more sustained phosphorylation of MET upon co-stimulation. While a synergistic behavior of EGF and HGF has also been described on invasiveness in mammary cell lines,<sup>[92]</sup> there are also many contradictory reports of direct transactivation of the two receptors from EGF to MET or from HGF to EGFR.

Regarding the transactivation of *EGFR* by *HGF* or *MET*, it was found that glioblastoma cells secrete heparin-binding EGF-like growth factor (HB-EGF) 6 to 24 hours post HGF stimulation.<sup>[47]</sup> In breast cancer cells, it was shown that EGFR phosphorylation at Tyr<sup>845</sup>, Tyr<sup>992</sup> and Tyr<sup>1068</sup> is maintained by MET activation via SRC even in the presence of EGFR-TKIs 30 min post application of the EGFR inhibitor.<sup>[96]</sup> On the other hand no transactivation of the EGFR by MET was found by Fischer *et al.* in pancreatic cancer cells.<sup>[101]</sup>

Directed activation of *MET* by *EGFR* or *EGF* stimulation has been described previously, yet the effect occurred only in some cell lines and the reported time scales varied from 3 min post EGF stimulation<sup>[101]</sup> to a transactivation after 1 to 2 days via SRC-induced increased MET protein abundance.<sup>[99]</sup> In colon cancer cells, transactivation of MET by the EGFR within 5 min has been reported to be mediated by prostaglandin E<sub>2</sub>.<sup>[100]</sup> The authors show that prostaglandin E<sub>2</sub>-induced transactivation of MET requires the functional EGFR and that inhibition of EGFR and MET reduce prostaglandin E<sub>2</sub>-induced invasiveness of the colon cancer cell lines. An other study in pancreatic cancer cells showed that the EGF-induced transactivation of MET by the EGFR after 3 min is mediated by reactive oxygen species (ROS).<sup>[101]</sup> The authors suggested not a directed transactivation of MET by the EGFR, but rather a common mechanism mediated by ROS that induced MET phosphorylation and that is common to EGFR and G-protein coupled receptors. On the other hand, a study by Xu *et al.* reported the transactivation of MET by EGFR-induced hypoxia.<sup>[98]</sup> They showed that induction of HIF1 $\alpha$  increases levels of total and phosphorylated MET that can be reduced by EGFR inhibition. A study performed by Breindel *et al.* in 32D cells that lack endogenous expression of the EGFR and MET showed by exogenous expression of EGFR or MET or both that EGFR kinase activity is sufficient to cause transphosphorylation of MET.<sup>[102]</sup> This result is in contrast to the observations of this work, because H838 and H1650 cells harbor functional EGFR kinase, but did not show direct transactivation of MET upon EGF stimulation. The discrepancy might be caused by the exogenous overexpression leading to artificially high levels of receptors that is reported to cause autophosphorylation.<sup>[143]</sup>

The underlying mechanism of enhanced MET phosphorylation upon co-stimulation was established by a mathematical model that was developed in collaboration with H. Hass (University of Freiburg). Different mechanistic hypotheses were considered to describe prolonged phosphorylation of MET. First, it was shown that a limited ubiquitinase that is common to EGFR and MET

could not explain the observed dynamics. This hypothesis was considered, since it is known that for high EGF concentrations the clathrin-mediated internalization of EGFR is saturated and the clathrin-independent endocytosis predominates.<sup>[77]</sup> Since MET is also internalized via the clathrin-dependent path,<sup>[82]</sup> one could assume that upon co-stimulation MET internalization is reduced due to saturation of the clathrin-dependent endocytosis. Second, it was shown that a limiting common phosphatase of EGFR and MET could not explain the dynamics and cell line dependency of the data. This mechanism was assumed, because it was reported that downregulation of PTP1B causes increase of EGFR and MET phosphorylation indicating that both receptors are a target of PTP1B and that PTP1B could be a potential candidate for a rate limiting phosphatase.<sup>[237]</sup> Third, it was shown that a negative feedback from phosphorylated ERK could neither explain the observed dynamics. A negative feedback from phosphorylated ERK to EGFR was previously suggested by Klinger *et al.*<sup>[71]</sup> Fourth, as suggested by previous reports indicating EGFR:MET association,<sup>[93,236]</sup> the direct interaction of EGFR and MET via heterodimer formation described the data well. Fifth, the extension of the heterodimer model by another human epidermal growth factor receptor (HER) family member led to also good description of the data. Association of HER3 with EGFR and MET has been suggested previously and was correlated with therapy resistance against EGFR-TKIs.<sup>[95]</sup> Yet, the model was rejected, since it was not significantly better compared to the heterodimer model. In sum, the model suggested direct interaction of EGFR and MET via heterodimer formation and reduced heterodimer internalization as most likely mechanism leading to enhanced MET phosphorylation.

#### **EGFR and MET form heterodimers *in vivo***

Within this work, the formation of EGFR:MET heterodimers *in vivo* was examined by an established fluorescent reporter cell line that stably co-expresses tagged EGFR and MET receptor (H838-EGFR<sub>SNAP</sub>MET<sub>HALO</sub>). Considering the fold overexpression of EGFR and MET in H838-EGFR<sub>SNAP</sub>MET<sub>HALO</sub> cells, one would not expect the observed enhanced MET phosphorylation upon co-stimulation, since wild type H838 cells exhibit a low EGFR to MET ratio and no enhanced MET phosphorylation and since the overexpression of both receptors was shown to be comparable. However, since no single cell clones were selected, single cells of the H838-EGFR<sub>SNAP</sub>MET<sub>HALO</sub> cell line showed heterogeneous expression ratios of the EGFR and MET. This heterogeneity was also observable in microscopic measurements. The enhanced MET phosphorylation is presumably visible on the population level by adding up the effect of single cells that harbor a high EGFR

to MET expression. Therefore, the established cell line is a suitable cell system to validate the heterodimer-mediated enhanced MET activation.

The dissociation rate constant of EGFR:MET heterodimers determined by live-cell single-molecule tracking was shown to be reduced upon EGF and HGF co-stimulation indicating an increased stability of EGFR:MET heterodimers in presence of the ligands. Within this work, a dissociation rate constant  $k_{\text{off}}$  for EGFR:MET heterodimers of about  $15 \text{ s}^{-1}$  was determined. This value is in a comparable order of magnitude as reported  $k_{\text{off}}$  values for EGFR:EGFR homodimers of  $0.2 \text{ s}^{-1}$  to  $1.2 \text{ s}^{-1}$  that were determined by life-cell tracking of two colour labeled EGFR.<sup>[211]</sup> This result suggests that EGFR:EGFR homodimers are more stable compared to EGFR:MET heterodimers due to the smaller dissociation rate constant. However, the authors of this study determined the  $k_{\text{off}}$  of EGFR:EGFR homodimers with quantum dot labeled ligands and antibody fragments that have a very high molecular weight and therefore the dimer stability might be overestimated due to slow diffusion. The impact of reduced mass transport influenced by molecular weight or immobilization on the apparent dissociation rate constant has been described by Glased *et al.*<sup>[238]</sup> On the other hand quantum dots have a high photostability, while the fluorescent dyes applied in this work show increased photobleaching and therefore might underestimate the receptor stability due to loss of particle tracks by photobleaching. Therefore, the reported dissociation rate constant for EGFR:EGFR homodimers and the dissociation rate constant of EGFR:MET heterodimers determined within this work could be in a similar range.

By co-immunoprecipitation experiments, evidence for EGFR:MET heterodimers was previously suggested *in vitro*.<sup>[93]</sup> The association of MET and the human epidermal growth factor receptor member HER3 has also been implicated in therapy resistance against EGFR-TKIs.<sup>[95]</sup> Yet, a study by Jo *et al.* showed by co-immunoprecipitation that EGFR:MET heterodimers were formed in epidermoid carcinoma cells, but not in normal hepatocytes.<sup>[94]</sup> Using the presented mechanistic model, these differences can be explained, since hepatocytes express high levels of MET and thereby have a low EGFR/MET ratio and low levels of EGFR:MET heterodimers.<sup>[214,239]</sup> The authors also reported a constitutive MET phosphorylation in human hepatoma cell lines and a human epidermoid carcinoma cell line, but not in normal human hepatocytes.<sup>[94]</sup> They showed that the cancer cell lines expressed TGF $\alpha$  leading to MET phosphorylation and that stimulation with exogenous TGF $\alpha$  induced MET phosphorylation only in the human epidermoid carcinoma cell line. The results obtained in the presented work could explain the observed cell line-specificity of the induction of MET phosphorylation. Because increased basal MET phosphorylation was only observed in cell lines that show a high EGFR/MET expression ratio and that harbor a substantial amount of EGFR:MET heterodimers according to the presented model.

For the EGFR, it was reported by live-cell single-molecule tracking that dimers can exist in three states: dissociated, co-confined and dimerized.<sup>[211]</sup> The receptor co-confinement was reported to range up to 500 nm. This is in line with reports that receptors exist in microdomains on the cell surface.<sup>[240]</sup> However, discrimination of dimerization and a more loose association remains difficult. While some studies report EGFR and MET association,<sup>[236]</sup> others describe EGFR and MET dimerization.<sup>[241]</sup> In the presented work, the co-confined state was neglected, since only associations within an interaction range were of interest. The threshold of dimerization was determined by the average distance of the particles of the positive control that was applied as input for the hidden Markov model.

Moreover, it was shown within this work that the presence of EGF seemed to be sufficient to induce heterodimer formation. The analysis of the displacement per frame of the fluorescently tagged receptors also suggested EGF-dependent formation of EGFR:MET heterodimers. This is in line with a recent study by Werbin *et al.* that showed increased association of EGFR and MET upon stimulation with EGF by multiplexed exchange-PAINt imaging.<sup>[236]</sup> Contrarily, an other study by Ortiz *et al.* using FRET measurements of different EGFR mutants in H1975 cells showed EGFR:MET heterodimerization only for EGFR harboring L858R and T790M mutation, but not for single L858R mutation and wild type EGFR.<sup>[241]</sup> The authors of this study measured FRET in fixed and permeabilized cells using antibodies against EGFR and MET. However, concerns about potential artifacts caused by formaldehyde fixation and permeabilization have been raised for the measurements of proteins and especially membrane-associated protein interactions.<sup>[242]</sup> Within this work, EGFR and MET receptor dimerization was detected in living cells labeled with fluorescent tags providing specific receptor labeling. Ortiz *et al.* further showed that EGFR:MET heterodimer formation is reduced in EGFR(L858R/T790M) mutated cells upon treatment with a MET-TKI, while in EGFR(L858R) mutated cells heterodimerization is promoted upon MET-TKI treatment. Since the MET-TKI could affect EGFR and MET expression levels also depending on the EGFR mutation status, the presented mechanism could explain the distinct behavior of EGFR:MET heterodimerization shown by Ortiz *et al.*

In sum, the novel link between relative EGFR and MET receptor abundance and amount of heterodimerization described within this work could be an explanation for the various controversial results described in literature.

**EGFR:MET heterodimers exhibit a reduced receptor internalization rate**

The model-predicted reduction of MET internalization and degradation upon co-stimulation was validated on total protein level as well as by live-cell imaging. A similar effect was previously described using iodinated ligand binding assays for EGFR and HER2 heterodimers that were shown to be more stable compared to EGFR homodimers.<sup>[243]</sup> A study in 32D cells reported an increase of MET protein after exogenous expression of the EGFR and stimulation with EGF without altering the MET mRNA levels.<sup>[102]</sup> This observation could be explained with the suggested EGF-dependent formation of EGFR:MET heterodimers that results in reduced internalization and degradation of receptor heterodimers.

Regarding the EGFR internalization rate, there were several studies performed. Mostly, the internalization speed was correlated with EGFR-TKI sensitivity or EGFR mutation status showing controversial results.<sup>[73]</sup> The influence of EGFR and MET receptor expression on MET internalization rate that has not been investigated so far was established within this work and was connected with therapy resistance. Shtiegman *et al.* found an increased half-life of L858R and  $\Delta$ 746-50 mutation in HeLa cells in which the endogenous EGFR was depleted using radiolabeled ligand,<sup>[72]</sup> while Chen *et al.* showed that overexpression of different EGF receptors with L858R and  $\Delta$ 746-50 mutants in H1299 cells does not affect receptor internalization by ligand uptake assays.<sup>[244]</sup> Huang *et al.* reported that the TKI sensitive cell lines H292 and H322 show a strong relative EGFR internalization, while TKI resistant H1703 cells showed a weak relative EGFR internalization, defined as fraction of membrane localized EGFR before and after EGF stimulation.<sup>[245]</sup> However, they showed that the localization of the EGFR in the unstimulated cells is mainly in the cytoplasm for H1703 cells that were shown in this work to harbor a EGFR/MET ratio of 14 and mainly on the membrane in H292 (EGFR/MET = 5.6) and H322 (EGFR/MET = 7.3) cells. The reduced basal internalization of EGFR in H292 and H322 cell could be caused by the larger fraction of EGF receptors bound in an more stable EGFR:MET complex. Although within this work, no change in EGFR internalization was detected by measurements of the fluorescently labeled receptors on the basal membrane upon stimulation with EGF or co-stimulation with EGF and HGF by TIRF microscopy, the presented model suggested that in cells with very high MET expression such as hepatocytes<sup>[214,239]</sup> the EGFR internalization could be reduced due to heterodimer formation. The results of the presented study demonstrate that receptor expression ratio rather than mutation status is essential for the determination of the receptor internalization rate, because enhanced MET phosphorylation was similar for H838 cells overexpressing wild type EGFR compared to H838 cells overexpressing EGFR harboring L858R and T790M mutation.

**EGFR/MET expression ratio determines amount of heterodimer formation**

The presented model predicted further that the EGFR to MET expression ratio determines to which extent heterodimers are formed. This novel mechanism was verified on one hand using retroviral overexpression of EGFR to increase the EGFR/MET ratio in H838 cells leading to a substantial change in the dynamics of MET phosphorylation. H838 cells that did not show enhanced MET phosphorylation upon co-stimulation beforehand, exhibited a strong enhancement after overexpression of EGFR. On the other hand, the mechanism was validated by a set of eight additional cell lines with distinct EGFR/MET ratios showing ratio-dependent enhanced MET phosphorylation. The dependency of signaling output on the expression ratio was previously suggested in the case of BCL2/BAX ratio influencing cell apoptosis.<sup>[246]</sup> A recent study showed that signal transduction highly depends on the relative abundance of AKT and ERK pathway components in regulating cell type-specific responses.<sup>[247]</sup> An involvement of EGFR to MET expression ratio in changing the dynamics of signal transduction has not been proposed so far, but was established as part of this work.

The observed impact of EGFR:MET heterodimers on EGFR-TKI efficacy is also in line with reports that showed an EGFR and MET association by co-immunoprecipitation only in EGFR-TKI sensitive NSCLC cell lines, but not in resistant cells.<sup>[134]</sup> Although they investigated cell lines with activating EGFR mutations, the gefitinib sensitivity they observed was not correlated with EGFR mutation status, since they report for H1650 cells an  $IC_{50} > 10 \mu\text{M}$  and for HCC827 cells an  $IC_{50} < 0.1 \mu\text{M}$  that harbor both and  $\Delta\text{E746-A750}$  mutation.<sup>[134]</sup> The relative abundance of EGFR and MET could explain the reported distinct responses to the EGFR-TKI. Interestingly, also the inhibition of EGFR by TKIs was reported to influence dimer formation.<sup>[152]</sup> The authors of that study showed that the EGFR-TKI gefitinib reduces EGFR:EGFR homodimer formation, but not EGFR:HER2 heterodimer formation by proximity ligation assays in esophageal cell lines. Although the formation of heterodimers of the HER family members is well established,<sup>[48]</sup> the quantitative amount of homo- and heterodimers that are formed is not understood so far. However, one could assume that the total receptor levels of the individual receptors have a strong impact on dimer formation. Because the authors detected heterodimer formation 30 hours post TKI treatment, the total EGFR and HER2 receptor expression levels might be completely changed potentially explaining the decreased EGFR:EGFR homodimer formation. A study by Kluba *et al.* showed by raster image correlation that EGFR homodimerization is a dynamic process that exhibited oscillatory behavior with an periodicity of 2.5 min.<sup>[248]</sup> They suggested a negative feedback altering binding affinity of two EGFR monomers to form an EGFR:EGFR homodimer. Their results indicated that

receptor homo- and heterodimer formation is a dynamic process that is influenced by many factors. For example, it was reported that receptor acetylation can also affect receptor dimerization and internalization.<sup>[249]</sup>

Likewise, the altered binding affinity for EGFR:EGFR homodimer formation could increase affinity for other receptors such as HER2 or MET causing increased heterodimer formation. To validate that altered binding affinities are able to explain the effects observed within this work, a model system of two components in thermodynamic equilibrium was assumed (Figure 3.3). The system was set to a high binding affinity or binding energy of EGFR:EGFR homodimers, a low binding energy of MET:MET homodimers and an intermediate binding energy of EGFR:MET heterodimers. In this case, EGFR would preferentially bind itself for all expression ratios of EGFR and MET leading to no substantial fraction of EGFR:MET heterodimers per EGFR:EGFR homodimer. One would also not obtain a large fraction of EGFR:MET heterodimers per MET:MET homodimer in case of a small EGFR/MET expression ratio, since EGFR concentration is low. On the other hand, these binding energies would lead to a large fraction of EGFR:MET heterodimers per MET:MET homodimer for large EGFR/MET expression ratios.

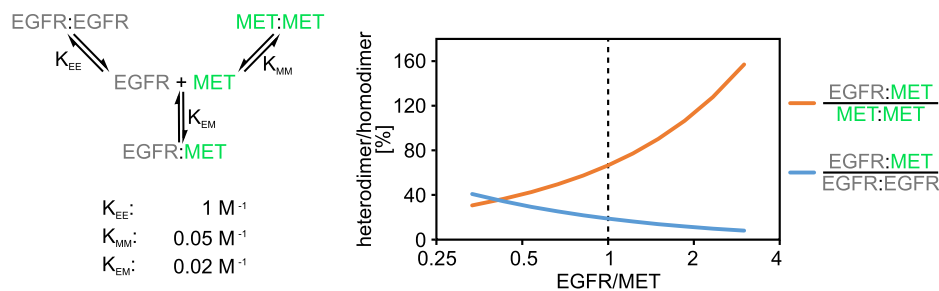


**Figure 3.3: Influence of EGFR to MET expression ratio heterodimer formation.** The fraction of homo- and heterodimer formation was estimated by three competing reactions for which different reaction constants have been assumed. The obtained fraction of heterodimer per homodimer in thermodynamic equilibrium is depicted for different EGFR/MET ratios. The receptor concentrations were calculated based on the COPASI framework in the CellDesigner program.

This dependency of heterodimer formation on the EGFR/MET expression ratio that was observed within this work could also explain the observed directed interaction of EGFR and MET. In this work, it was found that co-stimulation with EGF and HGF prolongs MET phosphorylation, but not EGFR phosphorylation. This could be caused by a similar internalization rate of EGFR:EGFR homodimers and EGFR:MET heterodimers compared to the fast internalization of MET:MET homodimers. It could also be caused by the ratio dependent fraction of heterodimers per receptor described in Figure 3.3. Because an excess of EGFR is needed to lead to substantial fraction of heterodimers per MET receptor, the fraction of heterodimers per EGF receptor is very small

leading to a negligible co-stimulation effect on EGFR degradation and phosphorylation. On the other hand, the fraction of heterodimers per MET receptors is large leading to a strong reduction of MET internalization and enhancement of MET phosphorylation.

This effect might also be an explanation for the controversial results obtained in cell lines of the direct interaction of EGFR and MET that were discussed above.

#### **TKI-mediated inhibition of MET phosphorylation**

The observed ratio dependent heterodimer formation led to the hypothesis that TKI treatment is more efficient in cells with a high EGFR/MET ratio due to the inhibition of the EGFR:MET heterodimers and reduced amount of signaling competent MET receptors. It could be shown that treatment with the EGFR-TKI erlotinib in combination with EGF and HGF had no impact on MET phosphorylation in cells with a low EGFR/MET ratio, while in cells with a high EGFR/MET ratio MET phosphorylation is inhibited upon treatment with erlotinib. This suggested that for heterodimer phosphorylation both ligands are required to activate the kinase domains and TKI treatment is sufficient to reduce receptor phosphorylation which is in line with the observation that upon stimulation with EGF alone no phosphorylation of MET and upon stimulation with HGF alone no phosphorylation of EGFR could be observed. It is well established that the kinases of EGFR:EGFR homodimers form an asymmetric complex in which one kinase is activated.<sup>[50]</sup> While structural investigations showed that phosphorylations in the activating loop of receptor tyrosine kinases (RTKs) have to be in *trans*,<sup>[250]</sup> it is not yet clear, if the juxtamembrane region and the C-terminal tail are phosphorylated in *cis* or in *trans*.<sup>[251]</sup> It was shown that in the unique case of EGFR:EGFR homodimers, the phosphorylation in the activation loop is not required for activation of the kinase, but the kinase is activated through the assembly of the juxtamembrane regions.<sup>[252]</sup> This is in line with reports that one EGF ligand per EGFR:EGFR homodimer is sufficient to activate the complex.<sup>[253]</sup> However, in an EGFR:MET heterodimer, this interaction is absent and an activating phosphorylation might be required for full kinase activity. For other RTKs it was described that these activating phosphorylations increase the RTK's activity by 150 to 1 000-fold.<sup>[51]</sup> This is in line with our findings that both ligands are required for full phosphorylation of EGFR and MET and treatment with EGFR-TKIs can reduce MET phosphorylation. In case of EGFR and HER2 heterodimers, a study by Hartman *et al.* reported that heterodimerization causes changes in the phosphorylation pattern of both receptors.<sup>[254]</sup> They showed upon overexpression of HER2 in breast cancer cell lines that heterodimer formation reduces phosphorylation of Tyr<sup>1045</sup> and Tyr<sup>1068</sup> on EGFR leading to increased receptor stability and sustained signal activation. Taken

together, the study by Hartmann *et al.* and the presented work suggest that heterodimer formation is a common mechanism used to enhance cellular signal activation.

### EGFR/MET ratio dependent inhibition by TKIs

In proliferation assays, this study showed that the EGFR/MET ratio influences EGFR-TKI efficacy as predicted by the described model by indirect inhibition of MET through binding of the EGFR-TKI to EGFR:MET heterodimers. While increasing the EGFR/MET ratio also increases EGFR-TKI efficacy, a low EGFR/MET ratio causes reduced EGFR-TKI efficacy. The ratio-dependency was confirmed in patient-derived tumor cell lines in which an identical behavior was observed upon changing the EGFR/MET expression ratio.

This mechanism provides a possible explanation of EGFR-TKI resistance mediated by *MET* gene amplification. *MET* amplification was detected by fluorescent in situ hybridization (FISH) in five to twenty percent of TKI resistant lung cancer patients.<sup>[124,255]</sup> Interestingly, high expression of the EGFR has also been correlated with better prognosis in a study with 102 NSCLC patients receiving the EGFR-TKI gefitinib by Cappuzzo *et al.*<sup>[256]</sup> The authors of this study analyzed EGFR expression by FISH, DNA sequencing and immunohistochemistry. Patients with high EGFR protein expression or *EGFR* gene amplification showed significantly increased time to progression of 9.0 versus 2.5 months. Although one would expect that high EGFR expression causes low fractional occupancy of the receptor with the drug and therefore decreased efficiency,<sup>[235]</sup> the results obtained by this work could explain the observations since a high EGFR to MET expression ratio increases the TKI efficacy. However, Cappuzzo *et al.* also reported that the EGFR is frequently overexpressed in lung tumors, which could not be observed in the results obtain within this work from the MERAV database<sup>[214]</sup> that showed decreased EGFR expression in tumor versus healthy tissue. Because in the study by Cappuzzo *et al.* treatment-naive samples were investigated, the values obtained from the MERAV database<sup>[214]</sup> might be post TKI treatment and therefore represent the resistant case with a low EGFR to MET ratio. An other study by Erjala *et al.* from 2006 reported that high relative *EGFR* copy number is predictive for gefitinib sensitivity. Yet, since involvement of *MET* amplification was not known at that time, they used the *MET* gene for normalization that is also located on chromosome seven. Because it is known by now that *MET* gene copy number strongly varies in lung cancer,<sup>[257]</sup> they showed that a high EGFR to MET copy number is predictive for gefitinib sensitivity in lung cancer strengthening the results of the presented work. A recent clinical study that investigated different parameters of TKI-treated patients for stratification identified the EGFR/MET ratio as a possible biomarker for therapeutic outcome.<sup>[215]</sup> The results of the presented work could mechanistically explain this effect on the molecular basis.

Further, it was shown within the presented work that the therapeutic MET antibody MM-131 downregulates MET expression in cell lines. While the antibody itself had no impact on cell viability in H1650 cells, pretreatment of the cells with MM-131 exhibited a synergistic effect on the reduction of cell viability in combination with erlotinib by increasing the EGFR/MET ratio. Although clinical studies applying the therapeutic MET antibody MetMAb failed to improve patient survival,<sup>[136]</sup> it is not clear, how this antibody affects total and phosphorylated MET levels. A recent study showed that a MET-TKI also inhibited MET endocytosis leading to increased number of MET molecules per cell and an overshoot of MET phosphorylation after withdrawal of the drug.<sup>[142]</sup> This might be caused by density-induced phosphorylation of MET.<sup>[143]</sup> In a clinical setting this effect would be highly undesirable and could cause increased recurrence and metastasis, since the cell to cell adhesion might be reduced by increased apoptosis in the tumor tissue. For the EGFR-TKI gefitinib, it was described that it blocks receptor internalization and degradation<sup>[119]</sup> and would thereby also increase EGFR expression and the EGFR/MET ratio. On the other hand, a report by Guo *et al.* showed that MET can also be downregulated upon EGFR-TKI treatment.<sup>[134]</sup> These findings highlight that the different therapeutic inhibitors might have distinct effects on total receptor levels. The presented results indicate that a detailed knowledge of the impact of therapeutic inhibitors on receptor expression is required and gives advice for improved combinatorial treatments, e.g. by combining EGFR-TKIs with an antibody down-regulating MET expression.

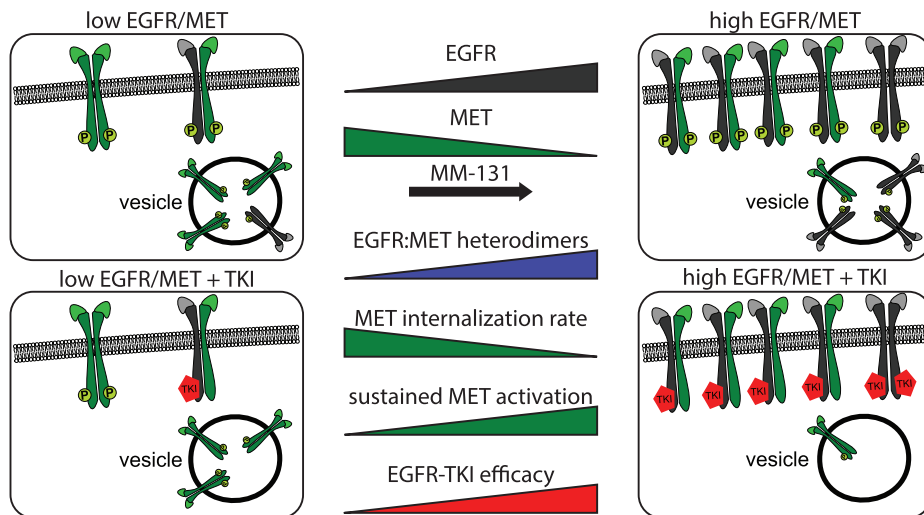


**Figure 3.4: Influence of EGFR to MET expression ratio on signal transduction and therapy outcome.** In case of low EGFR/MET, MET receptor is rapidly degraded from cell surface, while in case of high EGFR/MET more stable EGFR:MET heterodimers are formed leading to sustained MET activation. Inhibition of phosphorylation of homo- and heterodimers causes increased EGFR-TKI efficacy in case of high EGFR/MET. The therapeutic antibody MM-131 is able to downregulate MET expression and increase EGFR-TKI efficacy.

Concluding, the presented results suggest the measurement of the EGFR to MET expression ratio prior to patient therapy and application of MM-131 or a comparable MET-downregulating antibody in combination with EGFR-TKIs in patients with low EGFR/MET ratio. A standardized assessment of mRNA expression in cancer patients will facilitate application of the model-guided treatment strategy in the clinical routine. Moreover, since MET amplification is suspected to be preexisting in about 1% of the tumor cells,<sup>[133]</sup> a combined treatment might prevent selection for these clones and reduce relapse rate of all patients. Using mathematical modeling, the EGFR to MET expression ratio was proved to affect EGFR:MET heterodimer formation and MET phosphorylation dynamics by a reduced internalization rate. This mechanism also affects the efficacy of EGFR-TKIs such as erlotinib. Based on these results, a novel strategy was proposed to stratify patients according to the EGFR/MET ratio suggesting the application of therapeutic antibodies such as MM-131 to downregulate MET expression and improve therapy response.

### 3.5 Proposed further investigations

This work presents novel mechanistic insights in processes during lung cancer therapy and development of therapy resistance. The results could help to improve current therapeutic approaches such as chemotherapy and targeted therapy with EGFR-TKIs and medication with erythropoiesis stimulating agent during chemotherapy-mediated anemia. However, there are several questions that could be addressed in the future.

The identified cell-type specific differences in healthy and tumor cells can be further investigated and the potential drug targets could be tested in tumor cells lines in combination with cisplatin and ESAs. For this purpose, one could also quantify the number of Epo receptors per cell of lung tumor tissue and use these values as model input to predict the signal transduction in primary patient material.

The observed impact of the EGFR to MET expression ratio on TKI treatment efficacy could be further investigated on the mechanistic as well as on the clinical aspects. Regarding the mechanistic studies, the presented investigations could be repeated with transforming growth factor  $\alpha$  (TGF $\alpha$ ), since this ligand induces more transient EGFR phosphorylation and increases receptor recycling and therefore the EGFR phosphorylation dynamics might be influenced stronger by the reduced internalization of EGFR:MET heterodimers. Further, a mutation in Tyr845 and the juxtamembrane region of EGFR could be introduced preventing activation of the adjacent EGFR kinase in EGFR homodimers. Hence, all EGFR phosphorylations should be mediated by the MET kinase and EGFR phosphorylation should highly depend on the EGFR/MET expression ratio. This mutation could be introduced in cells lacking endogenous EGFR expression such as 32D cells, or by knock-down of the endogenous genes. Besides this, the role of the MET-related RTK RON could be investigated.

Regarding the clinical investigations, more of the available EGFR and MET antibodies and small molecule inhibitors could be tested for their impact on the EGFR/MET ratio to identify promising combinations or sequential treatment options. For this purpose, the amount of homo- and heterodimers in dependency of the EGFR and MET expression levels could be measured upon inhibitor treatment. Further, primary patient material could be used to measure mRNA and protein levels of the receptors to develop an applicable screening method that could standardly be applied in the clinics by correlating amount of mRNA to receptor surface expression levels.

Using the developed mathematical model, it would be possible to predict an optimized combination of EGFR and MET inhibitors affecting phosphorylation and total levels to increase response rates and avoid emergence of therapy resistance.

## 4 Material and methods

### 4.1 Molecular biology techniques

#### 4.1.1 Polymerase chain reaction

Amplification of specific DNA fragments was performed by polymerase chain reaction using a Phusion High-Fidelity Polymerase (NEB) according to the manufacturer’s instructions in 50  $\mu\text{L}$  total volume using a ThermoCycler (MyCycler, BioRad). In brief, 10  $\mu\text{L}$  5 $\times$  HF buffer were combined with 10 ng DNA template, 50 pmol forward and reverse primer respectively, 1  $\mu\text{L}$  dNTPs (10 mM, Roche) and 0.5  $\mu\text{L}$  Phusion polymerase. The length of newly designed primers was set to obtain a melting temperature  $T_m$  of 60  $^\circ\text{C}$ . The cycling program is depicted in Table 4.1. The PCR product was purified using the QIAquick PCR Purification Kit (QIAGEN) according to the manufacturer’s instructions. The yield was determined by absorption at 260 nm using a NanoDrop 2000 UV/Vis-spectrometer (Thermo Scientific).

**Table 4.1:** Cycling conditions for PCR reactions.

	<b>Temperature</b>	<b>Duration</b>	<b>Cycles</b>
<b>Denaturing</b>	98 $^\circ\text{C}$	30 s	$\times 1$
<b>Denaturing</b>	98 $^\circ\text{C}$	10 s	
<b>Annealing</b>	$T_m + 5$ $^\circ\text{C}$	30 s	
<b>Elongation</b>	72 $^\circ\text{C}$	30 s/kbp	$\times 35$
<b>Elongation</b>	72 $^\circ\text{C}$	10 min	$\times 1$

#### 4.1.2 Molecular cloning of DNA fragments

For the generation of specific DNA sequences, 1 to 3  $\mu\text{g}$  plasmidic DNA or PCR-purified DNA were subjected to restriction digestion with commercially available endonucleases (NEB) in a total volume of 50  $\mu\text{L}$  according to the manufacturer’s instructions. Blunt end DNA strands were generated in the presence of 300  $\mu\text{M}$  dNTPs (Roche) and 3 U T4 DNA polymerase (NEB) for 20 min at 12  $^\circ\text{C}$ . The DNA polymerase was subsequently heat inactivated for 15 min at 75  $^\circ\text{C}$ . The fragments

were separated by 1% agarose gel (Invitrogen) containing 1:20 000 MidoriGreen (NIPPON Genetics Europe GmbH) after addition of 5× GelPilot DNA Loading Dye (QIAGEN). The respective band was identified using 1kb+ DNA ladder (Invitrogen), excised using an AlphaImager EP (Alpha Innotech) and purified by QIAEX II Gel Extraction Kit (QIAGEN) according to the manufacturer's instructions. The fragments were ligated using Quick Ligation Kit (NEB) using different molar ratios of vector to insert (3:1 to 1:3) at room temperature for 10 min with an additional control without insert.

### 4.1.3 Transformation of *E. coli* cells

The *E. coli* strain Subcloning Efficiency DH5 $\alpha$  (Invitrogen) was used for transformation of plasmidic DNA. 50  $\mu$ L bacteria suspension were thawed on ice and 5  $\mu$ L of the ligation reaction were added and gently mixed. After 30 min on ice, cells were transferred for 5 min to 37°C to induce heat shock followed by 10 min on ice. The cells were then shaken in 500  $\mu$ L SOC medium for 30 min at 37°C. Cells were centrifuged for 2 min at 2 350  $\times g$  and resuspended in 100  $\mu$ L medium, plated on an ampicillin containing lysogeny broth (LB) agar plate and incubated overnight at 37°C.

### 4.1.4 Purification of plasmid DNA

A single bacteria colony was selected and incubated in 3 mL LB medium containing 100  $\mu$ g/mL ampicillin overnight at 37°C. The DNA was extracted using the QIAprep Spin Miniprep Kit (QIAGEN) and subjected to enzymatic test digestion. Positive colonies were amplified in 100 to 200 mL LB medium containing 100  $\mu$ g/mL ampicillin and the plasmidic DNA was purified using the JetStar 2.0 Maxi Kit (Genomed) according to the manufacturer's instructions. The sequence of all plasmids was checked by sequencing (Eurofins MWG GmbH) and the concentration was determined by measuring absorbance at 260 nm with a NanoDrop 2000 UV/Vis-spectrometer (Thermo Scientific).

### 4.1.5 Construction of plasmids

The vectors used for retroviral expression were pMOWS<sup>[203]</sup> and pBABE<sup>[258]</sup> containing an ampicillin resistance cassette and either SV40-puromycin or SV40-neomycin resistance cassette for selection in human cells. The pMOWS vector contains a hybrid of an MFG/murine embryonic stem cell virus (MESV) 5'-long terminal repeat (LTR) and a spleen focus-forming virus (SFFV) 3'-LTR. It further contains a woodchuck hepatitis B virus post-transcriptional regulatory element (WPRE) for increased expression. The LTR of the pBABE vector is based on the Moloney murine leukemia

virus (MoMLV). All utilized primers and synthesized vectors are displayed in Table 6.2 to Table 6.6 in the appendix. All vector maps were generated with the program Geneious (V5.3.6). The HALO-tag (pFN22A)<sup>[259]</sup> was purchased from Promega and the SNAPf-tag (pSNAPf)<sup>[260]</sup> was purchased from NEB.

#### **pSBP-EGFR (V01, appendix)**

The human EGFR mRNA was extracted from H1975 cells with the RNeasy kit (QIAGEN). cDNA was generated by reverse transcription (Agilent) with a poly T primer and specific primers against EGFR 5'-untranslated region (UTR) (P1a and P1b) designed for 46 °C and 60 °C annealing temperature respectively. Subsequently, the kinase domain of EGFR was amplified by PCR with primer P1f and P1r and subcloned in a pSBPEX vector backbone (derived from pGEX, GE Healthcare)<sup>[261]</sup> using PacI and MfeI restriction sites. This resulted in a 43.46 kDa fusion protein containing human EGFR from amino acid G696 till I1018.

#### **pGST-MET (V02, appendix)**

The human MET cDNA was kindly provided by Roche Diagnostics as MET-YFP (V08) construct containing an optimized coding sequence that translates to wild type MET receptor. Using this template, the cytoplasmic domain was amplified by PCR using the primer P2f and P2r and subcloned in a pGEX (GE Healthcare) vector backbone using BamHI and EcoRI restriction site. The resulting construct consists of MET receptor from amino acid R958 till the end of the coding sequence yielding a 76.67 kDa fusion protein.

#### **pMOWS-EGFR (V04, V05, appendix)**

The isolated cDNA of EGFR (described above) was amplified with primers against EGFR containing XhoI and PacI restriction sites (primer P4f and P4r). Wild type EGFR was subcloned in the pMOWS-neo vector backbone and mutant EGFR (T790M, L858R) was subcloned in the pMOWS-puro vector backbone.

#### **pMOWS-HER3 (V06, appendix)**

cDNA of HER3 was generated as described above using the specific primers P5a and P5b. The coding sequence was amplified by PCR using primers with EcoRV and PacI restriction sites (P5f and P5r). The insert was subcloned in a pMOWS-puro backbone.

##### **pMOWS-Lyn-HALO-linker-SNAPf (V07, appendix)**

The reporter fusion protein containing a membrane anchor, the HALO-tag with a helical linker, the SNAP-tag and a HIS-tag was cloned in collaboration with S. Hänselmann (University of Heidelberg).<sup>[262]</sup> The membrane anchor contains the N-terminus of Lyn-kinase leading to myristoylation and palmitoylation.<sup>[207]</sup> An insert lacking the HALO-tag was synthesized *de novo* and the HALO-tag was introduced by PCR amplification using the primer P6f and P6r.

##### **pMOWS-MET-HALO (V09, appendix)**

As first step, the provided MET-YFP plasmid was cloned into the pMOWS-puro vector backbone using BamHI and NdeI restriction enzymes resulting in the pMOWS-MET-YFP plasmid (V08). Second, the cDNA of the HALO-tag was amplified by PCR using primers containing EcoRI and NdeI restriction sites (primer P7f and P7r) and introducing a synonymous mutation in the HALO-tag removing a XhoI restriction site at the N-terminal end. The PCR product was inserted in the pMOWS-MET-YFP (V08) plasmid replacing YFP.

##### **pMOWS-MET-linker-SNAP (V10, appendix)**

For introduction of the helical linker, the pMOWS-Lyn-HALO-linker-SNAPf-puro (V07) plasmid was used as template for PCR using the primer P8f and P8r amplifying the linker and the SNAP-tag. The insert was digested using EcoRI and AseI restriction enzymes. The HALO-tag of pMOWS-MET-HALO-puro (V09) was removed by EcoRI and NdeI restriction site and replaced by the insert using the compatible cohesive ends.

##### **pBABE-M3 (V11, V12, appendix)**

A multiple cloning site was designed and introduced in the pBABE vector backbone. Complementary DNA fragments of the sequence shown in Table 6.3 were ordered with additional 3 bases overhang on each end. For annealing, 19  $\mu$ L of a 100 pmol/ $\mu$ L DNA dilution of each forward and reverse strand were combined with 2  $\mu$ L 1 M NaCl, heated to 95 °C and cooled down slowly. The DNA fragment was subsequently digested with XhoI and EcoRI restriction enzymes and inserted in the pBABE-puro vector backbone. Subsequently, the puromycin resistance cassette was replaced by a neomycin resistance. For this purpose, the pBABE-M3-puro vector (V11) was digested with ClaI restriction enzyme and the resulting overhangs were converted to blunt ends. After heat inactivation of the T4 polymerase, the plasmid was digested with HindIII restriction enzyme. In parallel the pMOWS-MCS-neo plasmid was digested with AseI restriction enzyme, blunted and di-

gested with HindIII to obtain the neomycin resistance cassette. Ligation of the two DNA fragments resulted in the pBABE-M3-neo (V12) construct.

#### **pBABE-MET-HALO (V13, appendix)**

The MET-HALO construct was extracted from the pMOWS-MET-HALO-puro vector (V09) cutting with XhoI and NdeI restriction sites and inserted in the vector pBABE-M3-puro (V11).

#### **pBABE-EGFR-SNAPf (V14, appendix)**

The EGFR(wt) cDNA (V04) was amplified by the primers P9f and P9r and cloned in the pMOWS-Lyn-HALO-linker-SNAPf-puro (V07) construct using XhoI and AseI restriction sites for the PCR product and XhoI and NdeI for the vector backbone. Subsequently, the EGFR-SNAP1f insert was cloned in the pBABE-M3-neo (V12) plasmid using XhoI and PacI restriction sites.

#### **pBABE-Lyn-HALO-linker-SNAPf (V15, appendix)**

The pMOWS-Lyn-HALO-linker-SNAPf-puro vector (V08) was transferred in the pBABE-M3-puro vector (V11) in collaboration with S. Hänselmann resulting in the displayed vector (V15).

#### **pBABE-Lyn-GFP (V16, appendix)**

The HALO-linker-SNAPf sequence of the pBABE-Lyn-HALO-linker-SNAPf-puro vector (V15) was replaced in collaboration with S. Hänselmann by EGFP amplified by PCR resulting in the displayed vector (V16).

#### **pBABE-Lyn-GFP-HALO-linker-SNAPf-puro (V17, appendix)**

EGFP was amplified by PCR and inserted into pBABE-Lyn-HALO-linker-SNAPf-puro (V15) in collaboration with S. Hänselmann resulting in the displayed vector (V17).

### **4.1.6 Methylation analysis**

For determination of differentially methylated genes, DNA was isolated from NSCLC cells using the High Pure PCR Template Preparation Kit (Roche) according to the manufacturer's instructions. Methylation was measured and analyzed by O. Ammerpohl (University of Kiel) according to Marwitz *et al.*<sup>[263]</sup> using the Infinium HumanMethylation450k BeadChip (Illumina).

## 4.2 Cell Culture Techniques

### 4.2.1 Culture of human lung cancer cell lines

Human lung cancer cell lines (H838, H1975, H1650, H23, H1299, H1703) were purchased from ATCC while H522, H322M, H292, H1993, H747, H441 and H596 were kindly provided by Merri-mack Pharmaceuticals. All cells were cultured in full growth medium: Dulbecco's modified Eagle's medium (DMEM) (Lonza) supplemented with 10 % fetal calf serum (FCS) (Gibco, Ref:10 270-106; Lot: 41 G3631K) , 100 µg/mL streptomycin (Gibco) and 100 U/mL penicillin (Gibco). For retrovirally transduced cells 1.5 µg/mL puromycin (Sigma) and/or 400 µg/mL geneticin (G418) (Sigma) was added. All cells were cultivated at 37 °C, 5 % CO<sub>2</sub> and 95 % relative humidity. For passaging, the medium was replaced by phosphate buffered saline (PBS) and incubated for 5 min at 37 °C. Subsequently, the cells were incubated for 5 min with 0.025 % trypsin (Gibco). NCI-H292 and NCI-H322M cells were incubated with 0.05 % trypsin at 37 °C. After removal of the supernatant by centrifugation at  $216 \times g$ , the cells were plated on coated cell culture dishes (TPP). Cells were kept in culture for up to 25 passages. All cell lines were authenticated using Multiplex Cell Authentication and the purity of cell lines was validated using the Multiplex Cell Contamination Test by Multiplexion (Heidelberg, Germany) as described recently.<sup>[264,265]</sup> The SNP profiles matched known profiles or were unique, while no Mycoplasma, SMRV or interspecies contamination was detected.

Cells were frozen in 80 % full growth medium combined with additional 10 % FCS and 10 % glycerol (Sigma) in a cryo freezer (Nunc) in isopropyl alcohol at  $-85^{\circ}\text{C}$  and stored in liquid nitrogen. Cells were thawed in a water bath and plated to a 10 cm cell culture dish (TPP). Media was changed the following day to remove the glycerol.

### 4.2.2 Culture of Phoenix amphi/eco cells

The Phoenix amphi/eco packaging cell line<sup>[266]</sup> was cultured in DMEM (Gibco) supplemented with 10 % FCS (Gibco), 100 µg/mL streptomycin (Gibco) and 100 U/mL penicillin (Gibco). Phoenix cells are third generation virus packaging cells based on the murine leukemia virus (MLV) producing non-replication competent virus particles. Virus produced by phoenix amphi cells was used for transduction of human cells and virus produced by phoenix eco cells was used for transduction of murine cells.

### 4.2.3 Culture of human umbilical vein endothelial cells

Human umbilical vein endothelial cells (HUVEC) were kindly provided by D. Doleschel (University of Aachen) and cultivated in DMEM (Gibco) supplemented with 10 % FCS (Gibco), 100 µg/mL streptomycin (Gibco) and 100 U/mL penicillin (Gibco). For experiment the cells were seeded 3 days in advance and growth factor depleted in DMEM (Gibco) supplemented with 100 µg/mL streptomycin (Gibco), 100 U/mL penicillin (Gibco) and 1 mg/mL BSA.

### 4.2.4 Culture of patient-derived tumor cell lines

Lung cancer tissue samples were provided by the Lung Biobank Heidelberg, the BioMaterialBank Heidelberg and the Biobank platform of the German Center for Lung Research (DZL) including written informed consent for the use of the tissue for research purpose for all patients. The investigation was approved by the local ethics committee of the University of Heidelberg (S-270/2001). The generation of patient-derived tumor cell lines from NSCLC patients who underwent resection for adenocarcinoma was performed by M. Meister (Thoraxklinik Heidelberg) and M. Schneider (Thoraxklinik Heidelberg). The tissue was cut in small pieces and digested with 0.28 Wuensch Units per mL liberase H (Roche, # 05401054001) on an overhead rotator for 2 h at 37 °C. The resulting cell suspension was filtered using 100 µm and 40 µm filter strainer (Corning, # 352360 and # 352340) and the tumor cells were then isolated performing a ficoll gradient using Histopaque (Sigma-Aldrich # 1077). Cells from the interphase were collected, washed with PBS, resuspended in fresh culture medium and transferred to a T-25 culture flask (Greiner). The culture medium (DMEM/Ham's F12 (Gibco)) was supplemented with 2 mM Glutamax (Gibco), the Airway Epithelial Cell Growth Medium SupplementPack (PromoCell, C-39160 without epinephrine and retinoic acid) and 50 µM ROCK inhibitor (Stemcell, 72308). Adherent cell line 4950T was cultivated without agar, suspension culture 170162T in an agar-coated flask. 4950T cells were splitted by rinsing with PBS and incubation with accutase (Sigma, A6964) for 5 min.

### 4.2.5 Transfection of Phoenix amphi cells

The generated plasmids were used for transfection of phoenix amphi cells by calcium phosphate precipitation. For this purpose, 800 000 phoenix cells were seeded in a 6-well plate (TPP) a day before transfection. 10 µg plasmidic DNA dissolved in 112.5 µL H<sub>2</sub>O were supplemented with 12.5 µL 2.5 M CaCl<sub>2</sub>. During vortexing 125 µL 2× HEPES buffered saline (2× HBS, Table 6.1) were added to precipitate the DNA. The mixture was added dropwise to each well of the Phoenix cells cultured in medium containing 25 µM chloroquine (Sigma). The media was removed 6 h after transfection

and replaced by normal growth medium. The virus was harvested 24 h after transfection by passing through a 0.22  $\mu\text{m}$  filter and used for spin infection or frozen at  $-80^\circ\text{C}$ .

### 4.2.6 Retroviral spin transduction

150 000 to 300 000 human NSCLC cells were seeded one day before the spin infection in a 6-well plate (TPP). The viral supernatant was supplemented with 8  $\mu\text{g}/\text{mL}$  polybrene (Sigma) and 1 mL of the supernatant per well was used for spin infection at  $340 \times g$  for 3 h. Subsequently, the supernatant was replaced by normal growth medium. Selection was started 24 h after transduction.

### 4.2.7 Flow cytometry

For determination of the ploidy of NSCLC cells, flow cytometric measurements were performed. Cells were growth factor depleted overnight in DMEM without phenol red (Lonza) supplemented with 100  $\mu\text{g}/\text{mL}$  streptomycin (Gibco), 100 U/mL penicillin (Gibco), 1 mg/mL bovine serum albumin (BSA) and 2 mM L-glutamine (Gibco) and subsequently harvested by trypsination. The cells were pelleted at  $500 \times g$  for 5 min after addition of 10 mL medium and washed with 5 mL ice cold PBS. The cells were counted and  $1 \cdot 10^6$  cells were resuspended in 400  $\mu\text{L}$  ice cold PBS and 800  $\mu\text{L}$  ice cold ethanol was slowly added for cell fixation. The cells were stored overnight at  $4^\circ\text{C}$ . The following day, cells were slowly heated up to room temperature and pelleted at  $500 \times g$  for 5 min. The cells were washed in 1 mL PBS and resuspended in 200  $\mu\text{L}$  propidium iodid (PI) staining solution (20  $\mu\text{L}$  PI (BioLegend, 421301), 10  $\mu\text{L}$  RNase A (1 mg/mL, Sigma R6513) and 170  $\mu\text{L}$  PBS). The cells were stained for 30 min in the dark at  $37^\circ\text{C}$  and directly placed on ice in the dark and measured using a FACS Canto II (BD). Fluorescence at 488 nm was measured as well as forward and side scatter. For data analysis the FlowJo software (V10.0.8) was used and single cells were gated as depicted in Figure 2.9. An unstained control was measured and three cell lines H292, H441 and H661 with described modal numbers (47, 52 and 142 respectively, obtained from ATCC<sup>[200]</sup>) were used for calibration. For calibration the modus of the PI-staining distribution was used. For ploidy determination used as input for the proteome ruler analysis,<sup>[199]</sup> the average PI signal was used as estimate of the cellular DNA content.

## 4.3 Protein biochemistry

### 4.3.1 Cell stimulation and lysis

For immunoblot and mass spectrometric experiments, cells were seeded three days in advance in DMEM without phenol red (Lonza) supplemented with 10 % FCS (Gibco) 100 µg/mL streptomycin (Gibco), 100 U/mL penicillin (Gibco) and 2 mM L-glutamine (Gibco). Cells were washed three times with DMEM without supplements and growth factor depleted overnight in DMEM without phenol red (Lonza) supplemented with 1 mg/mL BSA (Sigma), 100 µg/mL streptomycin (Gibco), 100 U/mL penicillin (Gibco) and 2 mM L-glutamine (Gibco). For immunoblot analysis, 200 000 cells were seeded in 6 cm plates (TPP). For mass spectrometric analysis,  $2 \cdot 10^6$  cells were seeded in 15 cm plates. The cells were stimulated with the indicated ligands or inhibitors shown in Table 4.2 for the indicated time points. Cells were subsequently lysed on ice by NP40-containing buffer (NP40-substitute, Roche, 11754599001; Lot: 10242500) for cytoplasmic fraction and a RIPA buffer for total cell lysates (see Table 6.1). The lysates were slowly rotated at 8 °C for 30 min and total cell lysates were further processed by two cycles of sonication for 1 min each on ice (Sonopuls, Bandelin, amplitude: 80 %; pulse-on: 0.5 s, pulse-off: 0.2 s). Subsequently, the lysates were centrifuged for 10 min at  $20\,000 \times g$  and 4 °C. The supernatant was transferred to a new reaction tube and protein concentration was measured using pre-diluted protein assay standards (Thermo Scientific) and BCA protein assay reagents (Pierce) in 96-well plates (Grainer bio-one). After incubation at 37 °C for 30 min, absorption at 560 nm was measured with an Infinite F200 Pro spectrometer (Tecan). The protein concentrations were adjusted to an equal level with lysis buffer, if the variations of individual samples were larger than 5 %. The supernatant was then either combined with 4× sample buffer (4× SB) or subjected to IP.

### 4.3.2 Immunoprecipitation

For immunoprecipitation (IP), the supernatant was combined with 27 µL protein A sepharose (PAS) and the indicated antibodies (Table 4.4). The suspension was slowly rotated at 8 °C overnight. The following day, the suspension was centrifuged for 5 min and the supernatant was removed. The sepharose beads were washed twice with 500 µL lysis buffer and once with 500 µL Tris NaCl EDTA (TNE) buffer. The supernatant was removed completely and 25 µL 2× sample buffer (2× SB) were added. The IP was stored overnight at 4 °C or frozen at –20 °C.

**Table 4.2:** Stimulation factors and inhibitors.

Ligand	Company	Catalog Nr.	Lot	Stock conc.
<b>Epo<math>\alpha</math></b>	Janssen	06301286	GDS2C00	10 U/ $\mu$ L
<b>Epo<math>\beta</math></b>	Roche	10021439	PZ1207N409	390 U/ $\mu$ L; 132 $\mu$ M
<b>CERA</b>	Roche	10076977	PZ1202P016	340 $\mu$ M
<b>EGF</b>	Millipore	GF144	2591345	1 mg/mL
<b>HRG</b>	PeptoTech	AF-100-03	1208AFC316	100 $\mu$ g/mL
<b>HGF</b>	R&D	294-HG-025	GJ6015021 GJ5513121 GJ4512081	10 $\mu$ g/mL
<b>Erlotinib</b>	Cayman Chemical	10483		50 mM
<b>Afatinib</b>	LC Laboratories	A-8644	AFT-103	10 mg/mL
<b>Cycloheximid</b>	Sigma	C1988		100 mg/mL
<b>AKTi (AKT VIII)</b>	Millipore	124017	2803932	10 mM
<b>MEKi (U0126)</b>	Cell Signaling	#9903S	14	10 mM

**Table 4.3:** SDS gel composition for one gel.

	stacking gel	10 % Gel
H <sub>2</sub> O	7.15 mL	8.5 mL
1.5 M Tris pH 8.8		5 mL
1 M Tris pH 6.8	1.25 mL	
10 % SDS	0.1 mL	0.2 mL
40 % Acrylamide	1 mL	5 mL
2 % Bisacrylamide	0.5 mL	1.3 mL
Ammonium persulfate (0.1 g/mL)	100 $\mu$ L	200 $\mu$ L
Tetramethylethylenediamine	10 $\mu$ L	20 $\mu$ L

### 4.3.3 SDS-PAGE

The samples were boiled for 2 min at 95 °C and mixed thoroughly. Subsequently, the samples were centrifuged for 2 min at 20000  $\times g$ . The samples were loaded to a 10 % sodium dodecyl sulfate (SDS) polyacrylamide gel (see Table 4.3). For immunoblotting the Magic Marker XP (Invitrogen) was used and for Coomassie stained gels a Precision Plus Protein dual color standard (BioRad) was applied. Samples for quantitative dynamics were loaded on the gel in a randomized manner. <sup>[204]</sup> Electrophoresis was performed using 40 mA per gel for 2 to 4 h.

#### 4.3.4 Coomassie gels

Gels for mass spectrometric analysis or measurement of protein concentration were stained with SimplyBlue SafeStain (Invitrogen) according to the manufacturer's instructions. Coomassie gels pictures were acquired with a LumiImager F1 (Roche).

#### 4.3.5 Immunoblot analysis

For immunoblot analysis, the gels were transferred to a membrane using a Hoefer TE 77 semi-dry transfer unit (Amersham Biosciences). The transfer chamber and all transfer layers were soaked in Laemmli buffer (Table 6.1). Nitrocellulose membranes (0.2  $\mu\text{m}$  pore size, Protran, Whatman GmbH) were used for IP and polyvinylidene fluoride membranes (PVDF, 0.45  $\mu\text{m}$  pore size, Immobilon Millipore) were used for total cell lysates. PVDF membranes were activated with methanol for 1 min and rinsed with water for 1 min. Two soaked Whatman papers (10  $\times$  15 cm, GE Healthcare) per electrode were used as buffer reservoir. Proteins were transferred with 260 mA per gel for 1 h. Subsequently, the membranes were stained with Ponceau S solution (Sigma), washed with  $\text{dH}_2\text{O}$  and blocked with 5 % BSA in TBS-T for 1 h. The membranes were incubated at 4  $^\circ\text{C}$  overnight with primary antibodies indicated in Table 4.4. The following day, the membranes were rinsed three times with water and washed twice for 5 min with TBS-T. The membranes were then incubated with secondary antibodies indicated in Table 4.4 for 1 h in 1 % BSA in TBS-T. The membranes were rinsed three times with water, washed twice with TBS-T and once with TBS. Membranes with secondary antibodies coupled to horseradish peroxidase (hrp) were incubated with a fresh 1:1 mixture of ECL reagent A and B (Table 6.1) for 1 min and chemiluminescence was detected with an ImageQuant LAS4000 (Version 1.3, GE Healthcare). For quantification of the signal intensities the ImageQuant TL (version 7.0, GE Healthcare) was used. For reprobing, membranes were either treated with 30 %  $\text{H}_2\text{O}_2$  for 15 min at 37  $^\circ\text{C}$ , if the species of the antibodies were different, or incubated with stripping buffer at 55  $^\circ\text{C}$  for 15 min (Table 6.1). After washing, the membranes were blocked again with 5 % BSA for 1 h and incubated with a new primary antibody overnight.

#### 4.3.6 Mass spectrometry

For mass spectrometric analysis of MET and STAT5 phosphorylation,<sup>[267]</sup> samples were separated by SDS-PAGE and stained with Coomassie. Subsequently, the bands were excised at the height corresponding to the molecular weight of MET or STAT5 respectively. For analysis of global proteome, the whole lane was separated in three to five fractions. For analysis using the proteome ruler approach<sup>[199]</sup> a RIPA lysis buffer was utilized to obtain also nuclear fractions (Table 6.1). The

**Table 4.4:** List of utilized antibodies.

<b>Primary Antibody</b>	<b>Use</b>	<b>Source</b>	<b>Company</b>	<b>Catalog Nr.</b>
Anti-EGFR	IB(1:5 000)	Rabbit	Cell Signaling	4267
Anti-EGFR	IB(1:5 000)	Rabbit	Santa Cruz	sc-03
Anti-EGFR	IP(3 $\mu$ L)	Rabbit	Santa Cruz	sc-03
Anti-pEGFR (Y1068)	IB(1:5 000)	Rabbit	Cell Signaling	2234
Anti-HER2	IB(1:5 000)	Rabbit	Cell Signaling	2165
Anti-pHER2 (Y1248)	IB(1:5 000)	Rabbit	Cell Signaling	2247
Anti-HER3	IB(1:5 000)	Rabbit	Santa Cruz	sc-285
Anti-pHER3 (Y1222)	IB(1:5 000)	Rabbit	Cell Signaling	4784
Anti-HER4	IB(1:5 000)	Rabbit	Santa Cruz	sc-283
Anti-MET	IP(8 $\mu$ L)	Rabbit	Santa Cruz	sc-10
Anti-MET	IB(1:5 000)	Rabbit	Cell Signaling	4560
Anti-pMET (Y1234/1235)	IB(1:5 000)	Rabbit	Cell Signaling	3129
Anti-pTyr	IB(1:10 000)	Mouse	Upstate	4G10
Anti-AKT	IB(1:10 000)	Rabbit	Cell Signaling	9272
Anti-pAKT (S473)	IB(1:10 000)	Rabbit	Cell Signaling	9271
Anti-MEK	IB(1:10 000)	Rabbit	Cell Signaling	9122
Anti-pMEK (T202/Y204)	IB(1:10 000)	Rabbit	Cell Signaling	9121
Anti-ERK	IB(1:10 000)	Rabbit	Cell Signaling	9102
Anti-pERK (T202/Y204)	IB(1:10 000)	Rabbit	Cell Signaling	9101
Anti-S6	IB(1:10 000)	Mouse	Cell Signaling	2317
Anti-pS6 (S235/236)	IB(1:10 000)	Rabbit	Cell Signaling	2211
Anti-pS6 (S240/244)	IB(1:10 000)	Rabbit	Cell Signaling	2215
Anti-Actin	IB(1:10 000)	Mouse	Sigma Aldrich	A5441
Anti-Vinculin	IB(1:10 000)	Mouse	Santa Cruz	sc-55465
<b>Secondary Antibody</b>	<b>Use</b>	<b>Source</b>	<b>Company</b>	<b>Catalog Nr.</b>
Anti-rabbit-hrp	IB(1:10 000)	Goat	Dianova	111-035-144
Anti-mouse-hrp	IB(1:10 000)	Goat	Dianova	115-035-146
Anti-rabbit-800CW	IB(1:10 000)	Goat	LI-COR	926-32211
Anti-mouse-800CW	IB(1:10 000)	Goat	LI-COR	926-32210

gel fractions were cut in pieces of 1 mm edge length and destained with 900  $\mu$ L 30 % acetonitrile in 0.1 M  $\text{NH}_4\text{HCO}_3$  shaking for 15 min at 1 100 rpm in a low binding reaction tube (nerbe plus).

Samples of MET and total proteome were dehydrated with 50 % acetonitrile and 0.1 % trifluoroacetic acid in 0.1 M  $\text{NH}_4\text{HCO}_3$ , while STAT5 samples were dehydrated with acetonitrile. The dehydrated gel pieces were vacuum dried in a centrifugal evaporator. STAT5 samples were directly

subjected to tryptic digestion, while the remaining samples were reduced and alkylated prior to tryptic digestion.

The proteins were reduced by shaking in 400  $\mu\text{L}$  of a fresh 1.54 mg/mL dithiothreitol solution in 0.1 M  $\text{NH}_4\text{HCO}_3$  at 56 °C for 45 min. The supernatant was then removed and the sample was dried for 10 min in a centrifugal evaporator. Subsequently, the proteins were alkylated by 400  $\mu\text{L}$  of a fresh 10 mg/mL iodoacetamide solution in 0.1 M  $\text{NH}_4\text{HCO}_3$  in the dark. The supernatant was removed and the samples were washed with 900  $\mu\text{L}$  0.1 M  $\text{NH}_4\text{HCO}_3$  and dehydrated by 400  $\mu\text{L}$  acetonitrile. The gel pieces were dried in a centrifugal evaporator and 250 ng trypsin gold (Promega) were added dissolved in 5 % acetonitrile and 95 % 0.1 M  $\text{NH}_4\text{HCO}_3$ . The gel pieces were stepwise rehydrated with 5 % acetonitrile in 0.1 M  $\text{NH}_4\text{HCO}_3$  at 38 °C and proteins were digested for 14 h at 38 °C.

The following day, 1  $\mu\text{L}$  MET or STAT5A one-source standard<sup>[267]</sup> was added to MET and STAT5 samples. For all samples, the supernatant was transferred into a new vial and the peptides were eluted from the gel pieces by sequential addition of 200  $\mu\text{L}$  acetonitrile, 200  $\mu\text{L}$  5 % formic acid and 200  $\mu\text{L}$  acetonitrile. The volume of the combined extracts was reduced in a centrifugal evaporator, resolved in 40  $\mu\text{L}$  0.5 % acetonitrile and 0.5 % acetate and further purified by stage tips.

For stage tip purification,<sup>[268]</sup> a 200  $\mu\text{L}$  MaxRecovery tip (Oxygen) was filled with three 1 mm<sup>2</sup> slices of Empore Octadecyl C18 (47 mm) Extraction Disks. The stage tip was activated with 40  $\mu\text{L}$  methanol, washed with 75 % acetonitrile and equilibrated with 40  $\mu\text{L}$  0.5 % acetonitrile and 0.5 % acetate. For each step, the stage tip was centrifuged for 5 min at 2500  $\times g$  and the flow through was discarded. Then, the sample was loaded and washed with 40  $\mu\text{L}$  0.5 % acetonitrile and 0.5 % acetate. The tip was transferred to a low binding collection tube and the peptides were eluted in two steps. First, with 30  $\mu\text{L}$  of 50 % acetonitrile, 0.5 % acetate and 10 mM citrate and second with 40  $\mu\text{L}$  of 50 % acetonitrile, 0.5 % acetate. The flow through was concentrated, resolved in 10  $\mu\text{L}$  of 2 % acetonitrile and stored in an auto sampler vial at -20 °C.

The samples were measured by an EASY-nLC 1000 (Thermo Scientific) coupled to a Q Exactive Hybrid Quadrupole-Orbitrap Mass Spectrometer (Thermo Scientific). Peptides were separated by a 40 cm liquid chromatography column with 75  $\mu\text{m}$  inner diameter (New Objective) packed with ReproSil-Pur 120 C18-AQ 3  $\mu\text{m}$  particles (Dr. Maisch HPLC GmbH). For determination of the degree of MET or STAT5 phosphorylation, intensities of native and labelled MET peptide and phosphopeptide pairs were analyzed manually using Xcalibur 3.0.63 (Thermo). For whole proteome analysis, the MaxQuant software was used.

### 4.3.7 Purification of recombinant proteins

For generation of recombinant calibrators, the generated GST- and SBP-tagged protein vectors (V01,V02) were used for transformation of the *E. coli* strain BL21-Codon plus (DE3) as described above (subsection 4.1.3). A single colony was cultivated in 50 mL LB medium containing 100 µg/mL ampicillin and 2 µg/mL chloramphenicol overnight at 37 °C. The culture was diluted 1:10, cultivated for 90 min at 37 °C and then induced with 200 µM isopropyl β-D-1-thiogalactopyranoside (IPTG) for 4 h at 37 °C. The bacteria were centrifuged for 20 min at 4500 × *g* and 4 °C, washed with PBS, centrifuged again and frozen at −20 °C. The pellet was resuspended with 15 mL lysis buffer (10 mM Tris pH 8.0, 100 mM NaCl, 1 mM EDTA, 0.23 mg/mL lysozyme, 5 mM dithiothreitol). After 20 min on ice 2.25 mL 0.1 g/mL sodium lauroyl sarcosinate were added. The suspension was vortexed for 1 min and sonicated (Sonopuls, Bandelin) twice for 1 min on ice (amplitude: 80 %; pulse-on: 0.5 s, pulse-off: 0.2 s). The lysate was centrifuged for 15 min at 10 000 × *g*, 4 °C and the supernatant was supplemented with 2 % TritonX100 (Roche, Lot: 12918922) and 1 mL glutathione or streptavidin sepharose beads (GE Healthcare). The suspension was slowly rotated at 8 °C for 1 h. The beads were washed four times with 4 mL buffer containing 9 % PBS, 5 mM dithiothreitol and 1 % NP40-substitute (Roche) and once with 15 mL PBS containing 5 mM dithiothreitol. The recombinant protein was eluted five times with 500 µL buffer containing 0.75 mM Tris pH 8.0, 150 mM NaCl, 0.1 % SDS, 5 mM dithiothreitol and either 20 mM glutathione or 2 mM biotin. Each fraction was stored at 4 °C. As control, small samples were collected before induction, after sonication, after precipitation and after elution. These samples were loaded together with 20 µL of each fraction on an SDS-gel and the fractions with the highest yield were combined. The concentration was determined with a calibration curve of BSA standards (Thermo Scientific) on a Coomassie gel. Aliquots of the calibrator were stored at −80 °C.

### 4.3.8 Determination of molecules per cell

**Quantitative immunoblot** For calculation of molecules per cell, the cells were lysed as described above in a 6 cm plate (TPP) and a biological replicate was used for manual cell counting (Neubauer Improved) to obtain the number of cells (*#cells*) per lysate. A defined fraction  $F_c$  of the lysate was combined with increasing amounts of recombinant protein and separated by SDS-PAGE. The recombinant protein was used to calculate a standard curve with the slope  $a$ . The molecular mass

of the calibrator  $M_{cal}$  and the intensity of the endogenous protein  $INT$  was used to estimate the number of molecules per cell according to Equation 4.1.

$$\frac{molecules}{cell} = \frac{INT \cdot N_A}{F_c \cdot \#cells \cdot a \cdot M_{cal}} \quad (4.1)$$

The error was estimated using the variation of the slope  $\Delta a$  obtained from linear regression and the standard deviation of the measured replicates for  $\Delta INT$  and  $\Delta \#cells$  using propagation of uncertainty according to Equation 4.2.

$$\Delta f(\vec{x}) = \sqrt{\sum_i \left( \frac{\partial f(\vec{x})}{\partial x_i} \cdot \Delta x_i \right)^2} \quad (4.2)$$

**Proteome ruler** For determination of molecules per cell by normalization to signal intensities of histones, the measured ploidy levels were used (subsection 4.2.7) as input for the Perseus program.<sup>[199]</sup> The normalization analysis was performed in collaboration with M. Stepath (DKFZ Heidelberg) and A. Gorol (DKFZ Heidelberg).

### 4.3.9 Proliferation analysis

For analysis of cell proliferation, the resazurin-based CellTiter-Blue Cell Viability Assay (Promega) was utilized. For this purpose, 5 000 to 8 000 cells in 70  $\mu$ L were seeded in a 96-well plate (TPP) in growth factor depletion medium. For patient-derived tumor cell lines, 10 000 cells were seeded in 70  $\mu$ L culture medium. After 4 hours cells were treated with 0.25 pmol siRNA against EGFR (Dharmacon, ON-TARGETplus SMARTpool, L-003114-00-0005) or 0.75 pmol siRNA against MET (Dharmacon, ON-TARGETplus SMARTpool, L-003156-00-0005) or with the indicated doses MM-131. Control cells were treated either with non-targeting siRNA (Dharmacon, D-001810-10-50) or medium to correct for the volume of the supernatant. The following day the cells were treated with the indicated concentrations erlotinib (Cayman Chemicals, 10483) or DMSO for 30 min and subsequently stimulated with 50 ng/mL EGF and 50 ng/mL HGF. The cells were incubated 0 to 7 days after stimulation with 12  $\mu$ L of CellTiter-Blue and incubated for 1 hour at 37 °C. Subsequently, the fluorescence at 610 nm was measured after excitation at 560 nm with the infinite F200 pro Reader (TECAN). Significance was tested using two way ANOVA (SigmaPlot 13.0,  $\alpha=0.05$ ). For cell viability of cisplatin treated cells, 5 000 to 8 000 cells were seeded in 70  $\mu$ L growth medium and treated the following day with the indicated doses of cisplatin.

### 4.3.10 Microscopy

Labeling and microscopic measurements were performed by S. Hänselmann (University of Heidelberg).<sup>[262]</sup> For labeling, a silicon rhodamine *N*-hydroxysuccinimide ester (SiR NHS ester, Spirochrome) was coupled to O<sub>6</sub>-benzyl guanine amine (BG) in dimethylformamid with the addition of *N,N*-diisopropylethylamine for 3 h at 40 °C. The conjugate (SiR-BG) was purified via high-performance liquid chromatography (HPLC) and identified via mass spectrometry. Tetramethylrhodamine HALO-tag (HALO-TMR) ligand was purchased from Promega. H838-EGFR<sub>SNAP</sub>-MET<sub>HALO</sub> cells were seeded in 8-well glass-bottom chambers (Nunc Lab-Tek, Thermo Fisher Scientific) in DMEM without phenol red containing FCS, penicillin, streptomycin and L-glutamine. The cells were labeled overnight with 10 nM SiR-BG and 10 nM HALO-TMR. The following day, cells were washed four times over one hour with DMEM without phenol red containing BSA, penicillin, streptomycin and L-glutamine to remove unbound dye and deplete the cells from growth factors. For positive control, H838 cells expressing Lyn-GFP-HALO-SNAP (H838-GHS cells) were treated in the same way. For negative control H838-GHS cells were labeled overnight with 10 nM HALO-TMR ligand and 10 nM HALO-SiR (gift from K. Johnson (École Polytechnique Fédérale de Lausanne)).

The cells were monitored by an inverted microscope (Nikon TiE) using total internal reflection fluorescence (TIRF) illumination with a four channel diode/DPSS fiber coupled laser (iChrome MLE-LFA, Toptica) a quadruple dichroic mirror (R405/488/561/635, AHF Analysetechnik) and an additional quadruple notch filter (ZET405/488/561/640, AHF Analysetechnik). Both dyes were simultaneously excited with a 561 nm diode pumped solid state (DPSS) laser at 1.2 mW and a 640 nm diode laser at 1.5 mW, respectively. A 100× magnification oil objective lens (Nikon Apo TIRF 100× 1.49 Oil) was used in combination with a 1.5× magnification lens in the emission path. The fluorescence signal was detected by a 512 × 512 pixel electron multiplying CCD camera (Andor iXon+ 897 Ultra, Andor Technology) with a pixel size of 104 nm. The emission light was separated using a spectral image splitter (Optosplit III, Cairn Research) in combination with a 605/70 band-pass filter for the TMR signal (605/70 Et, AHF Analysetechnik) and a 685/50 bandpass filter for the SiR emission (685/50 Et, AHF Analysetechnik). Each channel was projected to a 256 × 512 pixel wide field of view. Movies of living H838-EGFR<sub>SNAP</sub>-MET<sub>HALO</sub> cells were recorded at 37 °C and H838-GHS cells were imaged at room temperature at a frame rate of 50 Hz and a total length of 500 to 1000 frames. The registration of both channels was calculated using multicolor beads (TetraSpec Microspheres, 0.2 μm, Thermo Fisher Scientific) before each experiment. For receptor depletion time-lapse measurement, H838-EGFR<sub>SNAP</sub>-MET<sub>HALO</sub> cells were stained, washed and

imaged as described above, however TMR and SiR were sequentially imaged full frame for three frames every minute over 30 min. For each condition 10-20 cells were imaged.

#### 4.3.11 Image analysis

To determine the movement of EGFR and MET in the two-channel TIRF live-cell data, a particle tracking method was used based on probabilistic data association with elliptical sampling (PDAE)<sup>[210]</sup> performed in collaboration with Y. Qiang (University of Heidelberg). Image registration was performed to align the two-channel image data. The Iterative Closest Point algorithm was used with fiducial markers to determine the registration matrix and this transformation matrix was applied to the imaging data.<sup>[269]</sup> Automatic particle detection was performed as well as correspondence finding. Based on the computed trajectories, co-localization analysis of the receptors was performed using a two-state hidden Markov model and the Euclidean distance between the receptors to determine dimer events and their durations. Two states  $\omega_t$  were considered, a non-dimer state and a dimer state, at each time point  $t$  of the time-resolved image data. The state  $\omega_t$  was computed given a sequence of observed distances  $d_{1:t}$  between two particles in the two channels. This task was performed within a Bayesian framework using the posterior probability via  $\omega_t^* = \arg \max P(\omega_t | d_{1:t})$ . The posterior probability was calculated recursively based on the prior probability  $P(\omega_t | d_{1:t-1})$  and the likelihood function  $P(d_t | \omega_t)$ .

For receptor depletion, the average intensity of an outlined cell was measured for each time point using imageJ (V1.48) and a two-parameter exponential regression was performed for each cell using the nls-function of R (V3.3.2).

## 4.4 Mathematical modeling

Mechanistic mathematical modeling was performed by H. Hass (University of Freiburg) using the open-source D2D framework<sup>[191]</sup> in MATLAB as described in detail elsewhere.<sup>[270]</sup> The final model consists of 24 ODEs that are integrated to obtain the time evolution of their respective model components  $x(t)$ . The initial values of 15 model components were determined from analytic steady state equations comprising kinetic parameters.<sup>[114]</sup> The inner derivatives of the likelihood needed in gradient-based parameter estimation were computed via supplied forward sensitivities.<sup>[271]</sup> The dynamical system and its sensitivities were integrated numerically by the CVODES integrator.<sup>[272]</sup> Optimization was conducted using the LSQNONLIN algorithm<sup>[273]</sup> implemented in MATLAB. To grant identification of the global optimum, a multi-start optimization strategy was performed for each model variant starting from 500 random parameter sets. To compare the model response

to the 3030 data points the scaled log-likelihood was calculated. Within the maximum likelihood framework, the optimized parameter set  $\hat{\theta}$ , consisting of 345 parameters of initial concentrations, kinetic and observational parameters, and measurement noise is estimated through minimization of  $\chi^2(\theta)$ . In the applied non-linear model, the profile likelihood approach was utilized to acquire parameter uncertainties.<sup>[113,274]</sup>

### 4.5 Patient data analysis

Patient survival data was assembled by M. Schneider (Thoraxklinik Heidelberg). Tissue samples were provided by the Lung Biobank Heidelberg, member of the accredited Tissue Bank of the National Center for Tumor Diseases (NCT) Heidelberg, the BioMaterialBank Heidelberg and the Biobank platform of the German Center for Lung Research (DZL). All patients provided written informed consent for the use of the tissue for research purpose and the study was approved by the local ethics committee of the Heidelberg University (No. 270/2001). Tumor and matched normal lung tissue samples were collected from NSCLC patients who underwent resection at the Thoraxklinik at University Hospital, Heidelberg. Tumor histology was classified according to the 3<sup>rd</sup> edition of the World Health Organization classification system.<sup>[275]</sup> Tissue samples were snap-frozen within 30 min after resection and stored at  $-80^{\circ}\text{C}$ . For nucleic acid isolation 10 - 15 tumor cryosections (10-15  $\mu\text{m}$  each) were prepared for each patient. Only samples with a viable tumor content of  $\geq 50\%$  were used for subsequent analyses.

RNA-isolation from tissue, cDNA synthesis and qPCR experiments were performed by M. Schneider as described elsewhere.<sup>[276]</sup> The data of qPCR analyses were statistically analyzed under REMARK criteria<sup>[277]</sup> with SPSS 24.0 for Windows (IBM, Ehningen, Germany). The endpoint of the study was overall survival. Univariate analysis of survival data was performed according to Kaplan and Meier<sup>[278]</sup> using R (Version 3.3.2, package: survival).

## Bibliography

- [1] Ferlay, J. *et al.* Estimates of worldwide burden of cancer in 2008: GLOBOCAN 2008. *Int. J. Cancer* **127**, 2893–2917 (2010). [PubMed:21351269].
- [2] Siegel, R. L., Miller, K. D. & Jemal, A. Cancer Statistics, 2017. *CA Cancer J Clin* **67**, 7–30 (2017). [PubMed:28055103].
- [3] da Cunha Santos, G., Shepherd, F. A. & Tsao, M. S. EGFR mutations and lung cancer. *Annu Rev Pathol* **6**, 49–69 (2011). [PubMed:20887192].
- [4] Bender, E. Epidemiology: The dominant malignancy. *Nature* **513**, 2–3 (2014). [PubMed:25208070].
- [5] Thomas, A., Liu, S. V., Subramaniam, D. S. & Giaccone, G. Refining the treatment of NSCLC according to histological and molecular subtypes. *Nat Rev Clin Oncol* **12**, 511–526 (2015). [PubMed:25963091].
- [6] Pao, W. & Girard, N. New driver mutations in non-small-cell lung cancer. *Lancet Oncol.* **12**, 175–180 (2011). [PubMed:21277552].
- [7] Meza, R., Meernik, C., Jeon, J. & Cote, M. L. Lung cancer incidence trends by gender, race and histology in the United States, 1973-2010. *PLoS ONE* **10**, e0121323 (2015). [PubMed:25822850].
- [8] Blakely, C. M. & Bivona, T. G. Resiliency of lung cancers to EGFR inhibitor treatment unveiled, offering opportunities to divide and conquer EGFR inhibitor resistance. *Cancer Discov* **2**, 872–875 (2012). [PubMed:23071030].
- [9] Chen, N. *et al.* Upregulation of PD-L1 by EGFR Activation Mediates the Immune Escape in EGFR-Driven NSCLC: Implication for Optional Immune Targeted Therapy for NSCLC Patients with EGFR Mutation. *J Thorac Oncol* **10**, 910–923 (2015). [PubMed:25658629].
- [10] Ohashi, K. *et al.* Lung cancers with acquired resistance to EGFR inhibitors occasionally harbor BRAF gene mutations but lack mutations in KRAS, NRAS, or MEK1. *Proc. Natl. Acad. Sci. U.S.A.* **109**, E2127–2133 (2012). [PubMed:22773810].
- [11] Vendetti, F. P. *et al.* Evaluation of azacitidine and entinostat as sensitization agents to cytotoxic chemotherapy in preclinical models of non-small cell lung cancer. *Oncotarget* **6**, 56–70 (2015). [PubMed:25474141].

- [12] Ladanyi, M. & Pao, W. Lung adenocarcinoma: guiding EGFR-targeted therapy and beyond. *Mod. Pathol.* **21 Suppl 2**, 16–22 (2008). [PubMed:18437168].
- [13] Yun, C. H. *et al.* The T790M mutation in EGFR kinase causes drug resistance by increasing the affinity for ATP. *Proc. Natl. Acad. Sci. U.S.A.* **105**, 2070–2075 (2008). [PubMed:18227510].
- [14] Yu, H. A. *et al.* Analysis of tumor specimens at the time of acquired resistance to EGFR-TKI therapy in 155 patients with EGFR-mutant lung cancers. *Clin. Cancer Res.* **19**, 2240–2247 (2013). [PubMed:23470965].
- [15] Engel, J., Lategahn, J. & Rauh, D. Hope and Disappointment: Covalent Inhibitors to Overcome Drug Resistance in Non-Small Cell Lung Cancer. *ACS Med Chem Lett* **7**, 2–5 (2016). [PubMed:26819655].
- [16] Shi, Y. *et al.* Icotinib versus gefitinib in previously treated advanced non-small-cell lung cancer (ICOGEN): a randomised, double-blind phase 3 non-inferiority trial. *Lancet Oncol.* **14**, 953–961 (2013). [PubMed:23948351].
- [17] Jia, Y. *et al.* Overcoming EGFR(T790M) and EGFR(C797S) resistance with mutant-selective allosteric inhibitors. *Nature* **534**, 129–132 (2016). [PubMed:27251290].
- [18] Martinelli, E., De Palma, R., Orditura, M., De Vita, F. & Ciardiello, F. Anti-epidermal growth factor receptor monoclonal antibodies in cancer therapy. *Clin. Exp. Immunol.* **158**, 1–9 (2009). [PubMed:19737224].
- [19] Pirker, R. *et al.* Cetuximab plus chemotherapy in patients with advanced non-small-cell lung cancer (FLEX): an open-label randomised phase III trial. *Lancet* **373**, 1525–1531 (2009). [PubMed:19410716].
- [20] Silva, A. P., Coelho, P. V., Anazetti, M. & Simioni, P. U. Targeted therapies for the treatment of non-small-cell lung cancer: Monoclonal antibodies and biological inhibitors. *Hum Vaccin Immunother* **13**, 843–853 (2017). [PubMed:27831000].
- [21] Janjigian, Y. Y. *et al.* Dual inhibition of EGFR with afatinib and cetuximab in kinase inhibitor-resistant EGFR-mutant lung cancer with and without T790M mutations. *Cancer Discov* **4**, 1036–1045 (2014). [PubMed:25074459].
- [22] Krumbhaar, E. B. Role of the blood and the bone marrow in certain forms of gas poisoning: I. peripheral blood changes and their significance. *Journal of the American Medical Association* **72**, 39–41 (1919). [DOI:10.1001/jama.1919.26110010018009f].
- [23] Rosenberg, B. Platinum coordination complexes in cancer chemotherapy. *Naturwissenschaften* **60**, 399–406 (1973). [PubMed:4203933].
- [24] Basu, A. & Krishnamurthy, S. Cellular responses to Cisplatin-induced DNA damage. *J Nucleic Acids* **2010** (2010). [PubMed:20811617].

- 
- [25] Lau, J. K. & Deubel, D. V. Loss of amine from platinum(II) complexes: implications for cisplatin inactivation, storage, and resistance. *Chemistry* **11**, 2849–2855 (2005).
- [26] Jansen, B. A., Brouwer, J. & Reedijk, J. Glutathione induces cellular resistance against cationic dinuclear platinum anticancer drugs. *J. Inorg. Biochem.* **89**, 197–202 (2002). [PubMed:12062123].
- [27] Bellon, S. F., Coleman, J. H. & Lippard, S. J. DNA unwinding produced by site-specific intrastrand cross-links of the antitumor drug cis-diamminedichloroplatinum(II). *Biochemistry* **30**, 8026–8035 (1991). [PubMed:1868076].
- [28] Frankenberg-Schwager, M. *et al.* Cisplatin-mediated DNA double-strand breaks in replicating but not in quiescent cells of the yeast *Saccharomyces cerevisiae*. *Toxicology* **212**, 175–184 (2005). [PubMed:15950355].
- [29] McKay, B. C., Becerril, C. & Ljungman, M. P53 plays a protective role against UV- and cisplatin-induced apoptosis in transcription-coupled repair proficient fibroblasts. *Oncogene* **20**, 6805–6808 (2001). [PubMed:11709715].
- [30] Galluzzi, L. *et al.* Systems biology of cisplatin resistance: past, present and future. *Cell Death Dis* **5**, e1257 (2014). [PubMed:24874729].
- [31] Pirker, R., Wiesenberger, K., Pohl, G. & Minar, W. Anemia in lung cancer: clinical impact and management. *Clin Lung Cancer* **5**, 90–97 (2003). [PubMed:14596691].
- [32] Spivak, J. L. The anaemia of cancer: death by a thousand cuts. *Nat. Rev. Cancer* **5**, 543–555 (2005). [PubMed:15965494].
- [33] Hyman, G. A. Anemia in malignant neoplastic disease. *J Chronic Dis* **16**, 645–666 (1963). [PubMed:14047256].
- [34] Del Mastro, L., Gennari, A. & Donati, S. Chemotherapy of non-small-cell lung cancer: role of erythropoietin in the management of anemia. *Ann. Oncol.* **10**, S91–94 (1999).
- [35] Klingmuller, U. *et al.* Identification of a novel pathway important for proliferation and differentiation of primary erythroid progenitors. *Proc. Natl. Acad. Sci. U.S.A.* **94**, 3016–3021 (1997). [PubMed:9096338].
- [36] Tonia, T. *et al.* Erythropoietin or darbepoetin for patients with cancer. *Cochrane Database Syst Rev* **12**, CD003407 (2012). [PubMed:23235597].
- [37] Rodgers, G. M. *et al.* Cancer- and chemotherapy-induced anemia. *J Natl Compr Canc Netw* **10**, 628–653 (2012). [PubMed:22570293].
- [38] Acs, G. *et al.* Erythropoietin and erythropoietin receptor expression in human cancer. *Cancer Res.* **61**, 3561–3565 (2001). [PubMed:11325818].
- [39] Elliott, S. *et al.* Anti-Epo receptor antibodies do not predict Epo receptor expression. *Blood* **107**, 1892–1895 (2006). [PubMed:16249375].

- [40] Szenajch, J., Wcislo, G., Jeong, J. Y., Szczylik, C. & Feldman, L. The role of erythropoietin and its receptor in growth, survival and therapeutic response of human tumor cells From clinic to bench - a critical review. *Biochim. Biophys. Acta* **1806**, 82–95 (2010). [PubMed:20406667].
- [41] Elliott, S. & Sinclair, A. M. The effect of erythropoietin on normal and neoplastic cells. *Biologics* **6**, 163–189 (2012). [PubMed:22848149].
- [42] McKinney, M. & Arcasoy, M. O. Erythropoietin for oncology supportive care. *Exp. Cell Res.* **317**, 1246–1254 (2011). [PubMed:21396935].
- [43] Boehm, M. E. *et al.* Identification of isoform-specific dynamics in phosphorylation-dependent STAT5 dimerization by quantitative mass spectrometry and mathematical modeling. *J. Proteome Res.* **13**, 5685–5694 (2014). [PubMed:25333863].
- [44] Becker, V. *et al.* Covering a broad dynamic range: information processing at the erythropoietin receptor. *Science* **328**, 1404–1408 (2010). [PubMed:20488988].
- [45] Hilton, D. J., Watowich, S. S., Murray, P. J. & Lodish, H. F. Increased cell surface expression and enhanced folding in the endoplasmic reticulum of a mutant erythropoietin receptor. *Proc. Natl. Acad. Sci. U.S.A.* **92**, 190–194 (1995). [PubMed:7816815].
- [46] Sinclair, A. M. *et al.* Expression and function of erythropoietin receptors in tumors: implications for the use of erythropoiesis-stimulating agents in cancer patients. *Cancer* **110**, 477–488 (2007). [PubMed:17582631].
- [47] Lai, A. Z., Abella, J. V. & Park, M. Crosstalk in Met receptor oncogenesis. *Trends Cell Biol.* **19**, 542–551 (2009). [PubMed:19758803].
- [48] Baselga, J. & Swain, S. M. Novel anticancer targets: revisiting ERBB2 and discovering ERBB3. *Nat. Rev. Cancer* **9**, 463–475 (2009). [PubMed:19536107].
- [49] Olayioye, M. A., Neve, R. M., Lane, H. A. & Hynes, N. E. The ErbB signaling network: receptor heterodimerization in development and cancer. *EMBO J.* **19**, 3159–3167 (2000). [PubMed:10880430].
- [50] Zhang, X., Gureasko, J., Shen, K., Cole, P. A. & Kuriyan, J. An allosteric mechanism for activation of the kinase domain of epidermal growth factor receptor. *Cell* **125**, 1137–1149 (2006). [PubMed:16777603].
- [51] Shi, F., Telesco, S. E., Liu, Y., Radhakrishnan, R. & Lemmon, M. A. ErbB3/HER3 intracellular domain is competent to bind ATP and catalyze autophosphorylation. *Proc. Natl. Acad. Sci. U.S.A.* **107**, 7692–7697 (2010). [PubMed:20351256].
- [52] Roskoski, R. The ErbB/HER family of protein-tyrosine kinases and cancer. *Pharmacol. Res.* **79**, 34–74 (2014). [PubMed:24269963].
- [53] Song, H. *et al.* Transphosphorylation of EGFR at Y845 plays an important role in its autophosphorylation and kinase activity. *Oncol. Rep.* **31**, 2393–2398 (2014). [PubMed:24677053].

- [54] Tao, R. H. & Maruyama, I. N. All EGF(ErbB) receptors have preformed homo- and heterodimeric structures in living cells. *J. Cell. Sci.* **121**, 3207–3217 (2008). [PubMed:18782861].
- [55] Gadella, T. W. & Jovin, T. M. Oligomerization of epidermal growth factor receptors on A431 cells studied by time-resolved fluorescence imaging microscopy. A stereochemical model for tyrosine kinase receptor activation. *J. Cell Biol.* **129**, 1543–1558 (1995). [PubMed:7790353].
- [56] Herbst, R. S. Review of epidermal growth factor receptor biology. *Int. J. Radiat. Oncol. Biol. Phys.* **59**, 21–26 (2004). [PubMed:15142631].
- [57] Linggi, B. & Carpenter, G. ErbB receptors: new insights on mechanisms and biology. *Trends Cell Biol.* **16**, 649–656 (2006). [PubMed:17085050].
- [58] Macdonald-Obermann, J. L. & Pike, L. J. Different epidermal growth factor (EGF) receptor ligands show distinct kinetics and biased or partial agonism for homodimer and heterodimer formation. *J. Biol. Chem.* **289**, 26178–26188 (2014). [PubMed:25086039].
- [59] Zeng, F. & Harris, R. C. Epidermal growth factor, from gene organization to bedside. *Semin. Cell Dev. Biol.* **28**, 2–11 (2014). [PubMed:24513230].
- [60] Furcht, C. M., Buonato, J. M. & Lazzara, M. J. EGFR-activated Src family kinases maintain GAB1-SHP2 complexes distal from EGFR. *Sci Signal* **8**, ra46 (2015). [PubMed:25969544].
- [61] Gomperts, B., Kramer, I. M. & Tatham, P. E. R. *Signal Transduction (2nd revised edition)* (Academic Press, 2009). ISBN-13: 978-0123694416.
- [62] Aronheim, A. *et al.* Membrane targeting of the nucleotide exchange factor Sos is sufficient for activating the Ras signaling pathway. *Cell* **78**, 949–961 (1994). [PubMed:7923364].
- [63] Moodie, S. A., Willumsen, B. M., Weber, M. J. & Wolfman, A. Complexes of Ras.GTP with Raf-1 and mitogen-activated protein kinase kinase. *Science* **260**, 1658–1661 (1993). [PubMed:8503013].
- [64] Hauge, C. & Frodin, M. RSK and MSK in MAP kinase signalling. *J. Cell. Sci.* **119**, 3021–3023 (2006). [PubMed:16868029].
- [65] Niault, T. S. & Baccarini, M. Targets of Raf in tumorigenesis. *Carcinogenesis* **31**, 1165–1174 (2010). [PubMed:20047953].
- [66] Mendoza, M. C., Er, E. E. & Blenis, J. The Ras-ERK and PI3K-mTOR pathways: cross-talk and compensation. *Trends Biochem. Sci.* **36**, 320–328 (2011). [PubMed:21531565].
- [67] Li, X. *et al.* PI3K/Akt/mTOR signaling pathway and targeted therapy for glioblastoma. *Oncotarget* (2016). [PubMed:26967052].
- [68] Hoeffler, C. A. & Klann, E. mTOR signaling: at the crossroads of plasticity, memory and disease. *Trends Neurosci.* **33**, 67–75 (2010). [PubMed:19963289].
- [69] Hynes, N. E. & Lane, H. A. ERBB receptors and cancer: the complexity of targeted inhibitors. *Nat. Rev. Cancer* **5**, 341–354 (2005). [PubMed:15864276].

- [70] Citri, A. & Yarden, Y. EGF-ERBB signalling: towards the systems level. *Nat. Rev. Mol. Cell Biol.* **7**, 505–516 (2006). [PubMed:16829981].
- [71] Klinger, B. *et al.* Network quantification of EGFR signaling unveils potential for targeted combination therapy. *Mol. Syst. Biol.* **9**, 673 (2013). [PubMed:23752269].
- [72] Shtiegman, K. *et al.* Defective ubiquitinylation of EGFR mutants of lung cancer confers prolonged signaling. *Oncogene* **26**, 6968–6978 (2007). [PubMed:17486068].
- [73] Chung, B. M. *et al.* Nexus of signaling and endocytosis in oncogenesis driven by non-small cell lung cancer-associated epidermal growth factor receptor mutants. *World J Clin Oncol* **5**, 806–823 (2014). [PubMed:25493220].
- [74] Wu, P., Wee, P., Jiang, J., Chen, X. & Wang, Z. Differential regulation of transcription factors by location-specific EGF receptor signaling via a spatio-temporal interplay of ERK activation. *PLoS ONE* **7**, e41354 (2012). [PubMed:22984397].
- [75] Wang, Y. N., Yamaguchi, H., Hsu, J. M. & Hung, M. C. Nuclear trafficking of the epidermal growth factor receptor family membrane proteins. *Oncogene* **29**, 3997–4006 (2010). [PubMed:20473332].
- [76] Demory, M. L. *et al.* Epidermal growth factor receptor translocation to the mitochondria: regulation and effect. *J. Biol. Chem.* **284**, 36592–36604 (2009). [PubMed:19840943].
- [77] Tomas, A., Futter, C. E. & Eden, E. R. EGF receptor trafficking: consequences for signaling and cancer. *Trends Cell Biol.* **24**, 26–34 (2014). [PubMed:24295852].
- [78] Greig, M. J. *et al.* Effects of Activating Mutations on EGFR Cellular Protein Turnover and Amino Acid Recycling Determined Using SILAC Mass Spectrometry. *Int J Cell Biol* **2015**, 798936 (2015). [PubMed:26689952].
- [79] Peschard, P. & Park, M. Escape from Cbl-mediated downregulation: a recurrent theme for oncogenic deregulation of receptor tyrosine kinases. *Cancer Cell* **3**, 519–523 (2003). [PubMed:12842080].
- [80] Normanno, N., Bianco, C., De Luca, A., Maiello, M. R. & Salomon, D. S. Target-based agents against ErbB receptors and their ligands: a novel approach to cancer treatment. *Endocr. Relat. Cancer* **10**, 1–21 (2003). [PubMed:12653668].
- [81] Organ, S. L. & Tsao, M. S. An overview of the c-MET signaling pathway. *Ther Adv Med Oncol* **3**, S7–S19 (2011). [PubMed:22128289].
- [82] Gherardi, E., Birchmeier, W., Birchmeier, C. & Vande Woude, G. Targeting MET in cancer: rationale and progress. *Nat. Rev. Cancer* **12**, 89–103 (2012). [PubMed:22270953].
- [83] To, C. T. & Tsao, M. S. The roles of hepatocyte growth factor/scatter factor and met receptor in human cancers (Review). *Oncol. Rep.* **5**, 1013–1024 (1998). [PubMed:9683803].

- [84] Mizuno, S. & Nakamura, T. HGF-MET cascade, a key target for inhibiting cancer metastasis: the impact of NK4 discovery on cancer biology and therapeutics. *Int J Mol Sci* **14**, 888–919 (2013). [PubMed:23296269].
- [85] Nakamura, T., Sakai, K., Nakamura, T. & Matsumoto, K. Hepatocyte growth factor twenty years on: Much more than a growth factor. *J. Gastroenterol. Hepatol.* **26 Suppl 1**, 188–202 (2011). [PubMed:21199531].
- [86] Miller, M. A. *et al.* ADAM-10 and -17 regulate endometriotic cell migration via concerted ligand and receptor shedding feedback on kinase signaling. *Proc. Natl. Acad. Sci. U.S.A.* **110**, E2074–2083 (2013). [PubMed:23674691].
- [87] Shattuck, D. L. *et al.* LRIG1 is a novel negative regulator of the Met receptor and opposes Met and Her2 synergy. *Mol. Cell. Biol.* **27**, 1934–1946 (2007). [PubMed:17178829].
- [88] Wagner, J. P. *et al.* Receptor tyrosine kinases fall into distinct classes based on their inferred signaling networks. *Sci Signal* **6**, ra58 (2013). [PubMed:23861540].
- [89] Nakagawa, T. *et al.* Combined therapy with mutant-selective EGFR inhibitor and Met kinase inhibitor for overcoming erlotinib resistance in EGFR-mutant lung cancer. *Mol. Cancer Ther.* **11**, 2149–2157 (2012). [PubMed:22844075].
- [90] Stommel, J. M. *et al.* Coactivation of receptor tyrosine kinases affects the response of tumor cells to targeted therapies. *Science* **318**, 287–290 (2007). [PubMed:17872411].
- [91] Puri, N. & Salgia, R. Synergism of EGFR and c-Met pathways, cross-talk and inhibition, in non-small cell lung cancer. *J. Carcinog* **7**, 9 (2008). [PubMed:19240370].
- [92] Accornero, P., Miretti, S., Starvaggi Cucuzza, L., Martignani, E. & Baratta, M. Epidermal growth factor and hepatocyte growth factor cooperate to enhance cell proliferation, scatter, and invasion in murine mammary epithelial cells. *J. Mol. Endocrinol.* **44**, 115–125 (2010). [PubMed:19850646].
- [93] Tanizaki, J., Okamoto, I., Sakai, K. & Nakagawa, K. Differential roles of trans-phosphorylated EGFR, HER2, HER3, and RET as heterodimerisation partners of MET in lung cancer with MET amplification. *Br. J. Cancer* **105**, 807–813 (2011). [PubMed:21847121].
- [94] Jo, M. *et al.* Cross-talk between epidermal growth factor receptor and c-Met signal pathways in transformed cells. *J. Biol. Chem.* **275**, 8806–8811 (2000). [PubMed:10722725].
- [95] Engelman, J. A. *et al.* MET amplification leads to gefitinib resistance in lung cancer by activating ERBB3 signaling. *Science* **316**, 1039–1043 (2007). [PubMed:17463250].
- [96] Mueller, K. L., Hunter, L. A., Ethier, S. P. & Boerner, J. L. Met and c-Src cooperate to compensate for loss of epidermal growth factor receptor kinase activity in breast cancer cells. *Cancer Res.* **68**, 3314–3322 (2008). [PubMed:18451158].

- [97] Holgren, C. *et al.* Sprouty-2 controls c-Met expression and metastatic potential of colon cancer cells: sprouty/c-Met upregulation in human colonic adenocarcinomas. *Oncogene* **29**, 5241–5253 (2010). [PubMed:20661223].
- [98] Xu, L. *et al.* Epidermal growth factor receptor regulates MET levels and invasiveness through hypoxia-inducible factor-1 $\alpha$  in non-small cell lung cancer cells. *Oncogene* **29**, 2616–2627 (2010). [PubMed:20154724].
- [99] Dulak, A. M., Gubish, C. T., Stabile, L. P., Henry, C. & Siegfried, J. M. HGF-independent potentiation of EGFR action by c-Met. *Oncogene* **30**, 3625–3635 (2011). [PubMed:21423210].
- [100] Pai, R., Nakamura, T., Moon, W. S. & Tarnawski, A. S. Prostaglandins promote colon cancer cell invasion; signaling by cross-talk between two distinct growth factor receptors. *FASEB J.* **17**, 1640–1647 (2003). [PubMed:12958170].
- [101] Fischer, O. M., Giordano, S., Comoglio, P. M. & Ullrich, A. Reactive oxygen species mediate Met receptor transactivation by G protein-coupled receptors and the epidermal growth factor receptor in human carcinoma cells. *J. Biol. Chem.* **279**, 28970–28978 (2004). [PubMed:15123705].
- [102] Breindel, J. L. *et al.* EGF receptor activates MET through MAPK to enhance non-small cell lung carcinoma invasion and brain metastasis. *Cancer Res.* **73**, 5053–5065 (2013). [PubMed:23794705].
- [103] Klipp, E. *et al.* *Systems Biology: A Textbook* (John Wiley & Sons, 2009).
- [104] Marks, F., Klinmüller, U. & Mueller-Decker, K. *Cellular Signal Processing* (Taylor and Francis Ltd., 2008). ISBN-13: 978-0815342151.
- [105] Kauffman, S. A. Metabolic stability and epigenesis in randomly constructed genetic nets. *J. Theor. Biol.* **22**, 437–467 (1969). [PubMed:5803332].
- [106] Machado, D. *et al.* Modeling formalisms in Systems Biology. *AMB Express* **1**, 45 (2011). [PubMed:22141422].
- [107] Friedman, N. Inferring cellular networks using probabilistic graphical models. *Science* **303**, 799–805 (2004). [PubMed:14764868].
- [108] Szallasi, Z., Stelling, J. & Periwal, V. (eds.) *System Modeling in Cellular Biology: From Concepts to Nuts and Bolts* (The MIT Press, 2006), 1 edn. [DOI:10.7551/mitpress/9780262195485.001.0001].
- [109] Wilkinson, D. J. Stochastic modelling for quantitative description of heterogeneous biological systems. *Nat. Rev. Genet.* **10**, 122–133 (2009). [PubMed:19139763].
- [110] Kitano, H. Systems biology: a brief overview. *Science* **295**, 1662–1664 (2002). [PubMed:11872829].

- 
- [111] Barbolosi, D., Ciccolini, J., Lacarelle, B., Barlesi, F. & Andre, N. Computational oncology–mathematical modelling of drug regimens for precision medicine. *Nat Rev Clin Oncol* **13**, 242–254 (2016). [PubMed:26598946].
- [112] Raue, A. *et al.* Lessons learned from quantitative dynamical modeling in systems biology. *PLoS ONE* **8**, e74335 (2013). [PubMed:24098642].
- [113] Raue, A. *et al.* Structural and practical identifiability analysis of partially observed dynamical models by exploiting the profile likelihood. *Bioinformatics* **25**, 1923–1929 (2009). [PubMed:19505944].
- [114] Rosenblatt, M., Timmer, J. & Kaschek, D. Customized Steady-State Constraints for Parameter Estimation in Non-Linear Ordinary Differential Equation Models. *Front Cell Dev Biol* **4**, 41 (2016). [PubMed:27243005].
- [115] Swameye, I., Muller, T. G., Timmer, J., Sandra, O. & Klingmuller, U. Identification of nucleocytoplasmic cycling as a remote sensor in cellular signaling by databased modeling. *Proc. Natl. Acad. Sci. U.S.A.* **100**, 1028–1033 (2003). [PubMed:12552139].
- [116] Bachmann, J. *et al.* Division of labor by dual feedback regulators controls JAK2/STAT5 signaling over broad ligand range. *Mol. Syst. Biol.* **7**, 516 (2011). [PubMed:21772264].
- [117] Kholodenko, B. N., Demin, O. V., Moehren, G. & Hoek, J. B. Quantification of short term signaling by the epidermal growth factor receptor. *J. Biol. Chem.* **274**, 30169–30181 (1999). [PubMed:10514507].
- [118] Oda, K., Matsuoka, Y., Funahashi, A. & Kitano, H. A comprehensive pathway map of epidermal growth factor receptor signaling. *Mol. Syst. Biol.* **1**, 2005.0010 (2005). [PubMed:16729045].
- [119] Kleiman, L. B., Maiwald, T., Conzelmann, H., Lauffenburger, D. A. & Sorger, P. K. Rapid phospho-turnover by receptor tyrosine kinases impacts downstream signaling and drug binding. *Mol. Cell* **43**, 723–737 (2011). [PubMed:21884975].
- [120] D’Alessandro, L. A. *et al.* Disentangling the Complexity of HGF Signaling by Combining Qualitative and Quantitative Modeling. *PLoS Comput. Biol.* **11**, e1004192 (2015). [PubMed:25905717].
- [121] Singh, A., Nascimento, J. M., Kowar, S., Busch, H. & Boerries, M. Boolean approach to signalling pathway modelling in HGF-induced keratinocyte migration. *Bioinformatics* **28**, i495–i501 (2012). [PubMed:22962472].
- [122] Tafe, L. J. Molecular mechanisms of therapy resistance in solid tumors: chasing "moving" targets. *Virchows Arch.* (2017). [PubMed:28280929].
- [123] Bhang, H. E. *et al.* Studying clonal dynamics in response to cancer therapy using high-complexity barcoding. *Nat. Med.* **21**, 440–448 (2015). [PubMed:25849130].

- [124] Cheng, X. & Chen, H. Tumor heterogeneity and resistance to EGFR-targeted therapy in advanced nonsmall cell lung cancer: challenges and perspectives. *Onco Targets Ther* **7**, 1689–1704 (2014). [PubMed:25285017].
- [125] Hata, A. N. *et al.* Tumor cells can follow distinct evolutionary paths to become resistant to epidermal growth factor receptor inhibition. *Nat. Med.* **22**, 262–269 (2016). [PubMed:26828195].
- [126] Kathawala, R. J., Gupta, P., Ashby, C. R. & Chen, Z. S. The modulation of ABC transporter-mediated multidrug resistance in cancer: a review of the past decade. *Drug Resist. Updat.* **18**, 1–17 (2015). [PubMed:25554624].
- [127] Stewart, E. L., Tan, S. Z., Liu, G. & Tsao, M. S. Known and putative mechanisms of resistance to EGFR targeted therapies in NSCLC patients with EGFR mutations—a review. *Transl Lung Cancer Res* **4**, 67–81 (2015). [PubMed:25806347].
- [128] Lawrence, M. S. *et al.* Mutational heterogeneity in cancer and the search for new cancer-associated genes. *Nature* **499**, 214–218 (2013). [PubMed:23770567].
- [129] Jeong, W. J., Cha, P. H. & Choi, K. Y. Strategies to overcome resistance to epidermal growth factor receptor monoclonal antibody therapy in metastatic colorectal cancer. *World J. Gastroenterol.* **20**, 9862–9871 (2014). [PubMed:25110417].
- [130] Paul, I. & Jones, J. M. Apoptosis block as a barrier to effective therapy in non small cell lung cancer. *World J Clin Oncol* **5**, 588–594 (2014). [PubMed:25302163].
- [131] Cui, J. *et al.* EGFR inhibitors and autophagy in cancer treatment. *Tumour Biol.* **35**, 11701–11709 (2014). [PubMed:25293518].
- [132] Schildhaus, H. U. *et al.* MET amplification status in therapy-naive adeno- and squamous cell carcinomas of the lung. *Clin. Cancer Res.* **21**, 907–915 (2015). [PubMed:25492085].
- [133] Turke, A. B. *et al.* Preexistence and clonal selection of MET amplification in EGFR mutant NSCLC. *Cancer Cell* **17**, 77–88 (2010). [PubMed:20129249].
- [134] Guo, A. *et al.* Signaling networks assembled by oncogenic EGFR and c-Met. *Proc. Natl. Acad. Sci. U.S.A.* **105**, 692–697 (2008). [PubMed:18180459].
- [135] Spigel, D. R. *et al.* Randomized phase II trial of Onartuzumab in combination with erlotinib in patients with advanced non-small-cell lung cancer. *J. Clin. Oncol.* **31**, 4105–4114 (2013). [PubMed:24101053].
- [136] Spigel, D. R. *et al.* Results From the Phase III Randomized Trial of Onartuzumab Plus Erlotinib Versus Erlotinib in Previously Treated Stage IIIB or IV Non-Small-Cell Lung Cancer: METLung. *J. Clin. Oncol.* **35**, 412–420 (2017). [PubMed:27937096].
- [137] Ogino, A. *et al.* Emergence of epidermal growth factor receptor T790M mutation during chronic exposure to gefitinib in a non small cell lung cancer cell line. *Cancer Res.* **67**, 7807–7814 (2007). [PubMed:17699786].

- 
- [138] Iida, M. *et al.* Overcoming acquired resistance to cetuximab by dual targeting HER family receptors with antibody-based therapy. *Mol. Cancer* **13**, 242 (2014). [PubMed:25344208].
- [139] Wheeler, D. L. *et al.* Mechanisms of acquired resistance to cetuximab: role of HER (ErbB) family members. *Oncogene* **27**, 3944–3956 (2008). [PubMed:18297114].
- [140] Yallowitz, A. R. *et al.* Mutant p53 Amplifies Epidermal Growth Factor Receptor Family Signaling to Promote Mammary Tumorigenesis. *Mol. Cancer Res.* **13**, 743–754 (2015). [PubMed:25573952].
- [141] Song, X. *et al.* ERBB3-independent activation of the PI3K pathway in EGFR-mutant lung adenocarcinomas. *Cancer Res.* **75**, 1035–1045 (2015). [PubMed:25596284].
- [142] Pupo, E. *et al.* Rebound effects caused by withdrawal of MET kinase inhibitor are quenched by a MET therapeutic antibody. *Cancer Res.* (2016). [PubMed:27364553].
- [143] Wickramasinghe, D. & Kong-Beltran, M. Met activation and receptor dimerization in cancer: a role for the Sema domain. *Cell Cycle* **4**, 683–685 (2005). [PubMed:15846105].
- [144] Ge, X. *et al.* Induced IGF-1R activation contributes to gefitinib resistance following combined treatment with paclitaxel, cisplatin and gefitinib in A549 lung cancer cells. *Oncol. Rep.* **32**, 1401–1408 (2014). [PubMed:25198583].
- [145] Yano, S. *et al.* Hepatocyte growth factor induces gefitinib resistance of lung adenocarcinoma with epidermal growth factor receptor-activating mutations. *Cancer Res.* **68**, 9479–9487 (2008). [PubMed:19010923].
- [146] Faber, A. C. *et al.* BIM expression in treatment-naive cancers predicts responsiveness to kinase inhibitors. *Cancer Discov* **1**, 352–365 (2011). [PubMed:22145099].
- [147] Liu, Y. *et al.* Silencing of Receptor Tyrosine Kinase ROR1 Inhibits Tumor-Cell Proliferation via PI3K/AKT/mTOR Signaling Pathway in Lung Adenocarcinoma. *PLoS ONE* **10**, e0127092 (2015). [PubMed:25978653].
- [148] Awasthi, S., Ezelle, H., Hassel, B. A. & Hamburger, A. W. The ErbB3-binding protein EBP1 modulates lapatinib sensitivity in prostate cancer cells. *Mol. Cell. Biochem.* **405**, 177–186 (2015). [PubMed:25876877].
- [149] Seshacharyulu, P. *et al.* Targeting EGF-receptor(s) - STAT1 axis attenuates tumor growth and metastasis through downregulation of MUC4 mucin in human pancreatic cancer. *Oncotarget* **6**, 5164–5181 (2015). [PubMed:25686822].
- [150] Jaiswal, B. S. *et al.* Oncogenic ERBB3 mutations in human cancers. *Cancer Cell* **23**, 603–617 (2013). [PubMed:23680147].
- [151] Kiuchi, T. *et al.* The ErbB4 CYT2 variant protects EGFR from ligand-induced degradation to enhance cancer cell motility. *Sci Signal* **7**, ra78 (2014). [PubMed:25140053].

- [152] Fichter, C. D. *et al.* ErbB targeting inhibitors repress cell migration of esophageal squamous cell carcinoma and adenocarcinoma cells by distinct signaling pathways. *J. Mol. Med.* (2014). [PubMed:25091467].
- [153] Engelman, J. A. *et al.* ErbB-3 mediates phosphoinositide 3-kinase activity in gefitinib-sensitive non-small cell lung cancer cell lines. *Proc. Natl. Acad. Sci. U.S.A.* **102**, 3788–3793 (2005). [PubMed:15731348].
- [154] Moores, S. L. *et al.* A Novel Bispecific Antibody Targeting EGFR and cMet Is Effective against EGFR Inhibitor-Resistant Lung Tumors. *Cancer Res.* **76**, 3942–3953 (2016). [PubMed:27216193].
- [155] Hu, S. *et al.* Four-in-one antibodies have superior cancer inhibitory activity against EGFR, HER2, HER3, and VEGF through disruption of HER/MET crosstalk. *Cancer Res.* **75**, 159–170 (2015). [PubMed:25371409].
- [156] Chang, K., Karnad, A., Zhao, S. & Freeman, J. W. Roles of c-Met and RON kinases in tumor progression and their potential as therapeutic targets. *Oncotarget* **6**, 3507–3518 (2015). [PubMed:25784650].
- [157] Tape, C. J. *et al.* Oncogenic KRAS Regulates Tumor Cell Signaling via Stromal Reciprocity. *Cell* **165**, 910–920 (2016). [PubMed:27087446].
- [158] Grugan, K. D. *et al.* Fibroblast-secreted hepatocyte growth factor plays a functional role in esophageal squamous cell carcinoma invasion. *Proc. Natl. Acad. Sci. U.S.A.* **107**, 11026–11031 (2010). [PubMed:20534479].
- [159] Fu, F., Nowak, M. A. & Bonhoeffer, S. Spatial heterogeneity in drug concentrations can facilitate the emergence of resistance to cancer therapy. *PLoS Comput. Biol.* **11**, e1004142 (2015). [PubMed:25789469].
- [160] Thatcher, N. *et al.* Gefitinib plus best supportive care in previously treated patients with refractory advanced non-small-cell lung cancer: results from a randomised, placebo-controlled, multicentre study (Iressa Survival Evaluation in Lung Cancer). *Lancet* **366**, 1527–1537 (2005). [PubMed:16257339].
- [161] Tran, H. T. *et al.* Pharmacokinetic study of the phase III, randomized, double-blind, multicenter trial (TRIBUTE) of paclitaxel and carboplatin combined with erlotinib or placebo in patients with advanced Non-small Cell Lung Cancer (NSCLC). *Invest New Drugs* **29**, 499–505 (2011). [PubMed:20094773].
- [162] Wang, Y., Schmid-Bindert, G. & Zhou, C. Erlotinib in the treatment of advanced non-small cell lung cancer: an update for clinicians. *Ther Adv Med Oncol* **4**, 19–29 (2012). [PubMed:22229045].

- 
- [163] Van Schaeybroeck, S. *et al.* Chemotherapy-induced epidermal growth factor receptor activation determines response to combined gefitinib/chemotherapy treatment in non-small cell lung cancer cells. *Mol. Cancer Ther.* **5**, 1154–1165 (2006). [PubMed:16731747].
- [164] Zwang, Y. & Yarden, Y. p38 MAP kinase mediates stress-induced internalization of EGFR: implications for cancer chemotherapy. *EMBO J.* **25**, 4195–4206 (2006). [PubMed:16932740].
- [165] Knipp, M. Metallothioneins and platinum(II) anti-tumor compounds. *Curr. Med. Chem.* **16**, 522–537 (2009). [PubMed:19199919].
- [166] Sakai, W. *et al.* Secondary mutations as a mechanism of cisplatin resistance in BRCA2-mutated cancers. *Nature* **451**, 1116–1120 (2008). [PubMed:18264087].
- [167] Zeng, Z. *et al.* Reduced chemotherapy sensitivity in EGFR-mutant lung cancer patient with frontline EGFR tyrosine kinase inhibitor. *Lung Cancer* **86**, 219 – 224 (2014). [DOI:10.1016/j.lungcan.2014.09.008].
- [168] Servidei, T., Riccardi, A., Mozzetti, S., Ferlini, C. & Riccardi, R. Chemoresistant tumor cell lines display altered epidermal growth factor receptor and HER3 signaling and enhanced sensitivity to gefitinib. *Int. J. Cancer* **123**, 2939–2949 (2008). [PubMed:18803287].
- [169] Li, Y., Yang, X., Su, L. J. & Flaig, T. W. VEGFR and EGFR inhibition increases epithelial cellular characteristics and chemotherapy sensitivity in mesenchymal bladder cancer cells. *Oncol. Rep.* **24**, 1019–1028 (2010). [PubMed:20811684].
- [170] Ko, S. C. *et al.* Epidermal growth factor protects squamous cell carcinoma against cisplatin-induced cytotoxicity through increased interleukin-1b expression. *PLoS ONE* **8**, e55795 (2013). [PubMed:23383347].
- [171] Yamaguchi, H. *et al.* Caspase-independent cell death is involved in the negative effect of EGF receptor inhibitors on cisplatin in non-small cell lung cancer cells. *Clin. Cancer Res.* **19**, 845–854 (2013). [PubMed:23344263].
- [172] Menendez, J. A., Mehmi, I. & Lupu, R. Heregulin-triggered Her-2/neu signaling enhances nuclear accumulation of p21WAF1/CIP1 and protects breast cancer cells from cisplatin-induced genotoxic damage. *Int. J. Oncol.* **26**, 649–659 (2005). [PubMed:15703820].
- [173] Mandic, R. *et al.* Cisplatin resistance of the HNSCC cell line UT-SCC-26A can be overcome by stimulation of the EGF-receptor. *Anticancer Res.* **29**, 1181–1187 (2009). [PubMed:19414362].
- [174] Henke, M. *et al.* Erythropoietin to treat head and neck cancer patients with anaemia undergoing radiotherapy: randomised, double-blind, placebo-controlled trial. *Lancet* **362**, 1255–1260 (2003). [PubMed:14575968].
- [175] Leyland-Jones, B. *et al.* Maintaining normal hemoglobin levels with epoetin alfa in mainly nonanemic patients with metastatic breast cancer receiving first-line chemotherapy: a survival study. *J. Clin. Oncol.* **23**, 5960–5972 (2005). [PubMed:16087945].

- [176] Bohlius, J. *et al.* Recombinant human erythropoietins and cancer patients: updated meta-analysis of 57 studies including 9353 patients. *J. Natl. Cancer Inst.* **98**, 708–714 (2006). [PubMed:16705125].
- [177] Glaspy, J. & Dunst, J. Can erythropoietin therapy improve survival? *Oncology* **67 Suppl 1**, 5–11 (2004). [PubMed:15486447].
- [178] Dagnon, K. *et al.* Expression of erythropoietin and erythropoietin receptor in non-small cell lung carcinomas. *Clin. Cancer Res.* **11**, 993–999 (2005). [PubMed:15709164].
- [179] Acs, G. *et al.* Hypoxia-inducible erythropoietin signaling in squamous dysplasia and squamous cell carcinoma of the uterine cervix and its potential role in cervical carcinogenesis and tumor progression. *Am. J. Pathol.* **162**, 1789–1806 (2003). [PubMed:12759237].
- [180] Todaro, M. *et al.* Erythropoietin activates cell survival pathways in breast cancer stem-like cells to protect them from chemotherapy. *Cancer Res.* **73**, 6393–6400 (2013). [PubMed:24008319].
- [181] Saintigny, P. *et al.* Erythropoietin and erythropoietin receptor coexpression is associated with poor survival in stage I non-small cell lung cancer. *Clin. Cancer Res.* **13**, 4825–4831 (2007). [PubMed:17699861].
- [182] Sinclair, A. M. *et al.* Erythropoietin receptor transcription is neither elevated nor predictive of surface expression in human tumour cells. *Br. J. Cancer* **98**, 1059–1067 (2008). [PubMed:18349818].
- [183] Duffy, M. J. The biochemistry of metastasis. *Adv Clin Chem* **32**, 135–166 (1996). [PubMed:8899072].
- [184] Hockel, M. *et al.* Association between tumor hypoxia and malignant progression in advanced cancer of the uterine cervix. *Cancer Res.* **56**, 4509–4515 (1996). [PubMed:8813149].
- [185] Bindra, R. S. & Glazer, P. M. Genetic instability and the tumor microenvironment: towards the concept of microenvironment-induced mutagenesis. *Mutat. Res.* **569**, 75–85 (2005). [PubMed:15603753].
- [186] Graves, E. E., Maity, A. & Le, Q. T. The tumor microenvironment in non-small-cell lung cancer. *Semin Radiat Oncol* **20**, 156–163 (2010). [PubMed:20685578].
- [187] Hardee, M. E. *et al.* Human recombinant erythropoietin (rEpo) has no effect on tumour growth or angiogenesis. *Br. J. Cancer* **93**, 1350–1355 (2005). [PubMed:16288305].
- [188] Merkle, R. *et al.* Identification of Cell Type-Specific Differences in Erythropoietin Receptor Signaling in Primary Erythroid and Lung Cancer Cells. *PLoS Comput. Biol.* **12**, e1005049 (2016). [PubMed:27494133].
- [189] Huang, L. J., Constantinescu, S. N. & Lodish, H. F. The N-terminal domain of Janus kinase 2 is required for Golgi processing and cell surface expression of erythropoietin receptor. *Mol. Cell* **8**, 1327–1338 (2001). [PubMed:11779507].

- 
- [190] Schilling, M. *et al.* Computational processing and error reduction strategies for standardized quantitative data in biological networks. *FEBS J.* **272**, 6400–6411 (2005). [PubMed:16336276].
- [191] Raue, A. *et al.* Data2dynamics: a modeling environment tailored to parameter estimation in dynamical systems. *Bioinformatics* (2015). [DOI:10.1093/bioinformatics/btv405].
- [192] Le Novere, N. *et al.* The Systems Biology Graphical Notation. *Nat. Biotechnol.* **27**, 735–741 (2009). [PubMed:19668183].
- [193] Doleschel, D. *et al.* Erythropoietin improves the accumulation and therapeutic effects of carboplatin by enhancing tumor vascularization and perfusion. *Theranostics* **5**, 905–918 (2015). [PubMed:26000061].
- [194] Doleschel, D. *et al.* Targeted near-infrared imaging of the erythropoietin receptor in human lung cancer xenografts. *J. Nucl. Med.* **53**, 304–311 (2012). [PubMed:22228796].
- [195] EMA, European Medicines Agency. [www.ema.europa.eu](http://www.ema.europa.eu). Accessed: October 2017.
- [196] Miharada, K., Hiroyama, T., Sudo, K., Nagasawa, T. & Nakamura, Y. Lipocalin 2 functions as a negative regulator of red blood cell production in an autocrine fashion. *FASEB J.* **19**, 1881–1883 (2005). [PubMed:16157692].
- [197] Cavazzoni, A. *et al.* Combined use of anti-ErbB monoclonal antibodies and erlotinib enhances antibody-dependent cellular cytotoxicity of wild-type erlotinib-sensitive NSCLC cell lines. *Mol. Cancer* **11**, 91 (2012). [PubMed:23234355].
- [198] CCLE Cancer Cell Line Encyclopedia. <https://portals.broadinstitute.org/ccle>. Accessed: October 2017.
- [199] Wisniewski, J. R., Hein, M. Y., Cox, J. & Mann, M. A "proteomic ruler" for protein copy number and concentration estimation without spike-in standards. *Mol. Cell Proteomics* **13**, 3497–3506 (2014). [PubMed:25225357].
- [200] ATCC in Partnership with LGC Standards. <http://www.lgcstandards-atcc.org/>. Accessed: June 2017.
- [201] Hass, H. *et al.* Predicting ligand-dependent tumors from multi-dimensional signaling features. *NPJ Syst Biol Appl* **3**, 27 (2017). [PubMed:28944080].
- [202] Barretina, J. *et al.* The Cancer Cell Line Encyclopedia enables predictive modelling of anti-cancer drug sensitivity. *Nature* **483**, 603–607 (2012). [PubMed:22460905].
- [203] Ketteler, R., Glaser, S., Sandra, O., Martens, U. M. & Klingmuller, U. Enhanced transgene expression in primitive hematopoietic progenitor cells and embryonic stem cells efficiently transduced by optimized retroviral hybrid vectors. *Gene Ther.* **9**, 477–487 (2002). [PubMed:11948372].

- [204] Schilling, M. *et al.* Quantitative data generation for systems biology: the impact of randomisation, calibrators and normalisers. *Syst Biol (Stevenage)* **152**, 193–200 (2005). [PubMed:16986260].
- [205] Avraham, R. & Yarden, Y. Feedback regulation of EGFR signalling: decision making by early and delayed loops. *Nat. Rev. Mol. Cell Biol.* **12**, 104–117 (2011). [PubMed:21252999].
- [206] Schwarz, G. Estimating the dimension of a model. *Ann. Statist.* 461–464 (1978).
- [207] Zacharias, D. A., Violin, J. D., Newton, A. C. & Tsien, R. Y. Partitioning of lipid-modified monomeric GFPs into membrane microdomains of live cells. *Science* **296**, 913–916 (2002). [PubMed:11988576].
- [208] Arai, R., Ueda, H., Kitayama, A., Kamiya, N. & Nagamune, T. Design of the linkers which effectively separate domains of a bifunctional fusion protein. *Protein Eng.* **14**, 529–532 (2001). [PubMed:11579220].
- [209] Resh, M. D. Fatty acylation of proteins: new insights into membrane targeting of myristoylated and palmitoylated proteins. *Biochim. Biophys. Acta* **1451**, 1–16 (1999). [PubMed:10446384].
- [210] Godinez, W. J. & Rohr, K. Tracking multiple particles in fluorescence time-lapse microscopy images via probabilistic data association. *IEEE Trans Med Imaging* **34**, 415–432 (2015). [PubMed:25252280].
- [211] Low-Nam, S. T. *et al.* ErbB1 dimerization is promoted by domain co-confinement and stabilized by ligand binding. *Nat. Struct. Mol. Biol.* **18**, 1244–1249 (2011). [PubMed:22020299].
- [212] Tinoco, I. & Gonzalez, R. L. Biological mechanisms, one molecule at a time. *Genes Dev.* **25**, 1205–1231 (2011). [PubMed:21685361].
- [213] Maiwald, T. *et al.* Driving the Model to Its Limit: Profile Likelihood Based Model Reduction. *PLoS ONE* **11**, e0162366 (2016). [PubMed:27588423].
- [214] Shaul, Y. D. *et al.* MERAV: a tool for comparing gene expression across human tissues and cell types. *Nucleic Acids Res.* **44**, D560–566 (2016). [PubMed:26626150].
- [215] Park, S. *et al.* Low EGFR/MET ratio is associated with resistance to EGFR inhibitors in non-small cell lung cancer. *Oncotarget* **6**, 30929–30938 (2015). [PubMed:26439803].
- [216] Dunlop, E. A., Percy, M. J., Boland, M. P., Maxwell, A. P. & Lappin, T. R. Induction of signalling in non-erythroid cells by pharmacological levels of erythropoietin. *Neurodegener Dis* **3**, 94–100 (2006). [PubMed:16909043].
- [217] Gewirtz, D. A., Di, X., Walker, T. D. & Sawyer, S. T. Erythropoietin fails to interfere with the antiproliferative and cytotoxic effects of antitumor drugs. *Clin. Cancer Res.* **12**, 2232–2238 (2006). [PubMed:16609039].

- 
- [218] Westenfelder, C. & Baranowski, R. L. Erythropoietin stimulates proliferation of human renal carcinoma cells. *Kidney Int.* **58**, 647–657 (2000). [PubMed:10916088].
- [219] Shen-Orr, S. S. *et al.* Cell type-specific gene expression differences in complex tissues. *Nat. Methods* **7**, 287–289 (2010). [PubMed:20208531].
- [220] Tibshirani, R. Regression shrinkage and selection via the lasso. *J Roy Stat Soc B Met* **58**, 267–88 (1996).
- [221] Danko, C. G. *et al.* Signaling pathways differentially affect RNA polymerase II initiation, pausing, and elongation rate in cells. *Mol. Cell* **50**, 212–222 (2013). [PubMed:23523369].
- [222] Timney, B. L. *et al.* Simple kinetic relationships and nonspecific competition govern nuclear import rates in vivo. *J. Cell Biol.* **175**, 579–593 (2006). [PubMed:17116750].
- [223] Hoyt, R. *et al.* Cutting edge: selective tyrosine dephosphorylation of interferon-activated nuclear STAT5 by the VHR phosphatase. *J. Immunol.* **179**, 3402–3406 (2007). [PubMed:17785772].
- [224] Geyer, H. L. & Mesa, R. A. Therapy for myeloproliferative neoplasms: when, which agent, and how? *Blood* **124**, 3529–3537 (2014). [PubMed:25472969].
- [225] Adelibieke, Y., Shimizu, H., Saito, S., Mironova, R. & Niwa, T. Indoxyl sulfate counteracts endothelial effects of erythropoietin through suppression of Akt phosphorylation. *Circ. J.* **77**, 1326–1336 (2013). [PubMed:23337206].
- [226] Warren, J. S., Zhao, Y., Yung, R. & Desai, A. Recombinant human erythropoietin suppresses endothelial cell apoptosis and reduces the ratio of Bax to Bcl-2 proteins in the aortas of apolipoprotein E-deficient mice. *J. Cardiovasc. Pharmacol.* **57**, 424–433 (2011). [PubMed:21242808].
- [227] Okazaki, T. *et al.* Erythropoietin promotes the growth of tumors lacking its receptor and decreases survival of tumor-bearing mice by enhancing angiogenesis. *Neoplasia* **10**, 932–939 (2008). [PubMed:18714393].
- [228] Yang, J., Xiao, Z., Li, T., Gu, X. & Fan, B. Erythropoietin promotes the growth of pituitary adenomas by enhancing angiogenesis. *Int. J. Oncol.* **40**, 1230–1237 (2012). [PubMed:22086127].
- [229] Tovari, J. *et al.* Recombinant human erythropoietin alpha targets intratumoral blood vessels, improving chemotherapy in human xenograft models. *Cancer Res.* **65**, 7186–7193 (2005). [PubMed:16103069].
- [230] Assoun, S., Brosseau, S., Steinmetz, C., Gounant, V. & Zalcman, G. Bevacizumab in advanced lung cancer: state of the art. *Future Oncol* (2017). [PubMed:28812378].
- [231] Ebos, J. M. *et al.* Accelerated metastasis after short-term treatment with a potent inhibitor of tumor angiogenesis. *Cancer Cell* **15**, 232–239 (2009). [PubMed:19249681].

- [232] Carmeliet, P. & Jain, R. K. Principles and mechanisms of vessel normalization for cancer and other angiogenic diseases. *Nat Rev Drug Discov* **10**, 417–427 (2011). [PubMed:21629292].
- [233] Malnic, B., Hirono, J., Sato, T. & Buck, L. B. Combinatorial receptor codes for odors. *Cell* **96**, 713–723 (1999). [PubMed:10089886].
- [234] Zurney, J., Howard, K. E. & Sherry, B. Basal expression levels of IFNAR and Jak-STAT components are determinants of cell-type-specific differences in cardiac antiviral responses. *J. Virol.* **81**, 13668–13680 (2007). [PubMed:17942530].
- [235] Salahudeen, M. S. & Nishtala, P. S. An overview of pharmacodynamic modelling, ligand-binding approach and its application in clinical practice. *Saudi Pharm J* **25**, 165–175 (2017). [PubMed:28344466].
- [236] Werbin, J. L. *et al.* Multiplexed Exchange-PAINT imaging reveals ligand-dependent EGFR and Met interactions in the plasma membrane. *Sci Rep* **7**, 12150 (2017). [PubMed:28939861].
- [237] Sangwan, V. *et al.* Protein-tyrosine phosphatase 1B modulates early endosome fusion and trafficking of Met and epidermal growth factor receptors. *J. Biol. Chem.* **286**, 45000–45013 (2011). [PubMed:22045810].
- [238] Glaser, R. W. Antigen-antibody binding and mass transport by convection and diffusion to a surface: a two-dimensional computer model of binding and dissociation kinetics. *Anal. Biochem.* **213**, 152–161 (1993). [PubMed:8238868].
- [239] Trusolino, L., Bertotti, A. & Comoglio, P. M. MET signalling: principles and functions in development, organ regeneration and cancer. *Nat. Rev. Mol. Cell Biol.* **11**, 834–848 (2010). [PubMed:21102609].
- [240] Yang, S. *et al.* Mapping ErbB receptors on breast cancer cell membranes during signal transduction. *J. Cell. Sci.* **120**, 2763–2773 (2007). [PubMed:17652160].
- [241] Ortiz-Zapater, E. *et al.* MET-EGFR dimerization in lung adenocarcinoma is dependent on EGFR mutations and altered by MET kinase inhibition. *PLoS ONE* **12**, e0170798 (2017). [PubMed:28141869].
- [242] Schnell, U., Dijk, F., Sjollem, K. A. & Giepmans, B. N. Immunolabeling artifacts and the need for live-cell imaging. *Nat. Methods* **9**, 152–158 (2012). [PubMed:22290187].
- [243] Baulida, J., Kraus, M. H., Alimandi, M., Di Fiore, P. P. & Carpenter, G. All ErbB receptors other than the epidermal growth factor receptor are endocytosis impaired. *J. Biol. Chem.* **271**, 5251–5257 (1996). [PubMed:8617810].
- [244] Chen, Y. R. *et al.* Distinctive activation patterns in constitutively active and gefitinib-sensitive EGFR mutants. *Oncogene* **25**, 1205–1215 (2006). [PubMed:16205628].
- [245] Huang, D. H. *et al.* Quantum dot-based quantification revealed differences in subcellular localization of EGFR and E-cadherin between EGFR-TKI sensitive and insensitive cancer cells. *Nanotechnology* **20**, 225102 (2009). [PubMed:19433879].

- [246] Vatansever, H. S., Lacin, S. & Ozbilgin, M. K. Changed Bcl:Bax ratio in endometrium of patients with unexplained infertility. *Acta Histochem.* **107**, 345–355 (2005). [PubMed:16139338].
- [247] Adlung, L. *et al.* Protein abundance of AKT and ERK pathway components governs cell type-specific regulation of proliferation. *Mol. Syst. Biol.* **13**, 904 (2017). [PubMed:28123004].
- [248] Kluba, M., Engelborghs, Y., Hofkens, J. & Mizuno, H. Inhibition of Receptor Dimerization as a Novel Negative Feedback Mechanism of EGFR Signaling. *PLoS ONE* **10**, e0139971 (2015). [PubMed:26465157].
- [249] Goh, L. K., Huang, F., Kim, W., Gygi, S. & Sorkin, A. Multiple mechanisms collectively regulate clathrin-mediated endocytosis of the epidermal growth factor receptor. *J. Cell Biol.* **189**, 871–883 (2010). [PubMed:20513767].
- [250] Hubbard, S. R. Crystal structure of the activated insulin receptor tyrosine kinase in complex with peptide substrate and ATP analog. *EMBO J.* **16**, 5572–5581 (1997). [PubMed:9312016].
- [251] Hubbard, S. R. & Till, J. H. Protein tyrosine kinase structure and function. *Annu. Rev. Biochem.* **69**, 373–398 (2000). [PubMed:10966463].
- [252] Liu, Y. *et al.* A multiscale computational approach to dissect early events in the Erb family receptor mediated activation, differential signaling, and relevance to oncogenic transformations. *Ann Biomed Eng* **35**, 1012–1025 (2007). [PubMed:17273938].
- [253] Liu, P. *et al.* A single ligand is sufficient to activate EGFR dimers. *Proc. Natl. Acad. Sci. U.S.A.* **109**, 10861–10866 (2012). [PubMed:22699492].
- [254] Hartman, Z., Zhao, H. & Agazie, Y. M. HER2 stabilizes EGFR and itself by altering autophosphorylation patterns in a manner that overcomes regulatory mechanisms and promotes proliferative and transformation signaling. *Oncogene* **32**, 4169–4180 (2013). [PubMed:23027125].
- [255] Arcila, M. E. *et al.* Rebiopsy of lung cancer patients with acquired resistance to EGFR inhibitors and enhanced detection of the T790M mutation using a locked nucleic acid-based assay. *Clin. Cancer Res.* **17**, 1169–1180 (2011). [PubMed:21248300].
- [256] Cappuzzo, F. *et al.* Epidermal growth factor receptor gene and protein and gefitinib sensitivity in non-small-cell lung cancer. *J. Natl. Cancer Inst.* **97**, 643–655 (2005). [PubMed:15870435].
- [257] Bean, J. *et al.* MET amplification occurs with or without T790M mutations in EGFR mutant lung tumors with acquired resistance to gefitinib or erlotinib. *Proc. Natl. Acad. Sci. U.S.A.* **104**, 20932–20937 (2007). [PubMed:18093943].
- [258] Morgenstern, J. P. & Land, H. Advanced mammalian gene transfer: high titre retroviral vectors with multiple drug selection markers and a complementary helper-free packaging cell line. *Nucleic Acids Res.* **18**, 3587–3596 (1990). [PubMed:2194165].
- [259] Los, G. V. *et al.* HaloTag: a novel protein labeling technology for cell imaging and protein analysis. *ACS Chem. Biol.* **3**, 373–382 (2008). [PubMed:18533659].

- [260] Keppler, A. *et al.* A general method for the covalent labeling of fusion proteins with small molecules in vivo. *Nat. Biotechnol.* **21**, 86–89 (2003). [PubMed:12469133].
- [261] Raia, V. *et al.* Dynamic mathematical modeling of IL13-induced signaling in Hodgkin and primary mediastinal B-cell lymphoma allows prediction of therapeutic targets. *Cancer Res.* **71**, 693–704 (2011). [PubMed:21127196].
- [262] Haenselmann, S. *Quantitative Microscopy: Measuring membrane receptor interactions in live cells*. Ph.D. thesis, University of Heidelberg (2017).
- [263] Marwitz, S. *et al.* Downregulation of the TGF $\beta$  Pseudoreceptor BAMBI in Non-Small Cell Lung Cancer Enhances TGF $\beta$  Signaling and Invasion. *Cancer Res.* **76**, 3785–3801 (2016). [PubMed:27197161].
- [264] Castro, F. *et al.* High-throughput SNP-based authentication of human cell lines. *Int. J. Cancer* **132**, 308–314 (2013). [PubMed:22700458].
- [265] Schmitt, M. & Pawlita, M. High-throughput detection and multiplex identification of cell contaminations. *Nucleic Acids Res.* **37**, e119 (2009). [PubMed:19589807].
- [266] Kinsella, T. M. & Nolan, G. P. Episomal vectors rapidly and stably produce high-titer recombinant retrovirus. *Hum. Gene Ther.* **7**, 1405–1413 (1996). [PubMed:8844199].
- [267] Boehm, M. E., Hahn, B. & Lehmann, W. D. One-source peptide/phosphopeptide ratio standards for accurate and site-specific determination of the degree of phosphorylation. *Methods Mol. Biol.* **1156**, 367–378 (2014). [PubMed:24792001].
- [268] Rappsilber, J., Mann, M. & Ishihama, Y. Protocol for micro-purification, enrichment, pre-fractionation and storage of peptides for proteomics using StageTips. *Nat Protoc* **2**, 1896–1906 (2007).
- [269] Besl, P. J. & McKay, N. D. A method for registration of 3-d shapes. *IEEE Transactions on Pattern Analysis and Machine Intelligence* **14**, 239–256 (1992).
- [270] Hass, H. *Quantifying cell biology: Mechanistic dynamic modeling of receptor crosstalk*. Ph.D. thesis, University of Freiburg (2017).
- [271] Leis, J. R. & Kramer, M. A. The simultaneous solution and sensitivity analysis of systems described by ordinary differential equations. *ACM Transactions on Mathematical Software (TOMS)* **14**, 45–60 (1988).
- [272] Hindmarsh, A. C. *et al.* Sundials: Suite of nonlinear and differential/algebraic equation solvers. *ACM Transactions on Mathematical Software (TOMS)* **31**, 363–396 (2005).
- [273] Coleman, T. F. & Li, Y. An interior, trust region approach for nonlinear minimization subject to bounds. *SIAM Journal on Optimization* **6**, 418–445 (1996).
- [274] Venzon, D. J. & Moolgavkar, S. H. A method for computing profile-likelihood-based confidence intervals. *Applied Statistics* **37**, 87–94 (1988).

- [275] Beasley, M. B., Brambilla, E. & Travis, W. D. The 2004 World Health Organization classification of lung tumors. *Semin Roentgenol* **40**, 90–97 (2005). [PubMed:15898407].
- [276] Schneider, M. A. *et al.* Glycodelin: A New Biomarker with Immunomodulatory Functions in Non-Small Cell Lung Cancer. *Clin. Cancer Res.* **21**, 3529–3540 (2015). [PubMed:25901080].
- [277] McShane, L. M. *et al.* REporting recommendations for tumour MARKer prognostic studies (REMARK). *Eur. J. Cancer* **41**, 1690–1696 (2005). [PubMed:16043346].
- [278] Dinse, G. E. & Lagakos, S. W. Nonparametric estimation of lifetime and disease onset distributions from incomplete observations. *Biometrics* **38**, 921–932 (1982). [PubMed:7168795].
- [279] Basilico, C., Arnesano, A., Galluzzo, M., Comoglio, P. M. & Michieli, P. A high affinity hepatocyte growth factor-binding site in the immunoglobulin-like region of Met. *J. Biol. Chem.* **283**, 21267–21277 (2008). [PubMed:18495663].
- [280] Merkt, B., Timmer, J. & Kaschek, D. Higher-order Lie-symmetries in identifiability and predictability analysis of dynamic models. *Physical Review E* **92**, 12–20 (2015).



## 6 Appendix

**Table 6.1:** List of used buffers and solutions. AEBSF: 4-(2-aminoethyl)benzenesulfonyl fluoride hydrochloride, AP: aprotinin. If not stated otherwise, all chemicals were purchased from Sigma. 20 % SDS solution was obtained from Serva, Tris from AppliChem, NP40-substitute from Roche.

Buffer	Composition
2× HBS	16.4 g/L NaCl, 11.9 g/L HEPES, 0.21 g/L Na <sub>2</sub> HPO <sub>4</sub> , pH 7.05
0.5× TAE	4.84 g/L Tris, 1 mM EDTA, pH 8.0
2× NP40	300 mM NaCl, 40 mM Tris pH 7.4, 20 mM NaF, 2 mM EDTA pH 8.0, 2 mM ZnCl <sub>2</sub> , 2 mM MgCl <sub>2</sub> , 2 mM Na <sub>3</sub> VO <sub>4</sub> , 20 % glycerol, 2 % NP40 (fresh), 2 µg/mL AP (fresh), 200 µg/mL AEBSF (fresh)
2× RIPA	0.1 M Tris pH 7.4, 0.3 M NaCl, 2 mM EDTA, 2 g/L sodium deoxycholate, 1 mM sodium orthovanadate, 5 mM NaF, 2 % NP40 (fresh), 2 µg/mL AP (fresh), 200 µg/mL AEBSF (fresh)
TNE	10 mM Tris pH 7.4, 100 mM NaCl, 1 mM EDTA, 100 µM Na <sub>3</sub> VO <sub>4</sub>
2× SB	32 g/L SDS, 80 mM Tris pH 7.4, 16 % glycerol, 24.6 g/L dithiothreitol, 0.32 g/L bromophenol blue, 10 % 2-mercaptoethanol (fresh)
4× SB	64 g/L SDS, 160 mM Tris pH 7.4, 32 % glycerol, 49.3 g/L dithiothreitol, 0.64 g/L bromophenol blue, 20 % 2-mercaptoethanol (fresh)
Laemmli	14.4 g/L glycine, 3 g/L Tris, 1 g/L SDS
transfer	14.4 g/L glycine, 3 g/L Tris, 0.75 g/L SDS, 0.0925 g/L sodium vanadate, 15 % methanol
TBS	0.15 M NaCl, 0.01 M Tris pH 7.4
TBS-T	150 mM NaCl, 10 mM Tris pH 7.4, 0.2 % Tween 20
ECL A	0.1 M Tris pH 8.5, 1.1 mg/L luminol, 0.185 mg/L p-coumaric acid, 1 % DMSO
ECL B	0.1 M Tris pH 8.5, 0.018 % H <sub>2</sub> O <sub>2</sub>
stripping	62.5 mM Tris pH 6.8, 2 % SDS, 0.7 % 2-mercaptoethanol (fresh)

**Table 6.2: List of all utilized primer sequences.** Primers are depicted from 5' to 3'.

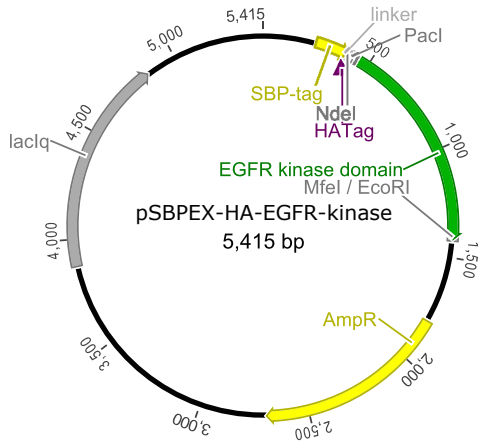
P1a	TCATGCTCCAATAAATTCAC
P1b	GGGATGGAGGACCTGCTGTG
P1f	CGGTTAATTAAACGGAGAAGCTCCCAACCAAGCTC 
P1r	CGCGCAATTGTCAGATGAGGTACTCGTCCGGCATCC 
P2f	CCTGGATCCCAGCAAGCAGATCAAGGATCTGGGC 
P2r	GCCATACGGGAAGCAATAGC
P4f	CGCCTCGAGATGCGACCCGCCGGACGG 
P4r	CGGTTAATTAAATCATGCTCCAATAAATTCACCTGCTTTGTG 
P5a	TTACGTTCTCTGGGCATT
P5b	GGGGAAAAGGGGCTGGGACC
P5f	CGCGATATCATGAGGGCGAACGACGCTCT 
P5r	CGGTTAATTAAATTACGTTCTCTGGGCATTAGCCTT 
P6f	CGCGGATCCGCAGAAATCGGTACTGGCTTTCCATTTC 
P6r	CGCACCGGTGCCGAAAATCTCCAGCGTCGAC 
P7f	CGGGAAUUCGCAGAAATCGGTACTGGCTTTCCATT 
P7r	CGCCATATGGCCGAAAATCTCCAGCGTCGA 
P8f	GGCGAATTCITGGCGGAGGCGGCGGC 
P8r	CGCATTAAATTAGCCCAGCCAGGCTTGCC 
P9f	CGCCTCGAGATGCGACCCGCCGGACGG 
P9r	CGGATTAAATTGCTCCAATAAATTCACCTGCTTTGTG 

**Table 6.3: Multiple Cloning site inserted in the pBABE vector.**

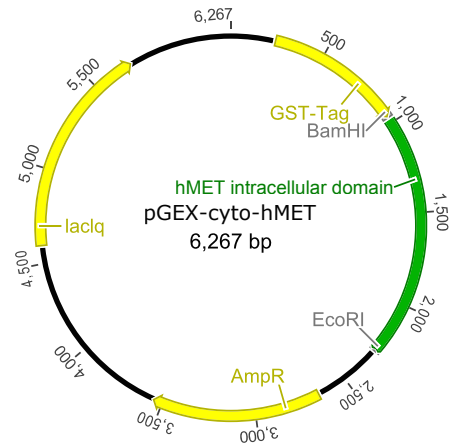


**Table 6.4: List of synthesized vectors.**

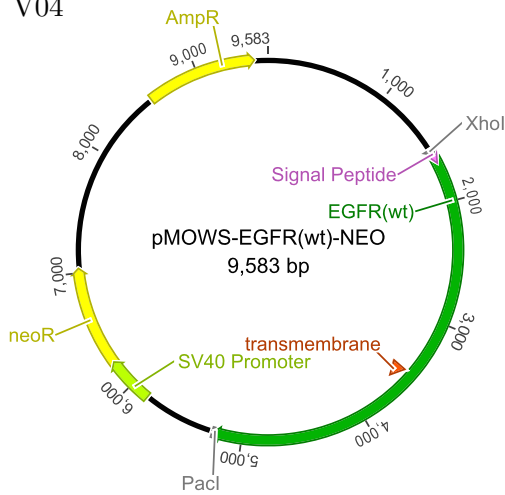
V01



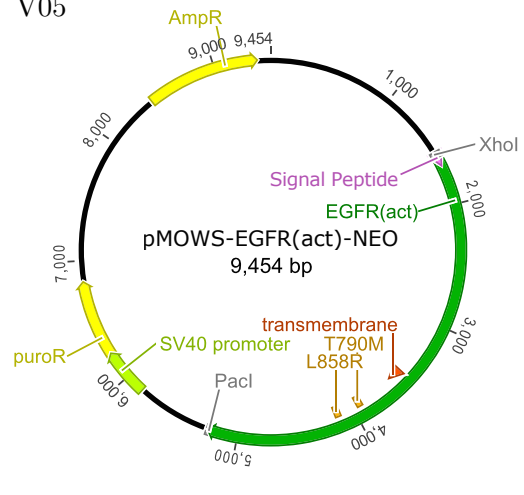
V02



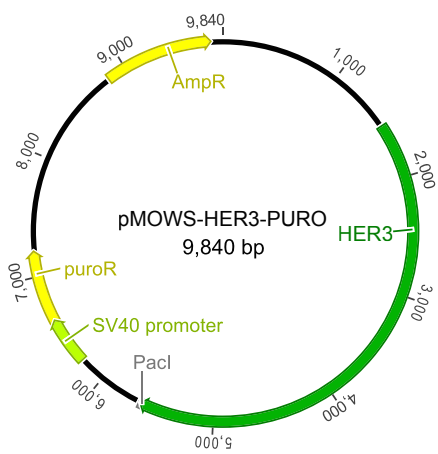
V04



V05



V06



V07

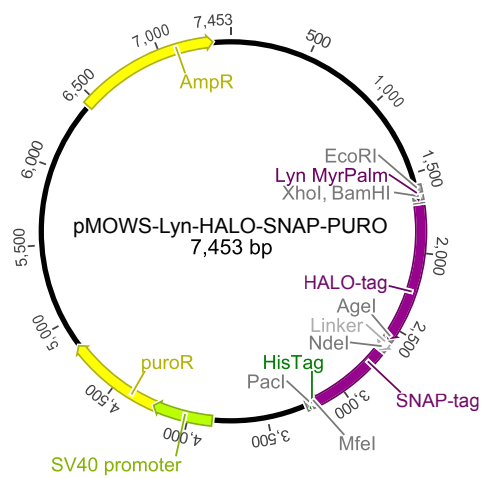


**Table 6.5: List of synthesized vectors.(2)**

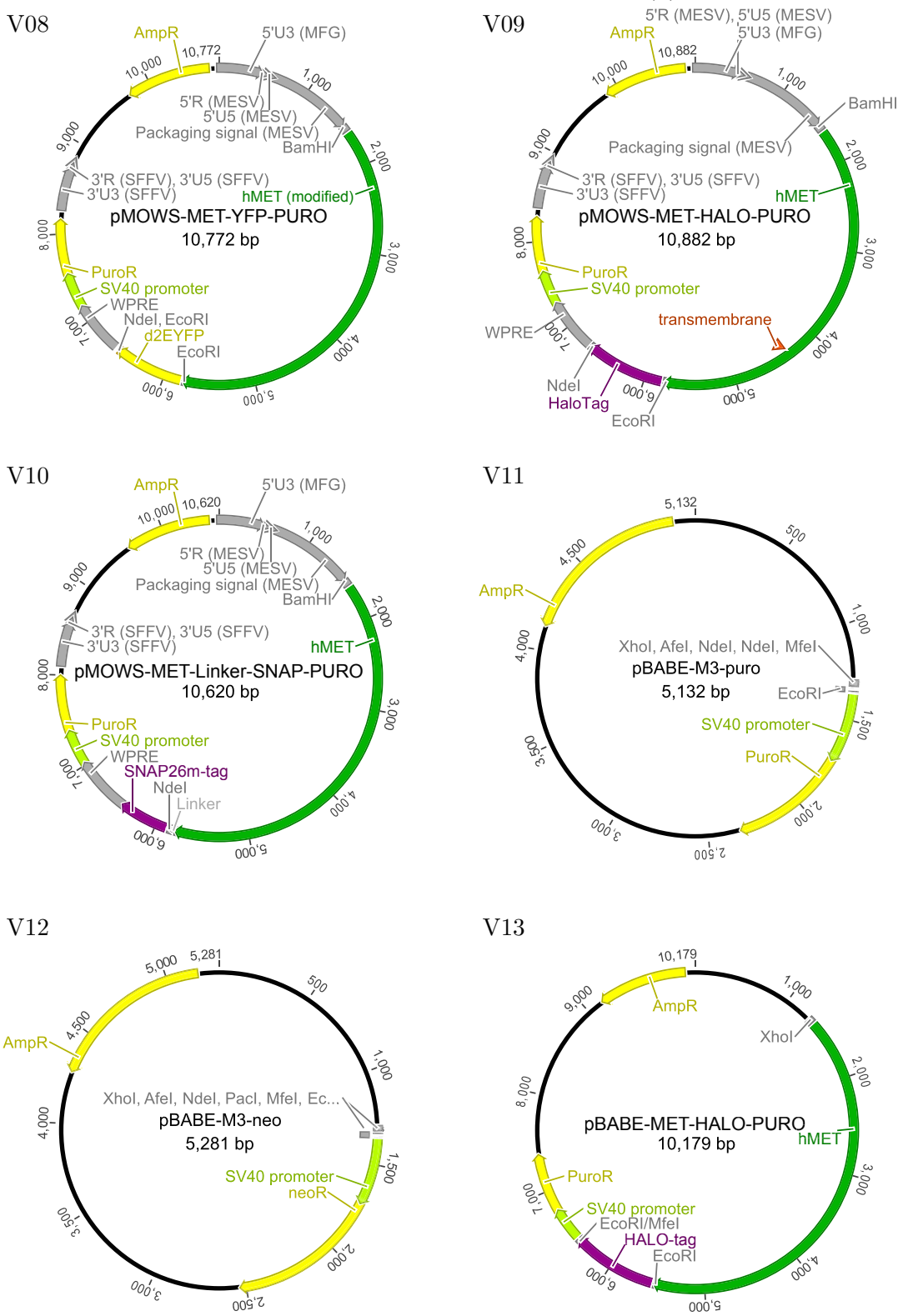
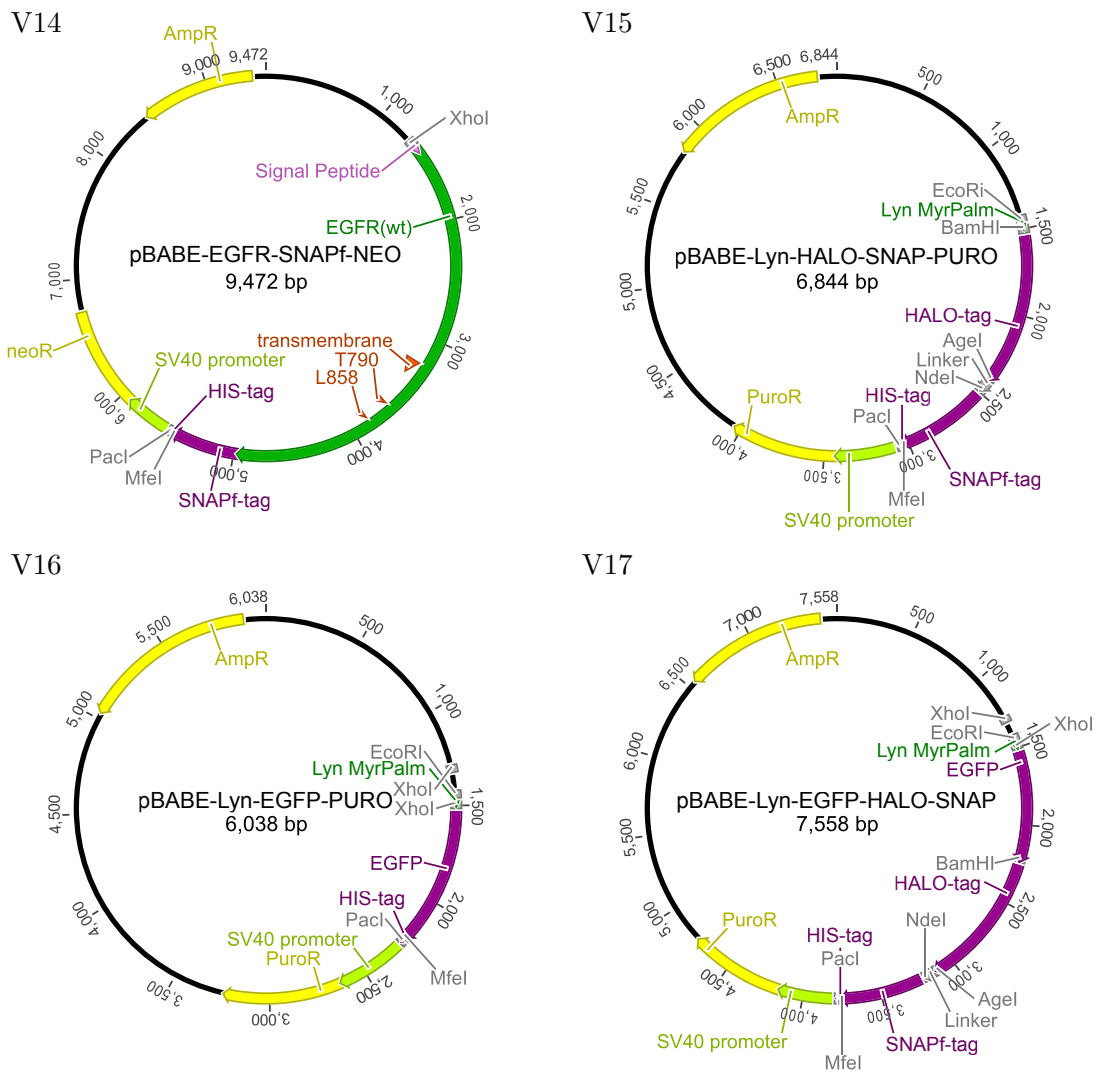
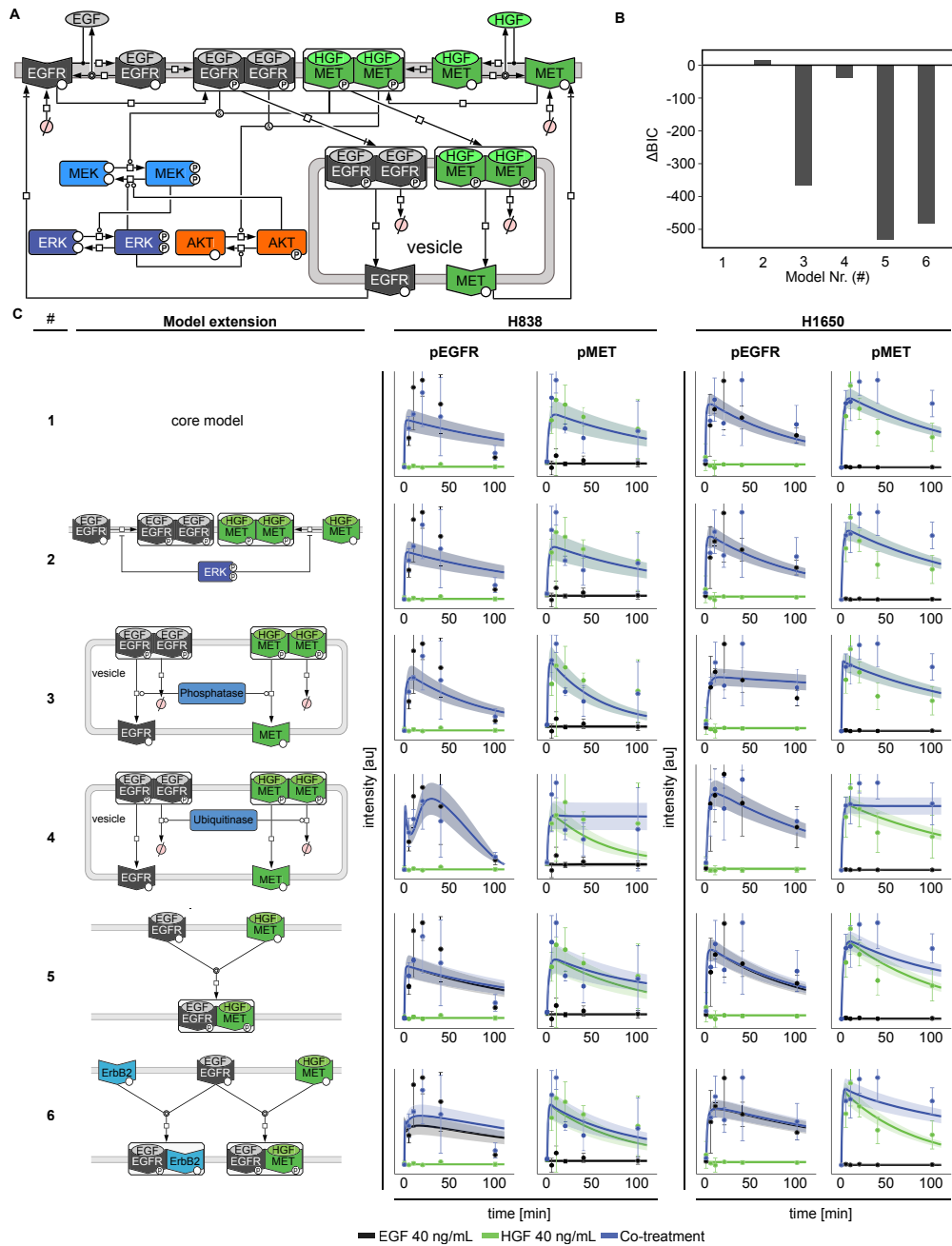


Table 6.6: List of synthesized vectors.(3)



**Table 6.7:** RNAseq data of H838, H1650 and H1975 cells analyzed by S. Krämer (DKFZ Heidelberg).

<b>FPKM</b>	<b>H1975</b>	<b>H1650</b>	<b>H838</b>
EGFR	29.5	67.1	5.7
HER2	61.0	72.3	42.1
HER3	30.5	11.0	2.5
HER4	0.0	0.0	0.0
HGF	0.1	0.0	0.0
EGF	1.6	0.2	1.1
NRG1	7.6	2.3	1.2
NRG4	1.3	3.7	12.3
EREG	15.8	0.4	0.1
TGFA	16.7	40.2	0.3
AREGB	26.9	2.9	0.4
AREG	29.4	3.0	0.5
BTC	3.9	1.5	0.0
AKT1	95.3	76.1	72.5
AKT2	24.8	108.7	90.6
AKT3	3.1	17.0	29.7
KRAS	6.5	7.8	79.0
NRAS	14.5	19.7	118.5
RRAS	23.9	53.0	84.9
HRAS	29.6	37.4	28.1
MAPK3	41.2	65.6	65.2
MAPK1	42.2	45.3	43.4
MAP2K1	33.8	32.2	28.5
MAP2K2	127.3	48.6	95.7
PIK3CA	9.4	8.8	19.1
PIK3CB	12.5	17.9	21.8
PIK3CD	1.3	1.0	18.9
PIK3R1	2.7	7.5	3.4
PIK3R2	25.8	24.8	40.5
PIK3R3	11.9	44.0	8.6
PIK3R4	14.0	11.6	17.2



**Figure 6.1: Model selection based on receptor response in H838 and H1650 cell lines.** **A:** Structure of the ODE-based core model according to the Systems Biology Graphical Notation.<sup>[192]</sup> The model selection was performed by H. Hass. **B:** Bayesian information criterion (BIC) for all tested model extensions relative to the best model #5. **C:** Model scheme of different extensions of the core model to test the agreement between model and dynamic signaling data. The receptor phosphorylation is shown for H838 and H1650 cells. Experimental data is shown as dots, the result of the best parameter estimation for each model is depicted as trajectory. The models represent the core model (#1) or extension by a regulating feedback loop (#2), a limiting phosphatase (#3), a shared ubiquitinase (#4), EGFR and MET heterodimerization (#5) or heterodimer formation of EGFR and MET as well as a HER family member (#6). This model describes the data similar to model #5, but the benefit of the extension is not statistically significant (p-value 0.083).

**Table 6.8: Ordinary differential equations (ODEs) of the final model.** The model consists of 21 differential equations, which are given by the following terms. The reaction velocities  $v$  are described in Table 6.9. d: dimer, i: internalized, p: phosphorylated, t:total. The mathematical model was developed by H. Hass.

$$\begin{aligned}d[\text{dose\_EGF}]/dt &= -v_5 + v_6 - v_7 + v_8 \\d[\text{dose\_HGF}]/dt &= -v_{11} + v_{12} \\d[\text{EGFR}]/dt &= v_1 - v_3 + v_4 - v_5 + v_6 - 2 \cdot v_{16} + 2 \cdot v_{23} \\d[\text{EGFR\_EGF}]/dt &= v_5 - v_6 - v_9 + v_{10} - v_{13} - 2 \cdot v_{18} - v_{28} \\d[\text{pEGFRd}]/dt &= v_{16} + v_{18} - v_{19} - v_{20} \\d[\text{pEGFRi}]/dt &= v_{19} + v_{20} - v_{22} - v_{23} \\d[\text{EGFR\_TKI}]/dt &= v_3 - v_4 - v_7 + v_8 \\d[\text{EGFR\_EGF\_TKI}]/dt &= v_7 - v_8 + v_9 - v_{10} - v_{13} - 2 \cdot v_{14} - v_{15} \\d[\text{EGFRd\_TKI}]/dt &= v_{13} + v_{14} - v_{21} \\d[\text{Met}]/dt &= v_2 - v_{11} + v_{12} - 2 \cdot v_{17} + 2 \cdot v_{27} \\d[\text{Met\_HGF}]/dt &= v_{11} - v_{12} - v_{15} - 2 \cdot v_{24} - v_{28} \\d[\text{pMetd}]/dt &= v_{17} + v_{24} - v_{25} \\d[\text{pMeti}]/dt &= v_{25} - v_{26} - v_{27} \\d[\text{pMet\_EGFR}]/dt &= v_{28} - v_{29} \\d[\text{pMet\_EGFRi}]/dt &= v_{29} \\d[\text{MEK}]/dt &= -v_{30} - v_{31} - v_{32} + v_{33} \\d[\text{pMEK}]/dt &= v_{30} + v_{31} + v_{32} - v_{33} \\d[\text{ERK}]/dt &= -v_{34} + v_{35} \\d[\text{pERK}]/dt &= v_{34} - v_{35} \\d[\text{AKT}]/dt &= -v_{36} - v_{37} - v_{38} + v_{39} \\d[\text{pAKT}]/dt &= v_{36} + v_{37} + v_{38} - v_{39}\end{aligned}$$

---

**Table 6.9:** Model flux expressions. All reaction velocities  $v$  and their dependency on the model parameters are listed for the final model.  $v_{19}$  and  $v_{20}$  describe ubiquitin-dependent and -independent internalization of EGFR. Concentrations are indicated by squared brackets. d: dimer, i: internalized, p: phosphorylated, t: total. The mathematical model was developed by H. Hass.

$$\begin{aligned}
v_1 &= \text{EGFR\_prod} \\
v_2 &= \text{Met\_prod} \\
v_3 &= [\text{EGFR}] \cdot \text{EGFR\_TKI\_binding} \cdot \text{Inh} \\
v_4 &= [\text{EGFR\_TKI}] \cdot \text{EGFR\_TKI\_unbinding} \\
v_5 &= [\text{EGFR}] \cdot \text{EGFR\_lig\_binding} \cdot [\text{dose\_EGF}] \\
v_6 &= [\text{EGFR\_EGF}] \cdot \text{EGFR\_lig\_binding} \cdot \text{EGF\_kD} \\
v_7 &= [\text{EGFR\_TKI}] \cdot \text{EGFR\_lig\_binding} \cdot [\text{dose\_EGF}] \\
v_8 &= [\text{EGFR\_EGF\_TKI}] \cdot \text{EGFR\_lig\_binding} \cdot \text{EGF\_kD} \\
v_9 &= [\text{EGFR\_EGF}] \cdot \text{EGFR\_TKI\_binding} \cdot \text{Inh} \\
v_{10} &= [\text{EGFR\_EGF\_TKI}] \cdot \text{EGFR\_TKI\_unbinding} \\
v_{11} &= [\text{Met}] \cdot \text{Met\_lig\_binding} \cdot [\text{dose\_HGF}] \\
v_{12} &= [\text{Met\_HGF}] \cdot \text{Met\_kD} \cdot \text{Met\_lig\_binding} \\
v_{13} &= [\text{EGFR\_EGF}] \cdot [\text{EGFR\_EGF\_TKI}] \cdot \text{EGFR\_activation} \\
v_{14} &= [\text{EGFR\_EGF\_TKI}]^2 \cdot \text{EGFR\_activation} \\
v_{15} &= [\text{EGFR\_EGF\_TKI}] \cdot [\text{Met\_HGF}] \cdot \text{diRatio} \cdot (\text{EGFR\_activation} \cdot \text{Met\_activation})^{0.5} \\
v_{16} &= [\text{EGFR}]^2 \cdot \text{EGFR\_basal\_activation} \\
v_{17} &= [\text{Met}]^2 \cdot \text{Met\_basal\_activation} \\
v_{18} &= [\text{EGFR\_EGF}]^2 \cdot \text{EGFR\_activation} \\
v_{19} &= \text{pEGFR\_internalize} \cdot [\text{pEGFRd}] \\
v_{20} &= \frac{\text{pEGFR\_internalize\_ub} \cdot [\text{pEGFRd}] \cdot [\text{pEGFRd}]^{\text{nH}}}{k\_EGFRub^{\text{nH}} + [\text{pEGFRd}]^{\text{nH}}} \\
v_{21} &= [\text{EGFRd\_TKI}] \cdot \text{pEGFR\_degradation} \\
v_{22} &= [\text{pEGFRi}] \cdot \text{pEGFR\_degradation} \\
v_{23} &= [\text{pEGFRi}] \cdot \text{pEGFRi\_dephosph} \\
v_{24} &= [\text{Met\_HGF}]^2 \cdot \text{Met\_activation} \\
v_{25} &= [\text{pMetd}] \cdot \text{pMet\_internalize}
\end{aligned}$$

$$v_{26} = [\text{pMeti}] \cdot \text{pMet\_degradation}$$

$$v_{27} = [\text{pMeti}] \cdot \text{pMeti\_dephosph}$$

$$v_{28} = [\text{EGFR\_EGF}] \cdot [\text{Met\_HGF}] \cdot \text{diRatio} \cdot (\text{EGFR\_activation} \cdot \text{Met\_activation})^{0.5}$$

$$v_{29} = [\text{pMet\_EGFR}] \cdot \text{pMet\_EGFR\_internalize}$$

$$v_{30} = [\text{MEK}] \cdot \text{MEK\_phosphorylation\_pEGFR} \cdot [\text{pEGFRd}]$$

$$v_{31} = [\text{MEK}] \cdot \text{MEK\_phosphorylation\_pMet\_EGFR} \cdot [\text{pMet\_EGFR}]$$

$$v_{32} = [\text{MEK}] \cdot \text{MEK\_phosphorylation\_pMet} \cdot [\text{pMetd}]$$

$$v_{33} = [\text{pMEK}] \cdot \text{pMEK\_dephosphorylation}$$

$$v_{34} = [\text{ERK}] \cdot \text{ERK\_phosphorylation\_pMEK} \cdot [\text{pMEK}]$$

$$v_{35} = [\text{pERK}] \cdot \text{pERK\_dephosphorylation}$$

$$v_{36} = [\text{AKT}] \cdot \text{AKT\_activation\_pEGFR} \cdot [\text{pEGFRd}]$$

$$v_{37} = [\text{AKT}] \cdot \text{AKT\_activation\_pMet\_EGFR} \cdot [\text{pMet\_EGFR}]$$

$$v_{38} = [\text{AKT}] \cdot \text{AKT\_activation\_pMet} \cdot [\text{pMetd}]$$

$$v_{39} = [\text{pAKT}] \cdot \text{pAKT\_deactivation} \cdot (\text{is838} \cdot (\text{relto\_AKT\_deact} - 1) + 1)$$

**Table 6.10: Estimated dynamic parameter values.** In total 345 parameters were estimated from the experimental data yielding a value of the objective function  $-2 \log(L) = -3244.86$  for a total of 3030 datapoints. Dynamic parameters are listed below.  $\hat{\theta}$  indicates the estimated value,  $\theta_{min}$  and  $\theta_{max}$  indicate the upper and lower bounds of the parameters. The log-column indicates, whether the value of a parameter was log-transformed (t) or not (f). The fitted-column indicates, whether the parameter value was estimated (t) or whether its value was fixed to a constant value (f). Fixed parameters comprise MET\_activation that could be fixed as part of model reduction. EGF\_kD and Met\_kD represent ligand binding affinities taken from the literature,<sup>[58,279]</sup> and EGFR\_TKI\_binding, init\_AKT, init\_ERK, init\_pEGFRd and init\_MEK could be fixed due to symmetries in the model structure leading to structural non-identifiabilities.<sup>[280]</sup> scale\_Ligand, describes the fitted scaling of the ligand concentration measured in ng/mL to count/ $\mu\text{m}^2$ , which was chosen for the initial receptor concentrations within the mathematical model. The mathematical model was developed by H. Hass.

Name	$\theta_{min}$	$\hat{\theta}$	$\theta_{max}$	log	non-log $\hat{\theta}$	fitted
AKT_activation_pEGFR	-5	-1.9441	3	t	$1.14 \cdot 10^{-02}$	t
AKT_activation_pMet	-5	-1.6900	3	t	$2.04 \cdot 10^{-02}$	t
AKT_activation_pMet_EGFR	-5	-2.3502	3	t	$4.46 \cdot 10^{-03}$	t
EGFR_TKI_binding	-5	3.0000	4	t	$1.00 \cdot 10^{+03}$	f
EGFR_TKI_unbinding	-5	2.5884	3	t	$3.88 \cdot 10^{+02}$	t
EGFR_activation	-5	0.1611	3	t	$1.45 \cdot 10^{+00}$	t
EGFR_lig_binding	-5	-2.4543	3	t	$3.51 \cdot 10^{-03}$	t
EGF_kD	-5	-1.3010	3	t	$5.00 \cdot 10^{-02}$	f
ERK_phosphorylation_pMEK	-5	0.4870	3	t	$3.07 \cdot 10^{+00}$	t
MEK_phosphorylation_pEGFR	-5	-1.4307	3	t	$3.71 \cdot 10^{-02}$	t
MEK_phosphorylation_pMet	-5	-1.4376	3	t	$3.65 \cdot 10^{-02}$	t
MEK_phosphorylation_pMet_EGFR	-5	-2.4451	3	t	$3.59 \cdot 10^{-03}$	t
Met_activation	-3	4	6	t	$1.00 \cdot 10^{+04}$	f
Met_basal_activation	-10	-6.9940	3	t	$1.01 \cdot 10^{-07}$	t
Met_kD	-5	-0.6021	3	t	$2.50 \cdot 10^{-01}$	f
Met_lig_binding	-5	-3.1930	3	t	$6.41 \cdot 10^{-04}$	t
diRatio	-5	-0.3781	3	t	$4.19 \cdot 10^{-01}$	t
init_AKT	-5	0.0000	3	t	$1.00 \cdot 10^{+00}$	f
init_EGFR	-5	2.9666	5	t	$9.26 \cdot 10^{+02}$	t
init_ERK	-5	0.0000	3	t	$1.00 \cdot 10^{+00}$	f
init_MEK	-5	0.0000	3	t	$1.00 \cdot 10^{+00}$	f
init_Met	-5	2.0508	3	t	$1.12 \cdot 10^{+02}$	t
init_pEGFRd	-4	0.0000	2	f	$0.00 \cdot 10^{+00}$	f
k_EGFRub	-5	0.3690	3	t	$2.34 \cdot 10^{+00}$	t
nH	0	3.0000	10	f	$3.00 \cdot 10^{+00}$	f
pAKT_deactivation	-5	-2.2598	3	t	$5.50 \cdot 10^{-03}$	t
pEGFR_degradation	-5	-2.2930	3	t	$5.09 \cdot 10^{-03}$	t
pEGFR_internalize	-5	-1.8222	3	t	$1.51 \cdot 10^{-02}$	t

## 6 Appendix

---

pEGFR_internalize_ub	-5	-0.5605	3	t	$2.75 \cdot 10^{-01}$	t
pEGFRi_dephosph	-5	-2.4644	3	t	$3.43 \cdot 10^{-03}$	t
pERK_dephosphorylation	-5	-0.1417	3	t	$7.22 \cdot 10^{-01}$	t
pMEK_dephosphorylation	-5	-0.9193	3	t	$1.20 \cdot 10^{-01}$	t
pMet_EGFR_internalize	-5	-1.8076	3	t	$1.56 \cdot 10^{-02}$	t
pMet_degradation	-5	-2.0260	3	t	$9.42 \cdot 10^{-03}$	t
pMet_internalize	-5	-0.5389	3	t	$2.89 \cdot 10^{-01}$	t
pMeti_dephosph	-5	-2.0203	3	t	$9.54 \cdot 10^{-03}$	t
relto_AKT_deact	-5	1.2696	3	t	$1.86 \cdot 10^{+01}$	t
relto_init_EGFR	-5	-0.6918	3	t	$2.03 \cdot 10^{-01}$	t
relto_init_MEK	-5	-0.1331	3	t	$7.36 \cdot 10^{-01}$	t
relto_init_Met	-5	-0.1250	3	t	$7.50 \cdot 10^{-01}$	t
scale_Ligand	-3	1.2618	6	t	$1.83 \cdot 10^{+01}$	t

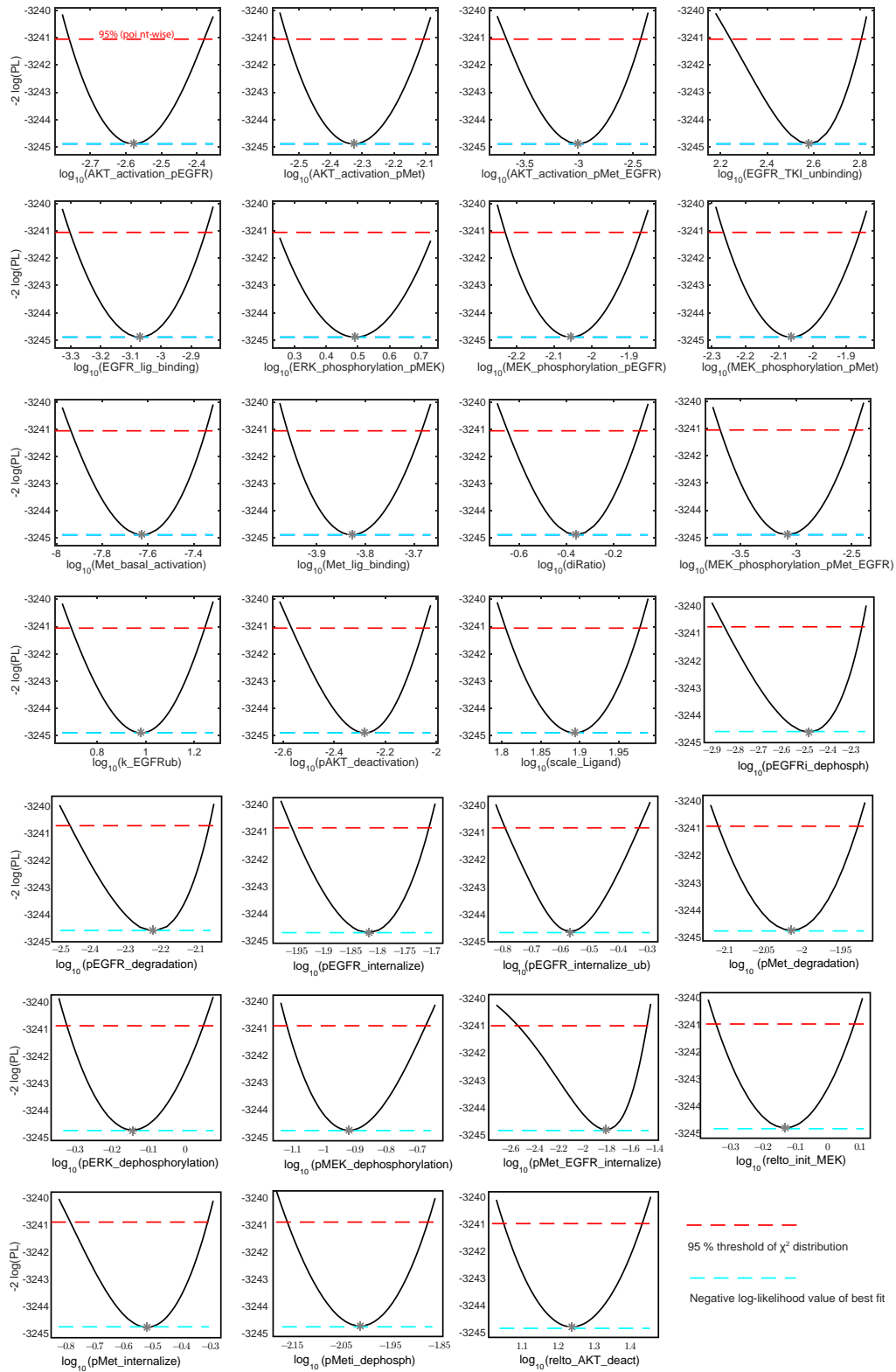


**Figure 6.2: Parameter profiles of final EGFR/MET crosstalk model.** Parameter profiles of the dynamic parameters used in the final mechanistic model. All parameters reach the 95 % threshold given by the  $\chi^2$  distribution, thus are identifiable. Parameter profiles were calculated by H. Hass.

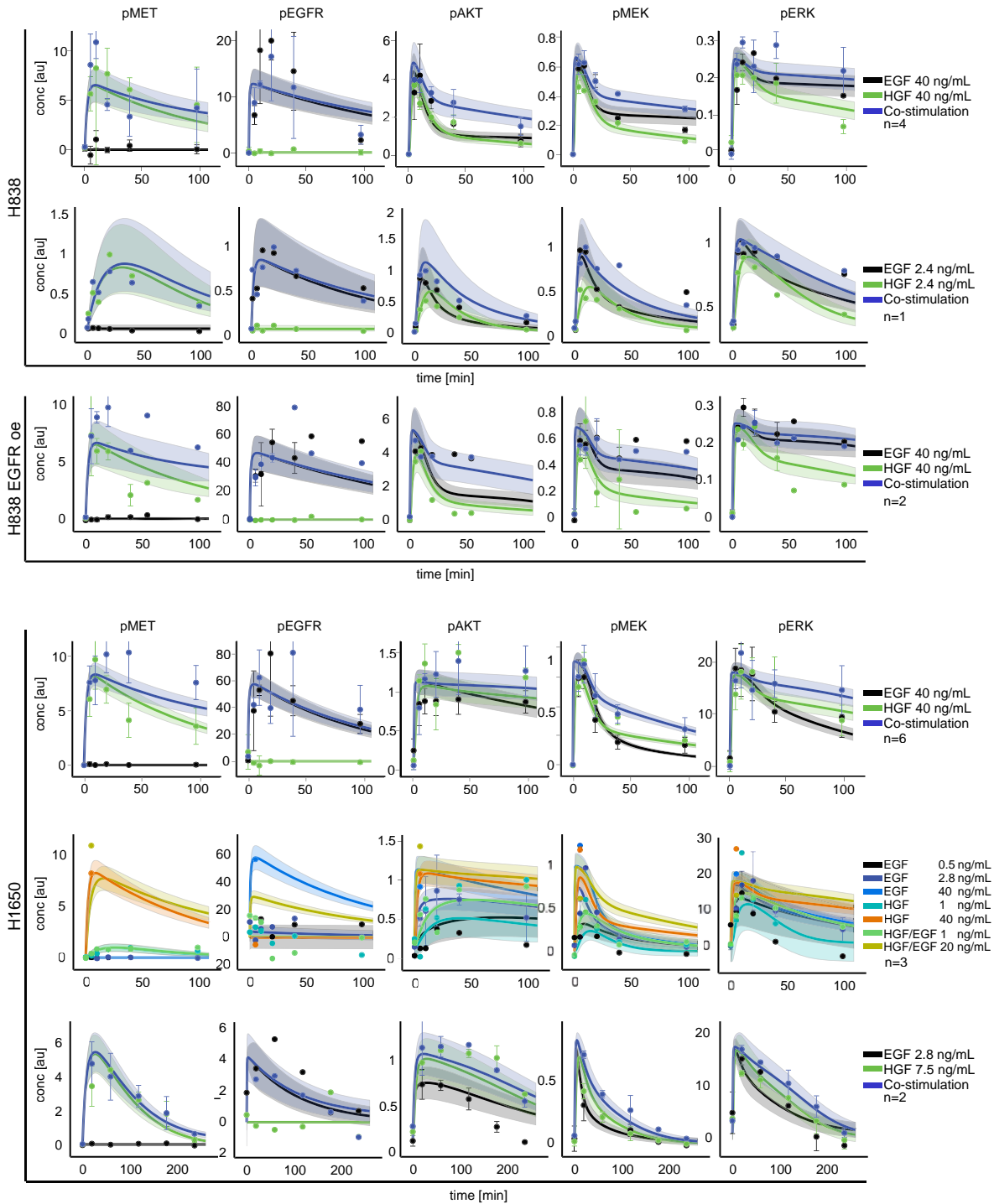


**Figure 6.3: Extended data used for parameter estimation.** Data of time-resolved response of H838, H1650 and H838-EGFR cells is shown as dots with error bars. Errors represent standard deviation from individual replicates indicated in the figure. Model trajectories are displayed as lines and shading represents the estimated error by the model. The error bars on the data represent the model-scaled measurement uncertainty of the biological replicates.

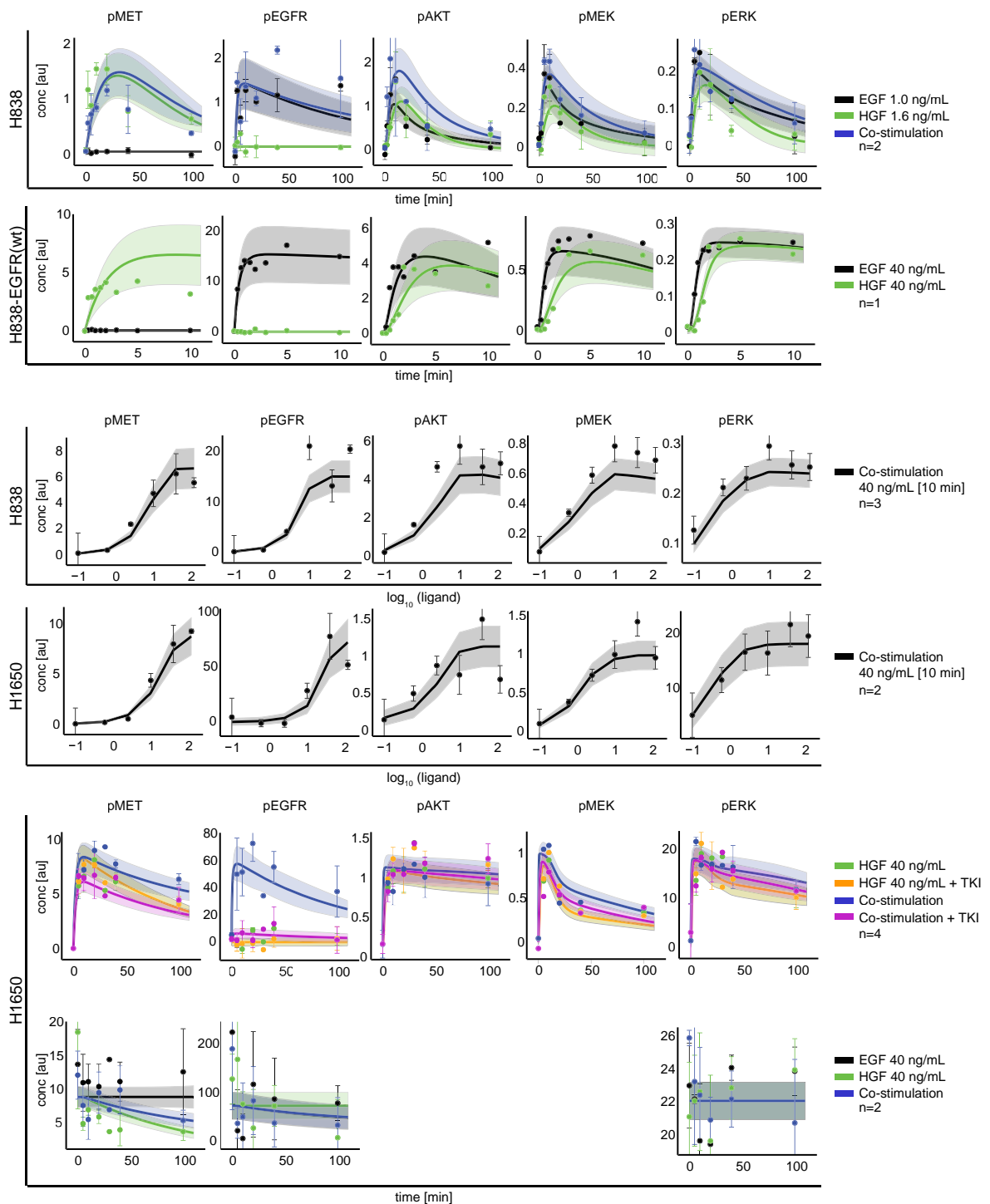


**Figure 6.4: Extended data used for parameter estimation.** Data of time- and dose-resolved response of H838, H1650 and H838-EGFR cells is shown as dots with error bars. Errors represent standard deviation from individual replicates indicated in the figure. Model trajectories are displayed as lines and shading represents the estimated error by the model. The error bars on the data represent the model-scaled measurement uncertainty of the biological replicates.

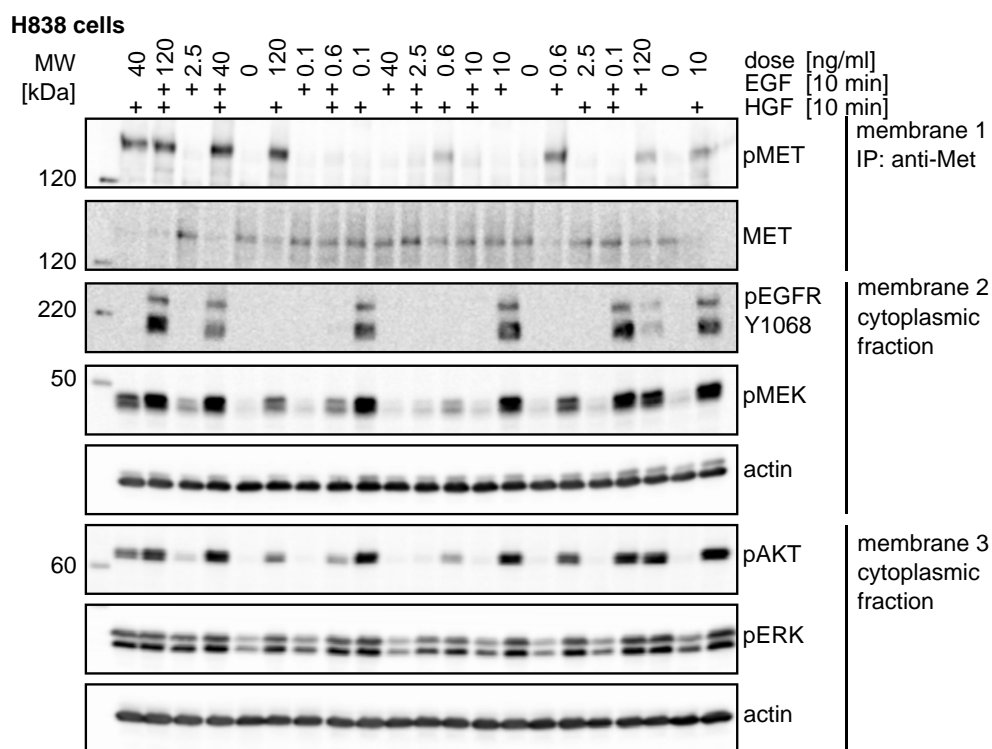


**Figure 6.5: Exemplary immunoblot of dose-dependent response in H838 cells.** Sample loading was randomized to avoid systematic blotting errors.<sup>[204]</sup> MET phosphorylation and total protein levels were detected after immunoprecipitation (IP). The remaining proteins were detected from cytoplasmic cell lysate. Utilized antibodies are described in Table 4.4.

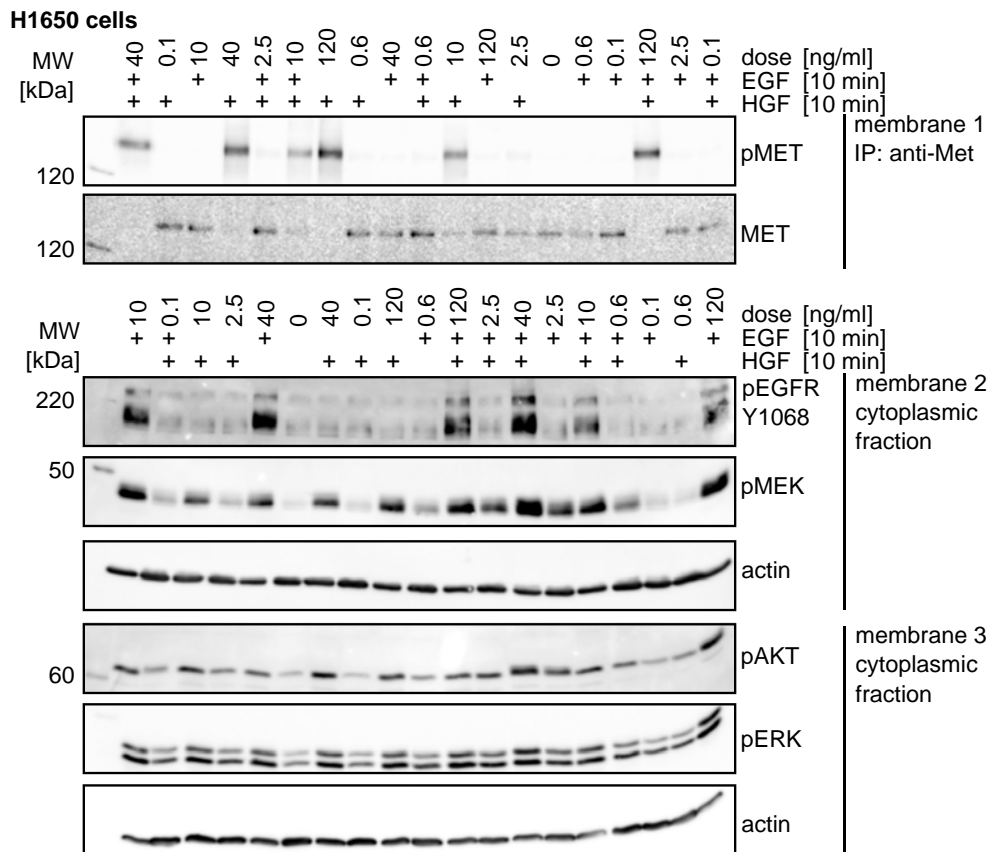


**Figure 6.6: Exemplary immunoblot of dose-dependent response in H1650 cells.** Sample loading was randomized to avoid systematic blotting errors.<sup>[204]</sup> MET phosphorylation and total protein levels were detected after immunoprecipitation (IP). The remaining proteins were detected from cytoplasmic cell lysate. Utilized antibodies are described in Table 4.4.

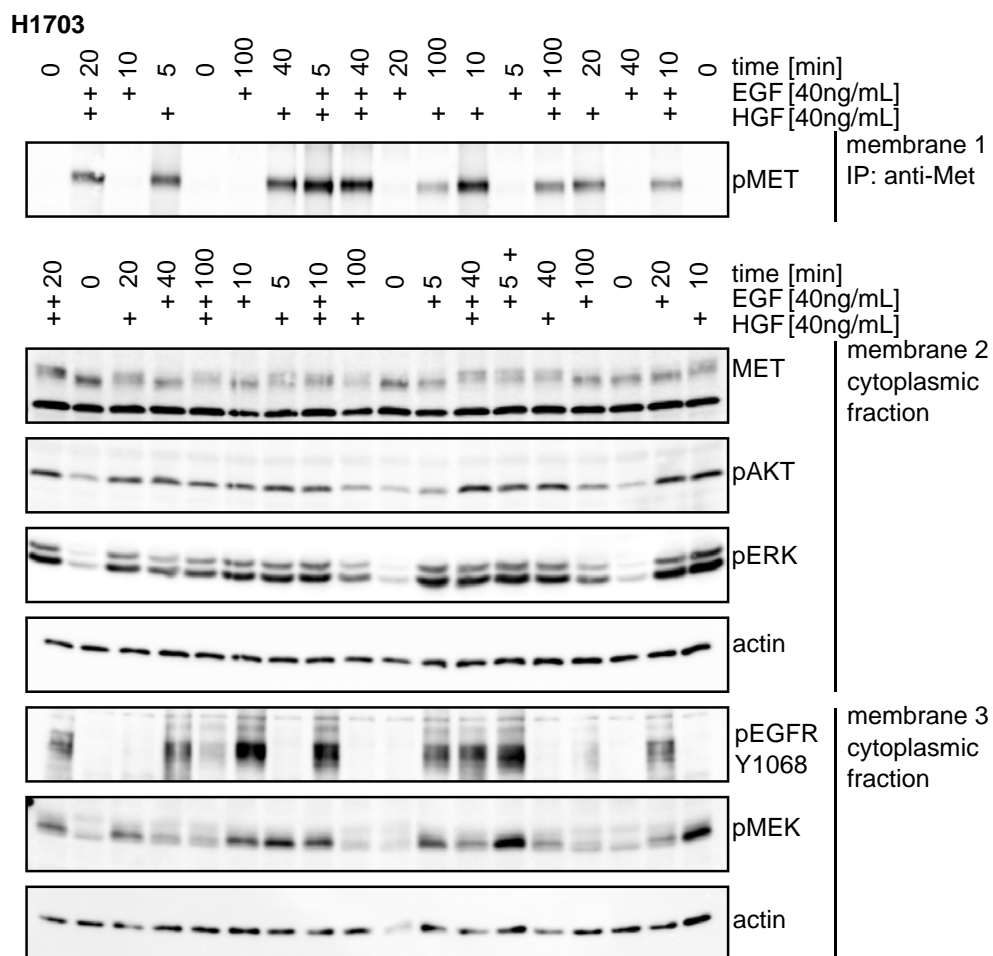


**Figure 6.7: Exemplary immunoblot of H1703 cells.** Sample loading was randomized to avoid systematic blotting errors.<sup>[204]</sup> MET phosphorylation levels were detected after immunoprecipitation (IP). The remaining proteins were detected from cytoplasmic cell lysate. Utilized antibodies are described in Table 4.4.

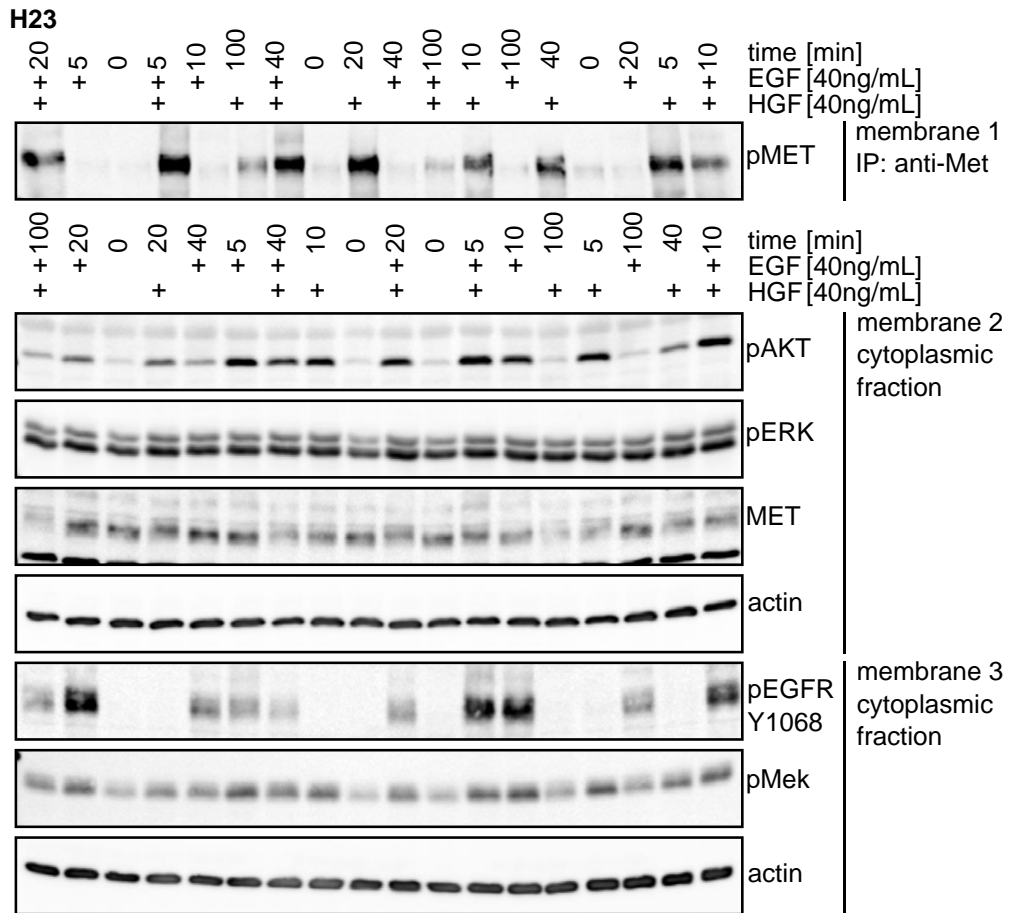


**Figure 6.8: Exemplary immunoblot of H23 cells.** Sample loading was randomized to avoid systematic blotting errors.<sup>[204]</sup> MET phosphorylation levels were detected after immunoprecipitation (IP). The remaining proteins were detected from cytoplasmic cell lysate. Utilized antibodies are described in Table 4.4.



## Acknowledgements

This thesis would not have been possible without the help of many people. First of all, I would like to thank Prof. Dr. Ursula Klingmüller for giving me the opportunity to work in her group on several exciting projects over the past years. I'm very grateful for her continuous support and advice.

I would like to thank Prof. Dr. Dirk-Peter Herten for his contribution to the project and for being the referee for this thesis. Additionally, I would like to thank Prof. Dr. Britta Brügger and Prof. Dr. Stefan Wiemann for acting as examiners.

I acknowledge funding from the BMBF supported projects LungSys and DZL.

Especially, I would like to thank Dr. Marcel Schilling for his steady, structured and constructive advice, for inspiring discussions and for his help with all experimental, theoretical and formal problems.

A very special thank you to all my collaboration partners who were part of various projects during my PhD and who became good friends during that time. I'm also very grateful for the unique collaboration with the Timmer group. Helge in particular has been an enormous help with his mathematical and conceptual support. It has been a very rewarding collaboration on a professional as well as personal level. I would like to thank Jens, Bernie, Andreas and Markus of the Timmer group for their ongoing efforts in explaining complex mathematical problems in an easy way.

I'm grateful to Sigi, not only my "Cloning-Padawan", but also a good friend and a great help during the difficult phases of the project. I would also like to thank my collaboration partners from BioQuant, Thoraxklinik and EMBL for their support.

I would like to thank all current and former B200 group members for the great, productive and cooperative atmosphere. Especially, all "Lung-people" for having a great time at multiple meetings and conferences, our TAs for a worry-free daily lab routine and Xizhe for his help with cells, blots and plasmids.

A special thank you to my box, for having a fantastic time day and night in the lab. I would like to thank Julie for introducing me into the secrets of systems biology and high throughput data production. I'm also grateful for the time with Katha, Marie, Frédérique, Melissa and Lorenz and their help with countless small things. I very much enjoyed our frequent "box cookings" and bouldering sessions that were and hopefully will be a great opportunity to chat and to relax.

Finally, I want to thank my parents, my brother Sebastian and my grandma Elfi for their love and support. Especially, I'm thankful for being together with my "Fee", for her love and patience.



## **Eidesstattliche Erklärung**

Hiermit versichere ich, die vorgelegte Dissertation selbstständig und nur unter Verwendung der von mir angegebenen Quellen und Hilfsmittel verfasst zu haben. Sowohl inhaltlich als auch wörtlich entnommene Inhalte wurden als solche kenntlich gemacht.

Weiterhin erkläre ich hiermit, an keiner anderen Stelle ein Prüfungsverfahren beantragt, bzw. die Dissertation in dieser oder anderer Form bereits anderweitig als Prüfungsarbeit verwendet oder einer anderen Fakultät als Dissertation vorgelegt zu haben.

Datum: \_\_\_\_\_ Unterschrift: \_\_\_\_\_